

# Quantum Gas Microscopy of Strongly Correlated Fermions

by

Lawrence W. Cheuk

A.B., Princeton University (2010)

Submitted to the Department of Physics  
in Partial Fulfillment of the Requirements for the Degree of  
Doctor of Philosophy

at the

MASSACHUSETTS INSTITUTE OF TECHNOLOGY

June 2017

© Massachusetts Institute of Technology 2017. All rights reserved.

Author .....  
Department of Physics  
May 26, 2017

Certified by .....  
Martin W. Zwierlein  
Professor of Physics  
Thesis Supervisor

Accepted by .....  
Nergis Mavalvala  
Associate Department Head



# Quantum Gas Microscopy of Strongly Correlated Fermions

by

Lawrence W. Cheuk

Submitted to the Department of Physics  
on May 26, 2017, in partial fulfillment of the  
requirements for the Degree of  
Doctor of Philosophy

## Abstract

This thesis describes experiments on ultracold fermionic atoms, and can be divided into two areas. The first concerns spin-orbit coupling; the second concerns quantum gas microscopy.

With the use of Raman transitions, 1D spin-orbit coupling of ultracold  ${}^6\text{Li}$  was realized. Using a novel type of spectroscopy, spin-injection spectroscopy, where the spin, energy, and momentum are all resolved, we directly observed the spinful dispersions of the spin-orbit bands. In addition, we demonstrated selective adiabatic loading of the spin-orbit bands, which can be used to create a spinless Fermi gas with effective  $p$ -wave interactions. Spin-injection spectroscopy was further applied to a novel spinful lattice system created using Raman and radio-frequency coupling, which allowed for state tomography of spinful bands.

The second part of this thesis describes quantum gas microscopy of ultracold fermions. This enables one to simulate the Fermi-Hubbard model, a prototypical strongly correlated model, with site-resolved detection and control capabilities.

A new apparatus that can detect fermionic  ${}^{40}\text{K}$  in a square lattice with single-site resolution was constructed. High-fidelity site-resolved imaging was achieved using Raman imaging, which allowed for the direct observation of the band-insulating, the metallic, and the Mott-insulating states of the Hubbard model. The interaction-driven Mott insulator, where doubly occupied sites are highly suppressed, illustrates the strongly correlated nature of the Hubbard model.

Harnessing the capability to measure the occupations of individual lattice sites with the microscope, we explored spatial correlations of both spin and charge in the Hubbard model as a function of doping. For the spin correlations, we observed weakening of antiferromagnetic correlations away from half-filling. However, in the charge correlations between local magnetic moments, non-monotonic behavior was observed. This can be understood as arising from competition between Pauli-blocking, dominant at low fillings, and doublon-holon bunching, which arises from superexchange and is strongest at half-filling. The anti-bunching correlations at low filling can be interpreted as the first direct real-space observation of the interaction-enhanced Pauli hole.

Thesis Supervisor: Martin W. Zwierlein  
Title: Professor of Physics

*To my family*



## Acknowledgments

First and foremost, I would like to thank my research advisor, Martin Zwierlein, for his guidance and support throughout the years. Martin has taught me a great deal about physics, ranging from how to understand strongly interacting fermions to practical advice on making ultracold fermions. I am always amazed by the many new ideas that come out of our discussions. In addition, I am thankful for the freedom that Martin gives me to pursue ideas that I find interesting.

I would also like to thank the people that I have directly worked with, both in BEC 1 and in Fermi 2. When I first started in BEC 1, Ariel and Mark taught me many of the essential skills of running an ultracold experiment. I also learned a lot from our two very talented post-docs, Waseem and Tarik.

With regards to Fermi 2, the new microscope experiment that I joined in my third year, I am indebted to Waseem, Thomas Gersdorf, Vinay, and David Reens for their groundwork on designing and setting up Fermi 2. Waseem was very knowledgeable, and provided invaluable guidance. Thomas Gersdorf accomplished a great deal with phenomenal speed during his short time at MIT. I had a great time working together with Vinay in setting up the optical lattices and observing  $^{23}\text{Na}$  Mott insulators in our experiment for the first time. My thanks also go out to the more recent generation of Fermi 2 members, Matt, Katherine, Melih, and Hao. During her time in Fermi 2, Katherine impressed me with her ability to quickly learn the various complexities of the experiment. Special thanks go out to Matt for his attention to detail, his ability to point out my mistakes, and for making the lab an enjoyable workplace. With Matt, Melih, and Hao, I am sure Fermi 2 will be in good hands.

I am also thankful for the other current and former members of Martin's group with whom I have interacted, and from whom I have learnt much. Special thanks go out to Sebastian, for his invaluable advice both in and out of lab.

In addition, I thank Wolfgang's group for fruitful discussions, and for their generous sharing of lab equipment. I would also like to thank Zoran, who visited us on many occasions, and contributed to our explorations of spin-orbit coupled Fermi

gases. My gratitude also goes out to my academic advisor, Dave Pritchard, and to the CUA and RLE staff who have made our research possible.

Finally, I would like to thank the following people who have added greatly to my time here outside of lab: my roommates Niki and Timur, Matt, Julian, Parth, Sebastian, Waseem, Tarik, Ariel, Peter, Zoe, Katherine, Zak, Colin, Jesse, Ivana, Michael Messer, Vinay, Thomas Gersdorf, Brad, Chris, Andrew, Dave, Amanda, Erin, Kara, Dan Rothenberg, Nathan, Dan Amrhein, Ian, and Malinda.

# Contents

<b>1</b>	<b>Overview</b>	<b>19</b>
1.1	Thesis Outline . . . . .	22
<b>2</b>	<b>Ultracold Fermi Gases</b>	<b>25</b>
2.1	Non-Interacting Fermions . . . . .	25
2.1.1	Ideal Fermi Gas in Free Space . . . . .	26
2.1.2	Ideal Fermi Gas in a Lattice . . . . .	30
2.2	Interacting Fermions in Free Space . . . . .	37
2.2.1	Feshbach Resonances . . . . .	40
2.2.2	Interacting Fermi Gas in Two Dimensions . . . . .	42
2.3	Interacting Fermions on a Lattice . . . . .	49
2.3.1	Fermi-Hubbard Model in the Tight-Binding Limit . . . . .	49
2.3.2	Phenomenology of the Hubbard Model: Metals, Band Insulators and Mott Insulators . . . . .	51
2.3.3	Some Theoretical Approaches . . . . .	55
<b>3</b>	<b>Spin-Orbit Coupled Fermions</b>	<b>59</b>
3.1	Why Spin-Orbit Coupling? . . . . .	60
3.1.1	The Su-Schrieffer-Heeger Model . . . . .	62
3.1.2	Obtaining $p$ -Wave Interactions via Spin-Orbit Coupling . . . . .	66
3.1.3	The Kitaev Chain . . . . .	68
3.2	Implementing Spin-Orbit Coupling with Raman Beams . . . . .	73
3.2.1	Raman Coupling in Alkali Atoms . . . . .	75

3.2.2	Raman Coupling in ${}^6\text{Li}$ . . . . .	77
3.3	Detecting Spin-Orbit Coupling . . . . .	81
3.3.1	Spin-Injection Spectroscopy . . . . .	85
3.3.2	Measuring Spinful Bands in an RF-Raman Lattice . . . . .	89
3.4	Some Concluding Thoughts . . . . .	94
<b>4</b>	<b>A Quantum Gas Microscope for Fermionic <math>{}^{40}\text{K}</math></b>	<b>97</b>
4.1	Producing Ultracold ${}^{40}\text{K}$ . . . . .	98
4.2	The High-Resolution Imaging System . . . . .	102
4.3	The 2D Square Optical Lattice . . . . .	105
4.4	Single-Site Imaging Beams . . . . .	107
4.5	Additional Optical Beams for Trapping and Transport . . . . .	107
4.5.1	The 5-Degree Beam . . . . .	108
4.5.2	The Accordion Beam . . . . .	109
4.5.3	The Movable Crossed Optical Dipole Trap . . . . .	110
4.5.4	The Dimple Beam . . . . .	110
4.6	Imaging Paths . . . . .	112
<b>5</b>	<b>Site-Resolved Imaging of <math>{}^{40}\text{K}</math></b>	<b>115</b>
5.1	Considerations for Single-Site Imaging . . . . .	116
5.2	Issues with Imaging ${}^{40}\text{K}$ in 1064 nm Light . . . . .	118
5.2.1	Anti-Trapping of the $4p$ States . . . . .	120
5.2.2	Mixing of Excited Hyperfine Levels . . . . .	121
5.3	Raman Sideband Cooling . . . . .	123
5.3.1	How Raman Sideband Cooling Works . . . . .	123
5.3.2	What to Do About the Excited States? . . . . .	126
5.4	Implementing Raman Imaging of ${}^{40}\text{K}$ . . . . .	131
5.4.1	Preparing a Single Layer of ${}^{40}\text{K}$ Atoms . . . . .	131
5.4.2	Raman and Optical Pumping Scheme . . . . .	134
5.4.3	How to Make Raman Imaging Work . . . . .	135
5.5	Image Reconstruction and Fidelity Estimation . . . . .	139

5.5.1	Identifying Lattice Axes and Spacings . . . . .	139
5.5.2	Image Deconvolution . . . . .	140
5.5.3	Identifying the Phases of the Lattices . . . . .	144
5.5.4	Identifying the Occupation of Lattice Sites . . . . .	144
5.5.5	Estimating Image Fidelity . . . . .	145
5.5.6	Bounding Possibility of Density Dependent Losses . . . . .	147
5.5.7	Estimating Raman Cooling Performance . . . . .	148
<b>6</b>	<b>Quantum Gas Microscopy of Metals and Insulators</b>	<b>151</b>
6.1	Producing Quantum Degenerate Gases Near the Substrate . . . . .	152
6.1.1	Moving the Magnetic Trap . . . . .	152
6.1.2	A New Transport Scheme . . . . .	154
6.1.3	Evaporation of a Single Layer . . . . .	160
6.2	Site-resolved Profiles of Metals and Insulators . . . . .	161
6.2.1	The Local Moment and Its Properties . . . . .	163
6.2.2	Thermometry Using Site-Resolved Images . . . . .	165
6.3	Charge and Spin Correlations in the Fermi-Hubbard Model . . . . .	171
6.3.1	How to Measure Spin Correlations . . . . .	172
6.3.2	Charge Correlations as a Function of Filling . . . . .	174
6.3.3	The Double Well at Half-Filling: a Toy Model . . . . .	180
<b>7</b>	<b>Summary and Outlook</b>	<b>185</b>
<b>A</b>	<b>Coils and Magnetic Fields for <math>^{40}\text{K}</math> Quantum Gas Microscope</b>	<b>189</b>
<b>B</b>	<b>Laser Systems for <math>^{40}\text{K}</math> Quantum Gas Microscope</b>	<b>193</b>
B.1	$^{40}\text{K}$ Laser System . . . . .	194
B.2	$^{23}\text{Na}$ Laser System . . . . .	198
B.3	Raman Imaging Laser System . . . . .	198
B.4	1064 nm Laser System . . . . .	201
<b>C</b>	<b><math>^{40}\text{K}</math> Feshbach Resonances</b>	<b>203</b>

<b>D Evolution of Fermion Pairing from Three to Two Dimensions</b>	<b>209</b>
<b>E Spin-Injection Spectroscopy of a Spin-Orbit Coupled Fermi Gas</b>	<b>215</b>
<b>F Quantum-Gas Microscope for Fermionic Atoms</b>	<b>221</b>
<b>G Observation of 2D Fermionic Mott Insulators of <math>^{40}\text{K}</math> with Single-Site Resolution</b>	<b>227</b>
<b>H Observation of Spatial Charge and Spin Correlations in the 2D Fermi-Hubbard Model</b>	<b>233</b>

# List of Figures

2-1	Friedel Oscillations at $T = 0$ . . . . .	29
2-2	Friedel Oscillations in 1D at Finite Temperature . . . . .	30
2-3	Ratio of Nearest Neighbor Hopping Amplitude to Next-Nearest Neighbor Hopping Amplitude . . . . .	33
2-4	Nearest Neighbor Hopping Amplitude Comparison . . . . .	34
2-5	$- G(\mathbf{r}) ^2$ on a Square Lattice . . . . .	36
2-6	Lippmann-Schwinger Equation . . . . .	39
2-7	Dissociation Spectrum of Bound Molecules in 2D . . . . .	48
2-8	Ratio of On-Site Interaction to Nearest-Neighbor Interaction . . . . .	50
2-9	States of the Fermi-Hubbard Model . . . . .	52
2-10	Nesting on the Half-Filled Square Lattice . . . . .	53
2-11	Schematic Phase Diagram of Cuprates . . . . .	55
3-1	The SSH Model . . . . .	63
3-2	Spin-Orbit Bands . . . . .	67
3-3	Two-Photon Coupling Diagram . . . . .	73
3-4	Raman Coupling via $p_{1/2}$ and $p_{3/2}$ Excited States . . . . .	77
3-5	Figure-of-Merit $\xi$ of Raman Coupling in ${}^6\text{Li}$ Ignoring Hyperfine Structure	78
3-6	Breit-Rabi and Magnetic Field dependence of Raman Coupling . . . . .	80
3-7	Raman Beam Geometry and Polarizations . . . . .	81
3-8	Spin and Momentum-Resolved Images and Profiles . . . . .	82
3-9	Raman Transfer Versus Two-Photon Detuning . . . . .	83
3-10	Momentum-Dependent Rabi Oscillations . . . . .	84

3-11	Adiabatic Loading of Spin-Orbit Bands . . . . .	85
3-12	Spin-Injection Spectroscopy . . . . .	86
3-13	Bare Spectra from Spin-Injection Spectroscopy of Spin-Orbit Coupled Fermions . . . . .	88
3-14	Spin-Orbit Bands Reconstructed from Spin-Injection Spectroscopy Spectra . . . . .	88
3-15	Simple Lattice Versus Raman Lattice . . . . .	90
3-16	Band Structure of Raman-RF Lattice . . . . .	91
3-17	Spin-Injection Spectroscopy on a Raman-RF Lattice . . . . .	93
3-18	Extracting Spin Composition for the Raman-RF Lattice . . . . .	94
4-1	Top View of Vacuum Chamber . . . . .	99
4-2	Side View Along $\hat{x}$ of Various Beams . . . . .	100
4-3	Side View Along $\hat{y}$ of Various Beams . . . . .	101
4-4	Coils Used for Generating Magnetic Fields . . . . .	102
4-5	High-Resolution Imaging System . . . . .	104
4-6	Side View of Lattice, Imaging and Raman Cooling Beams . . . . .	106
4-7	Trapping Potential Formed by the 5-Degree Beam . . . . .	108
4-8	The “Accordion” Beam . . . . .	109
4-9	$x$ and $y$ Crossed ODT Beams . . . . .	111
4-10	Vertical Imaging Paths $z_1$ and $z_2$ . . . . .	114
5-1	Energy Levels in a Deep Lattice . . . . .	118
5-2	Level Structure of Lowest Excited States in $^{40}\text{K}$ ; Hyperfine Structure of $4p$ Levels in $^{40}\text{K}$ . . . . .	119
5-3	Energy Diagram of $4p_{3/2}$ Levels in the Presence of 1064 nm Light . . . . .	122
5-4	The Sideband-Resolved Regime . . . . .	124
5-5	Sideband Cooling . . . . .	125
5-6	Dressed States at Zero Detuning . . . . .	129
5-7	Dressed States at Non-Zero Detuning . . . . .	130
5-8	“Slicing” Spectrum . . . . .	132

5-9	Sideband Asymmetry Measured via Raman Spectroscopy . . . . .	136
5-10	Stark Shifts of the D2 Transitions . . . . .	137
5-11	First Signal of Single Atoms . . . . .	139
5-12	Identifying Lattice Axes and Spacings . . . . .	141
5-13	Point-Spread Function . . . . .	142
5-14	Image Deconvolution . . . . .	143
5-15	Lattice Phase Identification . . . . .	144
5-16	Identifying Site Occupation . . . . .	145
5-17	Loss Rate and Hopping Rate During Imaging . . . . .	146
5-18	Single-Site Image with Optimized Imaging . . . . .	147
5-19	Bounding Distance-Dependent Losses with $g_2(r)$ . . . . .	148
5-20	Sideband Spectra After Raman Imaging . . . . .	149
6-1	Atom Number versus Magnetic Trap Position . . . . .	153
6-2	Trap Position of Offset Quadrupole Trap . . . . .	154
6-3	Heating Rate in Offset Quadrupole Magnetic Trap . . . . .	155
6-4	$^{23}\text{Na}$ Condensates in the Crossed ODT Before Optical Transport . . .	156
6-5	$^{23}\text{Na}$ Condensate After Transport to 160 $\mu\text{m}$ Below Substrate . . .	158
6-6	Transport Using the Accordion Beam . . . . .	159
6-7	$^{23}\text{Na}$ Condensate in 5-degree Beam After Optical Transport . . .	160
6-8	Slicing Spectrum After Loading from Accordion . . . . .	160
6-9	Site-Resolved Images of Metals and Insulators . . . . .	164
6-10	Band Transition Frequencies . . . . .	167
6-11	Calibrating $U$ Via Lattice Modulation . . . . .	168
6-12	Radially Averaged Profile of a Sample with Coexisting Metallic, Mott Insulating and Band Insulating Regions . . . . .	169
6-13	Nearest-Neighbor Moment Spin $C_s(1)$ . . . . .	174
6-14	Nearest-Neighbor Moment Correlator $C_m(1)$ . . . . .	175
6-15	$g_2(1)$ and $\bar{g}_2(1)$ as a Function of Doping . . . . .	177

6-16 Various Contribution to the Nearest-Neighbor Moment-Moment Correlator . . . . .	179
B-1 Main Laser Table for $^{40}\text{K}$ D2 Light . . . . .	196
B-2 Sub-system for $^{40}\text{K}$ Master Laser . . . . .	196
B-3 Sub-system for D2 Imaging Laser . . . . .	197
B-4 Main Laser Table for $^{23}\text{Na}$ D2 Light. . . . .	198
B-5 Locking Sub-system for $^{23}\text{Na}$ . . . . .	199
B-6 Laser System for D1 Light for $^{40}\text{K}$ . . . . .	199
B-7 Sub-system for D1 Master Laser . . . . .	200
B-8 Laser System for Raman Light for $^{40}\text{K}$ . . . . .	200
B-9 1064 nm Laser System Schematics . . . . .	201
C-1 Some Feshbach Resonances of $^{40}\text{K}$ . . . . .	208

# List of Tables

A.1	List of Power Supplies and Coils . . . . .	190
A.2	Magnetic Field and Gradient Calibration for Feshbach and Curvature Coils . . . . .	191
B.1	List of Fibers to Experiment . . . . .	195
B.2	D1 Locking Frequencies . . . . .	200
C.1	List of Feshbach Resonances of ${}^{40}\text{K}$ . . . . .	206
C.2	Higher Channel $l = 0$ Feshbach Resonances for $M_F = 0$ . . . . .	207



# Chapter 1

## Overview

Since the realization of quantum degeneracy of large ensembles of atoms, ultracold atomic gases has proven to be a highly flexible platform for experimentally exploring quantum many-body systems [14]. For example, the realization of Bose-Einstein condensates with bosonic atoms [5, 29] enabled experimental studies of a new form of quantum matter. The quantum statistics of bosons allowed a macroscopic number of particles into a single quantum state, realizing macroscopic matter waves. Measurements of the excitations and responses have revealed the interplay of interactions and quantum statistics, leading to new insights for these systems [72]. For example, questions such as whether a condensate has a phase [6], the relation between superfluidity and condensation [99, 115], and the nature of excitations [132, 139], can all be experimentally addressed.

A few years after the first Bose-Einstein condensates were realized, large ensembles of quantum degenerate gases of fermionic atoms were created [30, 127, 137, 66, 43, 48]. Compared to their bosonic counterparts, fermionic atoms obey different quantum statistics. These statistics, Fermi statistics, forbid two identical fermions to be in the same quantum state, a rule also known as the Pauli exclusion principle. This Pauli-blocking effect has profound consequences in both few-body and many-body systems, ranging from the electronic structure of atoms to the stability of neutron stars and white dwarfs.

Due to the pervasiveness of fermionic systems in nature, quantum-degenerate

samples of ultracold fermionic atoms opened up the possibility to simulate a large class of models that describe many different physical systems, ranging from the surface of neutron stars to the electrons in real-life materials. This idea of simulating a many-body system through an analogous realization - in this case, a system of atoms - is known as “quantum simulation.” This approach is particularly attractive in the case of strongly interacting many-body fermionic systems, which are generically difficult to solve due to the fermion sign problem, a consequence of Fermi exchange statistics [136]. Experiments on ultracold Fermi gas can thus provide invaluable benchmarks of different theoretical approaches, where uncontrolled approximations are often made [80, 138].

The use of ultracold fermions as “quantum simulators” have proven highly successful. For example, using a two-component ultracold Fermi gas with tunable *s*-wave interactions, experiments were able to explore the BEC-BCS crossover, where superfluids of Bose-condensed tightly-bound pairs of fermions are smoothly converted to superfluids of long-range BCS pairs [73, 63]. In the cross-over region where the superfluids are strongly-interacting, one can obtain some of the highest relative superfluid transition temperatures [119, 152, 151].

An alternative path to obtain strong interactions is through confining atoms in an optical lattice. By suppressing the motion of the particles, the kinetic energy is reduced and interactions play an increasingly important role. A two-component fermion gas trapped in an optical lattice simulates the Fermi-Hubbard model, a prototypical model in condensed matter physics that contains strong correlations [36]. The Hubbard model has generated intense interest since it is believed to describe the physics of high- $T_c$  cuprates [28, 83]. Nevertheless, despite the simplicity of the model, due to the fermion sign problem, it has remained unsolved except in limiting cases. Simulating the Hubbard model with ultracold fermions in an optical lattice could perhaps one day shed light on this long-standing problem.

The work in this thesis is concerned with the experimental study of ultracold fermions. In particular, this thesis covers two topics. The first concerns spin-orbit coupling, where the motion of a particle is coupled to an internal degree of freedom.

In condensed matter systems, spin-orbit coupling is often an essential ingredient necessary to produce non-trivial states of matter. For example, recently discovered topological insulators, which defy the conventional classification of phases via symmetry breaking, relies inherently on the presence of spin-orbit coupling [53]. Another exciting possibility arises when spin-orbit coupling is combined with superconductivity, where many-body states known as Majorana zero modes can be created [114]. In recent years, these have generated intense experimental interest, as these topologically protected Majorana modes have non-Abelian statistics, and thus can be used as a platform for fault-tolerant “topological” quantum computation [95, 3]. A specific route towards realizing these exotic excitations combines spin-orbit coupling in one dimension, a Zeeman field, and *s*-wave superconductivity [124, 100, 2]. Motivated in part by the prospects of Majoranas, we set out to implement spin-orbit coupling for ultracold fermionic  ${}^6\text{Li}$ , with which *s*-wave superfluids have previously been realized. We will describe how we realize spin-orbit coupling in 1D by using a two-photon Raman process. We also present a method that allows direct spin-resolved detection of the band structure in spin-orbit coupled systems. In addition, we demonstrate how this technique can be used to resolve bands in a novel spin-dependent lattice generated by combining Raman coupling and a radio-frequency drive.

The second area in this thesis concerns quantum gas microscopy of ultracold fermions trapped in an optical lattice, which allows quantum simulation of the Fermi-Hubbard model. While ultracold fermions have been previously trapped in optical lattices [77, 25], and signatures of the strongly correlated Mott-insulating state [67, 125] along with the appearance of short-range magnetic order have been detected [44, 52], these measurements relied on globally-averaged quantities in inhomogeneous samples.

We will describe a novel experimental apparatus - a fermionic quantum gas microscope - that offers an unprecedented level of local detection and control. This approach of quantum gas microscopy of fermions can open up new types of experiments on the spatial correlations and dynamics of fermions in the Hubbard regime.

For example, in previously realized quantum gas microscopes of bosonic atoms,

one has the ability to probe and manipulate atoms in a site-resolved fashion. This has led to new studies on correlations in the Bose-Hubbard model, novel experiments on quantum walks, and even experiments where the entanglement entropy in many-body systems can be characterized through interferometry of many-body states.

Although previous quantum gas microscopes for bosonic  $^{87}\text{Rb}$  atoms were realized in 2010, the fermionic versions proved more difficult. It was not until 2015 when the first fermionic quantum gas microscopes, one of which is described in this thesis, appeared. We will describe some of the challenges of quantum gas microscopy of fermionic  $^{40}\text{K}$ , and the methods we used to overcome them.

We will also discuss site-resolved measurements of quantum degenerate samples though the microscope. In particular, we have observed with site-resolved resolution three representative states of the Hubbard model: the metallic state, the band-insulating state and the Mott-insulating state. The Mott insulating state is the hallmark of strongly-correlated fermions. For the Mott insulator, although the band is half-filled and one expects a metallic state from band theory, the presence of strong repulsion between particles lead to an interaction-driven insulator.

In addition to measuring site-resolved occupations of atoms residing on a lattice, we have performed spatial correlations measurements, enabled directly by the site-resolving capabilities of the microscope. By extending the detection technique to be spin-sensitive, we have measured both spin and charge correlations between nearest neighbors as a function of filling (doping) in the strongly correlated regime. In the spin sector, we observed weakening anti-ferromagnetic correlations as the system is doped; in the charge sector, we observe a competition between Pauli blocking and doublon-holon correlations due to super-exchange.

## 1.1 Thesis Outline

This thesis is organized as follows.

In Chapter 2, we provide some theory relevant to ultracold fermions, both interacting and non-interacting. Since this is a broad topic, where many references are

available, we do not attempt to cover every aspect of this topic. Instead, we discuss aspects that are relevant to subsequent chapters, with a particular emphasis to spatial correlations. Some properties relevant to 2D Fermi gases will be also be given. When discussing interactions, we will follow an approach that highlights differences that arise in two dimensions compared to three dimensions.

In Chapter 3, we describe realizing spin-orbit coupling in ultracold fermionic  $^6\text{Li}$ . We first provide motivation for spin-orbit coupling using two simple 1D models. We next describe in detail how spin-orbit coupling is implemented and detected in a specific scheme using Raman lasers. Some experimental challenges of this scheme is discussed.

In Chapter 4, we describe the nuts and bolts of our quantum gas microscope apparatus for fermionic  $^{40}\text{K}$ . This chapter is rather technical.

In Chapter 5, we discuss the challenges of site-resolved imaging of fermionic  $^{40}\text{K}$  with high fidelity, and the solutions used to overcome these challenges.

In Chapter 6, we describe how we produce, observe and characterize different states in the Fermi-Hubbard model. We also discuss measurements of spatial spin and charge correlations.

Finally, in Chapter 7, we provide a brief summary, and an outlook on the quantum gas microscopy of strongly-correlated fermions.

Included in the appendices are:

1. Some technical details of the quantum gas microscope.
2. An incomplete but rather extensive list of  $s$  and  $p$ -wave Feshbach resonances in  $^{40}\text{K}$ .
3. Publications relevant to the research discussed in this thesis. Other topics that I have been involved in during my PhD, namely, measuring the equation of state of the unitary Fermi gas [80, 138] and the dynamics of solitonic vortices [149, 81], have been described in previous dissertations [130, 79] by others who led the effort, and will not be discussed here.



# Chapter 2

## Ultracold Fermi Gases

In this chapter, we present some background theory of fermions both in free space and in a lattice. In Section 2.1, we discuss some aspects of the ideal non-interacting Fermi gas, with an emphasis on spatial correlations. In Section 2.2, we describe the nature of interactions in ultracold fermionic atoms, and how they can be tuned using a Feshbach resonance. In Section 2.2.2, the specific case of interactions in 2D and its peculiarities are discussed. We next focus on the case of interacting fermions on a lattice. In a sufficiently deep lattice, the system can be described by the single-band Fermi-Hubbard model. Some features of the Fermi-Hubbard model and its relation to high- $T_c$  cuprates is discussed in Section 2.3.2. Research on interacting 2D gases described in this chapter have resulted in the following publication:

*A. T. Sommer, L. W. Cheuk, M. J. H. Ku, W. S. Bakr, and M. W. Zwierlein, “Evolution of Fermion Pairing from Three to Two Dimensions,” Phys. Rev. Lett. **108**, 045302 (2012)* [131]. Included in Appendix E.

### 2.1 Non-Interacting Fermions

In three or more dimensions, the spin-statistics theorem require that particles are either fermionic or bosonic. Fermionic particles obey fermionic statistics, which require that the wavefunction is anti-symmetric under exchange of two identical fermions.

This implies that two identical fermions cannot occupy the same quantum state, a rule also known as the Pauli exclusion principle. This Pauli-blocking effect is a key feature in fermionic systems, and leads to phenomena that range from the structure of the periodic table to the stability of white dwarfs and neutron stars.

In this following sections, we will discuss a some features of non-interacting ideal Fermi gases both in the bulk and on a lattice. Some of these results will be used in subsequent chapters.

### 2.1.1 Ideal Fermi Gas in Free Space

In this section, we present some properties of ideal Fermi gases in 3D and 2D, with a particular emphasis on spatial correlations. We first derive zero temperature  $T = 0$  results. For a homogeneous system, the momentum  $\mathbf{k}$  is a good quantum number. By the Pauli exclusion principle, the ground state is formed by populating these momentum states in order of energy up to  $k_F$ , the Fermi momentum. This forms the “Fermi sea,” where the Fermi surface is located at the Fermi energy of  $E = \frac{\hbar^2}{2m}k_F^2$ . The Hamiltonian in second quantization is given by

$$\hat{H} = \sum_{\mathbf{k}} \varepsilon_{\mathbf{k}} c_{\mathbf{k}}^\dagger c_{\mathbf{k}}, \quad (2.1)$$

where  $\varepsilon_{\mathbf{k}} = \frac{\hbar^2|\mathbf{k}|^2}{2m}$ . By counting the number of states below  $k_F$ , one can relate  $k_F$  to the number of atoms  $N$ . In 3D, one obtains

$$N = \frac{\frac{4}{3}\pi k_F^3}{(2\pi/L)^3}, \quad (2.2)$$

where  $L$  is the system size. After rearranging, we obtain

$$k_F = (6\pi^2 n)^{1/3}, \quad (2.3)$$

where  $n$  is the 3D density. The Fermi energy is thus related to the density by

$$E_F = \frac{\hbar^2}{2m} (6\pi^2 n)^{2/3} \quad (2.4)$$

In 2D, analogous reasoning gives

$$k_F = (4\pi n)^{1/2}. \quad (2.5)$$

One notices that in 2D, the Fermi energy  $E_F \propto n$ , and is given by

$$E_F = \frac{2\pi\hbar^2}{m} n. \quad (2.6)$$

For non-interacting (and weakly interacting) systems, the only states that can be perturbed must lie close to the Fermi surface at  $\mu$ . In this regime, properties of the system are governed by the energy density of states  $D(E) \propto \frac{\partial n}{\partial E}$ . Note that while the density of states scale as  $n^{1/3}$  in 3D, it is constant in 2D.

Although the ideal Fermi gas is most easily solved in momentum space, the presence of a Fermi surface, i.e. a special wave-vector  $|\mathbf{k}_F|$  leads to non-trivial spatial correlations. Consider, for example, the two-point correlator at equal times  $G(\mathbf{x}_1; \mathbf{x}_2) = \langle \hat{\psi}^\dagger(\mathbf{x}_2) \hat{\psi}(\mathbf{x}_1) \rangle$ , where the field operator  $\hat{\psi}(\mathbf{x})$  is defined by

$$\hat{\psi}(\mathbf{x}) = \frac{1}{V} \sum_{\mathbf{k}} c_{\mathbf{k}} e^{-i\mathbf{k}\cdot\mathbf{x}}, \quad (2.7)$$

with  $V$  being the volume of the system. Physically, this quantifies the correlation between removing a particle at  $x_1$  and simultaneously creating a particle at  $x_2$ . In a uniform system,  $G(\mathbf{x}_1, \mathbf{x}_2)$  depends only by the difference  $\mathbf{r} = \mathbf{x}_1 - \mathbf{x}_2$ . In addition, there is no preferred direction since the system is isotropic. One can thus define  $G(r) = G(r\hat{z}, \mathbf{0})$ , with  $r \geq 0$ . In general, for a uniform system (whether interacting or not),

$$G(r) = \frac{1}{V^2} \sum_{\mathbf{k}_2, \mathbf{k}_1} e^{i\mathbf{k}_2 \cdot \hat{z}r} \langle c_{\mathbf{k}_2}^\dagger c_{\mathbf{k}_1} \rangle = \frac{1}{V} \sum_{\mathbf{k}} e^{i\mathbf{k} \cdot \hat{z}r} \langle \hat{n}_{\mathbf{k}} \rangle, \quad (2.8)$$

where  $\hat{n}_{\mathbf{k}} = c_{\mathbf{k}}^\dagger c_{\mathbf{k}}$ . In other words  $G(r)$  is the Fourier transform of the occupation of momentum states. One immediately sees that any sharp feature in  $\hat{n}_{\mathbf{k}}$  will lead to oscillations in  $G(r)$ . Specifically, for the non-interacting Fermi gas,  $G(r)$  will contain oscillations at a spatial frequency of  $k_F$ .

To explicitly evaluate  $G(r)$  for the ideal Fermi gas in  $n$  dimensions, we make the substitution  $\sum_{\mathbf{k}} \rightarrow \frac{V}{(2\pi)^n} \int d^n k$ . This yields

$$G_{1\text{D}}(r) = \frac{1}{\pi} \frac{\sin(k_F r)}{r} = n \left( \frac{\sin(k_F r)}{k_F r} \right) \quad (2.9)$$

$$G_{2\text{D}}(r) = \frac{k_F J_1(k_F r)}{2\pi r} = n \left( \frac{2J_1(k_F r)}{(k_F r)^2} \right) \quad (2.10)$$

$$\begin{aligned} G_{3\text{D}}(r) &= \frac{1}{\pi r^3} \sin(k_F r) - \frac{k_F}{\pi r^2} \cos(k_F r) \\ &= n(j_2(k_F r) + j_0(k_F r)) \end{aligned} \quad (2.11)$$

in 1D, 2D and 3D respectively, where  $J_n$  are Bessel functions of the first kind and  $j_n$  are spherical Bessel functions of the first kind. As one expects,  $\lim_{r \rightarrow 0} G(r) = n$ . The oscillations occur in  $k_F$  and decay as  $r^D$ , where  $D$  is the dimension.

The measurement of  $G(r)$  requires annihilating and creating single-particle states at physically separated distances. In other words,  $G(r)$  can only be directly accessed when the system is perturbed. Another quantity that can reveal spatial correlations without manipulation of the system is the density-density correlator, i.e. the correlator between densities at different points in the system, i.e.  $C(r) = \langle \psi^\dagger(\mathbf{x})\psi(\mathbf{x})\psi^\dagger(0)\psi(0) \rangle$ , where  $\mathbf{x} = r\hat{x}$ . For non-interacting fermions, one can apply Wick's theorem to obtain

$$\begin{aligned} C(r) &= \langle \psi^\dagger(\mathbf{x})\psi(\mathbf{x}) \rangle \langle \psi^\dagger(0)\psi(0) \rangle + \langle \psi^\dagger(\mathbf{x})\psi(\mathbf{0}) \rangle \langle \psi(\mathbf{x})\psi^\dagger(0) \rangle \\ &= n^2 + G(r)(-G(-r)) \\ &= n^2 - |G(r)|^2, \end{aligned} \quad (2.12)$$

for  $r > 0$ . Defining the normalized two-point correlation function  $g_2(r) = C(r)/n^2$ , one finds that  $\lim_{r \rightarrow 0} g_2(r) = 0$ , a direct real-space manifestation of the Pauli exclusion

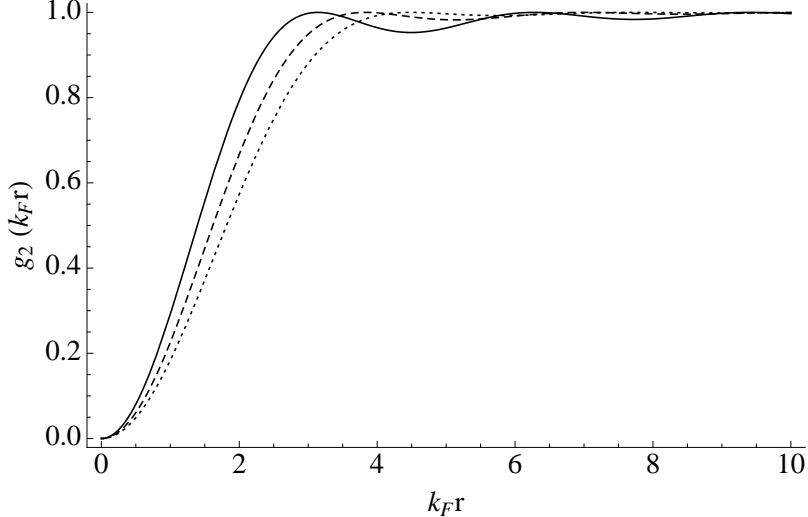


Figure 2-1: Friedel oscillations at  $T = 0$ . The two-point density correlation function  $g_2(kFr)$  for a 1D (solid), 2D (dashed), and 3D(dotted) Fermi gas at  $T = 0$ . Friedel oscillations occur at spatial frequency of  $2k_F$ . The Pauli exclusion principle results in  $g_2(kFr)$  vanishing as  $r$  approaches 0, and consequently produces the “Pauli hole” at short separations.

principle, which forbids two fermions from occupying the same quantum state. The resulting region around  $r = 0$  where  $g_2(r)$  is suppressed is known as the “Pauli hole.” The first direct measurement of the Pauli hole, enhanced by interactions, will be described in Chapter 6. In addition to the Pauli hole, one also notices that the oscillations occur at spatial frequency of  $2k_F$ . These oscillations are known as Friedel oscillations.  $g_2(r)$  for 1D, 2D and 3D are shown in Fig. 2-1.

We next discuss the case of finite temperature  $T > 0$ . At finite temperatures, some states below  $k_F$  are unoccupied, while some states above  $k_F$  become occupied. In the momentum basis, the occupation of each mode with momentum  $\mathbf{k}$  can be computed in the grand canonical ensemble. One finds that

$$\langle \hat{n}_\mathbf{k} \rangle = \frac{1}{1 + \exp(\beta(\epsilon_\mathbf{k} - \mu))}, \quad (2.13)$$

where  $\beta = 1/(k_B T)$ , with  $k_B$  being the Boltzmann constant and  $\mu$  the chemical potential.  $\mu$  is set to satisfy the constraint on the total particle number  $\langle \hat{N} \rangle$ . In the limit of  $T \rightarrow 0$ ,  $\mu \rightarrow \epsilon_F$  and  $n_\mathbf{k}$  becomes a step function with a step at  $k_F$ ,

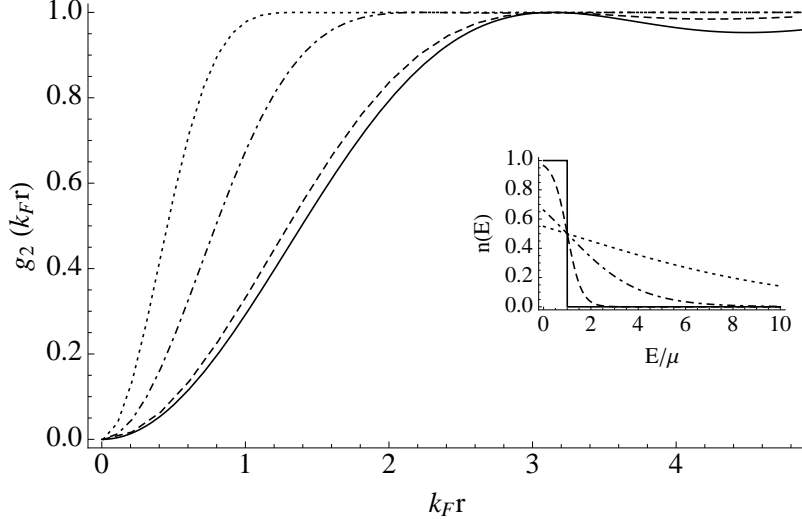


Figure 2-2: Friedel Oscillations in 1D at Finite Temperature. The two-point density correlation function  $g_2(k_{Fr})$  for  $1/\beta\mu = 0$  (solid),  $1/\beta\mu = 0.3$  (dashed),  $1/\beta\mu = 1.5$  (dot-dashed), and  $1/\beta\mu = 5.0$  (dotted) Fermi gas. At temperatures where  $\lambda_{dB} \sim 2\pi/k_F$ , Friedel oscillations are washed out, and the extent of the Pauli hole is now set by  $\lambda_{dB}$ .

signaling the location of the Fermi surface. As  $T$  increases, this step feature softens. Additionally, a new length scale  $\lambda_{dB}$ , the thermal de Broglie wavelength, emerges. The thermal de Broglie wavelength is defined by

$$\lambda_{dB} = \frac{h}{\sqrt{2\pi m k_B T}} \quad (2.14)$$

and is on the order wavelength associated with a particle with energy  $k_B T$ . As  $T$  increases, the de Broglie momentum  $2\pi/\lambda_{dB}$  shortens. When this becomes much less than  $k_F$ , the step in  $n_{\mathbf{k}}$ , and consequently Friedel oscillations, is highly suppressed. At finite temperature, the density correlation function is given by Eq. 2.8 with  $\langle \hat{n}_{\mathbf{k}} \rangle$  given by Eq. 2.13. Finite temperature results for  $g_2(r)$  in 1D are shown in Fig. 2-2.

### 2.1.2 Ideal Fermi Gas in a Lattice

Consider a particle in a lattice potential  $V(x) = V_0 \sin^2(k_L x/2)$ , where  $V_0$  is the depth of the potential and  $k_L$  is related to the lattice spacing via  $k_L = 2\pi/a$ . The

first-quantized Hamiltonian  $\hat{H}$  is given by

$$\hat{H} = -\frac{\hbar^2}{2m} \nabla^2 + V(x) \quad (2.15)$$

For a system with periodic boundary conditions, Bloch's theorem applies. The eigenfunctions have the form  $\psi_q(x) = e^{iqr} \phi(r)$ , where  $\phi(r)$  satisfies  $\phi(r + a) = u(r)$ , and  $q$  is the quasi-momentum restricted to  $q \in [k_L/2, k_L/2]$ . This implies that  $\phi(r)$  consists only of Fourier components of the form  $e^{imk_L x}$ , where  $m$  is an integer. For each quasi-momentum  $q$ , there are an infinite number of eigenfunctions that differ in energy. These can be labeled starting from the lowest to the highest with a band index  $n$ . One can expand the corresponding eigenfunction  $\psi_k^{(n)}(x)$  in the basis  $\{e^{i(q+mk_L)x}\}$  as

$$\psi_q^{(n)}(x) = \sum_m c_m^{(n)} e^{i(q+mk_L)x} = e^{iqx} \phi^{(n)}(x), \quad (2.16)$$

where  $c_j^{(n)}$  are complex numbers.

In this basis, the kinetic energy operator  $-\frac{\hbar^2}{2m} \nabla^2$  is diagonal, while the lattice potential couples components that differ by  $k_L$ . Thus the Hamiltonian can be written separated into a sum over terms  $\hat{H} = \sum_q \hat{H}_q$ , where each  $\hat{H}_q$  acts only on the subspace spanned by the states  $\{e^{i(q+nk_L)x}\}$ , corresponding to states of a single quasi-momentum  $q$ . The matrix representation in this basis is

$$\left(\hat{H}_q\right)_{nm} = \frac{\hbar^2}{2m} (q + nk_L)^2 \delta_{nm} + \frac{V_0}{4} (\delta_{n+1,m} + \delta_{n-1,m}) \quad (2.17)$$

For convenience, we define the energy scale  $E_R = \frac{\hbar^2}{2m} \left(\frac{k_L}{2}\right)^2$ , which corresponds to the free-particle energy at the band edge  $k_L/2 = \pi/a$ . We can then define the dimensionless lattice depth  $\tilde{V}_0 = V_0/E_R$ , and the dimensionless quasi-momentum  $\tilde{q} = q/k_L$ . Upon substitution,  $\left(\hat{H}_q\right)_{nm}$  becomes

$$\left(\hat{H}_q\right)_{nm} = E_R \left[ 4(\tilde{q} + n)^2 \delta_{nm} + \frac{\tilde{V}_0}{4} (\delta_{n+1,m} + \delta_{n-1,m}) \right] \quad (2.18)$$

For each quasi-momentum  $q$ , the resultant matrix can be numerically diagonalized. Here  $|n|$  gives the band index. Here, we consider the case where only the first band is occupied, and the band gap to the second band is much larger than all relevant energy scales. This limit is reached when the lattice potential is deep, and the chemical potential of the system is well below the second band. In this limit, the system is described by a single-band model. One can heuristically use a Hamiltonian of the form

$$\hat{H}_{\text{TB}} = -t \sum_{\langle i,j \rangle} \hat{c}_j^\dagger \hat{c}_i + \text{h.c.}, \quad (2.19)$$

where the creation (annihilation) operators  $\hat{c}_i^\dagger$  ( $\hat{c}_i$ ) create (annihilate) particles on a site  $i$ ,  $\langle i,j \rangle$  denotes a pair of nearest-neighbor sites  $i$  and  $j$ . This Hamiltonian describes particles hopping between neighboring sites with rate  $t$ . Here  $t > 0$ , indicates that delocalization is favored. This is known as the tight-binding approximation.

To relate the tight-binding Hamiltonian to the original Hamiltonian, one first defines localized orbitals at each site, which are known as Wannier functions. In a deep lattice, where only the lowest band is energetically accessed, the Wannier function for the lowest band centered at a lattice site at  $x_0$  can be constructed out of lowest band Bloch states as

$$w(x - x_0) = \sum_{k \in \text{FBZ}} \phi_k^{(1)}(x - x_0). \quad (2.20)$$

An effective single-band Hamiltonian for the lowest band can then be obtained by projecting  $\hat{H}$  onto the basis of Wannier functions. The nearest-neighbor hopping amplitude  $t$  in Eq. (2.19) is then given by

$$t = - \int_{-\infty}^{\infty} dx \left[ w(x) \left( -\frac{\hbar^2}{2m} \nabla^2 + V(x) \right) w^*(x + a) \right] \quad (2.21)$$

In principle, the projection procedure does give rise to next-nearest neighbor terms, such as next-nearest neighbor hopping term  $t' \sum_{\langle\langle i,j \rangle\rangle} \hat{c}_j^\dagger \hat{c}_i + \text{h.c.}$ , where  $\langle\langle i,j \rangle\rangle$  indicates a sum over next-nearest neighbors. At moderate lattice depths, this term (and longer-distance hopping terms) can be ignored, as shown in Fig. 2-3.

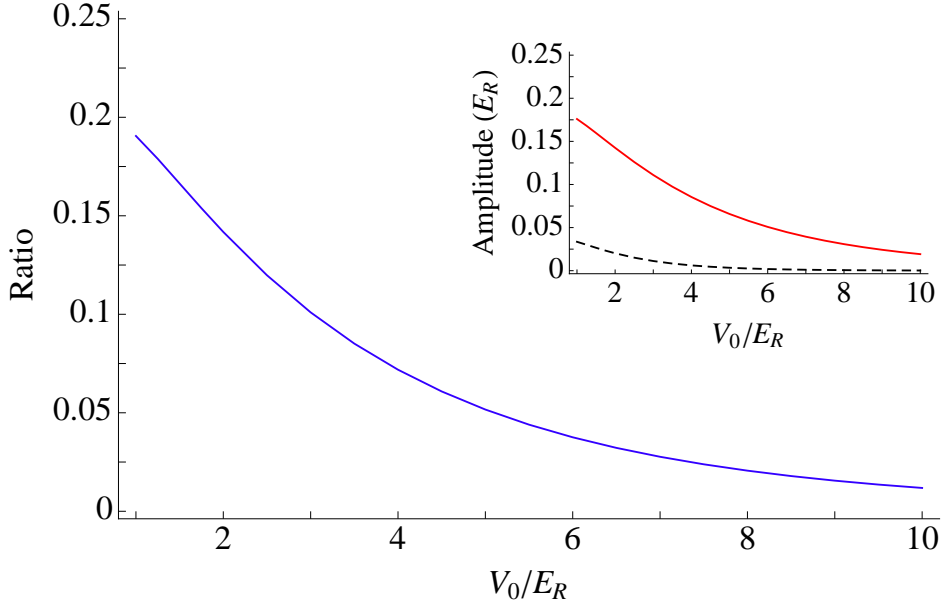


Figure 2-3: Ratio of nearest neighbor hopping amplitude to next-nearest neighbor hopping amplitude,  $|t'/t|$ , as computed from Eq. (2.21). The inset shows  $|t'|$  and  $|t|$  in dashed black and solid red lines respectively.

In experiments, the lattice depth  $V_0$  can be measured, and one must determine  $t$  from  $V_0$ . In practice, it is easier to determine  $t$  by first computing the bandwidth obtained by diagonalizing the lattice Hamiltonian in Eq. (2.18), and identifying it with the bandwidth of the tight-binding Hamiltonian  $\hat{H}_{\text{TB}}$ . For  $\hat{H}_{\text{TB}}$ , the bandwidth is simply given by  $4t$ . This can be easily seen by solving  $\hat{H}_{\text{TB}}$ . Defining operators  $\hat{b}_k = \sum_j e^{ikaj} \hat{c}_j$ , where  $j$  is the site index, one obtains

$$\hat{H}_{\text{TB}} = -t \sum_{k \in \text{FBZ}} (e^{ika} + e^{-ika}) \hat{b}_k^\dagger \hat{b}_k = \sum_{k \in \text{FBZ}} [-2t \cos(ka)] \hat{b}_k^\dagger \hat{b}_k. \quad (2.22)$$

The bandwidth of the lowest band can thus be identified with  $4t$ . The validity of this method is shown in Fig. 2-4, where  $t$  obtained from Eq. (2.21) is compared to that obtained from the bandwidth.

With relevance to later sections on microscopy of fermions in a lattice, we next discuss spatial correlation functions of non-interacting fermions on a lattice. We consider here the tight-binding limit where one only needs to consider a single band with dispersion  $\epsilon_k = -2t \cos(ka)$ . Since we will be discussing fermions in a 2D square

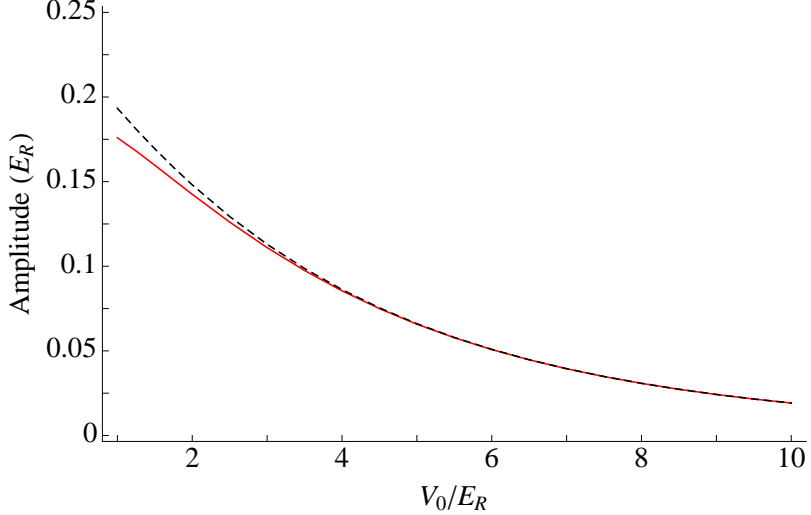


Figure 2-4: Nearest-neighbor hopping amplitude comparison. Shown in red solid line is the nearest-neighbor hopping amplitude  $t$  computed from Eq. (2.21); in black dashed line is  $t$  determined from the bandwidth of the lowest band.

lattice later, we discuss this case specifically. For a 2D square lattice, the dispersion is given by

$$\epsilon_{\mathbf{k}} = -2t [\cos(k_x a) + \cos(k_y a)]. \quad (2.23)$$

We restrict our discussion of the correlation function  $G(\mathbf{x}_1, \mathbf{x}_2)$  to where  $\mathbf{x}_1$  and  $\mathbf{x}_2$  are coordinates of lattice sites. Since discrete translation symmetry holds, in general, the correlation function can be written as  $G(\mathbf{r})$  where  $\mathbf{r} = n_x a \hat{x} + n_y a \hat{y}$  where  $n_x$  and  $n_y$  are integers. In this case, we obtain the general relation

$$G(\mathbf{r}) = \frac{1}{V} \sum_{\mathbf{k} \in \text{FBZ}} e^{i\mathbf{k} \cdot \mathbf{r}} \langle \hat{n}_{\mathbf{k}} \rangle, \quad (2.24)$$

where  $\langle \hat{n}_{\mathbf{k}} \rangle$  is given by Eq. 2.13.

In anticipation of interacting fermions, we next consider the case of a two-component Fermi gas with internal states  $\sigma = \uparrow, \downarrow$ . We consider the balanced case where  $\langle \hat{n}_{i,\uparrow} \rangle = \langle \hat{n}_{i,\downarrow} \rangle$ . The correlator  $\langle \hat{n}_{\sigma} \hat{n}_{\sigma} \rangle$  is unmodified, and is given by  $n_{\sigma}^2 - |G(\mathbf{r})|^2$ , while  $\langle \hat{n}_{\sigma} \hat{n}_{-\sigma} \rangle = n_{\sigma}^2$  where  $n_{\sigma} = \langle \hat{n}_{i,\uparrow} \rangle$ , since  $\uparrow$  and  $\downarrow$  particles are uncorrelated. To simplify notation, we define the connected correlator for two operators  $\hat{A}$  and  $\hat{B}$  as  $\langle \hat{A}, \hat{B} \rangle_C = \langle \hat{A} \hat{B} \rangle - \langle \hat{A} \rangle \langle \hat{B} \rangle$ . Note that when  $\hat{A}$  and  $\hat{B}$  are uncorrelated,  $\langle \hat{A}, \hat{B} \rangle_C = 0$ .

We define the connected density correlator

$$C_n(\mathbf{r}) = \langle \hat{n}_i, \hat{n}_{i+\mathbf{r}} \rangle_C, \quad (2.25)$$

where  $\hat{n}_i = \sum_{\sigma} \hat{n}_{i,\sigma}$ . Expressing in terms of the number operators  $\hat{n}_{\sigma,i}$ , we obtain

$$\begin{aligned} C_n(\mathbf{r}) &= \sum_{\sigma} [\langle \hat{n}_{\sigma,i}, \hat{n}_{\sigma,i+\mathbf{r}} \rangle_C + \langle \hat{n}_{\sigma,i}, \hat{n}_{-\sigma,i+\mathbf{r}} \rangle_C] \\ &= -2|G(\mathbf{r})|^2. \end{aligned} \quad (2.26)$$

The sign of the connected correlator reveals whether the particles bunch or anti-bunch spatially. One finds that, due to Pauli blocking, the total density anti-bunches.

Since we have a two-component system, we can also define spin-1/2 operators

$$\hat{S}_{z,i} = \frac{1}{2}(\hat{n}_{\uparrow,i} - \hat{n}_{\downarrow,i}). \quad (2.27)$$

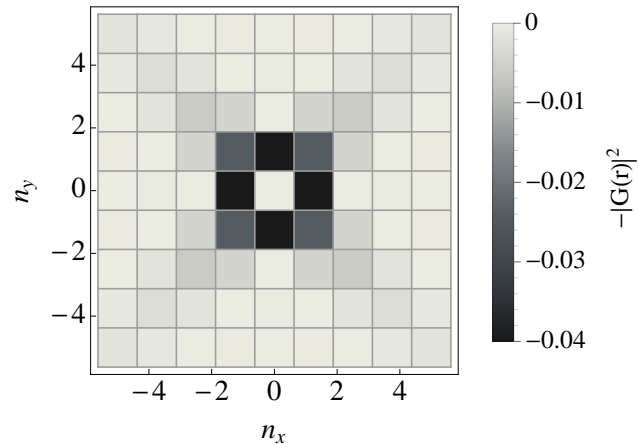
We define analogously the connected spin correlator

$$C_s(\mathbf{r}) = \langle \hat{S}_{z,i}, \hat{S}_{z,i+\mathbf{r}} \rangle_C \quad (2.28)$$

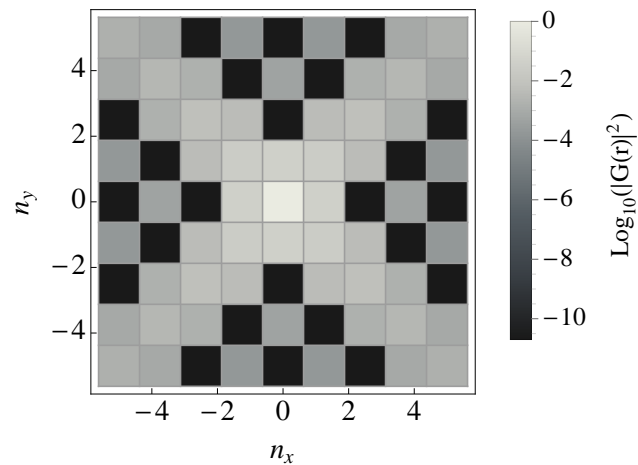
This is again related to  $G(\mathbf{r})$ , since

$$\begin{aligned} C_s(\mathbf{r}) &= \frac{1}{4} \sum_{\sigma} [\langle \hat{n}_{\sigma,i}, \hat{n}_{\sigma,i+\mathbf{r}} \rangle_C - \langle \hat{n}_{\sigma,i}, \hat{n}_{-\sigma,i+\mathbf{r}} \rangle_C] \\ &= -\frac{1}{2}|G(\mathbf{r})|^2. \end{aligned} \quad (2.29)$$

Thus, we find that for non-interacting Fermi gas of two-components, the magnetic moments  $\hat{S}_{z,i}$  are always anti-correlated. For fermions on a lattice, the lattice spacing forms an additional length scale. We focus here on the case of half-filling where  $\langle \hat{n}_i \rangle = 1$ . The function  $-|G(r)|^2$  at half-filling at  $T = 0$  is shown in Fig. 2-5. It is negative and displays oscillations at wavevectors  $(1, 0)$ ,  $(0, 1)$  and  $(1, 1)$ .



(a)



(b)

Figure 2-5:  $-|G(\mathbf{r})|^2$  and  $\log_{10} [|G(\mathbf{r})|^2]$  on a square lattice, with  $\mathbf{r} = n_x a\hat{x} + n_y a\hat{y}$ . In both cases, the point at  $\mathbf{r} = 0$  is set to zero.

## 2.2 Interacting Fermions in Free Space

Before discussing interacting fermions, we first summarize constraints that arise from fermionic statistics. We consider only two-particle interactions. The interaction Hamiltonian can be factored into angular and radial parts. The radial part is given by

$$\hat{H}_I = -\frac{\hbar^2}{m} \frac{\partial^2}{\partial r^2} - \frac{\hbar^2 l(l+1)}{m r^2} + V_l(r), \quad (2.30)$$

where  $r$  is the interparticle distance,  $l$  denotes the partial wave channel, and we assume the interaction potential is symmetric. At ultracold temperatures, we only need to consider collisions that occur in the only lowest partial wave ( $l = 0$ ) channel, as higher partial wave channels are frozen out by the centrifugal barrier of  $\hbar^2 l(l+1)/(mr^2)$ .

For the energetically accessible  $l = 0$  *s*-wave channel, the interaction potential is symmetric under exchange of two particles. Fermion exchange statistics require that the total two-particle wavefunction be anti-symmetric under exchange. To satisfy this constraint, the two fermions must be in different internal states. Further more, their internal degrees of freedom must be antisymmetric, i.e. they must form a singlet state. Consequently, one must need a minimum of two components for interactions to occur; a single-component Fermi gas at ultracold temperatures does not interact.

To quantify  $l = 0$  collisions, one can describe two-particle scattering in 3D by the wavefunction

$$\psi(\mathbf{r}) = \psi_0(\mathbf{r}) + f(k)\psi_s(\mathbf{r}), \quad (2.31)$$

where  $\psi_0(\mathbf{r}) = e^{i\mathbf{k}\cdot\mathbf{r}}$  is the incoming wavefunction,  $\psi_s(\mathbf{r}) = e^{ikr}/r$  is the outgoing wavefunction, and  $f(k)$  is the scattering amplitude at relative momentum  $k$ .

The amplitude  $f(k)$  can be written as  $e^{2i\delta} \sin(\delta)/k$ , where  $\delta$  is the phase shift of the outgoing wave. At low energies,  $f(k)$  is related to the *s*-wave scattering length  $a$  via

$$k \cot \delta = -\frac{1}{a} + \frac{1}{2} r_e k^2 \quad (2.32)$$

where  $k$  is the relative momentum of the two particles and  $r_e$  the effective range. At low enough energies where the effective range correction  $k^2 r_e$  is negligible, the

scattering is completely characterized by  $a$ , and the amplitude takes the form

$$f(k) = \frac{-a}{1 + ika}. \quad (2.33)$$

One notices that the function  $f(k) = \sqrt{m(E + i\epsilon)/\hbar^2}$  has a pole when analytically continuing  $E \rightarrow -\hbar^2/ma^2$ , for  $a > 0$ . This indicates that when the scattering length  $a > 0$ , there is a bound state in 3D at energy  $-E_b$ , where  $E_b = \hbar^2/(ma^2)$ .

Since the scattering is characterized by  $a$ , one can replace the interatomic potential with an  $s$ -wave pseudo-potential that produces equivalent phase shifts. A simple choice is a pseudo-potential of contact type,  $V_I(r) = g\delta(r)$ . This is reasonable as the length scale of the interatomic potential is given by the van der Waals length, which is much shorter than the interparticle spacing.

In order to describe an interacting two-component Fermi gas in the bulk, we use a quantum field model with contact interactions. We denote fermionic quantum fields by  $\psi_\sigma(\mathbf{x})$ , where  $\sigma = \uparrow, \downarrow$  denotes the internal state. The Hamiltonian is given by

$$\hat{H} = \int d\mathbf{x} \sum_\sigma \left\{ -\psi_\sigma^\dagger(\mathbf{x}) \frac{\hbar^2}{2m} \nabla^2 \psi_\sigma(\mathbf{x}) + \frac{g^{(\Lambda)}}{2} \psi_\sigma^\dagger(\mathbf{x}) \psi_{-\sigma}^\dagger(\mathbf{x}) \psi_{-\sigma}(\mathbf{x}) \psi_\sigma(\mathbf{x}) \right\} \quad (2.34)$$

with wavevector cutoff of  $\Lambda$ . When computing physical quantities, one needs to cut off the momentum at some scale  $\Lambda$ , since the delta function interaction potential requires renormalization in dimension higher than one. In order to relate to the scattering length  $a$ , one requires that the reflection amplitudes or equivalently the scattering phase shifts of this model agree with the  $s$ -wave scattering results when the collision energy approaches zero. This can be accomplished by solving the Lippmann-Schwinger equation for the amplitude  $\mathcal{A}(E)$  in this model. As shown graphically in Fig. 2-6, the Lippmann-Schwinger equation gives

$$i\mathcal{A}(E) = -ig^{(\Lambda)} + (-ig^{(\Lambda)})\square(E)(i\mathcal{A}(E)), \quad (2.35)$$

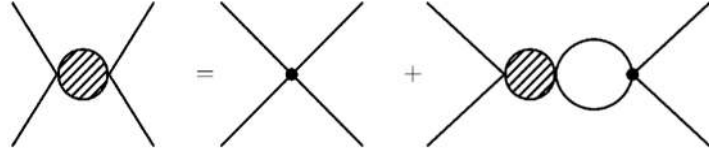


Figure 2-6: Graphical representation of the Lippmann-Schwinger equation. Here the dot denotes that interaction vertex  $-ig^{(\Lambda)}$  while the shaded circle represents the scattering amplitude  $i\mathcal{A}(E)$ . Figure reproduced from [16].

where  $\square(E)$  is given by

$$\begin{aligned}\square(E) &= \int \frac{d^3 k dE'}{(2\pi)^3} \frac{i}{E' - \hbar^2 k^2/2m + i\epsilon} \frac{i}{E - E' - \hbar^2 k^2/2m + i\epsilon} \\ &= -i \frac{m}{2\pi\hbar^2} \left( \Lambda + i \frac{\pi}{2} \sqrt{\tilde{E} + i\epsilon} \right),\end{aligned}\quad (2.36)$$

where  $\tilde{E} = mE/\hbar^2$  and we have used a wavevector cutoff of  $\Lambda$ . To find the value of  $g^{(\Lambda)}$ , we require that the low energy  $E \rightarrow 0$  gives the correct scattering amplitude. We find that

$$\mathcal{A}(E) = \frac{-g^{(\Lambda)}}{1 - ig^{(\Lambda)}\square(E)} = \frac{-g^{(\Lambda)}}{1 + \frac{mg^{(\Lambda)}}{2\pi\hbar^2} \left( \Lambda + i \frac{\pi}{2} \sqrt{\tilde{E} + i\epsilon} \right)} \quad (2.37)$$

To relate  $\mathcal{A}(E)$  to the scattering amplitude, we note that the scattered wave  $\psi_s(\mathbf{r})$  can be written as  $\psi_s(\mathbf{r}) = -\mathcal{A}(E)G_0(r)$ , where  $G_0(r)$  is the Green's function of the non-interacting Hamiltonian for the relative motion  $\hat{H}_0 = -\frac{\hbar^2}{m}\nabla^2$ . In 3D,  $G_0(r) = -\frac{m}{4\pi\hbar^2}e^{ikr}$ . One finds that when  $g^{(\Lambda)}$  is set to

$$g^{(\Lambda)} = \frac{4\pi\hbar^2}{m} \frac{a}{1 - 2\Lambda a/\pi}, \quad (2.38)$$

the correct scattering amplitude is obtained, as

$$\frac{m}{4\pi\hbar^2} A(E) = \frac{-a}{1 + ika} = f(k). \quad (2.39)$$

### 2.2.1 Feshbach Resonances

In this section, we summarize some properties of *s*-wave Feshbach resonances relevant for later chapters. For in-depth reviews of Feshbach resonances, one can refer to [73, 24]. A Feshbach resonance refers to enhanced scattering between two atoms when a molecular bound state becomes resonant. We restrict our discussion to *s*-wave ( $l = 0$ ) resonances. At the resonance, a molecular state becomes resonant with two free atoms with relative scattering energy of  $E \rightarrow 0$ . This physically corresponds to the phase shift  $\delta$  of the scattered wave approaching  $(n + \frac{1}{2})\pi$ , and the molecular bound state energy approaching  $-E_B \rightarrow 0$ . Since a molecular state can have a different magnetic moment than free atoms, the resonance condition can be tuned with a magnetic field. For example, ignoring the nuclear spin, which has a much smaller magnetic moment, a molecular state arising from the singlet potential has  $S = 0$ , and tunes differently from the state of two atoms that have non-zero spin projection  $m_S$ .

For the Feshbach resonances discussed in this thesis, they are classified as “broad” resonances, where the scattering length  $a$  is sufficient to determine all properties of the system near resonance. As a function of magnetic field  $B$ , the scattering length near a resonance can be parametrized by

$$a = a_{\text{bg}} \left( 1 - \frac{\Delta}{B - B_0} \right) \quad (2.40)$$

For practical purposes, a resonance is useful if its width  $\Delta$  is not too narrow ( $>\approx 1\text{G}$ ), and its location is easily accessible ( $<\approx 1000\text{G}$ ).

On the repulsive side of the resonances, where  $a > 0$ , there are in fact two branches. The branch above threshold ( $E > 0$ ) corresponds to unbound atoms that repulsively interact. The other branch is the molecular branch, where atoms are paired into dimers with energy  $-E_B = \hbar^2/ma^2$ . Since the lowest branch on the attractive side of the resonance ( $a < 0$ ) is adiabatically connected to the molecular branch, one can only stay on the repulsive branch by preparing atoms on the repulsive side far away from the resonance. Typically, near the resonance, the repulsive branch becomes unstable,

while the molecular branch can be long-lived. In the molecular branch, atoms are bound into bosonic dimers.

Our discussion so far has been restricted to the interactions of two particles. In a many-body system, qualitatively new phenomena can emerge. For example, while there is no two-body bound state on the attractive side ( $a > 0$ ), at low enough temperatures, there is a many-body bound state, corresponding to Cooper pairing of fermions. More precisely, when the temperature of the system is below the superfluid transition temperature  $T_C$ , Cooper pairing occurs and one obtains an *s*-wave BCS superfluid.

As the scattering length is tuned across resonance from  $a > 0$  to  $a < 0$ , the Cooper pairs are converted into tightly-bound dimers, which can condense to form a Bose-Einstein condensate, realizing the so-called BEC-BCS crossover. Experimentally, the tunability of interactions using a Feshbach resonance is crucial in achieving superfluids on the attractive side. Far on the attractive side, the superfluid transition temperature  $T_c$  follows the BCS scaling, and decreases exponentially with the interaction energy. Consequently, superfluids are achieved only near Feshbach resonances, where the interaction energy is strong relative to the kinetic energy. In this regime, the superfluid is strongly interacting, and theoretical calculations are difficult due to the fermion sign problem. Experiments on these superfluids can thus provide a valuable platform to benchmark many-body theories.

In anticipation of a discussion of interactions in two dimensions, we note that at the Feshbach resonance where the scattering length  $a$  diverges, the only length scale that remains is the interparticle distance. This can be seen from Eq. (2.33), where the scattering amplitude  $f(k) \rightarrow i/k$ , and the scattering cross-section approaches maximum value given by the unitary limit of  $\sigma = 4\pi/k^2$ . At  $T = 0$ , since the density sets the only length scale, the system is scale-invariant. We will see that the situation is very different in 2D.

## 2.2.2 Interacting Fermi Gas in Two Dimensions

In the previous two sections, we have discussed briefly interactions for ultracold fermions in three dimensions. In general, as dimensionality is reduced, the role of quantum fluctuations are enhanced, and qualitatively new phenomena can arise. Phase transitions can also take on a different character. For example, the low energy excitations of a 2D *s*-wave superfluid are vortex-anti-vortex pairs, and the superfluid transition is of BKT type, as observed directly in 2D BECs [49]. For fermions, one can ask whether many-body pairing can survive above the superfluid transition temperature  $T_c$ , and explore whether a psuedo-gap regime of preformed pairs exists. To investigate fermion pairing, we have performed RF spectroscopy on the dimensional crossover from three dimensions to two dimensions. This work has been described in detail in a previous dissertation [130]. Here, we will only discuss our measurements in the deep 2D limit, with a perspective focusing on scale invariance. Similar spectroscopic measurements focusing on the 2D regime were performed in [38], which was followed by momentum-resolved spectroscopy [37]. For a 2D Fermi gas in an isotropic harmonic trap, scale invariance leads to a dynamical hidden  $SO(2,1)$  symmetry [111]. Signatures of  $SO(2,1)$  symmetry breaking in 2D Fermi gases have been observed in measurements of collective excitations [140].

Before we describe the experimental measurements, we first discuss features of interactions in 2D, which are qualitatively different than 3D. Following the normalization convention in [109], the relative wavefunction of two particles scattering in 2D can be written as

$$\psi(\mathbf{r}) = \psi_0(\mathbf{r}) - f(k) \sqrt{\frac{i}{8\pi kr}} e^{ikr}, \quad (2.41)$$

in the asymptotic limit of  $r \rightarrow \infty$ . With this convention,  $f(k)$  is dimensionless.

To obtain the form of  $f(k)$ , we follow a slightly different approach than in 3D. We begin again with the low-energy effective model of point contact interactions in 2D, Eq. 2.34. We first perform dimensional analysis on the terms in the Hamiltonian. Setting  $\hbar = 1$  and  $m = 1$ , we express dimensions in units of length  $[L]$ . The kinetic energy term has units  $[L]^{-2}$ , while the interaction term carries units of  $[g^{(\Lambda)}] [L]^{-D}$ ,

where  $D$  is the dimension. In 2D, the coupling constant must take the form

$$g^{(\Lambda)} = \frac{\hbar^2}{m} C^{(\Lambda)} \quad (2.42)$$

where  $C^{(\Lambda)}$  is some dimensionless constant, that can possibly depend on the UV cutoff  $\Lambda$ . This means that when  $D = 2$ , the system is scale-invariant. This is different than the case in 3D, where one writes  $g^{(\Lambda)} = \frac{\hbar^2}{m} l$ , where  $l$  is some length scale. In 3D, the interacting Fermi gas is only scale-invariant at the Feshbach resonance, when the scattering length  $a$  diverges, and  $l \sim 1/\Lambda$  is only dependent on the cutoff.

The statement that scale invariance holds in 2D and  $C^{(\Lambda)}$  is constant, however, is not quite true. In fact, scale invariance does not survive renormalization. This is an example of an anomaly, where a symmetry present at the classical level is broken by renormalization. To see how this arises, recall that  $g^{(\Lambda)}$  has to be chosen such that the scattering amplitude  $\mathcal{A}(E = 0)$  agrees with the  $T$ -matrix. To find the form of  $g^{(\Lambda)}$ , we first compute the scattering amplitude  $\mathcal{A}(E) = -g^{(\Lambda)} / (1 + ig^{(\Lambda)} \square(E))$ , where the term  $\square(E)$  is given by

$$\begin{aligned} \square(E) &= \int \frac{d^2 q \, dE'}{(2\pi)^3} \frac{i}{E' - \hbar^2 q^2/2m + i\epsilon} \frac{i}{E - E' - \hbar^2 q^2/2m + i\epsilon} \\ &= -\frac{i}{(2\pi)^2} \frac{m}{\hbar^2} \int \frac{d^2 q}{q^2 - (\tilde{E} + i\epsilon)} \\ &= -\frac{i}{2\pi} \frac{m}{\hbar^2} \int_0^\Lambda \frac{qdq}{q^2 - (\tilde{E} + i\epsilon)} \end{aligned} \quad (2.43)$$

Here, in addition to a UV divergence, which we have seen earlier in 3D, there is an infrared divergence. This implies that an additional low-energy momentum scale  $\Lambda_0$  must be present. For the case of  $E = 0$ , one obtains

$$\begin{aligned} g^{(\Lambda)} &= \frac{C_0}{1 - C_0 \frac{m}{4\pi\hbar^2} \ln(\Lambda^2/\Lambda_0^2)} \\ &= \frac{4\pi\hbar^2/m}{-\frac{4\pi\hbar^2}{mC_0} + \ln(\Lambda^2/\Lambda_0^2)} \\ &= \frac{-4\pi\hbar^2/m}{\ln(\Lambda^2/\Lambda_1^2)}, \end{aligned} \quad (2.44)$$

where  $\Lambda_1^2 = \Lambda_0^2 \exp \left[ \frac{4\pi\hbar^2}{mC_0} \right]$ , and  $C_0$  is a constant. One observes that a new cut-off independent energy scale  $\frac{\hbar^2}{m}\Lambda_1^2$  emerges from renormalization. Furthermore, the coupling constant decreases logarithmically with the momentum scale, reminiscent of the running coupling constant in QCD. We thus find that while scale-invariance can be approximate for a limited range of energies, it is in general absent for *any* interaction parameter  $\Lambda_1$ . The only scale-invariant 2D Fermi gas with contact interactions is the non-interacting gas.

Another peculiar feature in 2D is that the scattering amplitude is logarithmically dependent on the energy. Using the Lippmann-Schwinger equation, for  $E > 0$ , we obtain

$$\begin{aligned} \mathcal{A}(E) &= \frac{-g}{1 + ig\Box(E)} \\ &= \frac{-C_0}{1 - C_0 \frac{m}{4\pi\hbar^2} \ln \left( \frac{\Lambda^2}{\Lambda_0^2} \right) + C_0 \frac{m}{4\pi\hbar^2} \left[ \ln \left( \Lambda^2 - \tilde{E} \right) - \ln \left| \tilde{E} - \Lambda_0^2 \right| + i\pi \right]} \end{aligned} \quad (2.45)$$

In the limit  $\Lambda \gg \tilde{E}$ , this becomes

$$\mathcal{A}(E) = \frac{-C_0}{1 - C_0 \frac{m}{4\pi\hbar^2} \left( \ln \left( \frac{|\Lambda_0^2 - \tilde{E}|}{\Lambda_0^2} \right) + i\pi \right)}, \quad (2.46)$$

where we have picked  $\Lambda_0^2 < \tilde{E}$ . To bring this into a more familiar form, we pick  $\Lambda_0$  such that  $\tilde{E} \gg \Lambda_0^2$ . Then

$$\begin{aligned} \mathcal{A}(E) &= \frac{4\pi\hbar^2/m}{-\frac{4\pi\hbar^2}{mC_0} + \ln \left( \frac{\tilde{E}}{\Lambda_0^2} \right) + i\pi} \\ &= \frac{4\pi\hbar^2/m}{\ln \left( \frac{E}{E_b} \right) + i\pi}, \end{aligned} \quad (2.47)$$

where  $E_b$  is defined as

$$E_b = \frac{\hbar^2}{m}\Lambda_1^2 = \frac{\hbar^2\Lambda_0^2}{m} \exp \left[ \frac{4\pi\hbar^2}{mC_0} \right] \quad (2.48)$$

This directly indicates that scattering by an *s*-wave short-range potential is energy dependent in 2D, with maximum scattering cross-section at  $E = E_b$ . Unlike in 3D,

where  $f(k)$  attains a maximal magnitude for any  $k$  at  $a \rightarrow \infty$ , in 2D, the maximal cross-section depends on the scattering energy. For a Fermi gas, the resonance occurs when  $E_F = E_b$ , and the resonance is thus density-dependent. To relate to the scattering amplitude in Eq. (2.41), we relate  $\mathcal{A}(E)$  to  $f(k)$  and find that

$$f(k) = \frac{4\pi}{\ln(E/E_b) + i\pi} \quad (2.49)$$

The reason that we label the energy scale in the logarithm by  $E_b$  is as follows. If one analytically continues  $E$  to  $-E_b - i\epsilon$ ,  $\mathcal{A}(-E_b - i\epsilon)$  diverges, indicating the presence of a bound state at  $-E_b$ . This implies that there is necessarily a bound state for any interaction strength in 2D. This is different from 3D, where a 2-body bound state only occurs for  $a > 0$ . Scattering in 2D can thus be parameterized by the energy of the bound state  $E_b$ .

We experimentally detect this bound state through measuring its disasscoiation spectrum with RF spectroscopy [46, 73]. To realize quasi-2D gases, we confine the atoms with a deep 1D optical lattice along the axial direction. In a deep lattice, different layers are decoupled, and each lattice well can be thought of as a harmonic oscillator with frequency  $\omega$ . In the regime where the chemical potential  $\mu \ll \hbar\omega$  and the temperature  $k_B T \ll \hbar\omega$ , particles only occupy the ground state of each lattice well, and the system is quasi-2D. In this quasi-2D limit, and in the case where  $E_b/\hbar\omega$ , the binding energy  $E_b$  is related to the 3D scattering length  $a$  via [109, 14]:

$$\frac{E_b}{\hbar\omega} = \frac{0.905}{\pi} \exp\left(-\sqrt{2\pi}l/|a|\right), \quad (2.50)$$

where  $l = \sqrt{\hbar/(m\omega)}$  is the harmonic oscillator length.

To observe the bound state, we prepare a gas of  ${}^6\text{Li}$  atoms in the lowest ( $|1\rangle$ ) and third lowest ( $|3\rangle$ ) hyperfine states. By applying a radio-frequency (RF) drive near resonant with the  $|1\rangle \rightarrow |2\rangle$  transition, and detecting arrivals of  $|2\rangle$  atoms, the energy of the bound state can be measured. When dissociating a bound state, one must supply at least an energy of  $E_b$ . The RF response must therefore start at an energy  $E_b$  away from the single atom resonance. Our measurements of the bound

state energy agree well with the energy from a two-body calculation. Although this might be surprisingly given that we have an interacting system with many particles, the unshifted bound state had been predicted earlier in a mean-field treatment of the BEC-BCS cross-over in 2D [117]. Here, we will not discuss the evolution from 3D to 2D, as it has been described previously. We will only focus on the line shape of the molecular response in the 2D limit.

RF spectroscopy can be interpreted as a tunneling experiment, since the perturbation due to the RF pulse is described by [73]

$$\hat{H}_I(t) = \frac{\hbar\Omega}{2} e^{i\omega t} \left( \hat{\psi}_2^\dagger \hat{\psi}_1 + \text{h.c.} \right), \quad (2.51)$$

which produces a tunneling current from the initially occupied  $|1\rangle$  states to the unoccupied  $|2\rangle$  states.

One can calculate the transition rate  $\Gamma_{\text{RF}}(\omega)$  out of an initial state  $i$  via Fermi's golden rule, which gives

$$\Gamma_{\text{RF}}(\omega) = \frac{2\pi}{\hbar} \sum_k \left| \langle k | \hat{V}_I | i \rangle \right|^2 \delta(E_k + \hbar\omega - E_i), \quad (2.52)$$

where  $E_i$  is the energy of the initial state,  $E_k = \hbar^2 k^2 / m$  and  $\hat{V}$  is given by

$$\hat{V} = \frac{\Omega}{2} \left( \hat{\psi}_2^\dagger \hat{\psi}_1 + \text{h.c.} \right). \quad (2.53)$$

In 3D, for an initial bound state  $|\psi_b\rangle \propto \sqrt{\kappa} e^{-\kappa r} / r$ ,  $\kappa = \sqrt{mE_b/\hbar^2}$ , we obtain

$$\begin{aligned} \Gamma_{\text{RF}}(\omega) &\propto \frac{\kappa}{(\kappa^2 + k^2)^2} \theta(\hbar\omega - E_b) \sqrt{\hbar\omega - E_b} \\ &\propto \frac{\sqrt{E_b}}{\omega^2} \theta(\hbar\omega - E_b) \sqrt{\hbar\omega - E_b}. \end{aligned} \quad (2.54)$$

The first term comes from the matrix element, while the term  $\theta(\hbar\omega - E_b) \sqrt{\hbar\omega - E_b}$  comes from the density of states in 3D. This immediately suggests that in 2D, where the density of states is constant, one might observe a step response at the threshold

value of  $\hbar\omega = E_b$ . In particular, in 2D,  $|\psi_b\rangle \propto \kappa K_0(\kappa r)$ , where  $K_n(x)$  are modified Bessel functions of the second kind. This results in a matrix element  $\propto \frac{\kappa}{\kappa^2 + k^2}$ . The total transition rate is thus

$$\begin{aligned}\Gamma_{\text{RF}}(\omega) &\propto \frac{\kappa^2}{(\kappa^2 + k^2)^2} \theta(\hbar\omega - E_b) \\ &\propto \frac{E_b}{\omega^2} \theta(\hbar\omega - E_b).\end{aligned}\quad (2.55)$$

One thus finds that applying Fermi's golden rule results in a lineshape that consists of a step feature at threshold  $\hbar\omega = E_b$  and a monotonic  $1/\omega^2$  tail.

In reality,  $|2\rangle$ , the final state that the atoms are transferred to, also interacts with  $|3\rangle$ . These final state interactions lead to modifications in the lineshape. To estimate the effect of final state interactions, one can examine the scattering amplitude  $\mathcal{A}(E)$  of the final state  $|2\rangle$  atoms with  $|3\rangle$ . In 3D, we have found that the scattering amplitude  $\mathcal{A}(E) \propto 1/(1 + ia\sqrt{\tilde{E}})$ . The final density of states acquires an additional factor proportional to  $|\mathcal{A}(E)|^2$ , which implies that the high-frequency behavior is modified from  $\omega^{-3/2}$  to  $\omega^{-5/2}$  beyond frequencies where  $(\hbar\omega - E_b) \approx \frac{\hbar^2}{ma_{23}^2}$ . Furthermore, from the form of  $\mathcal{A}(E)$ , one only expects final state effects at high energies, and the threshold behavior at  $\hbar\omega \approx E_b$  should be unmodified.

In 2D, the scattering amplitude  $\mathcal{A}(E)$  vanishes logarithmically as  $1/\ln(E)$  at both  $E \rightarrow 0$  and  $E \rightarrow \infty$ . One thus expects that the high frequency behavior is modified from  $\omega^{-2}$  to  $[\omega \ln(\omega)]^{-2}$ . At threshold, we have a suppression of the form  $|\ln((\hbar\omega - E_b)/E'_b)|^{-2}$ , where  $E'_b$  is the bound state energy characterizing the final state interactions. One finds that at  $\hbar\omega = E_b$ , the response vanishes, in stark contrast with the naive expectation of a step response due to the uniform density of states in 2D. Furthermore, as long as the final state interactions are not zero, there is always a final bound state. Thus, starting from a  $|1\rangle-|3\rangle$  bound state, one finds a bound-to-bound response to a  $|2\rangle-|3\rangle$  bound state in addition to the bound-to-free response.

The exact form of the RF line shape for a 2-body bound state, taking into final

state interactions, is given by [82]

$$\begin{aligned}\Gamma(\omega) \propto & \frac{E'_b E_b}{(E'_b - E_b)^2} \ln^2 [E'_b/E_b] \delta(\hbar\omega - E_b + E'_b) \\ & + \frac{E_b}{\omega^2} \frac{\ln^2 [E'_b/E_b]}{(\ln^2 [(\hbar\omega - E_b)/E'_b] + \pi^2)} \theta(\hbar\omega - E_b).\end{aligned}\quad (2.56)$$

The first term corresponds to a transition from the initial bound state to a bound state between  $|2\rangle$  and  $|3\rangle$ , hence the delta function. The second term contains the step response due to the uniform density of states in 2D, the simple  $\omega^{-2}$  scaling, and logarithmic final state corrections in the denominator. We find good agreement when comparing with the experimentally measured spectra, as shown in Fig. 2-7. The observation of the lineshape softening near the threshold thus reveal breaking of scale invariance in 2D in the interacting system of  $|2\rangle$  and  $|3\rangle$  atoms. This is in contrast to experiments on 2D Bose gases, where scale invariance was observed [62, 31]. Approximate scale invariance can be obtained if only a narrow range in energy relative to  $E_B$  is accessed.

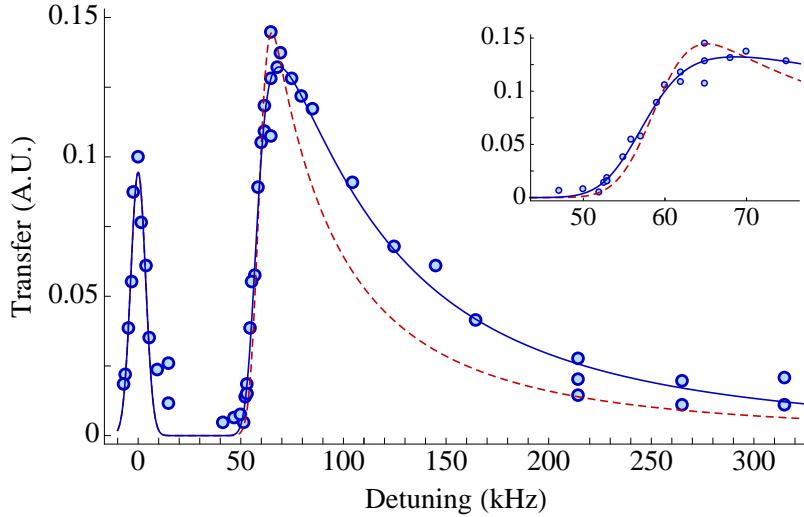


Figure 2-7: Dissociation Spectrum of Bound Molecules in 2D. The blue solid line indicates the fit to the lineshape taking into account logarithmic corrections from final state interactions, and finite frequency resolution of the experiment. The red dashed line shows a fit to the line shape without final state interactions. The peak on the left corresponds to response from free atoms. A convolution with a Gaussian response with width determined from the free atom peak is applied. The inset shows a zoomed-in view of the near-threshold response.

## 2.3 Interacting Fermions on a Lattice

In this section, we discuss some properties of interacting ultracold fermions confined in an optical lattice. We describe how the Fermi-Hubbard model arises in the tight-binding limit. The Fermi-Hubbard model is a prototypical lattice model for fermions exhibiting strongly correlated behavior, and was first proposed decades before the realization of ultracold atoms. One of the motivations to study the Hubbard model is that it is believed to contain some of the essential aspects of high- $T_c$  cuprates, a class of materials with a much higher  $T_c$  than typical BCS-type superconductors. Although superconductivity in these cuprates is not described by BCS pairing of electrons, the precise mechanism remains an open question. To what extent phenomena of high- $T_c$  cuprates are shared by the Hubbard model is not fully known, since the Hubbard model, despite being simple, is only solvable in limited regimes.

### 2.3.1 Fermi-Hubbard Model in the Tight-Binding Limit

In this section, we describe how the Fermi-Hubbard Model arises in the tight-binding limit. Suppose that the bandgap is much larger than all energy scales, i.e.  $V_0 \gg k_B T, \mu$ . Compared to the previous case of non-interacting fermions, we must now include a term that captures interactions. Since interactions are two-body, in the tight-binding limit, the interaction term must be of the form

$$\frac{U_{i,j}}{2} \sum_{i,j,\sigma} c_{i,\sigma}^\dagger c_{j,-\sigma}^\dagger c_{j,-\sigma} c_{i,\sigma}. \quad (2.57)$$

For a translationally invariant and inversion symmetric system,  $U_{i,j} = U_{|i-j|}$ . To find these coefficients, we project the bare Hamiltonian onto Wannier functions for the lowest band, which are denoted by  $w(x - ja)$ , for the Wannier function centered at lattice site  $j$ . We find that

$$\begin{aligned} U_j &= \int dx dx' g^{(\Lambda)} \delta(x - x') |w(x)|^2 |w(x' + ja)|^2 \\ &= g^{(\Lambda)} \int dx |w(x)|^2 |w(x + ja)|^2. \end{aligned} \quad (2.58)$$

Here, since we only consider the Wannier function for the lowest band, the cutoff  $\Lambda$  should be chosen as  $\sim \pi/l$ , where  $l$  is the size of the Wannier function. Thus the coupling constant to use is

$$g^{(\Lambda)} = \frac{4\pi\hbar^2 a}{m} \frac{1}{1 + 2a/l} \approx \frac{4\pi\hbar^2 a}{m} \quad (2.59)$$

where the last approximation holds as long as  $a/l \ll 1$ .

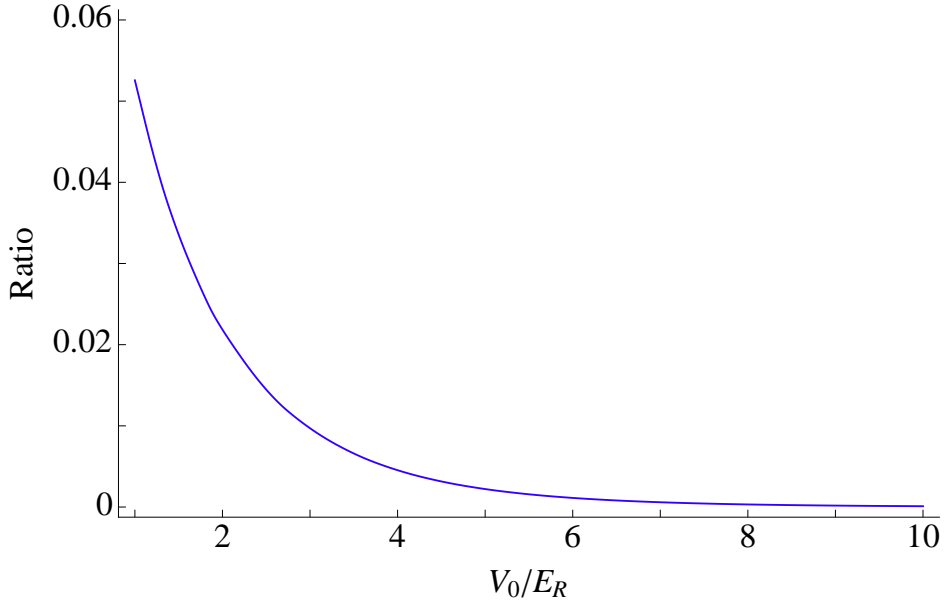


Figure 2-8: Ratio of on-site interaction to nearest-neighbor interaction  $U_0/U_1$ .

From the definition of the Wannier function, one finds that  $w(x) \propto \exp(-x/l)$  for a characteristic length  $l$ . In the deep lattice limit,  $l$  is approximately given by the harmonic oscillator length of the effective harmonic oscillator at a single well. Thus  $l \propto (\tilde{V}_0)^{-1/4}$ . This implies that for deep lattices,  $U_j/U_{j+1} \propto \exp(C\tilde{V}_0^{1/4})$  for some constant  $C$ . We show  $U_0/U_1$  as a function of  $\tilde{V}_0$  in Fig. 2-8. Since  $U_0$  is much larger than other terms, in practice, we only keep the on-site term  $U_0$ . In this limit, we obtain the Hubbard Hamiltonian

$$\hat{H} = -t \sum_{\langle i,j \rangle, \sigma} (c_{i,\sigma}^\dagger c_{j,\sigma} + \text{h.c.}) + \frac{U}{2} \sum_{i,\sigma} c_{i,\sigma}^\dagger c_{i,-\sigma}^\dagger c_{i,-\sigma} c_{i,\sigma} - \sum_{i,\sigma} \mu_\sigma c_{i,\sigma}^\dagger c_{i,\sigma}, \quad (2.60)$$

where  $U = U_0$ ,  $\mu_\sigma$  is the chemical potential for the  $\sigma$  species. When the populations

of the two components are identical  $\mu = \mu_\sigma = \mu_{-\sigma}$ , and we obtain

$$\hat{H} = -t \sum_{\langle i,j \rangle, \sigma} (c_{i,\sigma}^\dagger c_{j,\sigma} + \text{h. c.}) + \frac{U}{2} \sum_{i,\sigma} c_{i,\sigma}^\dagger c_{i,-\sigma}^\dagger c_{i,-\sigma} c_{i,\sigma} - \mu \sum_{i,\sigma} c_{i,\sigma}^\dagger c_{i\sigma}, \quad (2.61)$$

### 2.3.2 Phenomenology of the Hubbard Model: Metals, Band Insulators and Mott Insulators

In this section, we describe some aspects of the Hubbard model. In the non-interacting limit where  $U/t \ll 1$ , band theory is valid. When the chemical potential  $\mu$  is within the band, the system is in a metallic state. When the chemical potential is above the band, i.e.  $\mu > 2t$ , all states are occupied, and the system is band-insulating. As long as the chemical potential  $\mu$  is sufficiently large, even at non-zero  $t$ , the system remains band-insulating, as all states are filled.

An interesting scenario arises when  $\mu$  is at the middle of the band. Due to the symmetry of the dispersion relation, there is on average half a particle per site per spin state. This is the so-called half-filling point. From band theory, one expects a metal. However, when  $U/t \gg 1$ , the interaction term suppresses the probability of having two particles of opposite spin on the same site. Since having two particles of the same spin is forbidden by the Pauli exclusion principle, we obtain a state with exactly one particle per site (see Fig. 2-9). This state is insulating, and is known as a Mott insulator. Unlike typical systems where an insulator occurs when the chemical potential is within a bandgap, Mott insulators are insulating because of interactions. Here, single-particle properties such as the density-of-states at  $\mu$  and the dispersion relation are insufficient to describe the system.

Since the Mott insulator is driven by the interaction energy  $U$ , one expects that it forms below a temperature  $T \sim U/k_B$ . In the Mott-insulating state, the charge degrees of freedom are frozen out, as each site has almost exactly one particle. Nevertheless, there are residual degrees of freedom in how the spins align. As we shall see, the spins tend to align anti-ferromagnetically.

The first reason for anti-ferromagnetic alignment is geometric, arising from a

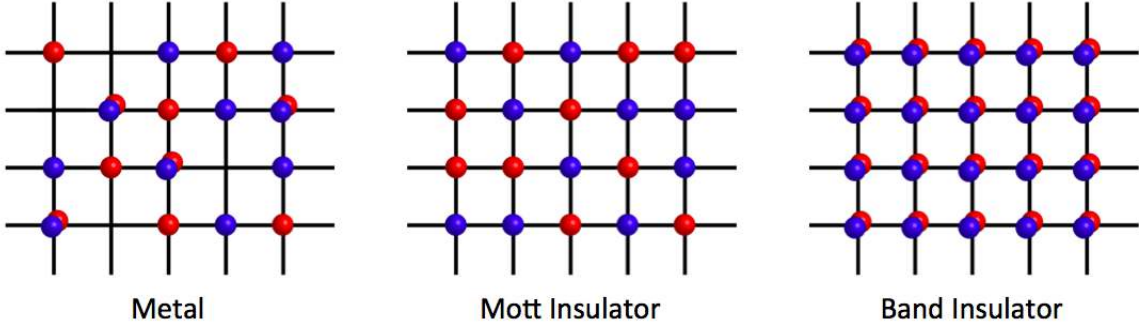


Figure 2-9: States of the Fermi-Hubbard Model. Shown are the real space pictures of the metallic state, the Mott-insulating state, and the band-insulating state.

property of the 2D square lattice known as “nesting.” In the tight-binding limit and on a square lattice, the dispersion satisfies the property of  $-\epsilon_{\mathbf{k}} = \epsilon_{\mathbf{k}+\mathbf{Q}}$ , where  $\mathbf{Q} = (\pi/a)(\pm 1, \pm 1)$ . This can be verified by inspection of Eq. 2.23, and is known as nesting.

The consequences can be understood graphically. Consider the case of half-filling of a non-interacting Fermi gas on a square lattice. The Fermi surfaces for each spin are squares with vertices at  $(\pi/a)(\pm 1, 0)$  and  $(\pi/a)(0, \pm 1)$ . A single wave vector at  $(\pi/a)(1, 1)$  can therefore connect two edges of the Fermi surface, as shown in Fig. 2-10. Due to the enhanced density of states at a specific separation of  $\mathbf{Q}$ , in the presence of interactions between  $\uparrow$  and  $\downarrow$  particles, the system becomes susceptible to formation of spin order along  $(\pi/a)(\pm 1, \pm 1)$ .

The tendency for spins to anti-ferromagnetically align has an additional energetic origin that does not depend on lattice geometry. Consider a system deep in the atomic limit ( $U/t \gg 1$ ), and at half-filling. Although double occupancies are suppressed due to the strong interactions, there is always a non-zero amplitude  $-t$  of a particle tunneling to a neighboring site, as long as the neighboring site has opposite spin. In this case, second order perturbation theory gives an energy correction of  $\Delta E = -4t^2/U$ . Anti-aligned spins on neighboring sites are thus energetically favored. This mechanism is known as super-exchange, and gives rise to anti-ferromagnetism when  $U > 0$ . Thus, both nesting and super-exchange help in establishing AF order along  $(1, 1)$ .

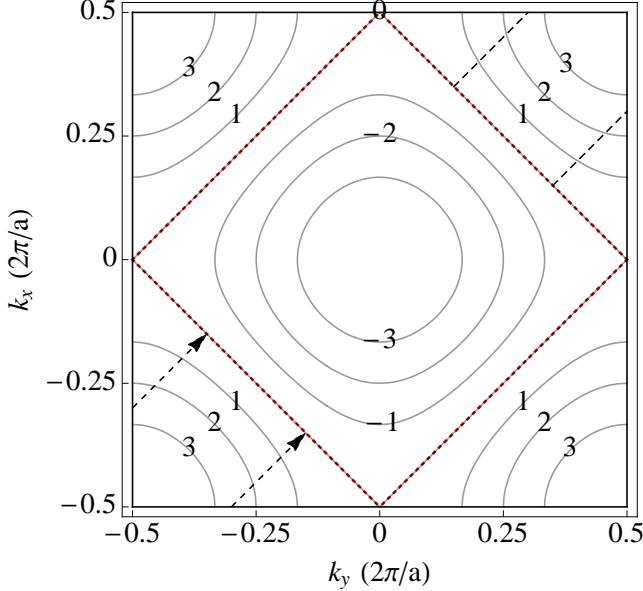


Figure 2-10: Nesting on the half-filled square lattice. Solid lines mark the Fermi surfaces for difference energies. The energy contours are marked in units of the tunneling amplitude  $t$ . The red dotted lines indicates the Fermi surface ( $E = 0$ ) for the half-filled square lattice. The nesting wavevector  $(1, 1)$  shown by the dashed arrows connect two edges of the Fermi sea.

Although these arguments at half-filling, one at  $U = 0$  and one at  $U \gg t$ , seem to suggest that an anti-ferromagnet should form generically, the Hubbard model is remains unsolved except for the special case of  $\langle \hat{n}_i \rangle = 1$ , where the fermion sign problem is avoided.

The reason that the half-filling case can avoid the sign problem arises from the bi-partite nature of the square lattice. (The square lattice can be decomposed into two sub-lattices  $A$  and  $B$  where the neighbor of one site of  $A$  is always in  $B$  and vice versa). Although the bi-partite nature does not eliminate the sign problem away from half-filling, it does lead to some additional symmetries, one of which we will discuss below.

Consider the particle-hole transformation  $\hat{c}_{\sigma,i}^\dagger \rightarrow \hat{c}_{\sigma,i}^\dagger$ . The following properties follow.

$$\begin{aligned}
 n_{\sigma,i}^\dagger &\rightarrow 1 - n_{\sigma,i}^\dagger \\
 c_{\sigma,i}^\dagger c_{\sigma,j} + c_{\sigma,j}^\dagger c_{\sigma,i} &\rightarrow - \left( c_{\sigma,i}^\dagger c_{\sigma,j} + c_{\sigma,j}^\dagger c_{\sigma,i} \right).
 \end{aligned} \tag{2.62}$$

Upon substitution, the Hubbard Hamiltonian becomes

$$\hat{H} = t \sum_{\langle i,j \rangle, \sigma} (c_{i,\sigma}^\dagger c_{j,\sigma} + \text{h.c.}) + \frac{U}{2} \sum_{i,\sigma} c_{i,\sigma}^\dagger c_{i,-\sigma}^\dagger c_{i,-\sigma} c_{i,\sigma} - (-\mu - U) \sum_{i,\sigma} c_{i,\sigma}^\dagger c_{i\sigma}, \quad (2.63)$$

where we have discarded terms that are overall energy offsets.

On a square lattice, nearest neighbors are always on different sub-lattices. One can thus apply a phase factor of  $e^{i\pi}$  to one of the sub-lattices with no physical consequences, while changing  $t \rightarrow -t$ . This maps the original Hamiltonian with chemical potential  $\mu$  to the same Hamiltonian with chemical potential  $-\mu - U$ . The point about which the transformation is symmetric is  $\langle n_{\sigma,i} \rangle = 1$  and  $\mu = U/2$ . In other words, the half-filling point always occurs at chemical potential  $\mu = U/2$ . As will be described in later sections, this symmetry upon particle-hole transformation simplifies the analysis of some measurements.

We have described above some basic phenomenology of the repulsive Fermi-Hubbard model on a square lattice. As mentioned earlier, the Hubbard model has received considerable interest as it is generally believed to apply to high- $T_c$  cuprate materials [83], but it remains unsolved except in limiting cases. Although it is not known fully to what extent the Hubbard model describe cuprates, the phase diagram of high- $T_c$  materials show some features that coincide with those predicted of the Hubbard model (see Fig. 2-11). Namely, at half-filling, i.e. “zero doping” in the language of cuprates, one finds an anti-ferromagnetic Mott insulator. The anti-ferromagnetic phase decreases as the system is doped away from half-filling, eventually giving way to a superconducting phase at low temperatures. The superconducting phase is known to have  $d_{x^2-y^2}$  symmetry, which indicates unconventional pairing [28]. The origin of this however remains debated. In addition, there are a myriad of atypical phenomena in the cuprates way from half-filling, ranging from pseudo gap behavior and anomalous resistivity to the emergence of stripe order. How much of this is captured by the Hubbard model remains to be seen.

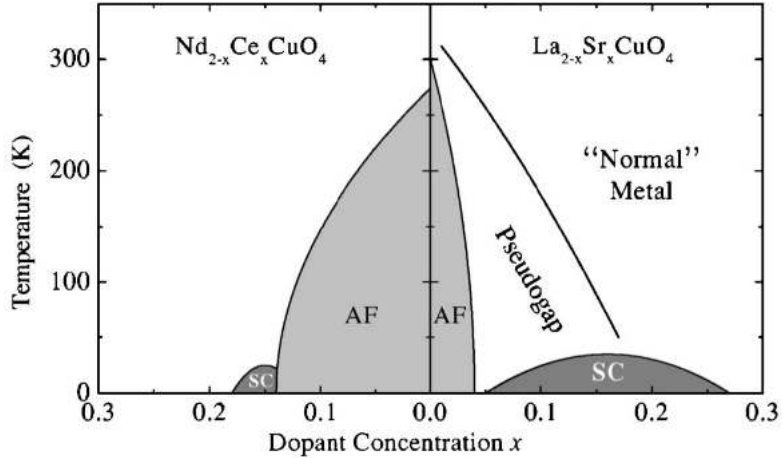


Figure 2-11: Schematic phase diagram of cuprates. Here, the dopant concentration of  $x$  corresponds to half-filling  $\langle \hat{n}_i \rangle = 1$ . Note that unlike the phase diagrams for cuprates, the phase diagram for the Hubbard model with only nearest-neighbor tunneling is symmetric across half-filling. This symmetry is broken if a next-nearest-neighbor tunneling term is added. Figure reproduced from [28].

### 2.3.3 Some Theoretical Approaches

In this section, we describe some of the theoretical approaches for solving the Hubbard model. We describe briefly those that are mentioned in this thesis. There is a large amount of literature on various approaches that the interested reader can refer to. Here, we describe 1) the atomic limit, 2) the High Temperature Series Expansion (HTSE) in  $t$ , 3) the Numerical Linked Cluster Expansion (NLCE), and 4) Determinantal Quantum Monte Carlo (DQMC). Only the first will be derived.

By the atomic limit, we mean the case of  $U \gg t$ , where the effect of  $t$  is ignored. Here, to a good approximation, the lattice sites are isolated. The micro-state of each site can be one of four possibilities: empty, filled with an  $\uparrow$  particle, filled with a  $\downarrow$  particle, or filled with two particles. In the grand canonical ensemble, the partition function can be written as

$$\mathcal{Z}[\beta, \mu] = (1 + 2\zeta + \zeta^2 w)^N \equiv z_0^N, \quad (2.64)$$

where  $\zeta \equiv \exp(\beta\mu)$ ,  $w \equiv \exp(-\beta U)$ , and  $N$  is the number of particles. From the

partition function, the density can be obtained as

$$n(\beta, \mu) = \frac{\zeta}{N} \frac{\partial \log \mathcal{Z}}{\partial \zeta} = \frac{1}{N} \frac{1}{\beta} \frac{\partial \log \mathcal{Z}}{\partial \mu}. \quad (2.65)$$

The doublon density is given by

$$d(\beta, \mu) = \frac{w}{N} \frac{\partial \log \mathcal{Z}}{\partial w} = -\frac{1}{N} \frac{1}{\beta} \frac{\partial \log \mathcal{Z}}{\partial U}. \quad (2.66)$$

In the case of a trapped sample, one can use the local density approximation, where  $\mu$  varies locally.

To improve this approximation, one can perform perturbation theory about the atomic limit. The perturbation arise from the tunneling term  $-t \sum_{\langle i,j \rangle} c_i^\dagger c_j + \text{h.c.}$ , and one can therefore perform a series expansion in  $t$ . For a more detailed discussion on how this is carried out, we refer the reader to [97].

For convenience, we reproduce here the specific results for a isotropic square lattice [97]. The grand partition function  $\Omega$  can be expressed as

$$-\beta\Omega/N = \ln z_0 + \sum_{r=2}^{\infty} z_0^{-r} A_r(\zeta, \beta U)(\beta t)^r. \quad (2.67)$$

Specifically, up to fourth order in  $\beta t$ , the non-vanishing terms are  $A_2 = 2X_1$  and

$A_4 = 2z_0^2 X_2 + 6z_0 X_3 - 7X_4 + X_5$ , with

$$\begin{aligned}
X_1 &= 2\zeta(1 + \zeta^2 w) + \frac{4\zeta^2}{\beta U}(1 - w) \\
X_2 &= \frac{1}{6}\zeta(1 + \zeta^2 w) + \frac{8\zeta^2}{(\beta U)^2}(1 + w) - \frac{16\zeta^2}{(\beta U)^3}(1 - w) \\
X_3 &= \frac{1}{3}\zeta(1 + \zeta^2 w)(1 + 2\zeta + \zeta^2 w) + \frac{6\zeta^2}{\beta U}(1 - 2\zeta w + \zeta^2 w) \\
&\quad - \frac{4\zeta^2}{(\beta U)^2}((2 - w) - 2\zeta(1 - 2w) + \zeta^2 w(2 - w)) \\
&\quad + \frac{4\zeta^2}{(\beta U)^3}(1 - w)(1 + 2\zeta + \zeta^2 w) \\
X_4 &= X_1^2 \\
X_5 &= \frac{2}{3}\zeta(1 - 4\zeta + \zeta^2 + \zeta^4 w - 4\zeta^5 w^2 + \zeta^6 w^3) \\
&\quad + \frac{8\zeta^2}{\beta U}((1 - \zeta) + \zeta(1 - 2\zeta - \zeta^3)w + 2\zeta^3(1 + \zeta)w^2) \\
&\quad - \frac{8\zeta^2}{(\beta U)^2}((2 - \zeta) - \zeta(1 + 8\zeta - \zeta^2)w + \zeta^3(1 - 2\zeta)w^2) \\
&\quad + \frac{16\zeta^2}{(\beta U)^3}((1 - \zeta - \zeta^2) - (1 - \zeta + 2\zeta^2 + \zeta^3)w \\
&\quad + \zeta^2(3 + \zeta + \zeta^2)w^2 - \zeta^4 w^3).
\end{aligned} \tag{2.68}$$

All thermodynamic quantities can be obtained from  $\mathcal{Z}$ . The case of the an anisotropic square lattice is described in [44].

HTSE is valid for high temperatures, but fails at low temperatures, when  $k_B T \sim t$ . A different theoretical approach that compare experimental results with is the numerical linked-cluster expansion (NLCE) [121, 74, 134]. This method can be used down to temperatures of  $k_B T/t \approx 0.3$  for  $U/t \approx 8$ . The basis of NLCE is a linked-cluster expansion (LCE), where the properties of a site is expressed as a sum over contributions of clusters that contain the site. One can show that the only non-zero contributions arise from linked clusters. In principle, LCEs allow one to compute correlations up to the size of the largest cluster used. However, as correlations grow beyond the size of the largest cluster, convergence issues can arise. In NLCE, the properties of the clusters are determined by exact diagonalization rather than through

series expansion methods. This means that as long as the range of correlations is much smaller than the largest cluster size, the results should be reliable. For the Hubbard model on a square lattice, at low temperatures, the magnetization displays staggered order. The correlation length for the staggered order grows as the temperature is lowered. When the correlation length becomes on the order of the size of the largest clusters used, NLCE ceases to converge. For the temperatures experimentally reached in this thesis, NLCE is reliable.

A different method that is in principle exact is determinantal quantum Monte-Carlo (DQMC) [12, 146, 32]. In DQMC, one first applies the Hubbard-Stratonovich transform to convert the Hamiltonian into bilinear form of fermion operators. The new Hamiltonian can be made quadratic in fermion operators and thus can be integrated exactly. This, however, comes at the expense of an auxiliary field  $\sigma(x, t)$ , which is a priori unknown. Using a path-integral approach, the partition function  $\mathcal{Z}$  can be written as a sum of determinants over auxiliary field configuration  $\{\sigma\}$ .

$$\mathcal{Z} = \sum_{\{\sigma\}} \rho_{\{\sigma\}}, \quad (2.69)$$

where the determinants  $\rho_{\{\sigma\}}$  are given by

$$\rho_{\{\sigma\}} = \text{Tr}_{\{\sigma\}} \prod_{i=1}^{N_\tau} \exp[\hat{a}_i], \quad (2.70)$$

and the trace is performed over all fermionic degrees of freedom for a specific auxiliary field configuration  $\{\sigma\}$  [86, 93]. The origin of the sign problem in DQMC simulation lies in the determinants, which in the case of the repulsive fermi Hubbard model away from half-filling is not positive-definite. Nevertheless, for the interaction and temperature regimes explored in this thesis, DQMC is adequate. The calculations for NLCE and DQMC presented in this thesis are carried out by two collaborating theory groups.

# Chapter 3

## Spin-Orbit Coupled Fermions

In this chapter, we discuss spin-orbit coupling of fermions. First, we will give some examples of how spin-orbit coupling can give rise to topological phases. The case of spin-orbit coupling in 1D, and how it gives rise to  $p$ -wave interactions is discussed. The possibility to generate  $p$ -wave interactions has generated intense interest, since when combined with  $s$ -wave superfluidity, Majorana zero modes can arise. These quasi-particle excitations are non-abelian in nature and have been proposed as a platform for fault-tolerant quantum computation. We will briefly describe some basic properties of Majoranas and how they arise in a simple 1D model with  $s$ -wave superfluidity in the presence of spin-orbit coupling.

After describing some motivations of realizing spin-orbit coupling, we describe how we implemented and detected spin-orbit coupling in ultracold fermionic  ${}^6\text{Li}$ . Through a two-photon process using a pair of Raman beams, two hyperfine states are coupled with momentum transfer, realizing spin-orbit coupling along with a Zeeman field. To verify the presence of spin-orbit coupling and directly measure the spinful dispersion relations, we used a method that we call “spin-injection spectroscopy”. We have also applied spin-injection spectroscopy to a novel spinful lattice system by adding an additional RF field on the spin-orbit coupled states. We demonstrate that spin-injection spectroscopy can be used to measure both the band structure and the spin compositions of the bands. The research described in this chapter have resulted in the following publication:

*L. W. Cheuk, A. T. Sommer, Z. Hadzibabic, T. Yefsah, W. S. Bakr, and M. W. Zwierlein, “Spin-Injection Spectroscopy of a Spin-Orbit Coupled Fermi Gas,” Phys. Rev. Lett. **109**, 095302 (2012) [23]. Included in Appendix E.*

### 3.1 Why Spin-Orbit Coupling?

Spin-orbit coupling gives rise to many interesting phenomena, ranging from the fine-structure in atoms to topological insulators in electronic systems. With “quantum simulation” in mind, we describe a few examples that arise in condensed matter systems. One of the exciting recent discoveries are topological insulators, insulators that are “topologically non-trivial” [53, 114]. Similar to ordinary band insulators, topological insulators are band insulators in the bulk. They differ from ordinary insulators not by symmetry breaking, but by a topological index, which is a global property of the system. This new paradigm of classifying states that differ in a topological index, but are identical in symmetry is the central notion of topological phases of matter. A physical consequence of a non-trivial topological index in topological insulators is the appearance of topologically-protected edge states that are immune to non-magnetic disorder.

To see how spin-orbit coupling is connected to topological insulators, we start with a well-known topological system - a 2D fermi gas in a magnetic field. This system exhibits the quantum hall effect, where the magnetic field splits the spectrum into degenerate Landau levels. If the chemical potential lies within a gap between Landau levels, one obtains an insulator. This insulator is topological, and can be characterized by a topological number known as the Chern number. On a finite system, the topological index must necessarily become trivial outside the system. This in general produces topological edge states at the boundary that can exist inside the bulk gap. In the quantum hall example, the edge states can simply be identified with skipping orbits, since cyclotron motion is inhibited at the edge.

With topology in mind, and the idea that the edge states can reveal topologically non-trivial states (“bulk-edge correspondence”), one can explore how other

topological materials can be generated. Using the 2D fermi gas in a magnetic field as motivation, one can wonder whether a magnetic field, which breaks time-reversal symmetry, is always required. This turns out not to be the case, as shown in the Haldane model [50]. The Haldane model is a lattice model with next-nearest neighbor tunneling matrix elements that are complex. Although no magnetic field is applied, the system exhibits the quantum hall effect. The Haldane model, initially thought to be not realizable, has in fact been simulated with ultracold gases, and the topological index in different regimes has been directly measured [68]. Nevertheless, the Haldane model still breaks time-reversal symmetry, as evident in the complex tunneling phases.

To realize a *time-reversal invariant* topological material for a spin-1/2 fermionic system, spin-orbit coupling is essential [53]. To see why this is the case, one can make use of the “bulk-edge correspondence.” Without spin-orbit coupling, the Bloch states inside a material are always two-fold degenerate, with the two-fold degeneracy arising from the two possible spin states. This is a specific case of Kramer’s degeneracy, where states appear in pairs in a time-reversal symmetric system. In the presence of spin-orbit coupling, which still preserves time-reversal symmetry, the degeneracy is lifted except at special points in the lattice. There are two ways the degeneracy can be lifted, corresponding to two topologically distinct cases.

We will not describe topological insulators in detail, but rather describe two simple examples that show how the topological properties can arise in the presence of spin-orbit coupling. Both of these examples are 1D lattice systems that can be described by a Hamiltonian of the form  $\hat{H} = \sum_k \hat{H}_k$ , where

$$\hat{H}_k = \hat{\Psi}_k^\dagger \hat{h}(k) \hat{\Psi}_k, \quad (3.1)$$

$\hat{\Psi}$  is a spinors and  $\hat{h}(k)$  is a  $2 \times 2$  matrix. The topological properties are encoded how the matrix  $\hat{h}(k)$  evolves as a function of momentum  $k$ .

The first example is the Su-Schrieffer-Heeger (SSH) model, which is a simple Hamiltonian of non-interacting particles on a 1D lattice with two orbitals. The second ex-

ample, the Kitaev chain, is an interacting system with novel topologically protected many-body excitations. These excitations are Majorana modes, which can emerge in a 1D superconducting wire composed of spinless fermions. The Kitaev chain can be thought of as the lattice analog of a 1D *p*-wave superconductor, which has similar excitations.

Recently, it has been proposed that the 1D *p*-wave systems can be generated when one combines spin-orbit coupling, a transverse Zeeman field and *s*-wave superconductivity [124, 100, 2]. This has generated considerable interest, as Majorana modes have been proposed as a platform for topological quantum computation [95, 3]. In fact, recent condensed matter experiments on Kitaev wires produced in this fashion have demonstrated signatures consistent with Majoranas [92, 1]. We will describe briefly how effective *p*-wave interactions, necessary for a Kitaev chain, emerge from underlying *s*-wave interactions when spin-orbit coupling is present. This is directly applicable to the experimental scheme described in later sections.

### 3.1.1 The Su-Schrieffer-Heger Model

The Su-Schrieffer-Heger (SSH) model describes a 1D system with alternating *A* and *B* sites, with two tunneling matrix elements *t* and *t'* describing tunneling from *A* to *B*, and from *B* to *A* respectively (see Fig. 3-1a). This was first proposed to describe polyacetylene, where the *A*-*B* structure emerges due to the Peierls's instability [54]. The SSH Hamiltonian is given by

$$\hat{H} = -t \sum_i \hat{c}_{A,i}^\dagger \hat{c}_{B,i} - t' \sum_i \hat{c}_{A,i}^\dagger \hat{c}_{B,(i-1)} + \text{h.c.} \quad (3.2)$$

Defining  $\uparrow$  ( $\downarrow$ ) to represent the internal index *A* (*B*), we can define the operators  $\hat{c}_{\sigma,k}$  as

$$\hat{c}_{\sigma,l} = \sum_k \hat{c}_{\sigma,k} e^{ik(la)} \quad (3.3)$$

where  $\sigma = \uparrow, \downarrow$  and  $a$  is the spacing between adjacent sites. In the thermodynamic limit,  $\hat{H}$  is diagonal in  $k$ , and  $\hat{H}_k$  is given by

$$\hat{H}_k = -t\hat{c}_{\uparrow,k}^\dagger\hat{c}_{\downarrow,k} - t'\hat{c}_{\uparrow,k}^\dagger\hat{c}_{\downarrow,k}e^{ika} + \text{h.c.} \quad (3.4)$$

One can rewrite  $\hat{H}_k$  as

$$\hat{H}_k = \hat{\Psi}_k^\dagger \hat{h}(k) \hat{\Psi}_k \quad (3.5)$$

where  $\hat{\Psi}_k = (\hat{c}_{\uparrow,k}, \hat{c}_{\downarrow,k})^T$  and

$$\hat{h}(k) = - \begin{pmatrix} 0 & t + t'e^{-ika} \\ t + t'e^{ika} & 0 \end{pmatrix} = -[t + t' \cos(ka)] \hat{\sigma}_x - t' \sin(ka) \hat{\sigma}_y \quad (3.6)$$

where  $\hat{\sigma}_i$  are Pauli matrices and  $t$  and  $t'$  are assumed to be real and positive. The single particle states are thus characterized by  $k$ -dependent spinors.

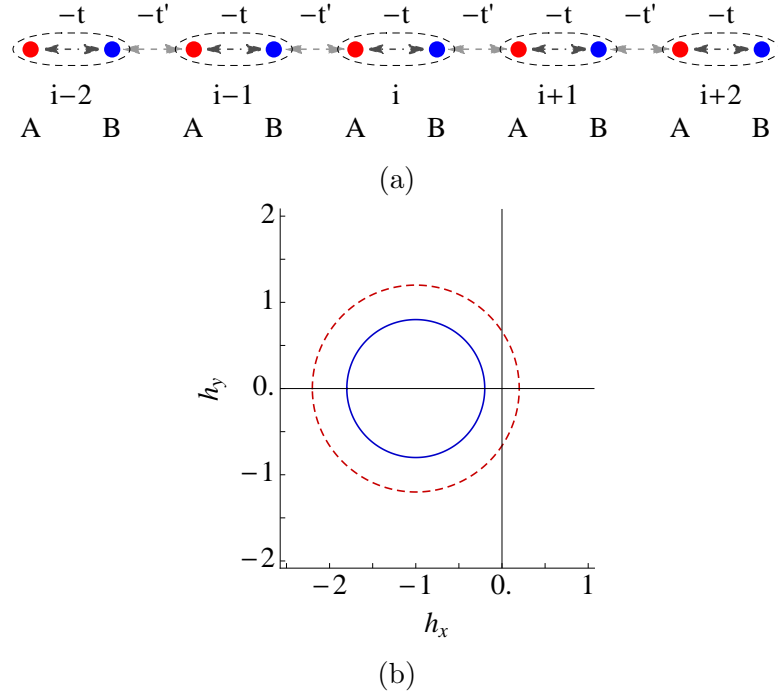


Figure 3-1: The SSH Model. (a) Diagram of SSH Model.  $A$  and  $B$  sites are marked by red and blue respectively. (b) Shown are the paths traced out by the  $\sigma_x$  and  $\sigma_y$  components of  $\hat{h}(k)$  as  $k$  goes through the Brillouin zone. The red dashed line indicates the case when  $t'/t = 1.2$ , while the blue solid line is for  $t'/t = 0.8$ . The origin is forbidden as long as  $t, t' \neq 0$ .

The extra spin-1/2 internal degree of freedom, compared to the spinless case, leads to the qualitatively new feature of a topological index. The origin of this topological index can be simply understood by considering a generic spin-1/2 system. For a spin-1/2 system, a  $2\pi$  rotation on the Bloch sphere results in a phase factor of  $e^{i\pi}$ ; a  $4\pi$  rotation is needed for the spinor to return to itself. Consider now  $\hat{h}(k)$  for different ratios of  $t/t'$ . In the case of a lattice, after a round trip on the Brillouin zone, the state must return to itself modulo a phase factor. For a spin-1/2 system, the phase can be either 0 or  $\pi$ . These two cases are topologically distinct, as they are not connected by any perturbation of the Hamiltonian that does not close any gaps.

Specifically, the eigenvectors of  $\hat{h}(k)$  are given by  $|\pm\rangle$  at energies  $\mp\sqrt{(t+t')^2 + (t')^2}$ . When  $t/t' > 1$ , as a function of  $k \in [-\pi/a, \pi/a]$ , the Bloch vector  $\langle \pm | \vec{\sigma} | \pm \rangle$  traces out a path that does not enclose the poles with  $\langle \sigma_x \rangle = \langle \sigma_y \rangle = 0$  (Fig. 3-1b). Thus when one adiabatically goes through the Brillouin zone by  $2\pi/a$ , the state returns to itself. However, when  $t/t' < 1$ , the pole is enclosed, which implies that the state accumulates a phase factor of  $e^{i\pi} = -1$ . As long as  $t, t' \neq 0$  and  $t \neq t'$ , the Bloch vector can never reach the poles. We thus see that even though both case of  $t/t' > 1$  and  $t/t' < 1$  are gapped, they differ by the phase accumulated in one round trip of the Brillouin zone. This phase factor for a 1D spin-1/2 lattice Hamiltonian is known as the Zak phase, and is a topological index. More generally, this phase factor can be written as the integral of the Berry connection  $\langle \pm | i\partial_k | \pm \rangle$  over the Brillouin zone. In this form, the phase factor can be extended to higher dimensions. For example, in 2D, the Zak phase generalizes to the Chern number.

So far, the topological index has been obtained by considering how the eigenstate varies in a round trip around the Brillouin zone. We next describe a physical consequence of topology, the appearance of edge states in the interface between two topologically distinct materials. We show specifically how edge states arise the SSH model, or in general any spin-1/2 Hamiltonian that respects chiral symmetry. Consider the case where  $t/t'$  changes spatially from  $> 1$  at  $x < 0$  to  $< 1$  at  $x > 0$ . Clearly, the two sides are topologically distinct, and gapped. At  $t = t'$ , the gap must closes.

Setting  $t' = 1$ , and  $t = t'(1 + m(x))$  and expanding at  $k = \pi/a$ , we find that

$$\hat{h}(k) = t'(m(x)\hat{\sigma}_x - ak\hat{\sigma}_y). \quad (3.7)$$

We can replace  $k \rightarrow (\hbar/i)\partial_x$  to obtain

$$\hat{h}(k) = t'(m(x)\hat{\sigma}_x + ia\partial_x\hat{\sigma}_y) \quad (3.8)$$

This equation is also known as the Jackiw-Rebbi equation [65], and has the following properties. Since  $\{\sigma_z, \hat{h}(k)\} = 0$  (chiral symmetry), eigenvectors come in pairs at energies  $\pm E$ . The special case is when  $E = 0$ . Here, suppose the spinor is given by  $(u, v)^T$ . Then the coefficients  $u, v$  must satisfy the following equations:

$$\begin{aligned} (m(x)\hat{\sigma}_x + a\partial_x)v &= 0 \\ (m(x)\hat{\sigma}_x - a\partial_x)u &= 0 \end{aligned} \quad (3.9)$$

At large  $|x|$ , one of the solutions exponentially decrease, while the other exponentially increases. In order to satisfy the condition of normalizability, one finds that the state must be given by

$$\psi(x) = e^{-\int_0^x m(x')/adx'} \begin{pmatrix} 1 \\ 0 \end{pmatrix}. \quad (3.10)$$

At large  $|x|$ , one finds that the state decreases exponentially as  $\exp[-(m(\pm\infty)/a)x]$ . If the slope of  $m(x)$  is changed, then the normalizable state is proportional to  $(0, 1)^T$ . This implies that if one has a finite region where the Zak phase is  $\pi$ , localized states occur at the edges of this region. Energetically, they occur in the middle of the band, which is gapped in the bulk. At one edge, the bound state is  $\uparrow$ , and at the other edge, the state is  $\downarrow$ . These correspond to the state being entirely on site  $A$  or site  $B$ . Thus one sees that at the location where the topological index changes, or where the mass term  $m(x)$  in the Jackiw-Rebbi equation changes sign, there exists a localized state. These states are pinned at the boundary, and survive as long as the topological indices on each side are unchanged.

### 3.1.2 Obtaining $p$ -Wave Interactions via Spin-Orbit Coupling

In the previous section, we showed that the coupling of an internal degree of freedom (“spin”) with the orbital motion produces topologically non-trivial bandstructures, and how localized zero energy states occur at the boundaries of topologically distinct regions. In this section, we discuss how interactions can be modified with spin-orbit coupling. Specifically, we discuss how  $p$ -wave interactions can arise out of underlying  $s$ -wave interactions. It turns out that  $p$ -wave interactions can lead to interesting many-body states.

To see how  $p$ -wave interactions arise, we first consider the dispersion relation in the presence spin-orbit coupling. Spin-orbit coupling is simply the coupling of the motion of a particle with its spin. For simplicity, we assume it has the form  $\lambda_{SO}q\sigma_z$ . The free-particle Hamiltonian for the two spin states can be written as

$$\hat{H} = \frac{\hbar^2 q^2}{2m} + \lambda_{SO}q\sigma_z \quad (3.11)$$

The dispersion is shown in Fig. 3-2a, and consists of two parabolas displaced by  $Q = (2m\lambda_{SO})/\hbar$ . At this point, for interactions to occur, one must still have two Fermi seas. The spin-orbit coupling term alone is simply a spin-dependent momentum shift, and the two energy bands for different spins are not coupled. The situation changes when one applies a transverse Zeeman field  $(\hbar\Omega_R/2)\sigma_x$ . The Hamiltonian becomes

$$\hat{H} = \frac{\hbar^2 q^2}{2m} + \lambda_{SO}q\sigma_z + \frac{\hbar\Omega_R}{2}\sigma_x, \quad (3.12)$$

and an avoided crossing appears where the two free-particle dispersions touch. The resulting dispersion contains two spinful bands separated by the spin-orbit gap. When the chemical potential  $\mu$  lies within the spin-orbit gap, only the lower band is occupied, and one effectively a single-component Fermi gas. Nevertheless, the fermions are able to interact, since opposing momenta have different admixtures of spin up and spin down. The interactions vanish when the momentum difference of two fermions approach zero, since the spin compositions become identical. Thus, one obtains effec-

tive  $p$ -wave interactions in a single-component Fermi gas, which at low temperatures can exhibit BCS-type pairing.

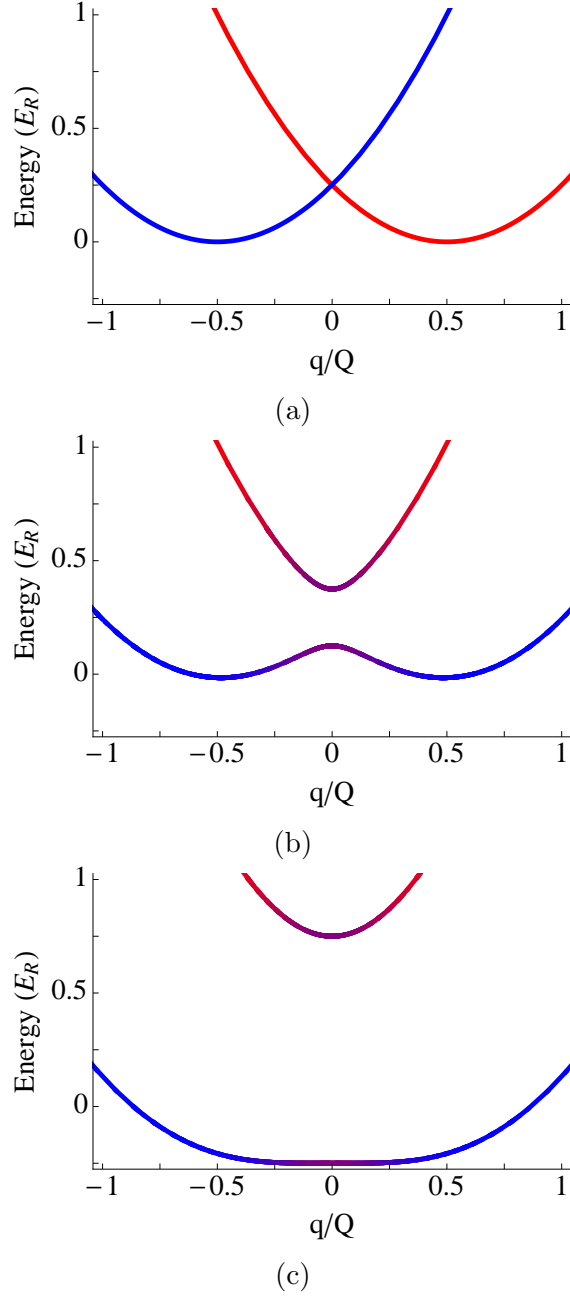


Figure 3-2: Spin-orbit bands. Here, the color denotes the spin composition, with blue (red) indicating  $|\uparrow\rangle$  ( $|\downarrow\rangle$ ). (a) With only the spin-orbit coupling term, we obtain two free particle dispersions shifted by momentum  $Q = E_R/\lambda_{SO}$ , with  $E_R = \hbar^2 Q^2/(2m)$ . (b) In the presence of a transverse Zeeman field of amplitude  $\hbar\Omega/2$ , the crossing at  $Q = 0$  becomes an avoided crossing. A spin-orbit gap emerges with size  $\hbar\Omega_R$ . (c) When  $\hbar\Omega_R = E_R$ , the bottom band changes from having two minima at  $Q \neq 0$  to having a single minimum at  $Q = 0$ .

### 3.1.3 The Kitaev Chain

We showed in the previous section how spin-orbit coupling along with a Zeeman field can lead to effective  $p$ -wave interactions, thus also pairing, in a spinless Fermi gas. In this section, we give an example of how this can lead to interesting many-body states. Specifically, we will discuss the 1D Kitaev chain, which has topologically protected Majorana zero modes. These Majorana modes possess non-Abelian exchange statistics, and has been proposed as building blocks for topologically protected quantum computation [95, 3].

Before discussing the Kitaev chain, we briefly describe some properties of Majorana zero modes. The defining feature of a Majorana zero mode is that it is described by a fermion operator that is self-conjugate. One can construct two Majorana operators  $\gamma_1$  and  $\gamma_2$  from fermionic creation and annihilation operators  $\hat{c}^\dagger$  and  $\hat{c}$  simply via:

$$\begin{aligned}\hat{\gamma}_1 &= \frac{1}{\sqrt{2}}(\hat{c}^\dagger + \hat{c}) \\ \hat{\gamma}_2 &= \frac{1}{\sqrt{2}i}(\hat{c}^\dagger - \hat{c})\end{aligned}\tag{3.13}$$

For now, this is just a mathematical transformation. By inspection, one sees that the new operators satisfy  $\hat{\gamma}_i^\dagger = \hat{\gamma}_i$ . They also obey the commutation property

$$\{\gamma_i, \gamma_i^\dagger\} = 2\gamma_i^2 = \frac{1}{2}(\{c^\dagger, c\} + \{c^\dagger, c\}) = 1.\tag{3.14}$$

One can also check that  $\{\gamma_1, \gamma_2\} = 0$ . In other words, these operators obey fermionic commutation relations. In terms of  $\gamma_1$  and  $\gamma_2$ , one finds that the number operator is

given by

$$\begin{aligned}
c^\dagger c &= \frac{1}{2}(\hat{\gamma}_1 + i\hat{\gamma}_2)(\hat{\gamma}_1 - i\hat{\gamma}_2) \\
&= \frac{1}{2}(\hat{\gamma}_1^2 + \hat{\gamma}_2^2 + i[\hat{\gamma}_2, \hat{\gamma}_1]) \\
&= 1 + i[\hat{\gamma}_2, \hat{\gamma}_1] \\
&= 1 + 2i\hat{\gamma}_2\hat{\gamma}_1
\end{aligned} \tag{3.15}$$

Although one can always apply the above transformation to obtain Majorana operators, these operators are only physically relevant in systems where they diagonalize the Hamiltonian. In the context of many-body systems, this translates to finding systems whose quasi-particle excitations can be described by Majorana operators. We saw that the Majorana operators are a combination of a creation and annihilation operators. This suggests that the Hamiltonian must contain terms that involve  $\hat{c}^\dagger\hat{c}^\dagger$  or  $\hat{c}\hat{c}$ , in order to mix particles and holes. For the usual  $s$ -wave superconductors, particles and holes are mixed by the superconducting order parameter  $\Delta$ . However, due to the nature of the interactions, i.e. only opposite spins interact, the mixing is between  $\sigma$  particles, and  $-\sigma$  holes. We thus require a Hamiltonian of paired *spinless* fermions. The Kitaev chain is precisely this. It is a 1D lattice model of spinless fermions with nearest-neighbor pairing, and is described by the following Hamiltonian

$$\hat{H} = -\mu \sum_j \hat{c}_j^\dagger \hat{c}_j - t \sum_j (\hat{c}_j^\dagger \hat{c}_{j+1} + \text{h.c.}) + \Delta \sum_j (\hat{c}_j^\dagger \hat{c}_{j+1}^\dagger + \text{h.c.}) . \tag{3.16}$$

To see how Majoranas arise, we consider the case where  $\Delta = t$ , and  $\mu = 0$ , and the chain is  $N$  sites long. We define Majorana operators  $\hat{\gamma}_{1,j}$  and  $\hat{\gamma}_{2,j}$  in analogy to Eq. (3.13), which are given by

$$\begin{aligned}
\hat{\gamma}_{1,j} &= \frac{1}{\sqrt{2}}(\hat{c}_j^\dagger + \hat{c}_j) \\
\hat{\gamma}_{2,j} &= \frac{1}{\sqrt{2}i}(\hat{c}_j^\dagger - \hat{c}_j)
\end{aligned} \tag{3.17}$$

The Hamiltonian can then be expressed as

$$\begin{aligned}
\hat{H} &= -t \sum_{j=0}^{N-1} \left( \hat{c}_j^\dagger (\hat{c}_{j+1} + \hat{c}_{j+1}^\dagger) + (\hat{c}_{j+1}^\dagger + \hat{c}_{j+1}) \hat{c}_j \right) \\
&= -\sqrt{2}t \sum_{j=0}^{N-1} \left( \hat{c}_j^\dagger \hat{\gamma}_{1,j+1} - \hat{c}_j \hat{\gamma}_{1,j+1} \right) \\
&= -2it \sum_{j=0}^{N-1} \hat{\gamma}_{2,j} \hat{\gamma}_{1,j+1}
\end{aligned} \tag{3.18}$$

It is evident that in this form the Hamiltonian does not contain the terms  $\hat{\gamma}_{2,N}$  or  $\hat{\gamma}_{1,0}$ . These Majorana modes, which are at zero energy ( $\mu = 0$ ), cost no energy, and are completely localized on the edges. The two Majorana modes can be described in terms of a pair of normal fermion operators  $f$  and  $f^\dagger$  that are delocalized on the two edges. We thus find that at  $\mu = 0$ , the ground state is two-fold degenerate, where the two many-body states differ from one another by the occupation of a highly non-local zero-energy fermionic mode. A crucial property of these Majorana modes is that they are non-Abelian under exchange [3]. More precisely, suppose one has  $N$  wires with Majorana modes  $\hat{\gamma}_{A,i}$  and  $\hat{\gamma}_{B,i}$  at the edge of each wire labeled by  $i$ . This results in a  $2^N$  degenerate sub-space. In a single wire, two majorana modes are either both occupied each by 1/2 a real fermion, or unoccupied. This cannot be changed since the parity of the fermion occupation is conserved. However, with multiple wires, one can engineer couplings of the form  $\hat{\gamma}_{A,i} \hat{\gamma}_{B,j}$ , which conserved the parity of the total system. Adiabatically switching on these terms, however, can change the internal state within the degenerate subspace. By moving Majoranas in this fashion, one can exchange Majoranas, and the operation is non-Abelian, since the state does not return to itself. This type of operation, known as “braiding,” is not sensitive to the details as long as the system is adiabatic. In this sense, a quantum state can be encoded in the degenerate subspace spanned by the Majorana modes. Since a real fermion is highly delocalized, this can be immune to local noise.

So far, we have only shown that Majorana fermions arise for a specific choice of  $\Delta$  and  $\mu$ . To connect the existence of these edge states with topology of the

bandstructure, we rewrite the Kitaev Hamiltonian in the form  $\hat{H} = \Psi_k^\dagger \hat{h}(k) \Psi_k$ . Here, due to pairing terms, we choose  $\Psi = (\hat{c}_k, \hat{c}_{-k}^\dagger)^T$ . One then finds that  $\hat{h}(k)$  is given by

$$\begin{aligned}\hat{h}(k) &= \begin{pmatrix} -\mu/2 - t \cos(ka) & -i \sin(ka) \\ i \sin(ka) & \mu/2 + t \cos(ka) \end{pmatrix} \\ &= -\left(\frac{\mu}{2} + t \cos(ka)\right) \hat{\sigma}_z + \Delta \sin(ka) \hat{\sigma}_y.\end{aligned}\quad (3.19)$$

Using a similar argument to the one we used earlier when discussing the SSH model, namely, whether the poles corresponding to eigenstates of  $\hat{\sigma}_x$  are enclosed, one finds that there are two topologically distinct phases for  $|\mu| < 2t$ , and  $|\mu| > 2t$ . The specific example with Majoranas correspond to the first case. One specific example of the second case is when  $\mu \gg 2t$ . If we take the limit of  $t \rightarrow 0$  and  $\Delta \rightarrow 0$ , this corresponds to isolated sites. The Majorana operators  $\hat{\gamma}_{1,i}$  and  $\hat{\gamma}_{2,i}$  are only coupled to each other at every site  $i$ , and there are no decoupled Majorana edges modes.

We next explicitly show for the Kitaev chain, why one needs a spinless Fermi gas to realize Majoranas. Suppose for the moment that the pairing arises in the usual fashion from  $s$ -wave interactions. The analogous 1D Hamiltonian now has an additional spin index  $\sigma = \uparrow, \downarrow$ , and is given by

$$\hat{H} = -\mu \sum_{j,\sigma} \hat{c}_{j,\sigma}^\dagger \hat{c}_{j,\sigma} - t \sum_{j,\sigma} \left( \hat{c}_{j,\sigma}^\dagger \hat{c}_{j+1,\sigma} + \text{h.c.} \right) + \Delta \sum_{j,\sigma} \left( \hat{c}_{j,\sigma}^\dagger \hat{c}_{j+1,-\sigma}^\dagger + \text{h.c.} \right). \quad (3.20)$$

We again consider the case where  $\mu = 0$ , i.e. the chemical potential is exactly half-way inside the gap. Just as for the Kitaev chain, we consider the special case of  $t = \Delta$ . We define new operators, which as we shall see are not Majorana operators,  $\hat{\gamma}_{1,j,\sigma}$  and  $\hat{\gamma}_{2,j,\sigma}$  by

$$\begin{aligned}\hat{\gamma}_{1,j,\sigma} &= \frac{1}{\sqrt{2}} (\hat{c}_{j,\sigma}^\dagger + \hat{c}_{j,-\sigma}) \\ \hat{\gamma}_{2,j,\sigma} &= \frac{1}{\sqrt{2}i} (\hat{c}_{j,\sigma}^\dagger - \hat{c}_{j,-\sigma})\end{aligned}\quad (3.21)$$

Although one can rewrite the Hamiltonian in terms of the new operators as

$$\hat{H} = -2it \sum_{j=0,\sigma}^{N-1} \hat{\gamma}_{2,j,\sigma} \hat{\gamma}_{1,j+1,-\sigma}, \quad (3.22)$$

where the localized modes  $\hat{\gamma}_{1,1,\sigma}$  and  $\hat{\gamma}_{2,N,\sigma}$  are decoupled, these modes are not Majorana modes. From Eq. (3.21), one sees that  $\hat{\gamma}_{1,j,\sigma}^\dagger = \hat{\gamma}_{1,j,-\sigma}$  and  $\hat{\gamma}_{2,j,\sigma}^\dagger = \hat{\gamma}_{2,j,-\sigma}$ . We see explicitly that in this case,  $\sigma$  particles are mixed with  $-\sigma$  holes. These states are in fact the lattice analog of Andreev bound states.

Motivated by the prospect of creating Majorana fermions, the method of generating effective  $p$ -wave superconductors with spin-orbit coupling is actively pursued in 1D nanowires [124, 100, 2], where signatures consistent with Majoranas have been detected [94, 1].

As described in the following sections, although we have not yet combined spin-orbit coupling with BCS pairing and obtain  $p$ -wave superfluids, we have implemented spin-orbit coupling with a transverse Zeeman field in ultracold fermionic  ${}^6\text{Li}$  atoms, and directly observed the spin-orbit bands. By adiabatically loading atoms into the lower spin-orbit band, we have also observed spinless Fermi gases with spin compositions that allow for effective  $p$ -wave interactions. Effective interactions in a single component Fermi gas with spin-orbit coupling have been observed directly [147].

## 3.2 Implementing Spin-Orbit Coupling with Raman Beams

Many different methods, ranging from Raman coupling to super-lattices, have been proposed to realize spin-orbit coupling in ultracold systems [27, 40]. In general, “spin” denotes an internal degree of freedom, and can correspond to hyperfine states, energy bands or different orbitals in a lattice [85, 133, 39, 84]. For the research described in this chapter, we use a simple scheme that produces spin-orbit coupling in 1D. The spin is mapped to hyperfine states of the ground manifold, and the coupling is realized by a pair of non-copropagating Raman beams [57]. The perspective of viewing Raman-coupled internal states as spin-orbit coupling was pioneered with  $^{87}\text{Rb}$  BECs [85], where the modification of the dispersion relation was inferred by the momentum of the condensates.

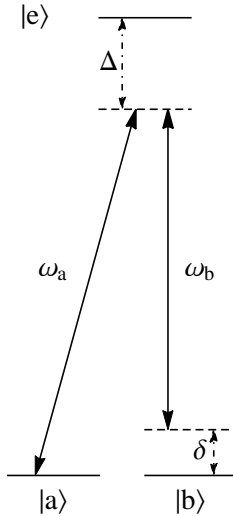


Figure 3-3: Raman coupling two ground states with two photons via an intermediate excited state.

In this section, we describe how Raman coupling leads to spin-orbit coupling with a transverse Zeeman field. First, we describe Raman coupling without considering the motional state of the atom. In Raman coupling, we change the internal state of an atom via a two-photon process. In the simplest example, we consider a 3-level system with two ground states  $|a\rangle$ ,  $|b\rangle$  and an excited state  $|e\rangle$ . Without loss of generality, we

consider the case when  $|a\rangle$  and  $|b\rangle$  are degenerate, and are  $\hbar\omega_0$  lower in energy than  $|e\rangle$ . Consider two laser beams with frequency  $\omega_a = \omega_0 - \Delta$  and  $\omega_b = (\omega_0 - \Delta) - \delta$  that couple only to the  $|a\rangle \rightarrow |e\rangle$  and  $|b\rangle \rightarrow |e\rangle$  transitions respectively, as shown in Fig. 3-3. We consider the case where the single photon detuning  $\Delta$  is much larger than the excited state linewidth  $\Gamma$ . Suppose the beams have equal intensity such that the  $|a\rangle$ - $|e\rangle$  and  $|b\rangle$ - $|e\rangle$  matrix elements are both  $\hbar\Omega$ , where  $\Omega/2$  is the single photon Rabi frequency. When  $\delta = 0$ , second order perturbation theory gives a matrix element of  $\hbar\Omega^2/(4\Delta)$ , corresponding to a two-photon Rabi frequency  $\Omega_R$  of  $\Omega_R = \Omega^2/(2\Delta)$ . To derive the Hamiltonian in the case of non-zero  $\delta$ , it is simpler to consider the dressed state picture, where we take into account the energy of the photon. We dress  $|a\rangle$  atoms with the  $\omega_a$  light field and  $|b\rangle$  atoms with the  $\omega_b$  light field. These two states are coupled by  $\hbar\Omega_R/2$ , but are split by  $\hbar\delta$ . The effective 2-level Hamiltonian is then

$$\hat{H} = \begin{pmatrix} \delta/2 & \hbar\Omega_R/2 \\ \hbar\Omega_R^*/2 & -\delta/2 \end{pmatrix} = \frac{\delta}{2}\hat{\sigma}_z + \frac{\hbar\Omega_R}{2}\hat{\sigma}_x, \quad (3.23)$$

where in the last equality we take  $\Omega_R$  to be real, and  $\hat{\sigma}_i$  denote Pauli matrices.

To see how spin-orbit coupling arises, we next consider the motional degrees of freedom. Suppose the two Raman beams are not co-propagating. An atom in state  $|a\rangle$  with momentum  $k$  can absorb an  $\omega_a$  photon and emit an  $\omega_b$  photon. As a result, the internal state changes to  $|b\rangle$ . In order to conserve total momentum, the atom also receives a momentum transfer of  $\hbar Q$ , where  $Q$  is the wavevector difference between the two Raman beams. The internal degree of freedom (spin) is thus coupled with the motion (orbit) of the atom. To take into account momentum, we extend the Hamiltonian in Eq. 3.23 by adding the free-particle dispersion  $\varepsilon_k = \hbar^2 k^2/(2m)$ .

$$\begin{aligned} \hat{H} &= \sum_k \hat{H}_k \\ &= \sum_k \begin{pmatrix} \frac{\hbar^2(k+Q)^2}{2m} + \frac{\delta}{2} & \frac{\hbar\Omega_R}{2} \\ \frac{\hbar\Omega_R}{2} & \frac{\hbar^2 k^2}{2m} - \frac{\delta}{2} \end{pmatrix}. \end{aligned} \quad (3.24)$$

Up to a constant energy shift, we rewrite the Hamiltonian in a symmetric form

$$\hat{H} = \sum_q \begin{pmatrix} \frac{\hbar^2}{2m} \left( q + \frac{Q}{2} \right)^2 + \frac{\delta}{2} & \frac{\hbar\Omega_R}{2} \\ \frac{\hbar\Omega_R}{2} & \frac{\hbar^2}{2m} \left( q - \frac{Q}{2} \right)^2 - \frac{\delta}{2} \end{pmatrix}. \quad (3.25)$$

In this form, we define  $q$  to be the quasi-particle momentum. Note that the  $|\uparrow\rangle$  and  $|\downarrow\rangle$  states for each  $q$  have real momentum  $q + Q/2$  and  $q - Q/2$  respectively. One must keep this in mind when interpreting the experimental measurements.

Rewriting  $\hat{H}_q$  in terms of Pauli matrices  $\hat{\sigma}_i$  acting on the subspace for the internal states, one obtains

$$\hat{H}_q = \frac{\hbar^2 q^2}{2m} \mathbb{1} + \frac{\delta}{2} \hat{\sigma}_z + \frac{\hbar\Omega_R}{2} \hat{\sigma}_x + \frac{\hbar^2}{2m} q Q \hat{\sigma}_z, \quad (3.26)$$

where  $E_R = \hbar^2 Q^2 / (2m)$ , and constant energy offset terms are dropped. Note that  $E_R$  is defined differently here than in Section 2.1.2. Performing a rotation in the internal space of  $\hat{\sigma}_z \rightarrow \hat{\sigma}_y$ ,  $\hat{\sigma}_y \rightarrow \hat{\sigma}_x$  and  $\hat{\sigma}_x \rightarrow \hat{\sigma}_z$ , and rewriting in terms of the dimensionless quantities  $\tilde{q} = q/Q$ ,  $\tilde{\delta} = \delta/E_R$  and  $\tilde{\Omega}_R = \Omega_R/E_R$ , we obtain

$$\hat{H}_q = E_R \left[ \tilde{q}^2 \mathbb{1} + \left( \tilde{q} + \frac{\tilde{\delta}}{2} \right) \hat{\sigma}_y + \frac{\tilde{\Omega}_R}{2} \hat{\sigma}_z \right]. \quad (3.27)$$

Expressed in this form, it is apparent that we obtain a spin-orbit coupling term proportional to  $\tilde{q}\hat{\sigma}_y$ , and a mixing term  $\tilde{\Omega}_R\hat{\sigma}_z$  that acts as a transverse Zeeman field. The transverse Zeeman field is directly proportional to the two-photon Rabi frequency  $\Omega_R$ . One also notices that spin-orbit coupling can be thought of as a momentum dependent Zeeman field  $\mathbf{B} = \frac{E_R}{g\mu_B} (0, 2\tilde{q} + \tilde{\delta}, \tilde{\Omega}_R)$ , where  $g$  is the electron  $g$ -factor and  $\mu_B$  is the Bohr magneton.

### 3.2.1 Raman Coupling in Alkali Atoms

In the case of alkali atoms, the two-photon Raman coupling relies inherently on spin-orbit coupling inside the atom, between the spin  $S$  and the orbital momentum  $L$  of

the valence electron. This is because the light field couples to the orbital momentum  $L$ , and cannot change either the nuclear spin  $I$  or electron spin  $S$ . The spin-orbit coupling term in  $L \neq 0$  states in the atom thus allows two-photon transitions to couple different hyperfine states in the ground  $L = 0$  manifold. Here, we discuss the specific case of spin-orbit coupling between hyperfine states in the ground  $s_{1/2}$  manifold using a two-photon transition, with excited  $p_{1/2}$  and  $p_{3/2}$  levels acting as intermediate states. The  $p_{1/2}$  and  $p_{3/2}$  states are split by  $\Delta_{\text{SO}}$ . For simplicity, we ignore hyperfine structure here. Consider a two-photon Raman process that couples the two  $|J = 1/2, m_J = \pm 1/2\rangle$  states. For concreteness, suppose the two beams have polarizations  $\sigma_+$  and  $\pi$  and are on two-photon resonance. The Raman process involves transitions shown in Fig. 3-4, and proceeds as follows. An atom in  $|1/2, -1/2\rangle$  absorbs a photon from the  $\sigma_+$  beam and emits into the  $\pi$  beam, ending in  $|1/2, +1/2\rangle$ . Suppose that the Raman beams are red-detuned  $\Delta$  from the  $J = 3/2$  manifold. The matrix element due to the  $|3/2, 1/2\rangle$  state is proportional to  $\sqrt{2}\hbar\Omega^2/(3\Delta)$ , while that due to  $|1/2, 1/2\rangle$  is  $-\sqrt{2}\hbar\Omega^2/(3[-\Delta_{\text{SO}} + \Delta])$ , where we assume both  $\sigma_+$  and  $\pi$  beams are of equal intensity with single-photon Rabi frequency of  $\Omega$ . The effective two-photon coupling is thus given by

$$\Omega^{(2)} = \frac{\Omega^2}{2} \frac{\sqrt{2}}{3} \left( \frac{1}{\Delta} + \frac{1}{\Delta_{\text{SO}} - \Delta} \right). \quad (3.28)$$

At large detuning  $\delta$ , this is approximately

$$\Omega^{(2)} \approx \Omega^2 \frac{1}{3\sqrt{2}} \left( \frac{\Delta_{\text{SO}}}{\Delta^2} \right). \quad (3.29)$$

One inevitable effect of near-resonant light is spontaneous scattering. In the limit where the single-photon detunings  $\Delta$  and  $\Delta_{\text{SO}} - \Delta$  are large relative to the natural line width  $\Gamma$ , the off-resonant spontaneous scattering rate is given by

$$\Gamma_{sc} = \left( \frac{\Omega}{2} \right)^2 \frac{\Gamma}{3} \left( \frac{2}{\Delta^2} + \frac{1}{(\Delta_{\text{SO}} - \Delta)^2} \right), \quad (3.30)$$

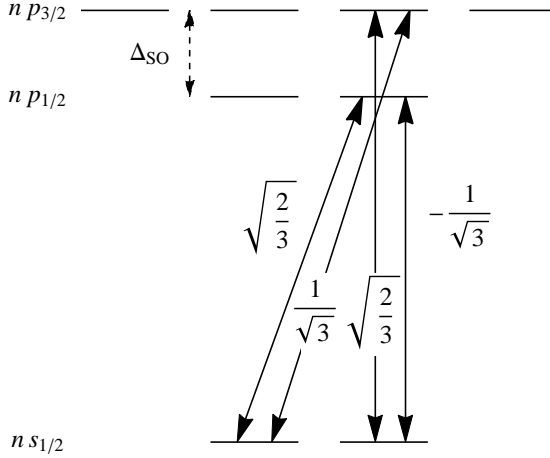


Figure 3-4: Raman coupling via  $p_{1/2}$  and  $p_{3/2}$  excited states. Shown are the Clebsch-Gordan coefficients for the relevant transitions that couple  $m_s = -1/2 \rightarrow m_s = 1/2$  via  $\sigma_+$  and  $\pi$  polarized light. As expected, the contributions to the two-photon transition amplitude from the  $p_{1/2}$  and  $p_{3/2}$  states are opposite and cancel at large single-photon detuning.

where we have assumed that the population is equally distributed between  $m_s = \pm 1/2$ . At larger detunings  $\Delta \gg \Delta_{SO}$ , one notices that the spontaneous emission rate scales as  $1/\Delta^2$ , similar to the Raman coupling. Unlike the case for optical dipole traps, further detuning does not reduce the relative spontaneous scattering rate. A useful figure of merit is the two-photon Rabi frequency to spontaneous emission rate to  $\xi = |\Omega^{(2)}|/\Gamma_{sc}$ . At large detunings,  $\xi \rightarrow \frac{2\sqrt{2}}{3}\Delta_{SO}/\Gamma$ . Since spin-orbit coupling is a relativistic effect that strengthens with the atomic number  $Z$ , heavier atoms have a larger splitting  $\Delta_{SO}$  and hence a better figure-of-merit  $\xi$ . In Fig. 3-5, we show  $\xi$  for  ${}^6\text{Li}$ , as a function of detuning  $\Delta$ .

### 3.2.2 Raman Coupling in ${}^6\text{Li}$

Our apparatus for generating spin-orbit coupled Fermi gases starts with degenerate fermionic  ${}^6\text{Li}$  sympathetically cooled by  ${}^{23}\text{Na}$ , as described previously [47, 150]. In this section, we discuss specifically Raman coupling for  ${}^6\text{Li}$ . Due to its low mass,  ${}^6\text{Li}$  has a  $2p_{1/2}$ - $2p_{3/2}$  splitting of only  $\hbar \times 10 \text{ GHz}$  and a linewidth of  $\hbar \times 6 \text{ MHz}$ . The resulting maximum ratio of two-photon Rabi frequency to spontaneous emission rate  $\xi$ , ignoring hyperfine structure, is only  $\sim 2\pi \times 250$ . Hyperfine structure further reduces

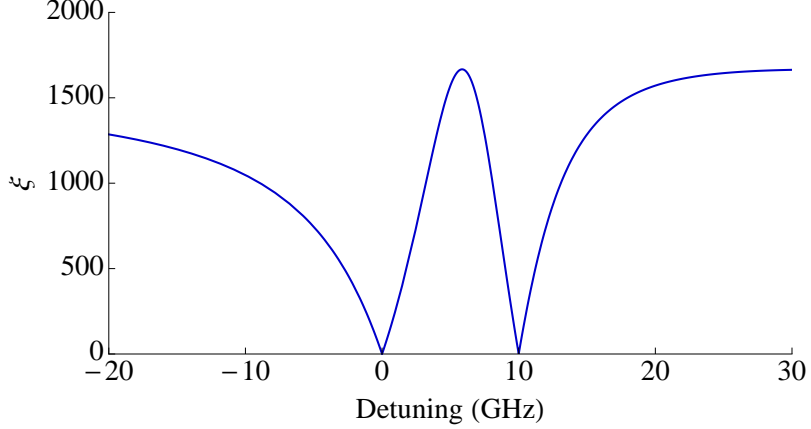


Figure 3-5: Figure-of-merit  $\xi$  of Raman coupling in  ${}^6\text{Li}$  ignoring hyperfine structure. Shown is  $\xi$  as a function of red detuning  $\Delta$  from the  $p_{3/2}$  level. The optimal ratio  $\xi$  is obtained 4.0 GHz to the blue of the D1 line.

this number by some factor  $\beta$ . Therefore, in order to minimize the spontaneous scattering rate, one must choose judiciously which hyperfine states to use.

In the presence of a magnetic field, the Hamiltonian for the ground state manifold is given by

$$\hat{H} = A\hat{\mathbf{I}} \cdot \hat{\mathbf{S}} + g_S\mu_B B\hat{S}_z + g_I\mu_B B\hat{I}_z, \quad (3.31)$$

where  $A$  is the hyperfine constant,  $g_S$  ( $g_I$ ) the electron (nucleon)  $g$ -factor, and  $\mu_B$  is the Bohr magneton. Since  $\hat{H}$  commutes with  $\hat{F}_z = \hat{S}_z + \hat{I}_z$ , the quantum number  $m_F = m_S + m_I$  remains good when  $B \neq 0$ . Furthermore, it is clear that only pairs of states  $|m_s = 1/2 \equiv \uparrow, m_I\rangle$  and  $|\downarrow, m_I + 1\rangle$  are coupled. For  $|m_F| < I + 1/2$ , the Hamiltonian projected on to this spin-1/2 subspace is

$$\hat{H}_{m_F} = \left( \frac{A}{4} + g_I m_F B \right) \hat{\mathbb{1}} + \left( \frac{\mu_B B}{2} (g_S - g_I) + \frac{m_F}{2} A \right) \hat{\sigma}_z + \frac{\alpha_{m_F}}{2} A \hat{\sigma}_x, \quad (3.32)$$

where  $\alpha = \sqrt{I(I+1) - m_F^2 + 1/4}$ . Diagonalizing this matrix gives the Breit-Rabi energy levels, shown in Fig. 3-6a. For  $|m_F| = I + 1/2$ , the eigenstates are the stretched states  $|\uparrow, I\rangle$  and  $|\downarrow, -I\rangle$ , with energies  $(AI/2) \pm (g_S/2 + g_I I)\mu_B B$ .

Since the Raman coupling changes  $m_S$  by 1, the strongest coupling occurs between states with maximally different  $m_S$  projections. At high-magnetic fields, where  $m_S$  and  $m_I$  are approximately good quantum numbers, the coupling is strongest for states

with opposite  $m_S$  and identical  $m_I$ . At low fields, the hyperfine interaction couples the electron spin  $S$  and the nuclear spin  $I$ , and  $m_S$  and  $m_I$  are no longer good quantum numbers. The experiments described in this chapter take place at low magnetic fields. In  ${}^6\text{Li}$ , the nuclear spin  $I = 1$ , which gives two hyperfine manifolds  $F = 1/2$  and  $F = 3/2$ . In the presence of a magnetic field, the six hyperfine states, labeled  $|1\rangle$  to  $|6\rangle$  from lowest to highest energy, can be written in the  $|m_S, m_I\rangle$  basis as

$$\begin{aligned}
|1\rangle &= \cos \theta_{-1/2} |\downarrow, 0\rangle + \sin \theta_{-1/2} |\uparrow, -1\rangle \\
|2\rangle &= \cos \theta_{1/2} |\downarrow, 1\rangle + \sin \theta_{1/2} |\uparrow, 0\rangle \\
|3\rangle &= |\downarrow, -1\rangle \\
|4\rangle &= \cos \theta_{-1/2} |\uparrow, -1\rangle - \sin \theta_{-1/2} |\downarrow, 0\rangle \\
|5\rangle &= \cos \theta_{1/2} |\uparrow, 0\rangle - \sin \theta_{1/2} |\downarrow, 1\rangle \\
|6\rangle &= |\uparrow, 1\rangle
\end{aligned} \tag{3.33}$$

where  $\tan(2\theta_{m_F}) = -\alpha_{m_F} A / (B(-g_I \mu_I + g_S \mu_S) + m_F A)$ . The mixing due to hyperfine coupling  $A$  is maximal at  $B = 0$ . At high fields  $B \gg A/(g_S \mu_B)$ ,  $\theta_{m_F} \rightarrow 0$ ; this is the Paschen-Back regime, where the magnetic moments are determined primarily by  $m_S$ .

The lowest three hyperfine states in  ${}^6\text{Li}$  are stable towards pairwise collisions among any two. From Eq. (3.33), at low magnetic fields, it is clear that one should use one of the stretched states ( $|3\rangle$  or  $|6\rangle$ ) in order to have maximally opposite  $m_S$  projection. Using Eq. (3.33), we compute the magnetic field dependence of the Raman coupling, shown in Fig. 3-6a. We find that the optimal combination is  $|2\rangle-|3\rangle$ . In order to satisfy selection rule of  $\Delta m_F = 1$ , one requires a pair of Raman beams with  $\pi$  and  $\sigma_{\pm}$  polarization. With this choice of polarizations, and at the optimal detuning is 4.0 GHz to the D1 line, we obtain a maximum Rabi coupling to spontaneous emission ratio of  $\sim 2\pi \times 220$ .

For our experiments, in order to resolve different hyperfine levels, a magnetic field of 11.6 G is applied along  $\hat{z}$ . The two Raman beams propagate in the  $\hat{x} - \hat{z}$  plane at an angle of  $\pm 19^\circ$  relative to  $\hat{y}$ , as shown in Fig. 3-7a. Relative to the quantization axis

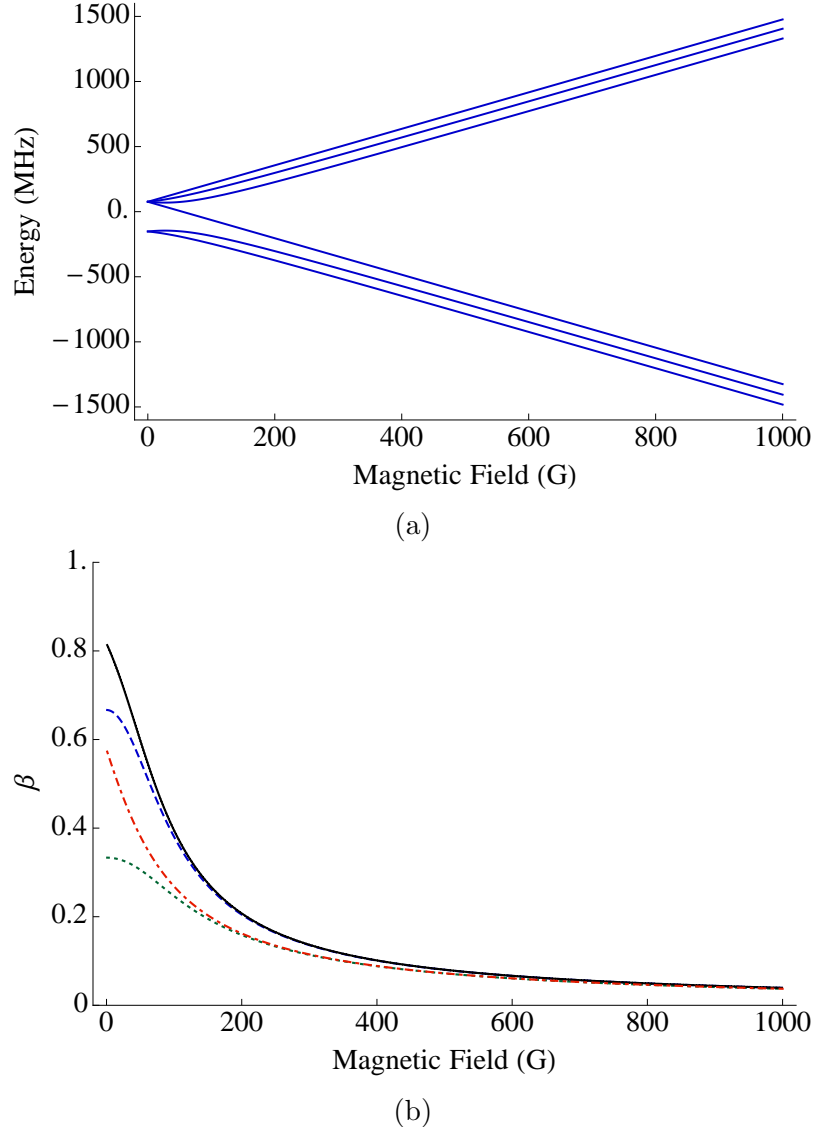


Figure 3-6: (a) Magnetic field dependence of hyperfine levels obtained from Breit-Rabi equation. (b) Magnetic field dependence of the suppression factor in Raman coupling due to hyperfine mixing. The combinations shown are:  $|2\rangle-|3\rangle$  in black solid,  $|1\rangle-|2\rangle$  ( $\sigma_-$  light coupled to  $|1\rangle$ ) in green dotted,  $|1\rangle-|2\rangle$  ( $\sigma_+$  light coupled to  $|1\rangle$ ) in blue dashed, and  $|1\rangle-|3\rangle$  in red dot-dashed.

$\hat{y}$ , these beams have  $\sigma_+ + \sigma_-$  and  $\pi$  polarizations respectively. We tune the relative frequency of the two Raman beams such that the two-photon resonance condition only holds for the combination of  $\sigma_+$  and  $\pi$ , as shown in Fig. 3-7b. The momentum transfer is along  $\hat{x}$ , and results in 1D spin-orbit coupling along this direction.

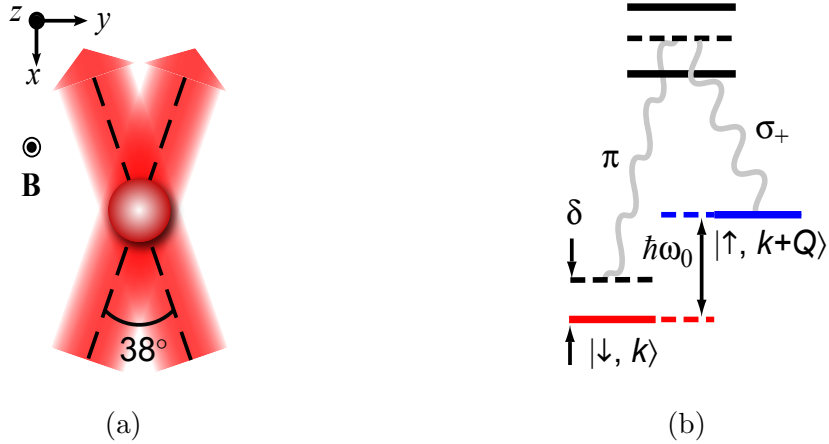


Figure 3-7: Raman beam geometry and polarizations. (a) Geometry of the two Raman Beams. (b) Schematic Diagram showing transitions and levels for Raman coupling. Figures reproduced from [23].

### 3.3 Detecting Spin-Orbit Coupling

In previous experiments with spin-orbit coupling in BECs with Raman beams, the modification of the dispersion relation was detected via measuring the momenta of the BECs after time-of-flight (TOF) [85]. Concurrent with our work, another experiment using fermionic  $^{40}\text{K}$  observed effects of spin-orbit coupling by measuring a spin-dependent shift in the average momentum [142]. Unlike the case for BECs, where a narrow range of momenta  $\ll Q$  is populated, the signal for fermions is more difficult to observe, as many momentum states are occupied in a Fermi gas. However, if combined with momentum-resolved detection via TOF, a Fermi gas allows many momenta to be probed simultaneously.

To verify that spin-orbit coupling and a transverse Zeeman field are present, we first pulsed on the Raman beams for a duration corresponding to a  $\pi$ -pulse, and subsequently released the atoms after TOF. After a TOF time that is much longer than the inverse trap frequency, we image the atoms. The density profile after TOF reveals directly the momentum distribution. Since the Raman beams are only resonant for a narrow momentum class, one can observe selective transfer between  $|\downarrow, q\rangle$  and  $|\uparrow, q+Q\rangle$ , as shown in Fig. 3-8a. By integrating along the direction orthogonal to the Raman transfer ( $\hat{x}$ ), one obtains integrated profiles as a function of momentum

for both spin states. The location of the transfer is used to calibrate the magnitude of the momentum transfer  $k$ . The integrated profiles can then be plotted in terms of the quasi-momentum  $\tilde{q}$ , as shown in Fig. 3-8b. The ratio of the signal in the two spin channels as a function of  $\tilde{q}$  allows one to extract the spin  $S_z \equiv (n_\uparrow - n_\downarrow)/(n_\uparrow + n_\downarrow)$ , where  $n_\uparrow$  ( $n_\downarrow$ ) is the integrated density for  $\uparrow$  ( $\downarrow$ ) atoms. The spin composition  $S_z$  can then be re-expressed as a color map as a function of both the quasi-momentum  $\tilde{q}$  and some other quantity.

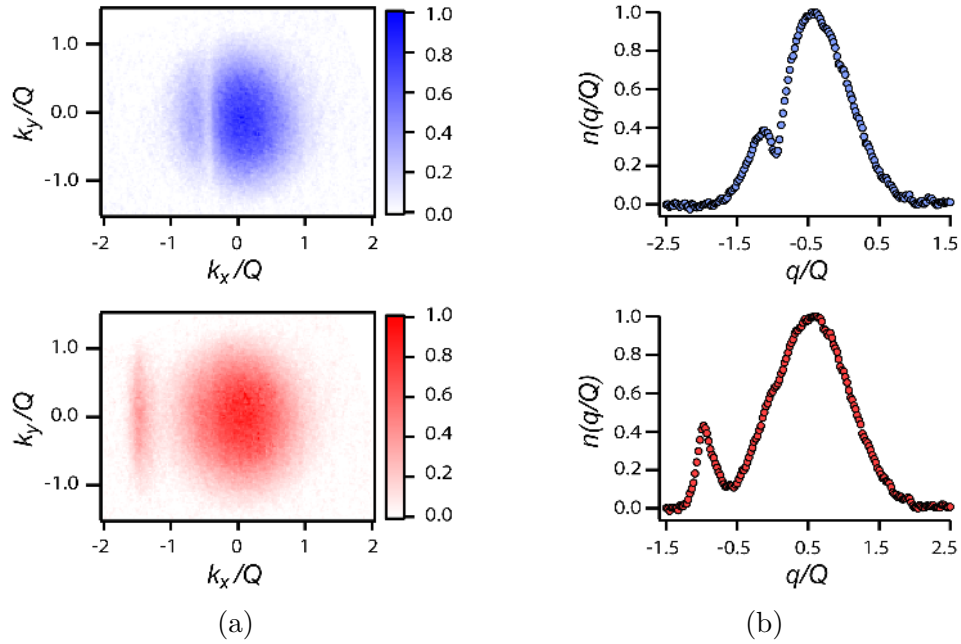


Figure 3-8: Spin and momentum-resolved images and profiles. (a) Spin and momentum-resolved images after a  $\pi$ -pulse is applied. The top (blue) and bottom (red) are the  $|\uparrow\rangle$  and  $|\downarrow\rangle$  channels respectively. Atoms in a momentum class satisfying the two-photon resonance condition are transferred from  $|\uparrow\rangle$  to  $|\downarrow\rangle$  while simultaneously receiving a momentum kick of  $-Q$ . (b) Corresponding integrated spin and momentum-resolved profiles as a function of quasi-momentum  $q/Q$ . Figures reproduced from [23].

When the detuning  $\Delta$  is varied, the momentum where the transfer occurs changes, in accordance to Eq. (3.27). The shift in the momentum is given by  $\Delta\tilde{k} = -\frac{\tilde{\Delta}}{2}$ . Since  $\Delta$  can be read off, and  $\tilde{k}$  can be measured without calibration of the imaging system, one can use the measured  $\Delta\tilde{k}$  versus  $\Delta$  curve to determine  $E_R$ . From the known mass  $m$ , one can thus obtain  $Q$ , which also precisely calibrates the imaging

magnification.

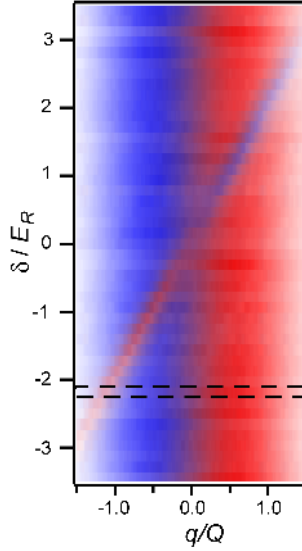


Figure 3-9: Raman transfer as a function of the two-photon detuning  $\delta$ . The Raman strength is  $\hbar\Omega_R = 0.035(5)E_R$ , and the pulse time corresponds to that of a  $\pi$ -pulse. Figures reproduced from [23].

When one suddenly turns on the Raman lasers, Rabi oscillations occur between two states with opposite spin  $\sigma$  and offset by momentum  $Q$ , as shown in Fig. 3-10a. To understand how the momentum-dependent Rabi oscillations arise, we recall that for a two-level system coupled with Rabi frequency  $\Omega$  and detuning  $\Delta$ , the population in the initially unoccupied state, say  $|\uparrow\rangle$ , is given by

$$P_{\uparrow} = \frac{\Omega^2}{\Omega^2 + \delta_0^2} \sin^2 \left( \frac{1}{2} \sqrt{\Omega^2 + \delta_0^2} t \right), \quad (3.34)$$

where  $t$  is the elapsed time. In the present case, the Doppler shift gives rise to a momentum-dependent detuning  $\delta_0 = 2\tilde{q}E_R/\hbar$ . As a result, the oscillation frequency and amplitude vary as a function of  $\tilde{q}$ . The evolution of  $P_{\uparrow}$  at different momentum is shown in Fig. 3-10c. One can also identify the times  $t_n$  when  $P_{\uparrow}$  is minimal, as shown in Fig. 3-10b. From Eq. (3.34), these times are given by

$$t_n = \frac{2\pi n}{\sqrt{\Omega^2 + \delta_0^2}}. \quad (3.35)$$

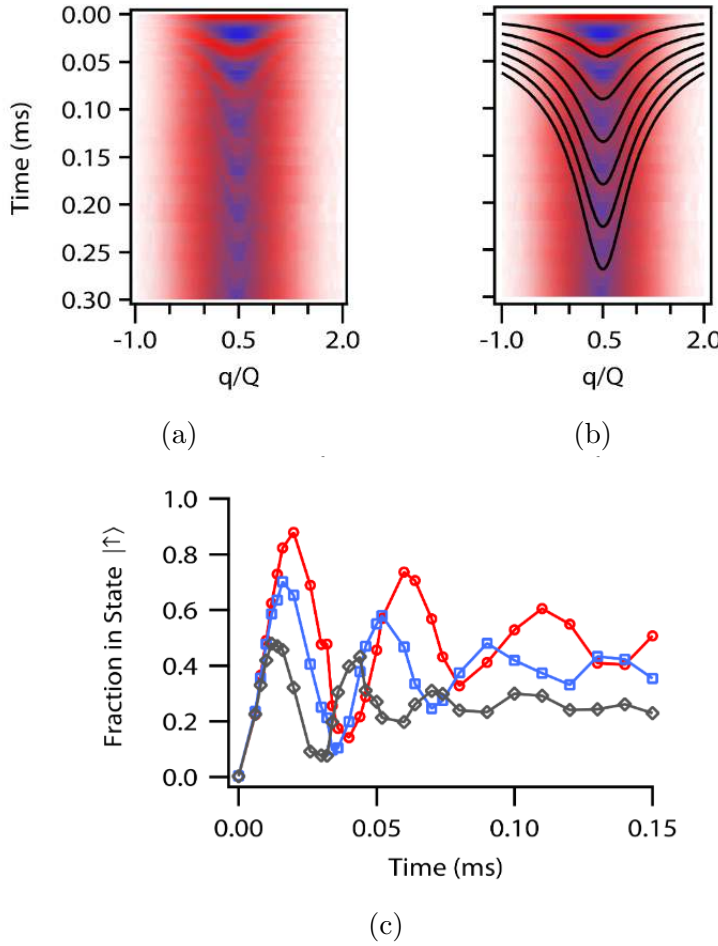


Figure 3-10: Momentum-dependent Rabi oscillations at  $\hbar\Omega_R = 0.78(2)E_R$  and detuning  $\delta = 0.25(1)E_R$ . (a) Spin and momentum-resolved profiles as a function of time after spin-orbit coupling is turned on suddenly. Here,  $\hbar\Omega_R = 0.71(2)E_R$  and  $\hbar\delta = -0.25(1)E_R$ . (b) Profiles with contours indicating minima of  $|\downarrow\rangle$ . (c) In circles, squares and diamonds are the  $|\uparrow\rangle$  fraction of as a function of time for  $\tilde{q} = 0.5, 0.25$ , and  $0.05$  respectively. Figures reproduced from [23].

In addition to Rabi oscillations, another way to verify the coherence of the spin-orbit coupling is to adiabatically turn on the coupling. Rather than ramping the intensity adiabatically, we ramp the detuning, starting far from away from two-photon resonance with any occupied momentum class. Depending on the sign of the initial detuning, the system is adiabatically loaded into either the upper or lower spin-orbit bands. Again, by measuring the spin and momentum after TOF, we observe profiles consistent with an adiabatic ramp, as shown in Fig. 3-11. When the ramp is

reversed, the spin composition is recovered, which shows that the process is reversible and adiabatic. This also directly demonstrates that we can realize a single Fermi sea with varying momentum-dependent spin composition, either in the upper or lower spin-orbit bands. Although the upper band is metastable, the lower spin-orbit band should be stable even in the presence of collisions. As discussed in Section 3.1.2, a *single-component* interacting Fermi gas with effective  $p$ -wave interactions emerge when underlying  $s$ -wave interactions are switched on for Fermions in the lower spin-orbit band.

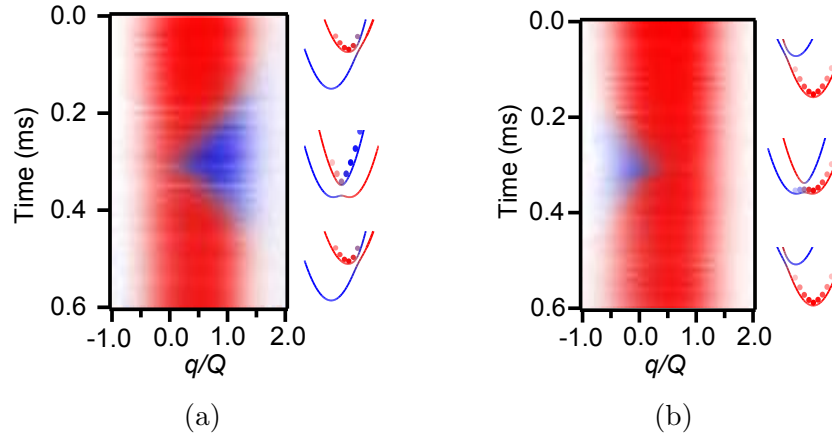


Figure 3-11: Adiabatic loading of spin-orbit bands at  $\hbar\Omega_R = 0.53(5)E_R$ . (a) Starting with detuning  $\delta = -8.5\Omega_R$ ,  $\delta$  is swept linearly at a rate of  $|\dot{\delta}| = 0.27(5)\Omega_R^2$  to  $\delta = 0$ , and swept back. The atoms remain in the upper spin-orbit band at all times. A diagram indicating the population along in the spin-orbit bands is shown on the right. (b) Starting with detuning  $\Delta = 8.5\Omega_R$ ,  $\delta$  is swept linearly at a rate of  $|\dot{\delta}| = 0.27(5)\Omega_R^2$  towards  $\delta = 0$ , and swept back. The atoms are loaded into the lower spin-orbit band. A diagram indicating the population along in the spin-orbit bands is shown on the right. Figures reproduced from [23].

### 3.3.1 Spin-Injection Spectroscopy

Although the measurements in the previous section verify that spin-orbit coupling is present, it does not directly measure the dispersion relation of the spin-orbit coupled bands. To directly detect the modified spinful dispersion, we implemented a new technique that we call spin-injection spectroscopy. Spin-injection spectroscopy is

similar to spin-resolved inverse ARPES, where free electrons are injected into a sample with specific momenta and energies. In our case, we utilize two additional hyperfine states that are not coupled by Raman beams. Specifically, we use states  $|1\rangle$  and  $|4\rangle$  which we denote as  $|\uparrow\rangle_R$  and  $|\downarrow\rangle_R$ . Via selection rules, RF transitions only couple  $|\uparrow\rangle_R$  to  $|\uparrow\rangle$ , and  $|\downarrow\rangle_R$  to  $|\downarrow\rangle$ . We use either  $|\uparrow\rangle_R$  or  $|\downarrow\rangle_R$  as reservoir states, and inject atoms from these reservoirs into the spin-orbit coupled  $|\uparrow\rangle$ - $|\downarrow\rangle$  system. By spin-selectively imaging  $|\uparrow\rangle$  and  $|\downarrow\rangle$ , one can determine the admixture of  $|\uparrow\rangle$  and  $|\downarrow\rangle$  in the spin-orbit coupled states.

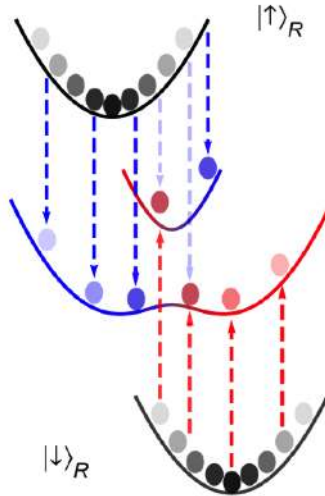


Figure 3-12: Spin-Injection Spectroscopy. The spin-orbit coupled system involves states  $|\uparrow\rangle$  and  $|\downarrow\rangle$  shown in blue and red respectively. In spin-injection spectroscopy, we make use of two reservoir states  $|\uparrow\rangle_R$  and  $|\downarrow\rangle_R$ , indicated by the gray parabolas shown above and below the spin-orbit coupled states. The reservoir states do not experience spin-orbit coupling. Their dispersion relation is that of free particles. Using RF pulses, selection rules allow for two transitions,  $|\uparrow\rangle_R \rightarrow |\uparrow\rangle$  and  $|\downarrow\rangle_R \rightarrow |\downarrow\rangle$ . Due to the long wavelength of RF radiation, the RF pulses do not impart any momentum. The two gray parabolas corresponding to the energy bands of the reservoir states are shifted in quasi-momentum by the spin-orbit momentum transfer  $Q$ . Figure reproduced from [23].

In detail, the procedure for spin-injection spectroscopy proceeds as follows.

- 1) Fermionic  ${}^6\text{Li}$  atoms are initially prepared in  $|\uparrow\rangle_R$  ( $|\downarrow\rangle_R$ ).
- 2) An RF pulse with frequency near the  $|\uparrow\rangle_R \rightarrow |\uparrow\rangle$  ( $|\downarrow\rangle_R \rightarrow |\downarrow\rangle$ ) transition is applied. This injects atoms into the spin-orbit coupled system, which is formed

by Raman-coupling the bare states  $|\uparrow\rangle$  and  $|\downarrow\rangle$ .

3) The Raman beams and the dipole trapping beams are switched off, and the atoms are allowed to expand ballistically for some time.

4) Atoms in each spin state  $|\uparrow\rangle$  and  $|\downarrow\rangle$  are imaged separately. This allows one to measure the arrivals in each spin channel as a function of the RF frequency. Furthermore, the ballistic expansion allows one to determine the momentum distribution of the atoms that are successfully transferred.

This procedure is depicted in Fig. 3-12. A total of four spectra are obtained. Two spectra, corresponding to the separately imaged  $|\uparrow\rangle$  and  $|\downarrow\rangle$  channels, are obtained with atoms prepared initially in the reservoir state  $|\uparrow\rangle_R$ . The other two are obtained with atoms starting in the other reservoir state  $|\downarrow\rangle_R$ . An example of these four spectra is shown in Fig. 3-14, where the presence of a spin-orbit gap in the bare spectra is already directly observable. In principle, the dispersion relation and the spin composition of the spin-orbit coupled bands are contained in these spectra. In order to reconstruct the dispersion, we must add back the free particle dispersion of the reservoir states  $|\uparrow\rangle_R$  and  $|\downarrow\rangle_R$ . The ratio of the arrivals in the two channels  $|\uparrow\rangle$  and  $|\downarrow\rangle$  for each quasi-momentum  $Q$  directly reveals the spin composition of the two spin-orbit coupled bands. It is interesting to note the arrivals in the  $|\uparrow\rangle$  channel when starting with atoms in  $|\downarrow\rangle_R$  are only present because of spin-orbit coupling.

Combining the four spectra along with the free particle dispersion of the reservoir states, we are thus able to extract the spin-resolved dispersion relations, as shown in Fig 3-14. The expected spinful dispersion and the spin-orbit gap are directly observed. We also see how the spin-orbit gap increases with the Raman coupling, and the merging of the two minima in the lower spin-orbit band into a single minimum. A unique feature of spin-injection spectroscopy is that the spin-orbit system is initially empty, and specific states are only briefly populated after injection with the spectroscopy pulse. This allows for a clean background, as only arrivals are imaged. Furthermore, the spin-orbit states that can be accessed are thus only limited by the initial momentum distribution of the reservoir states. This illustrates one of the practical

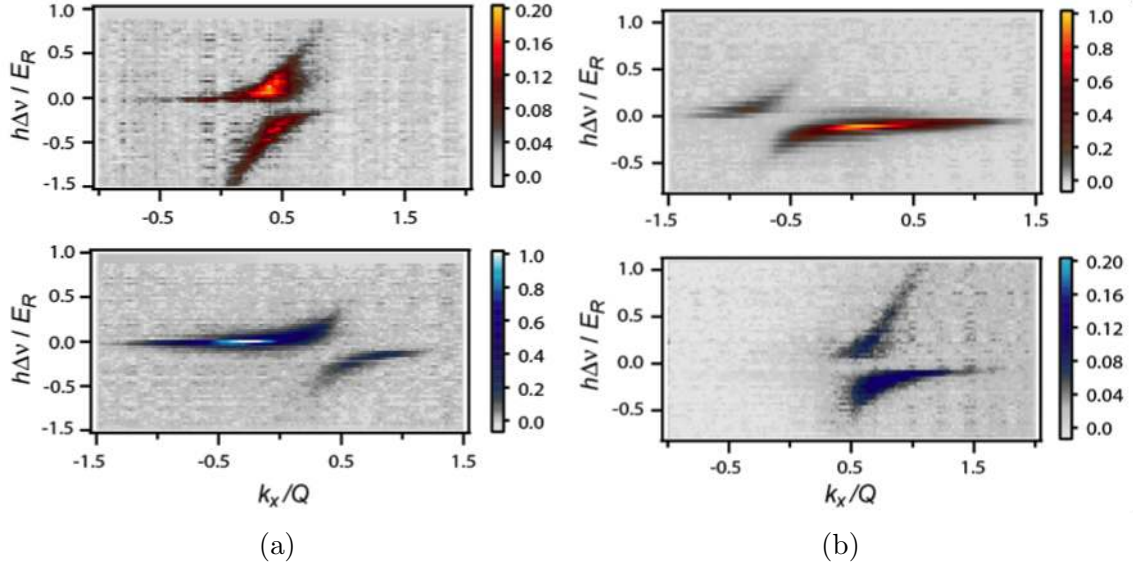


Figure 3-13: Bare spectra from spin-injection spectroscopy of spin-orbit coupled fermions. Here,  $\Delta\nu$  is the detuning in the RF frequency from the bare transition. (a) Shown are the spectra in the two channels  $|\downarrow\rangle$  (top) and  $|\uparrow\rangle$  (bottom), with atoms prepared in reservoir state  $|\uparrow\rangle_R$ . (b) Same as (a), except atoms are initially prepared in  $|\downarrow\rangle_R$ . Figures reproduced from [23].

advantages of the Fermi gas compared to Bose-Einstein condensates. Rather than occupying a single momentum, the Fermi gas occupies a large range of momentum with a width  $\sim 2|k_F|$ .

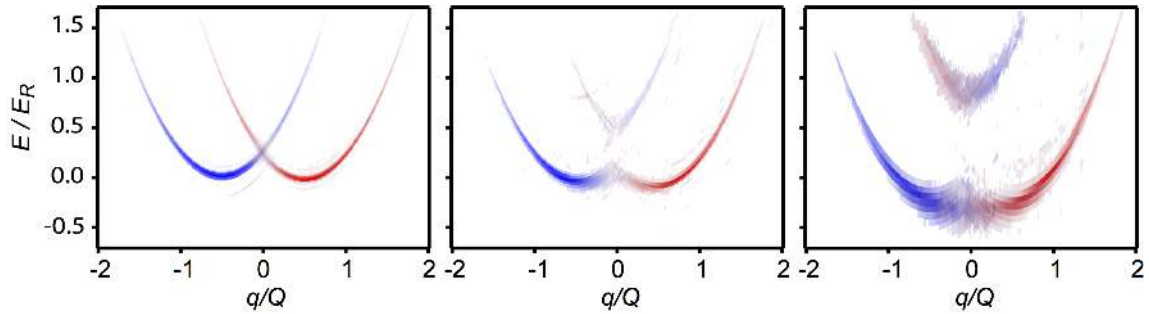


Figure 3-14: Spin-orbit bands reconstructed from spin-injection spectroscopy spectra. Shown from left to right are cases corresponding to  $\tilde{\Omega}_R = 0, 0.43(5)$  and  $0.9(1)$ , respectively. The opening of the spin-orbit gap with increasing  $\tilde{\Omega}_R$  is seen. For the rightmost case, the merging of the two minima in the lower spin-orbit gap is evident. Figures reproduced from [23].

### 3.3.2 Measuring Spinful Bands in an RF-Raman Lattice

To illustrate the technique of spin-injection spectroscopy, we engineered another situation where dispersions are spinful. By applying an additional RF drive between  $|\uparrow\rangle$  and  $|\downarrow\rangle$ , we created a novel spin-dependent lattice. To see how the lattice structure arises, we consider an atom in state  $|\downarrow, q\rangle$ . The Raman coupling couples  $|\downarrow, q\rangle$  to  $|\uparrow, q+k\rangle$ . The RF drive couples  $|\uparrow, q+k\rangle$  back to  $|\downarrow, q+k\rangle$ , with no imparted momentum. This produces a lattice Hamiltonian similar to Eq. (2.18), where each entry is a  $2 \times 2$  matrix. Specifically,

$$\begin{aligned}\hat{H} &= \sum_q \hat{H}_q \\ \hat{H}_q &\equiv E_R \left[ \left( \left( \tilde{q} - \frac{1}{2} + n \right)^2 \hat{\mathbb{1}} + \frac{\tilde{\Omega}_{RF}}{2} \hat{\sigma}_x \right) \delta_{n,m} \right. \\ &\quad \left. + \frac{\tilde{\Omega}}{2} (\hat{\tau} \delta_{n,m+1} + \hat{\tau}^\dagger \delta_{n,m-1}) \right]\end{aligned}\quad (3.36)$$

where  $(n, m)$  denotes a  $2 \times 2$  block,  $\tilde{\Omega} = \hbar\Omega_R/E_R$ ,  $\tilde{\Omega}_{RF} = \hbar\Omega_{RF}/E_R$ , and  $\hat{\tau}$  is given by

$$\hat{\tau} = \begin{pmatrix} 0 & 0 \\ 1 & 0 \end{pmatrix}. \quad (3.37)$$

In this form, it is clear that one needs  $\tilde{\Omega}_{RF}$  and  $\tilde{\Omega}$  to open up all gaps at the zone edge  $\pm k/2$ . The difference from a simple lattice is shown schematically in Fig. 3-15.

To understand the structure of the bands, we first start with the case where the Raman coupling is off but the RF coupling is on, i.e.  $\tilde{\Omega} = 0$  and  $\tilde{\Omega}_{RF} \neq 0$ . The RF coupling splits the  $|\uparrow\rangle$  and  $|\downarrow\rangle$  states by exactly  $\hbar\Omega_{RF}$ . In the reduced zone scheme, we have two pairs of free-particle bands for each spin, with a vanishing bandgap at the zone edges at  $\pm Q/2$ , and no avoided crossings. The two pairs of free-particle bands are not coupled, as shown in Fig. 3-16c. The spin composition of the two bands are equal and orthogonal superpositions of  $|\uparrow\rangle$  and  $|\downarrow\rangle$ . The spin state and the motional states are decoupled at this point.

Next, we switch on the Raman coupling. The four band crossings near  $E_R/4$  all

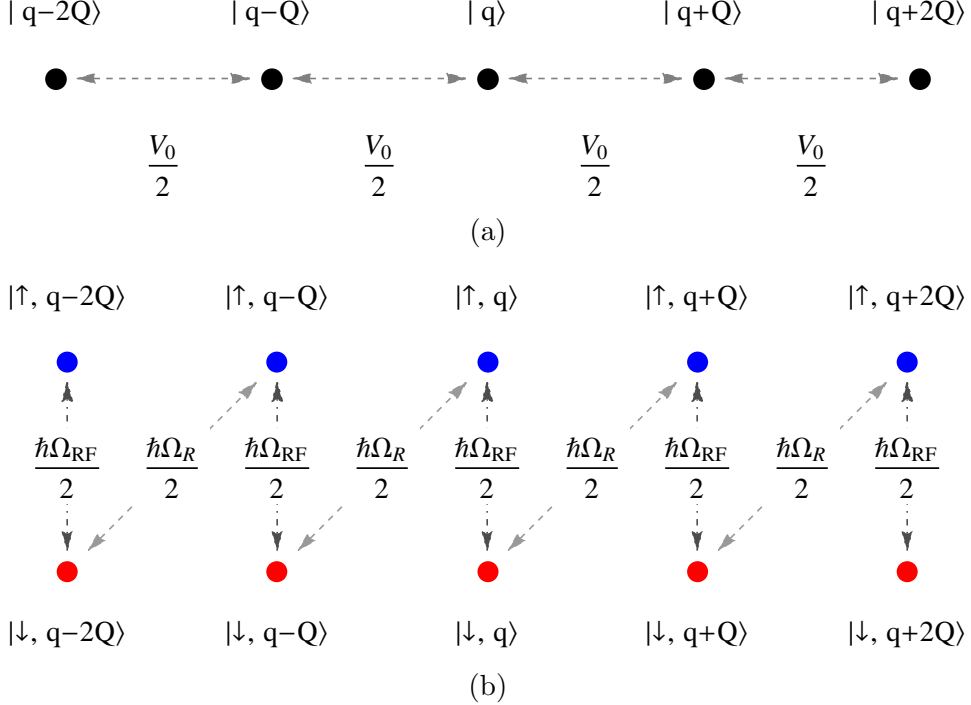


Figure 3-15: Simple Lattice Versus Raman Lattice. (a) Graphical representation of the momentum space structure of a normal lattice. States  $|\mathbf{q} + nQ\rangle$  are coupled by the lattice with amplitude  $V_0/4$ , where  $V_0$  is the depth of the lattice. (b) Graphical representation of the momentum space structure of the Raman-RF lattice. Each momentum state has an additional spin index  $\sigma = \uparrow, \downarrow$ . States  $|\downarrow, \mathbf{q} + nQ\rangle$  and  $|\uparrow, \mathbf{q} + (n+1)Q\rangle$  are coupled by the Raman beams, while states  $|\downarrow, \mathbf{q} + nQ\rangle$  and  $|\uparrow, \mathbf{q} + nQ\rangle$  are coupled by the RF drive.

become avoided crossings. Although the Raman can only couple a right-moving  $\downarrow$  state with a left-moving  $\uparrow$  state, the RF coupling allows all states to have admixtures of both  $\uparrow$  and  $\downarrow$ , and hence all states that are at the same quasi-momentum can couple.

Explicitly, when  $\Omega_{RF} = 0$ , there are four states  $|\alpha_i, q\rangle$ ,  $i = 1, 2, 3, 4$ , where  $q$  is the quasi-momentum. Initially, these are quadruply degenerate at  $E = E_R/4$ , and given

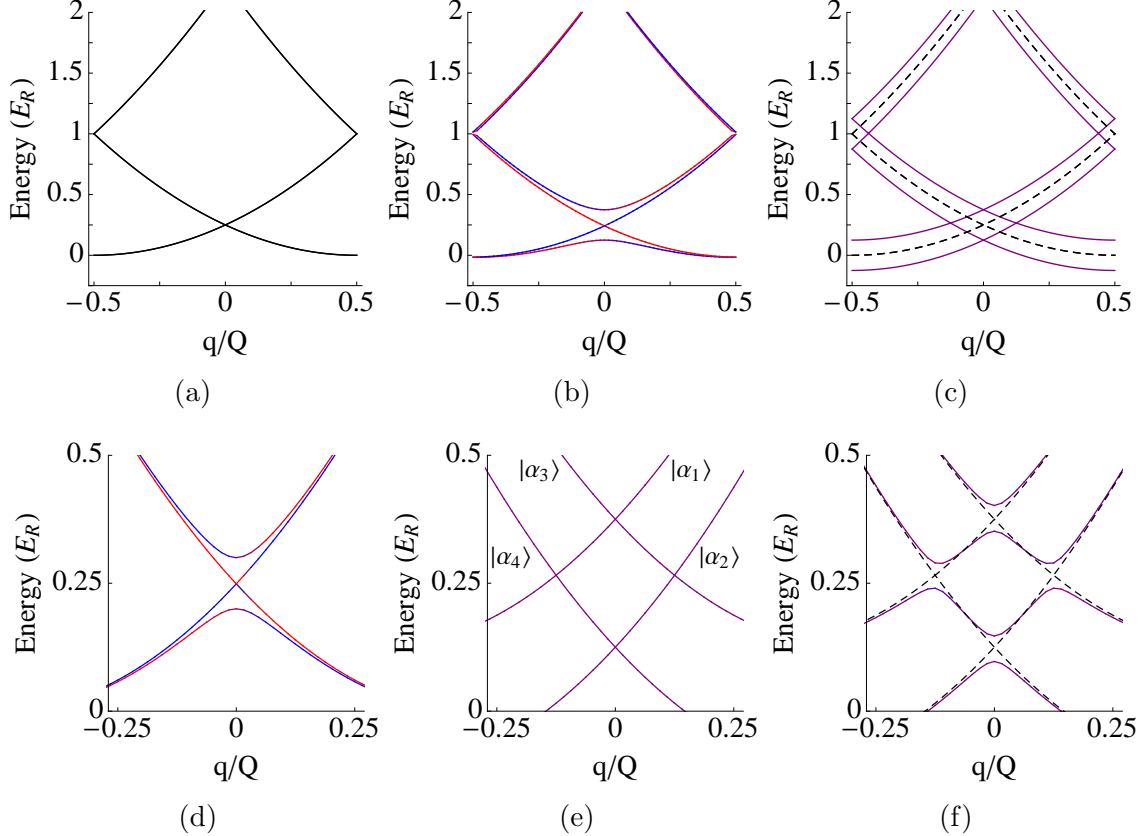


Figure 3-16: Band structure of Raman-RF lattice. The color indicates the spin composition  $\langle S_z \rangle$ , with blue and red corresponding to  $\langle S_z \rangle = 1$  and  $\langle S_z \rangle = -1$  respectively. (a) Band structure in the absence of Raman and RF coupling. We have chosen the spin-dependent gauge such that quasi-momentum  $q = 0$  corresponds to real momentum of  $k = q + (n \pm 1)Q/2$  for  $\uparrow$  and  $\downarrow$  atoms respectively. Each band is doubly degenerate with the two spin states. The point at  $E = 0.25E_R$  at  $q = 0$  is quadruply degenerate. (b) Shown is the case with only Raman coupling, where  $\tilde{\Omega}_R = 0.10$ . This is simply the reduced zone representation of the same Hamiltonian shown in Fig. 3-2. (c) Shown is the case with only RF coupling, where  $\tilde{\Omega}_{RF} = 0.25$ . This splits the two degenerate bands for each spin shown in (a) by  $\hbar\Omega_{RF}$ . (d) Zoomed-in view of the initially quadruply degenerate point when  $\tilde{\Omega}_R = 0.1$ . In this case, two of the bands are coupled, and the degeneracy is partially split. This is the only gap that opens up at all energies and all quasi-momentum, and corresponds to the two-photon resonance of the Raman beams. (e) Zoomed-in view of the case in (b), where only RF coupling is present, and  $\tilde{\Omega}_{RF} = 0.25$ . The states are labeled Eq. (3.39) are labeled. The quadrupole degeneracy is lifted, and forms four pairs of degeneracies, two at  $q = 0$ , and two at  $q = \pm\kappa$ . (f) When the Raman coupling is switched on, all the band crossings shown in (e) become avoided crossings. Shown in dashed are the bands when  $\Omega_R = 0$ . In general, the case of  $\tilde{\Omega}_R \neq 0$  and  $\tilde{\Omega}_{RF} \neq 0$ , all band crossings become gapped.

in terms of free space momentum states as

$$\begin{aligned}
|\alpha_1, q = 0\rangle &= |\uparrow, +Q/2\rangle \\
|\alpha_2, q = 0\rangle &= |\downarrow, +Q/2\rangle \\
|\alpha_3, q = 0\rangle &= |\uparrow, -Q/2\rangle \\
|\alpha_4, q = 0\rangle &= |\downarrow, -Q/2\rangle
\end{aligned} \tag{3.38}$$

In this case, the Raman coupling  $\Omega_R$  can only couple  $|\alpha_4\rangle$  with  $|\alpha_1\rangle$ , as shown in Fig. 3-16d. However, when at small  $\Omega_{RF} \neq 0$ ,  $\Omega_{RF} \ll E_R/\hbar$ , and  $\Omega_R = 0$ , the states  $|\alpha_i, q\rangle$  become

$$\begin{aligned}
|\alpha_1, q\rangle &= \frac{1}{\sqrt{2}} (|\uparrow, q + Q/2\rangle + |\downarrow, q + Q/2\rangle) \\
|\alpha_2, q\rangle &= \frac{1}{\sqrt{2}} (|\downarrow, q + Q/2\rangle - |\uparrow, q + Q/2\rangle) \\
|\alpha_3, q\rangle &= \frac{1}{\sqrt{2}} (|\uparrow, q - Q/2\rangle + |\downarrow, q - Q/2\rangle) \\
|\alpha_4, q\rangle &= \frac{1}{\sqrt{2}} (|\downarrow, q - Q/2\rangle - |\uparrow, q - Q/2\rangle).
\end{aligned} \tag{3.39}$$

The quadruple degeneracy now splits into four pairs of band crossings, as shown in Fig. 3-16e. Two occur at  $q = 0$  between  $|\alpha_1, q\rangle$  and  $|\alpha_3, q\rangle$ , and two occur between  $|\alpha_2, q\rangle$  and  $|\alpha_4, q\rangle$ . The latter two degeneracies occur at  $q = \pm\kappa$ , where  $\kappa = \tilde{\Omega}_{RF}Q$  and are between  $|\alpha_1, q\rangle$  and  $|\alpha_4, q\rangle$ , and between  $|\alpha_2, q\rangle$  and  $|\alpha_3, q\rangle$ . By inspection, Raman coupling leads to couplings between  $|\alpha_1\rangle$  and  $|\alpha_2\rangle$ , with  $|\alpha_3\rangle$  and  $|\alpha_4\rangle$ . Thus all four crossings become avoided when  $\tilde{\Omega}_R$  is switched on, as shown in Fig. 3-16f.

We again use spin-injection spectroscopy to directly measure the spinful bands. Just as before, the reservoir states  $|\uparrow\rangle_R$  and  $|\downarrow\rangle_R$  do not experience any Raman or RF coupling. Nevertheless, we can still analyze the free particle Hamiltonian in the reduced zone scheme. Analogous to the case in the previous section, we obtain four spectra: two channels starting from two reservoirs. By identifying different features in the spectra, we can reconstruct both the dispersion and spin distribution of the spinful lattice system. An example of how this is carried out is shown in Fig. 3-17.

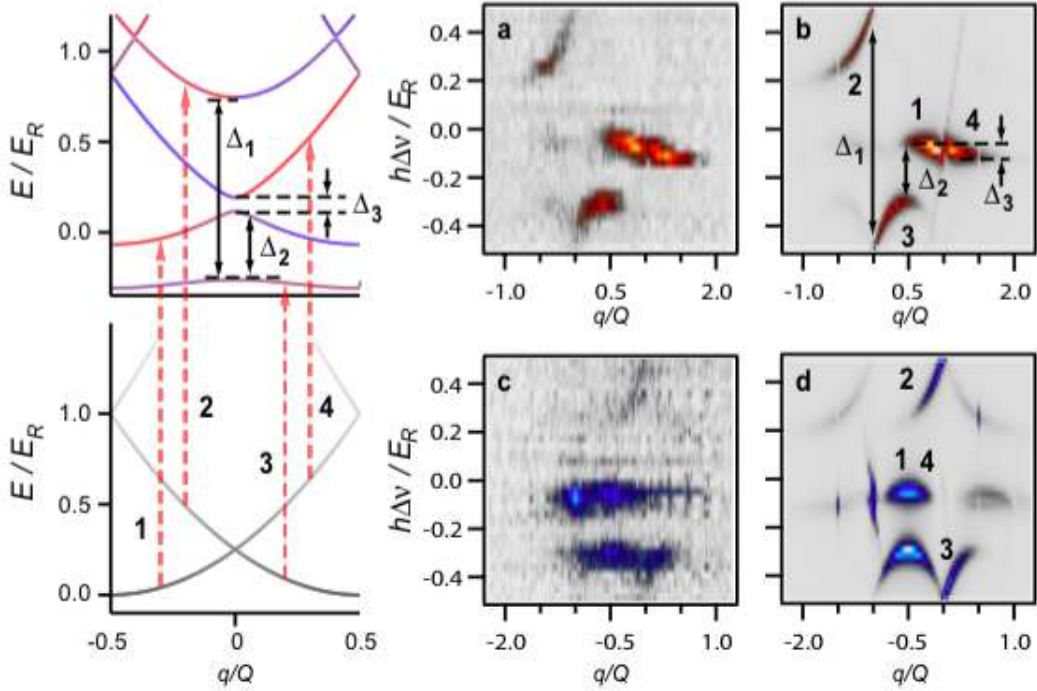


Figure 3-17: Spin-injection spectroscopy on a Raman-RF lattice. Shown on the left are the Raman-RF bandstructure (top), and the bandstructure (bottom) of the reservoir states. The experimental bare spectra corresponding to starting in reservoir state  $|\downarrow\rangle_R$  is shown in panels (a) and (c) on the right. The corresponding theoretical spectra is shown in panels (b) and (d). The transitions 1 to 4, and gaps  $\Delta_1$ ,  $\Delta_2$  and  $\Delta_3$  are identified on the theoretical spectra. By selecting certain features, the dispersions and spin compositions of various bands can be reconstructed.

There is however, one difference from the previous case where spin-injection spectroscopy was applied. Since there is a lattice structure, one can in principle couple to an infinite number of bands, as atoms can exchange momentum with the RF-Raman lattice. Another consequence is that when the RF drive and the Raman beams are switched off, the Bloch states are projected back onto free particles states. One can thus read off the projection of a state in band  $n$  with quasi-momentum  $q$  onto free-space momentum states with momentum  $q+nk$ . Furthermore, each momentum state  $q+nk$  also has a spin composition. While the final measurement is in one specific spin basis, which we label here as  $\sigma_y$  basis, one can in principle measure the orthogonal  $\sigma_z$  and  $\sigma_x$  components by applying the appropriate RF pulse before measurement. With just the spin composition in the  $\sigma_y$  basis, we can obtain the average spin  $\langle S_y \rangle$ . Since

the state is normalized to the total density, this immediately gives the magnitude of the orthogonal spin component. Without loss of generality, we define this component to be along  $\sigma_z$ . The measurement of  $\langle S_y \rangle$  thus also gives  $|\langle S_z \rangle|$ .

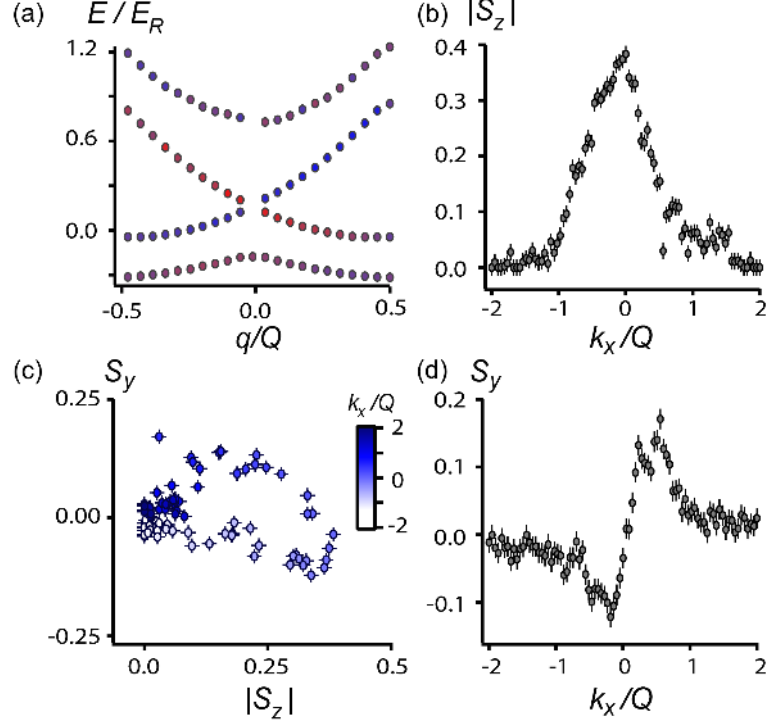


Figure 3-18: Extracting spin composition for the Raman-RF Lattice, with  $\tilde{\Omega}_R = 0.93$  and  $\tilde{\Omega}_{RF} = 0.28$ . (a) Reconstructed spin composition and dispersion for the lowest four bands, for  $\tilde{\Omega}_R$  and  $\tilde{\Omega}_{RF}$ . (b,d) Extracted spin composition of the lowest band in the basis of free space momentum states labeled by  $k_x$ . Here, a spin-dependent gauge is applied such that the  $k_x$  is shifted from the laboratory frame momentum by  $\pm Q/2$ , for  $\uparrow$  and  $\downarrow$  atoms respectively. (c) The extracted spin as a function of momentum  $k_x$ . Figures reproduced from [23].

### 3.4 Some Concluding Thoughts

We have shown directly in our experiment that Raman beams can be used to realize spin-orbit coupling with a Zeeman field in ultracold fermions. We have shown directly the presence of a spin-orbit gap, and the adiabatic loading of spin-orbit bands, creating a single-component Fermi sea that supports interactions. Nevertheless, the interesting case of topological superconductors and Majorana excitations requires

many-body pairing of fermions, which occur at temperatures much lower than  $T_F$ . In  ${}^6\text{Li}$ , fermionic superfluids have been created with the use of Feshbach resonances, which significantly enhance the superfluid transition temperature to experimentally accessible values. The Feshbach resonances, however, occur at high magnetic fields. Here, the relevant states have predominantly electron spin projection of  $m_S = -1/2$ . As discussed in Section 3.2.2, this highly suppresses the two-photon Raman coupling. For example, for the  $|2\rangle$ - $|3\rangle$  mixture at the Feshbach resonance at 812 G, the maximum Rabi coupling to spontaneous emission ratio is reduced from the zero field value by a factor of 17, to  $2\pi \times 13$ . In order to have a large enough spin-orbit gap to occupy only the lowest band, one requires  $\Omega_R \sim E_F$ . For a superfluid, one requires  $T/T_F \sim 0.2$ . Assuming that each scattering event adds an amount of energy  $E_R \sim E_F$ , the lifetime of a superfluid is then  $\sim 10\times$ , where  $t_F = \hbar/E_F$  is the Fermi time. In experimental timescales, this is on the order of milliseconds, sufficient for thermalization over short distances, but insufficient for full thermalization for typical samples.

Nevertheless, in addition to coupling two hyperfine states with Raman lasers, there are other methods to generate spin-orbit coupling that do not suffer from the same limitations. If one still wished to use Raman beams, there are some improvements that can be made. For example, using shaped laser beams, one can have spin-orbit coupling present only in a small region. As long as the rest of the sample is large enough, and the heating rate is lower than the time-scale required for pairs to move into the spin-orbit coupled region, the rest of the system can act as a reservoir. Provided that thermalization occurs quickly, such that heat generated due to the Raman beams can be dissipated into the reservoir, one might be able to momentarily combine fermion pairing and spin-orbit coupling. By reducing the momentum transfer in the Raman beams, and lowering the density of the Fermi gas, the two-photon coupling  $\Omega_R$  that is required is also reduced. Recent advances in shaping the optical beams can potentially allow these ideas to be implemented.



# Chapter 4

## A Quantum Gas Microscope for Fermionic $^{40}\text{K}$

The advent of degenerate atomic gases has allowed for the quantum simulation of many-body systems in a pristine and well-controlled environment. In recent years, quantum gas microscopes, which are characterized by their ability to measure occupations of individual lattice sites, have emerged as new tools to probe and manipulate ultracold atoms trapped in 2D optical lattices. The site-resolving ability not only offers unprecedented access to a large number of degrees of freedom that is on the order of the number of sites  $N$ , it also allows for direct probing of spatial correlations [35]. Furthermore, the high-resolution imaging system can be used in reverse to project arbitrary optical potentials, providing a new level of control for quantum gas experiments.

The first quantum gas microscopes, realized in 2009, were used to image bosonic gases of  $^{87}\text{Rb}$  [10, 128]. The newfound ability of quantum gas microscopy enabled novel experiments on bosons in the Hubbard regime, from studies of the superfluid to Mott-insulator transition to antiferromagnetic spin chains [8, 34, 129]. Using these microscopes in reverse, site-resolved control was also realized, leading to new methods of preparing and probing many-body states [145]. These capabilities led to studies on bosonic systems ranging from quantum walks to measurement of entanglement entropy in many-body systems via interferometry of many-body states [112, 64].

As discussed in Section 2.3, fermionic atoms trapped in an optical lattice allow one to simulate an equally interesting many-body system that has direct connections to high- $T_c$  cuprates [36, 83]. The possibility to achieve what was made possible with bosonic microscopes led to many efforts to realize analogous microscopes for fermionic atoms. Nevertheless, for technical reasons, quantum gas microscopy of fermions turned out to be more difficult, and the first fermionic quantum gas microscopes were not realized until 2015 [51, 22, 106], one of which is described here. For alkali atoms, the two stable fermionic isotopes that can be used are  $^6\text{Li}$  and  $^{40}\text{K}$ , both of which have their own challenges. We have chosen to work with the latter.

In this chapter, we describe our experimental apparatus for quantum gas microscopy of fermionic  $^{40}\text{K}$ . Some of the setup, specifically the vacuum chamber and the coils for magnetic fields, have been described in detail in [41, 116], and will only be described briefly here. Additional components, such as the optical lattice, and optical trapping and transport beams, are described in detail here.

## 4.1 Producing Ultracold $^{40}\text{K}$

In order to produce ultracold  $^{40}\text{K}$ , we employ a single vacuum chamber design and use two species of atoms, fermionic  $^{40}\text{K}$  and bosonic  $^{23}\text{Na}$  [116]. First, we load a dark-spot magneto-optical trap (MOT) of  $^{23}\text{Na}$  atoms in 4 s from a  $^{23}\text{Na}$  oven via a Zeeman slower. As shown in Fig. 4-1, the center of the MOT coils are displaced along  $\hat{x}$  by 12 mm. After loading of the MOT, the MOT beams are switched off and a 4.2 G magnetic field along  $\hat{x}$  is switched on. We then optically pump the atoms into the magnetically trappable  $|F = 2, m_F = 2\rangle$  state using a  $\sim 100\ \mu\text{s}$  pulse of  $\sigma_+$  light. The current in the MOT coils is then rapidly switched on in order to magnetically catch the optically-pumped  $^{23}\text{Na}$  atoms. The relevant coils used are shown in Fig. 4-4.

For sympathetic cooling of  $^{40}\text{K}$ , it is important to use stable combinations of hyperfine states. In *s*-wave collisions, the total  $M_F$  of a pair of atoms is conserved. By considering all possible magnetically trapped configurations, one finds that the only stable mixture is  $^{23}\text{Na}$  in  $|2, 2\rangle$  and  $^{40}\text{K}$  in  $|9/2, 9/2\rangle$ . Due to the inverted hyperfine

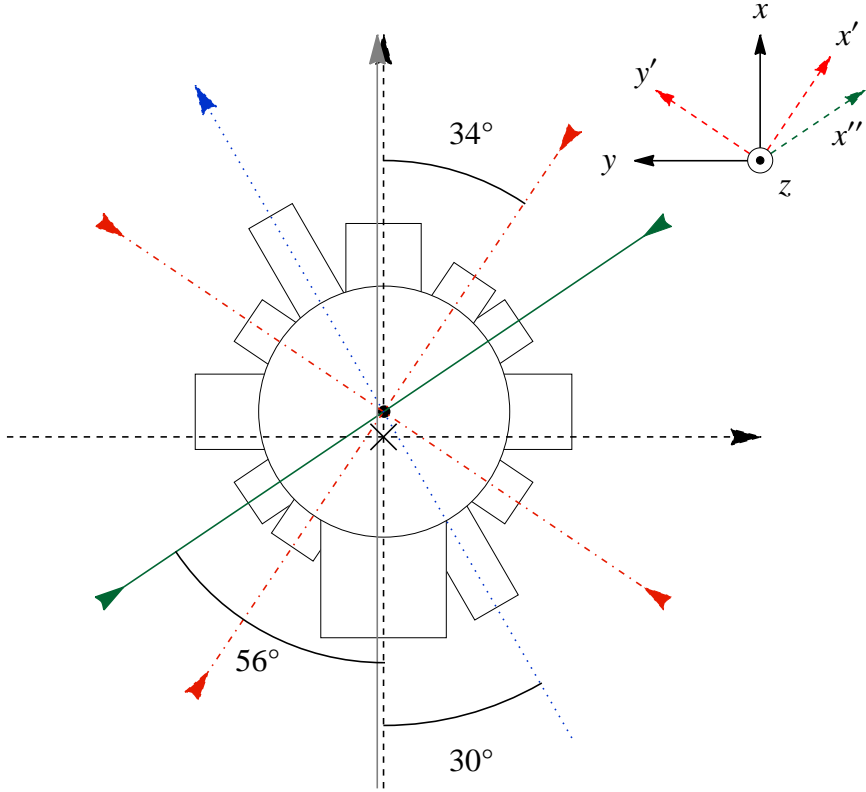


Figure 4-1: Top view of vacuum chamber. Gravity is along  $-\hat{z}$ . The center of the chamber is marked by the black circle. The center of the quadrupole magnetic trap, and the center of the high-resolution imaging axis is marked by the cross. The MOT beams are along the  $x'$  and  $y'$  axes, indicated by the dot-dashed red lines. The slower axis and slowing beam direction is indicated by the blue dotted line. The  ${}^{40}\text{K}$  2D MOT is attached to the chamber along  $\hat{x}''$ , on the positive  $x$  side. The  ${}^{23}\text{Na}$  dark-spot  $F = 1$  MOT repumping beam also propagates along  $\hat{x}''$ . The direction of the optical pumping beam is indicated by the solid gray arrow. It intersects the MOT, which is displaced along  $\hat{x}$  by  $\sim 12$  mm and  $\sim 1$  mm along  $-\hat{y}$ . The  $x$  and  $y$  optical lattices enter the chamber as indicated by the black arrows along  $\hat{x}$  and  $-\hat{y}$ . The black arrows indicate the directions of “bouncing” imaging paths along  $\hat{x}$  and  $-\hat{y}$ .

structure in  ${}^{40}\text{K}$ , the magnetically trappable mixture of  $|1, -1\rangle$  and  $|7/2, -7/2\rangle$  is unstable as it can decay to  $|1, -1\rangle$  and  $|9/2, -7/2\rangle$  or  $|1, 0\rangle$  and  $|9/2, -9/2\rangle$ .

In order to ensure  ${}^{23}\text{Na}$  atoms are in the  $|2, 2\rangle$  state before loading  ${}^{40}\text{K}$ , we perform a cleanup procedure [105, 148]. The gradient of the magnetic trap is lowered such that residual  $|2, 1\rangle$  atoms are spilled by gravity while  $|2, 2\rangle$  atoms remain due to their

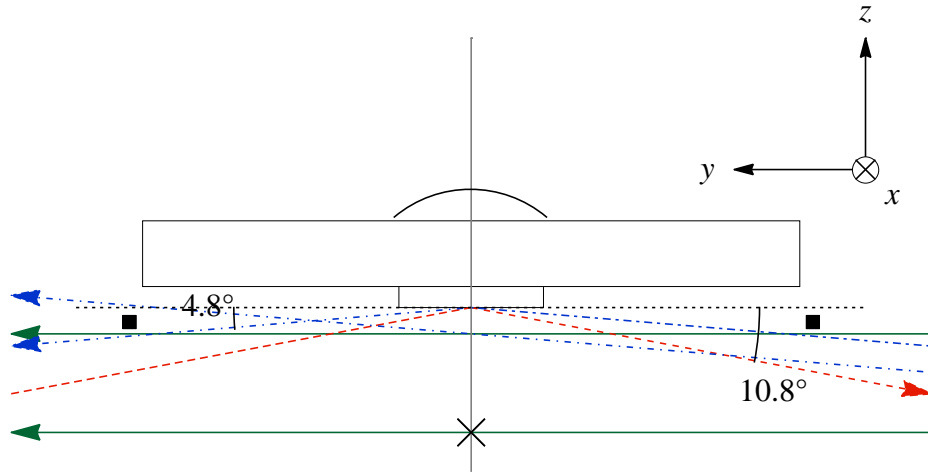


Figure 4-2: Side view along  $\hat{x}$  of various beams. The high-resolution imaging axis is shown in gray. The intersection of the vertical center of the chamber with the high-resolution imaging axis is marked by the cross, and is 9.5 mm below the substrate. The dashed red arrow indicates the direction of the “bouncing” imaging beam along  $-\hat{y}$ , and also the direction of the incoming  $y$  lattice beam. The dot-dashed blue arrow indicates the direction of the  $y$  arm of the movable cross dipole trap. Two cases are shown: 1) when it is aligned to the center of the substrate; 2) when it is aligned to intersect the high-resolution imaging axis 2 mm below the substrate. The black squares indicate the location of the in-vacuum RF antenna. The green solid arrows indicate the direction of the optical plug. The upper arrow corresponds to the case when the magnetic trap is  $\sim 2$  mm below the substrate, while the lower arrow corresponds to the case when the magnetic trap is at the center of the chamber. The first scenario applies to Chapter 5, while the second applies to Chapter 6.

larger magnetic moment. Subsequently, the  $^{40}\text{K}$  MOT beams are switched on, and  $^{40}\text{K}$  atoms are loaded from a 2D MOT. In order to increase the flux of  $^{40}\text{K}$  atoms, we rely on light-induced atomic desorption [42]. We illuminate the 2D MOT glass cell with a 1 W beam of 455 nm light collimated to a diameter of 25 mm. This light originates from a THORLABS M455D2 LED, and releases atoms adsorbed to the glass surface [4, 75]. The 455 nm light is on only during the loading of the  $^{40}\text{K}$  MOT.

After the  $^{40}\text{K}$  MOT is loaded in  $\sim 1$  s, the current in the MOT coils is again switched off, and both  $^{23}\text{Na}$  and  $^{40}\text{K}$  atoms are released. A magnetic field of 4.2 G along  $\hat{x}$  is applied. We wait 400  $\mu\text{s}$  for the fields to ramp up, then apply a 100  $\mu\text{s}$  pulse of  $\sigma_+$   $m_F$ -pumping light. During this time, the MOT repumper beams are left

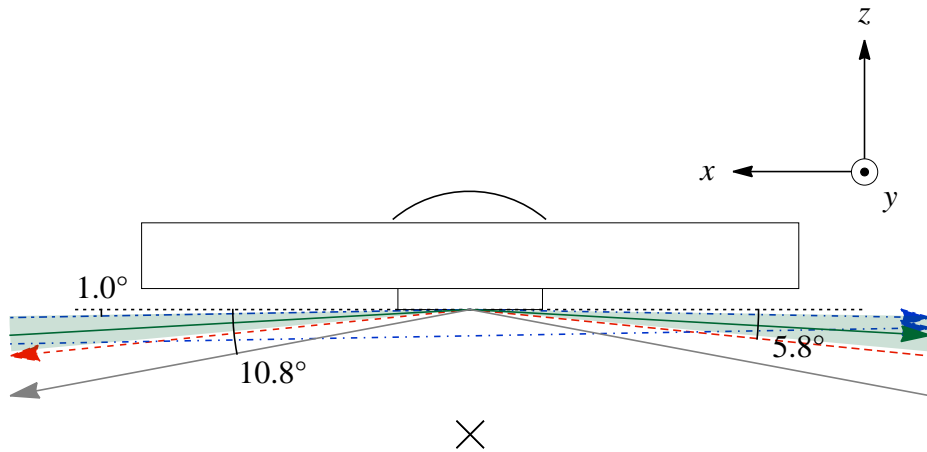


Figure 4-3: Side view along  $\hat{y}$  of the solid immersion lens and various beams. The intersection of the vertical center of the chamber and the high-resolution imaging axis is marked by the cross. The solid gray arrow indicates the direction of the “bouncing” imaging beam along  $\hat{x}$ , and also the direction of the incoming  $x$  lattice beam. The dashed red arrow indicates the direction of the 5-degree beam. The dot-dashed blue arrow indicates the direction of the  $x$  arm of the movable cross dipole trap. Two cases are shown: 1) when the beam is aligned to the center of the substrate; 2) when the beam is aligned to intersect the high-resolution imaging axis at 2 mm below the substrate. The green solid arrow indicates the direction of the accordion beam. The green shaded area indicates the range of angles ( $\sim 1.0^\circ$  to  $\sim 5.0^\circ$ ) achievable with the accordion beam.

on. A quadrupole magnetic trap formed by the MOT coils is then rapidly switched on to catch both  $^{23}\text{Na}$  and  $^{40}\text{K}$  atoms.

The atoms are then magnetically transported into the center high-resolution imaging axis by ramping down the current in the MOT coils while simultaneously ramping up the current in the curvature coils. The curvature coils are run in anti-Helmholtz configuration to form a quadrupole magnetic trap. The center of the curvature coils is located 9.5 mm below the surface of the substrate on the top window, as shown in Fig. 4-2. For the results in Chapter 5, the quadrupole trap is centered vertically at the center of the chamber. For the results in Chapter 6, the quadrupole trap was moved 7.5 mm upwards towards the substrate. This will be discussed in detail in Section 6.1.1. The following description for the optical plug applies to both configu-

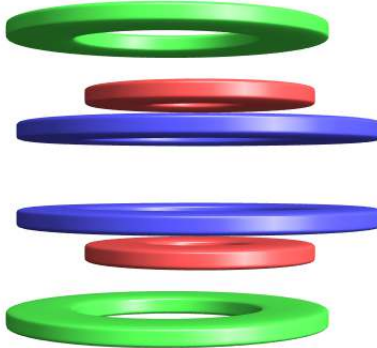


Figure 4-4: Coils used for generating magnetic fields. Shown is a view of the three relevant pairs of coils used. Shown in green are the MOT coils, which are displaced 12 mm along  $\hat{x}$  relative to the high-resolution imaging axis. Shown in red are the curvature coils, which are run in anti-Helmholtz configuration and used to generate a quadrupole field for the plugged quadrupole trap and for “slicing.” Concentric to the curvature coils are a pair of Feshbach coils, shown in blue, which are run in Helmholtz configuration and are used to generate a uniform bias field. In combination with the curvature coils, they can be used to move the center of the quadrupole trap.

rations.

In order to suppress Majorana losses, an optical plug of 532 nm light, focused to a waist of  $30 \mu\text{m}$ , propagates along  $\hat{y}'$  and intersects the center of the quadrupole magnetic trap. The  ${}^{40}\text{K}$  atoms are sympathetically cooled in the plugged quadrupole trap by forced evaporation of  ${}^{23}\text{Na}$  carried out using the  $|2, 2\rangle \rightarrow |1, 1\rangle$  microwave transition. During evaporation, hot atoms are preferentially transferred into the magnetically untrapped  $|1, 1\rangle$  state. At the end of the evaporation, all  ${}^{23}\text{Na}$  atoms are removed, and  $\sim 10^6 {}^{40}\text{K}$  atoms at  $10 \mu\text{K}$  remain.

Details of the  ${}^{23}\text{Na}$  laser system and  ${}^{40}\text{K}$  laser system are described in Appendix B.

## 4.2 The High-Resolution Imaging System

Central to any quantum gas microscope is a high-resolution imaging system. In our experiment, we use an integrated solid immersion lens combined with a high-resolution objective. The integrated solid immersion lens is formed from three parts that are

optically contacted to each other. We optically contacted a spherical cap of fused silica to the outside of a vacuum window, and a super-polished substrate on the vacuum side [41], as shown in Fig. 4-5a. In a solid immersion lens, light originating from a spot close to the surface and on the imaging axis experiences minimal aberrations, since light rays at the air-glass interface are minimally refracted. This allows us to use a standard long working distance microscope objective. An important advantage of the solid immersion lens is the increased effective numerical aperture (NA). Due to refraction between the substrate and vacuum, the NA is increased by the ratio of the refractive indices, as shown in Fig. 4-5b. The enhanced NA has two benefits. First, the diffraction limit  $d$ , given by  $d = 1.22\lambda/(2NA)$ , is lowered; second, the light collection efficiency is increased.

In our system, we use an EDMUND OPTICS 20X PLAN HR INFINITY CORRECTED OBJECTIVE that has an NA of 0.60, an effective focal length of 10 mm, and a working distance of 13 mm. The solid immersion lens increases the effective NA to 0.87, which gives a diffraction limit of  $\sim 500$  nm, and a light collection efficiency of 0.25. For fine alignment and focusing, the objective is mounted on a 3-axis translation stage with NEWFOCUS PICOMOTOR piezo actuators, directly mounted onto the vacuum chamber.

For single-site imaging, another parameter to consider is the location of the atoms. If one's goal is to reduce imaging aberrations, the optimal location is directly at the surface of the substrate, since aberrations increase with the distance from the surface. However, one must consider the effect of van der Waals forces, which arise from atoms adsorbed onto the substrate. We chose to trap atoms  $\sim 7\mu\text{m}$  away, as a compromise between reducing these forces and minimizing aberrations [88, 96].

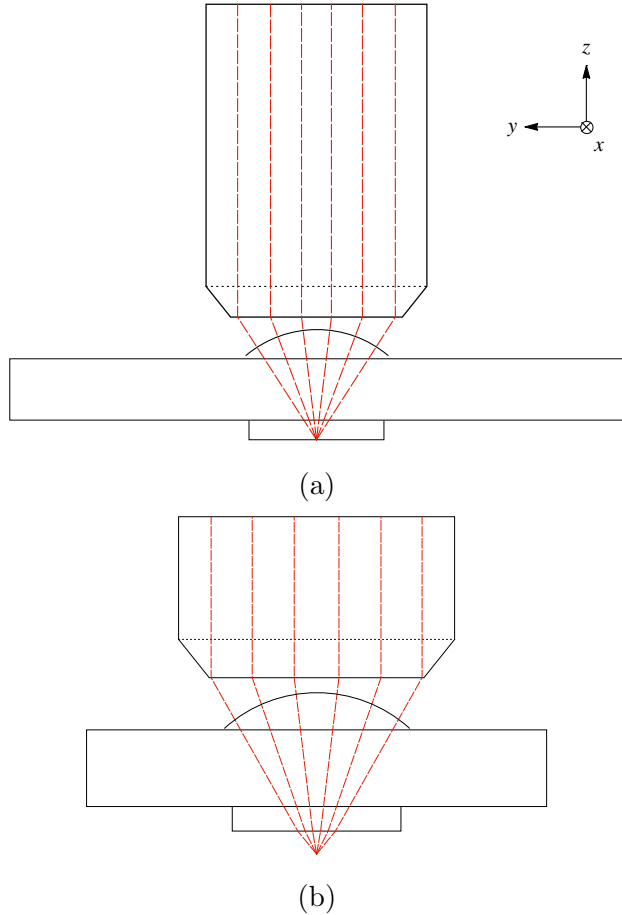


Figure 4-5: High-resolution imaging system. The high-resolution imaging system consists of a solid immersion lens that is integrated with the vacuum window, along with a high-NA (NA=0.6) EDMUND OPTICS 20X PLAN HR INFINITY CORRECTED OBJECTIVE. Specifically, the solid immersion lens, consisting of a 9 mm radius spherical cap, 5 mm thick fused silica vacuum window, and a 1.8 mm thick super-polished substrate, is shown. (a) Shown in dashed red lines are light rays originating from the surface of the super-polished substrate, at the center of the imaging axis. Light rays originating from the center propagate orthogonal to the air-glass interface of the solid immersion lens, thus avoiding imaging aberrations. (b) Shown is the case where the light still originates from a point on the imaging axis, but below the surface. For our experiments, the atoms are situated  $7\mu\text{m}$  below the surface. In addition to reducing aberrations, the solid immersion lens increases the effective NA. Since the atoms are displaced from the surface, the refraction at the vacuum-substrate interface increases the collection angle.

## 4.3 The 2D Square Optical Lattice

The other ingredient for a quantum gas microscope is a 2D optical lattice. In our experiment, the optical lattices are formed from 1064 nm light, derived from NUFERN fiber amplifiers seeded by a COHERENT MEPHISTO laser. The output of the fiber amplifiers are delivered via single-mode fibers to the experiment. The detailed setup for generating light is contained in Appendix B.4.

There are three lattice beams. We first describe the two beams that form a lattice in the  $x$ - $y$  plane. 1064 nm light for the two beams are delivered to the experiment via two single-mode photonic crystal fibers (NKT PHOTONICS LMA-25), which have a  $25\ \mu\text{m}$  core. These fibers are connectorized by ALPHANOV, and are terminated with short fused silica endcaps, which increase the damage threshold due to a larger beam size at the tip. The large mode area of the fiber also reduces the problem of spontaneous brillouin scattering (SBS) that typically occurs at high powers. The effect is negligible for the highest powers that we are able to generate. The two lattice beams enter the vacuum chamber along  $\hat{x}$  and  $-\hat{y}$ , and are angled upwards (along  $+\hat{z}$ ) at an angle of  $10.8^\circ$  relative to the  $x$ - $y$  plane (see Fig. 4-1, Fig. 4-2 and Fig. 4-3). They reflect off the substrate, which is custom-coated to reflect 1064 nm light at  $0^\circ$  incidence (reflection  $\sim 0.998$ ) and  $10^\circ$  incidence (reflection of 0.9995 and 0.973) while transmitting light (transmission  $> 0.95$ ) from 613 nm to 799 nm from  $0^\circ$  up to  $53^\circ$ . The two in-plane lattice beams are then retro-reflected (see Fig. 4-6), forming a square lattice with a lattice spacing of 541 nm in the  $x$ - $y$  plane, and a vertical lattice with  $3\ \mu\text{m}$  spacing. Due to constructive interference with the reflections from the retro-reflection mirror and the substrate, we obtain an enhancement in lattice depth by a factor of 16 compared to the depth of a single beam of the same power. This is helpful for single-site imaging where deep lattices are required. To further reduce the power requirement on the lattice beams, the  $x$  and  $y$  beams are shaped cylindrically with beam waists of  $135\ \mu\text{m}$  along the horizontal and  $40\ \mu\text{m}$  along the vertical axis.

As we will describe in Section 5.3, strong confinement along all directions is necessary for single-site imaging. In order to increase the confinement in the vertical

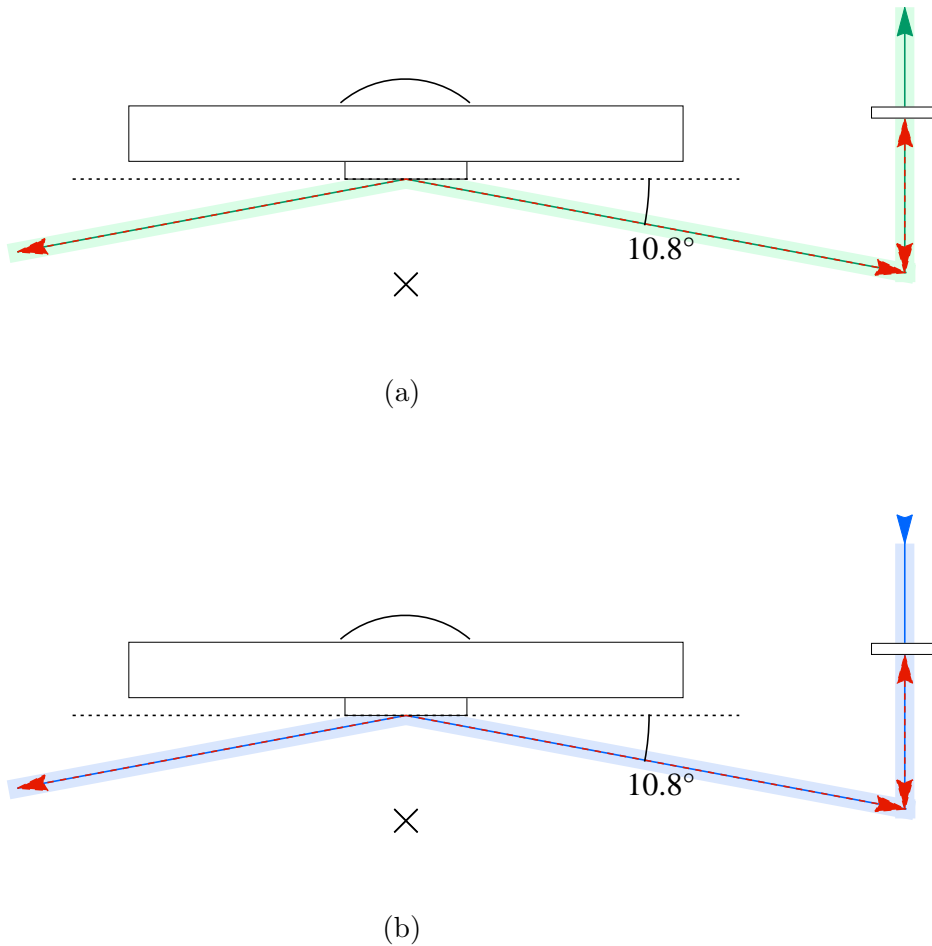


Figure 4-6: Side view of lattice, imaging and Raman cooling beams. (a) Side view of the lattice beams and the bouncing imaging beams along  $\hat{x}$  or  $-\hat{y}$ . The lattice beam path is indicated by the dashed red arrow. The “bouncing” imaging beam, indicated by the thick green arrow is transmitted through the retro mirror. (b) Side view of lattice and Raman cooling beams. For the case where one is looking down  $\hat{x}$ , the thick blue arrow indicates the path of the Raman beam along  $\hat{y}$ . The dashed red arrow indicates the path of the  $y$  lattice. For the case of looking down  $-\hat{y}$ , the thick blue arrow indicates the path of the Raman beam along  $-\hat{x}$ , and also the optical pumping beam used for Raman imaging. The Raman beams and the optical pumping beam are partially transmitted through the lattice retro-reflection mirror.

direction, an additional 1064 nm beam along  $\hat{z}$  is retro-reflected off the substrate to form a 532 nm spacing vertical lattice. This beam has a waist of  $60 \mu\text{m}$ , and is delivered to the experiment with a THORLABS PM-980 fiber. Although this limits the

power to  $\sim 5$  W due to SBS in the fiber, it is sufficient to produce a lattice depth of  $190 \mu\text{K}$ , enough for single-site imaging. For the vertical beam, the lattice depth is enhanced by a factor of 4 compared to the depth of a single beam.

## 4.4 Single-Site Imaging Beams

In this section, we describe the beams required to perform single-site imaging, which will be discussed in detail in Section 5.4. Three beams are used: two Raman beams and an optical pumping beam. The Raman beams enter the chamber opposite to the lattice beams, along  $-\hat{x}$  and  $\hat{y}$ . Similar to the lattice beams, they are angled slightly upwards at an angle of  $10.8^\circ$  relative to the  $x$ - $y$  plane and are reflected off the substrate. The Raman beams are sent through the lattice retro-reflection mirrors, which are highly reflective for 1064 nm light, but transmit the Raman beams, which are at 767 nm, with  $\sim 0.8$  efficiency. The polarizations of the Raman beams are parallel to the surface of the substrate. The optical pumping beam is combined with the  $x$  Raman beam on the experiment table with a non-polarizing beamsplitter, and follows the same path. Its polarization is optimized for optical pumping. The details of the Raman light source and optical pumping light source are described in Appendix B.3.

## 4.5 Additional Optical Beams for Trapping and Transport

In order to produce degenerate samples at the imaging location  $\sim 7 \mu\text{m}$  below the substrate, several additional laser beams are necessary for trapping and transport of the atoms. These are described in the following sections.

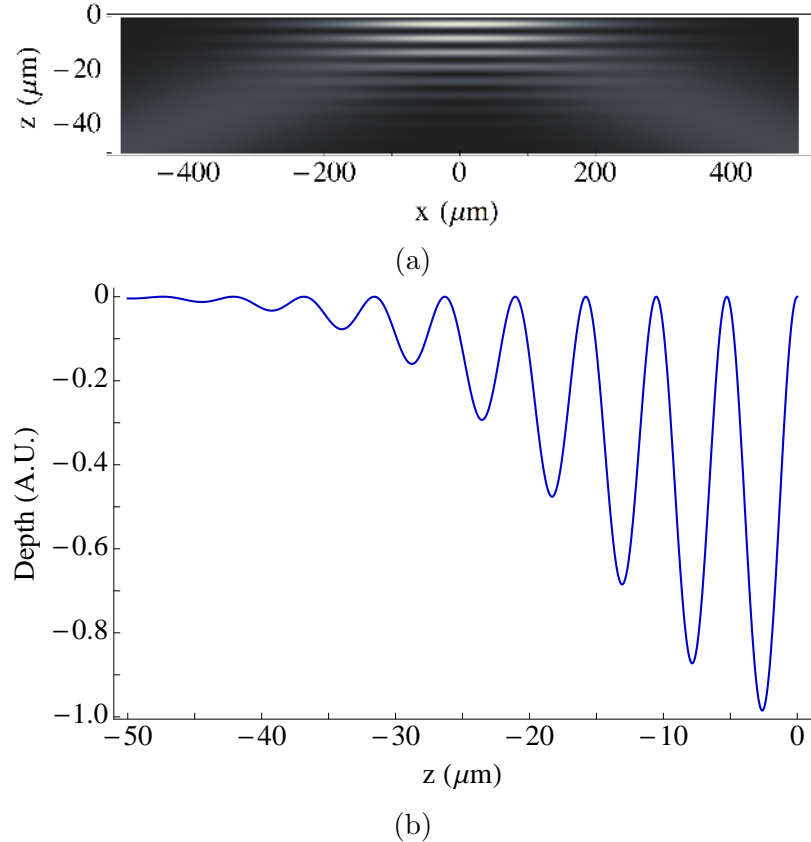


Figure 4-7: Trapping potential formed by the 5-degree beam. Shown is the case when the vertical waist of the beam is  $35\ \mu\text{m}$ . (a) Side view of the trapping potential formed by the 5-degree beam, viewed along  $\hat{y}$ . The reflection from the substrate interferes with the incoming beam to form a vertical lattice along  $\hat{z}$ . The trapping depth is indicated by the brightness. (b) A cut of the trapping potential along the  $z$ -axis.

#### 4.5.1 The 5-Degree Beam

In order to trap and evaporate atoms at the imaging location  $\sim 7\ \mu\text{m}$  from the substrate, we added an additional 1064 nm trapping beam that propagates along  $\hat{x}$  at an angle of  $5.8^\circ$  relative to the  $x$ - $y$  plane. This beam is also reflected off the substrate, and forms a vertical lattice with a larger spacing of  $\sim 5\ \mu\text{m}$ , as shown in Fig. 4-7. In this trap, the atoms form pancake-like layers. By lowering the power of this beam, the layers can be evaporatively cooled. The light source for this beam is the same as for the  $z$  lattice beam, and is described in detail in Appendix B.4.

### 4.5.2 The Accordion Beam

While the 5-degree beam was sufficient to produce dilute samples near the substrate needed for implementing single-site imaging, it was not able to produce quantum degenerate samples on its own. The main limitation was the transfer efficiency into the 5-degree beam. In an improved scheme to produce cold samples near the substrate, which is discussed in detail in Section 6.1.2, the transfer efficiency was improved. This required three additional 1064 nm beams, and a 830 nm dimple beam.

The first of these is the “accordion” lattice beam, which forms a vertical lattice along  $\hat{z}$  whose spacing can be dynamically tuned [61, 13]. This beam propagates along  $-\hat{x}$  and is focused to a waist of  $72 \mu\text{m}$  at the center of the substrate. Similar to the 5-degree beam, the reflection from the substrate interferes with the incoming light to form a vertical lattice. In order to tune the lattice spacing, the center of the substrate is imaged onto a galvo mirror (THORLABS GVS311), as shown in Fig. 4-8. By tuning the angle of the galvo mirror, the angle of the beam at the substrate is tuned, while its position remains unchanged. The lattice spacing, which is determined by the angle, can thus be dynamically adjusted. To compensate for residual motion due to imperfect imaging of the galvo onto the substrate, an additional galvo with a 3 mm thick fused silica plate is placed in the beam path. By adjusting the angle of the glass plate, the position of the beam at the substrate can be steered. The light for the accordion lattice originates from the same source as that for the  $z$  lattice, and is described in Appendix B.4.

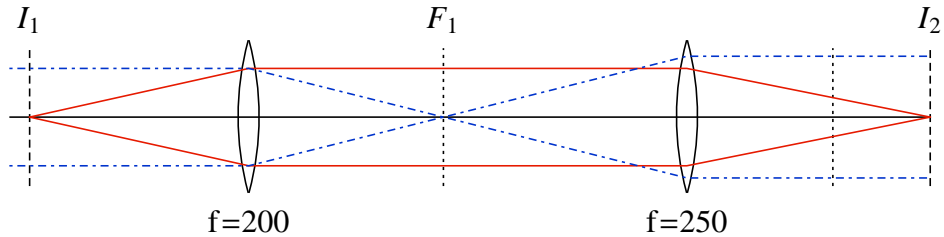


Figure 4-8: The “accordion” beam. The atoms are at  $I_1$ ; focal lengths are in units of mm. The galvo mirror is placed in the image plane  $I_2$ . An additional galvo with a 3 mm glass plate is placed  $\sim 30$  mm after the galvo mirror.

### 4.5.3 The Movable Crossed Optical Dipole Trap

The accordion lattice allows for loading atoms at a lattice spacing that is twice as large as that of the 5-degree beam, and further way from the surface. However, this does not address the issue of efficient transport of atoms into the accordion lattice. In order to transport atoms from the magnetic trap, centered  $\sim 2$  mm below the substrate, to the accordion lattice, located within  $\sim 100 \mu\text{m}$  of the substrate, two more transport beams were needed. These two beams form a crossed optical dipole trap, and their intersection point can be tuned anywhere from  $\sim 2$  mm below the substrate to directly at the center of the substrate, while maintaining the same incident angle. The positions of these beams are controlled by two INTRAACTION DTD-274HA6 shear mode acousto-optic deflectors (AOD), which have high diffraction efficiency over a large range of deflection angles. The AODs are placed in the Fourier plane, such that the beam position can be steered while maintaining the same incident angle at the atoms (See Fig. 4-9a and Fig. 4-9b). The beam paths of these two beams are shown in Fig. 4-2 and Fig. 4-3. One beam propagates along  $-\hat{x}$  with an angle of  $1.2^\circ$ , while the other beam propagates along  $\hat{y}$  at an angle of  $5.4^\circ$ . The latter angle is chosen to avoid hitting the in-vacuum antenna, which at full power can lead to an increased vacuum pressure of  $\sim 10^{-8}$  Torr,  $\sim 1000\times$  higher than required for vacuum lifetimes of  $\sim 100$  s. The former angle was chosen to have good overlap with the accordion beam while minimizing the number of vertical lattice sites due to reflection from the substrate. To achieve sufficient trap depths, the  $x$  ODT beam is focused to a beam waist of  $40 \mu\text{m}$  while the  $y$  ODT beam is elliptical with beam waists of  $40 \mu\text{m}$  in the vertical and  $90 \mu\text{m}$  in the horizontal. The light source of these two beams is the same as that for the  $y$  lattice. A detailed description of the setup is described in Appendix B.4.

### 4.5.4 The Dimple Beam

The fourth beam used to produce degenerate samples near the substrate is a small “dimple” beam. This beam is used to provide additional radial confinement in the  $x$ - $y$

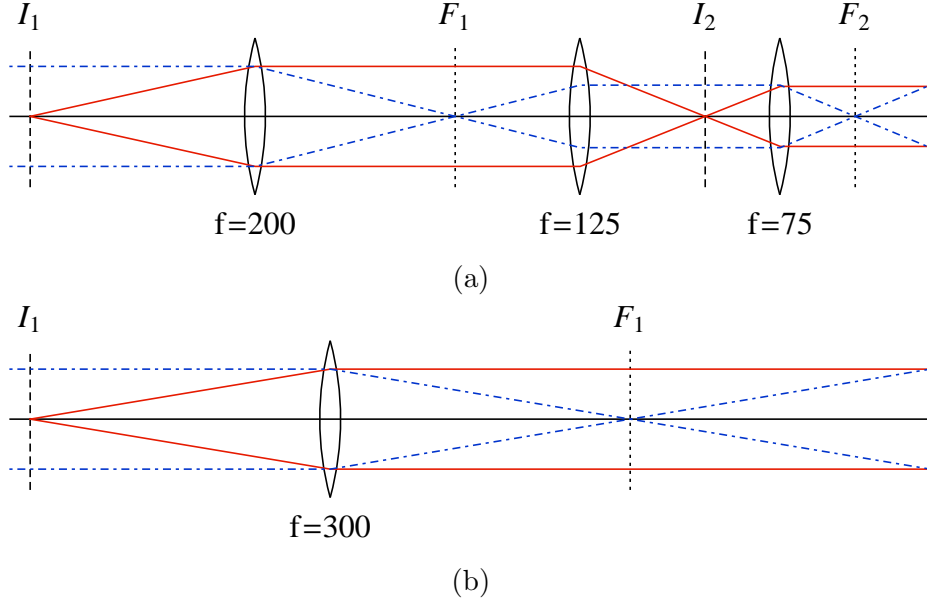


Figure 4-9:  $x$  and  $y$  crossed ODT beams. The atoms are at  $I_1$ ; focal lengths are in units of mm. (a)  $x$  ODT beam path. The AOD is placed in the Fourier plane  $F_2$ . This beam is combined with the accordion lattice beam at a polarizing beamsplitter placed near  $F_1$ . (b)  $y$  ODT beam path. The AOD is placed in the Fourier plane  $F_1$ . The beam is pre-shaped to be elliptical before reaching  $F_1$ .

plane. This helps during vertical transport in the accordion lattice since the accordion beam provides little confinement along  $\hat{x}$ , as will be discussed in Section 6.1.2. The main purpose of the dimple beam, however, is to provide confinement in the  $x$ - $y$  plane for the final stage of evaporation in the 5-degree beam. For efficient evaporation to occur, atoms must be able to thermalize. The thermalization time is determined by the density  $n$  and the scattering cross-section  $\sigma$ . Since our experiments are conducted far from any Feshbach resonances, the cross-section  $\sigma$  is fixed by the background scattering length. One must therefore have sufficient density to achieve a thermalization rate on a reasonable timescale. Although one can increase the trap frequency by increasing beam power, atoms must still be able to leave the trap during evaporation. The increased trap depth due to the increased power must then be counteracted. The simplest method is to use a magnetic gradient. However, due to the differential magnetic moment of the different hyperfine states of  $^{40}\text{K}$ , large gradients in deep traps can spatially separate the two spin components, again reducing thermalization. The other solution is to decrease the trap size, which allows one to increase the density

without the need of higher optical powers.

The dimple beam is formed from incoherent light from a super-luminescent diode (SLD) at 830 nm (THORLABS SLD830S), which is amplified by a tapered amplifier. Incoherent light is used to avoid formation of interference fringes that arise from reflections from optical elements in the beam path. The light is sent through the high-resolution objective (see Fig. 4-10) and focused to a waist of  $30\ \mu\text{m}$  at the atoms, much smaller than the size of the 5-degree beam. Evaporation in the dimple trap, along with a magnetic gradient along  $\hat{x}$ , successfully produced degenerate samples. Subsequently, following loading of the atoms into the 2D lattice, we were able to observe Mott and band insulators. By tuning the power of the dimple beam, one also has control over the trap curvature. This can be used to tune the chemical potential of the system at a fixed atom number, enabling one to access different many-body states. It also allows one to tune the initial sample size, which can be useful for optimizing loading of the atoms into the lattice.

## 4.6 Imaging Paths

In this section, we give a list of the imaging paths used in the apparatus. This is necessary for understanding some of the images in later sections. There are a total of five imaging axes, shown in Fig. 4-1, Fig. 4-2 and Fig. 4-3. They are as follows.

- 1) MOT imaging along  $\hat{x}$ . This path intersects the MOT, and is also used by the optical pumping beams for  $^{40}\text{K}$  and  $^{23}\text{Na}$ . It is displaced from the chamber center by  $\sim 1\ \text{mm}$  along  $\hat{y}$ . This axis can be used to image the MOT, and to image atoms after the initial magnetic catch. Both  $^{23}\text{Na}$  and  $^{40}\text{K}$  can be imaged along this path.
- 2) Plug trap imaging along  $-\hat{y}$ . This path intersects the high-resolution imaging in the  $x$ - $y$  plane. Vertically, it can be aligned from the vertical center of the chamber up to  $\sim 2\ \text{mm}$  below the substrate, at which point it is blocked by the in-vacuum RF antenna. The imaging path is opposite the direction of the optical

plug, and is used to image atoms in the quadrupole magnetic trap, and in the movable crossed ODT. It can be used to image the location of the optical plug. Both  $^{23}\text{Na}$  and  $^{40}\text{K}$  can be imaged along this path.

3) “Bouncing” imaging along  $\hat{x}$ . This beam follows the path of the  $x$  lattice beam, and is reflected off the substrate. This allows imaging of the region starting from the surface of the substrate and extending to  $\sim 500\text{ }\mu\text{m}$  below it. This path can be used for rough alignment of the  $y$  lattice beam, the  $y$  optical dipole trap, and the  $y$  Raman beam. Both  $^{23}\text{Na}$  and  $^{40}\text{K}$  can be imaged along this path.

4) “Bouncing” imaging along  $-\hat{y}$ . This beam follows the path of the  $y$  lattice, and is reflected off the substrate. This allows imaging of the region starting from the surface of the substrate and extending to  $\sim 500\text{ }\mu\text{m}$  below it. This can be used for rough alignment of the  $x$  lattice beam and 5-degree beam, and is used for aligning the  $x$  optical dipole trap, the accordion beam, and the  $x$  Raman beam. Both  $^{23}\text{Na}$  and  $^{40}\text{K}$  can be imaged along this path.

5) The vertical imaging path. This passes through the high-resolution objective, which transmits both  $^{23}\text{Na}$  and  $^{40}\text{K}$  light. This path is split into two by a dichroic after the high-resolution objective. The two paths, labeled  $z_1$  and  $z_2$ , are split according to the wavelength of the imaging light. The  $z_1$  path only transmits  $^{40}\text{K}$  D1 light, while the  $z_2$  path transmits all other wavelengths. The  $z_1$  path is used for single-site imaging. It has a magnification of  $\sim 90$ , and is imaged using an ANDOR iXON 897 EMCCD camera. For better signal-to-noise for absorption imaging, the  $z_2$  path has a lower magnification of  $\sim 10$ , and is imaged using a PCO.PIXELFLY USB camera. The  $z_2$  path is used for fine alignment of all three lattice beams, the 5-degree beam, and the dimple beam. Alignment is performed through absorption imaging of  $^{40}\text{K}$  atoms on the D2 line. The  $z_1$  and  $z_2$  paths are shown in Fig. 4-10.

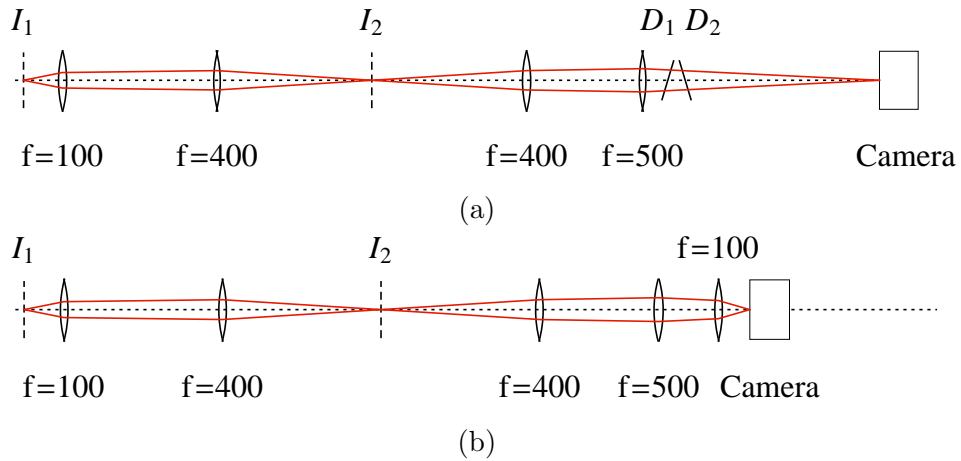


Figure 4-10: Vertical imaging paths  $z_1$  and  $z_2$ . The atoms are at  $I_1$ ; a secondary imaging plane  $I_2$  is formed 400 mm from the second lens, away from  $I_1$ . Focal lengths are in units of mm. (a) Path  $z_1$ . This path is used for single site imaging. The first lens on the right represents the combined objective and solid immersion lens system. The distances between the subsequent lenses are 620 mm, 800 mm and 300 mm. The distance from the last lens to the camera is 604 mm. These parameters are optimized for the smallest spot size though simulations with OSLO. Two SEMROCK LL01-780-25 dichroic filters are placed at positions  $D_1$  and  $D_2$ , 50 mm from the last lens. They are angled-tuned to pass 770 nm light resonant with the D1 transition of  $^{40}\text{K}$ , and have a bandwidth of 3 nm. They are angled at opposite angles to minimize aberrations. The dimple beam, which has wavelength  $\sim 830$  nm, is sent into the objective with the dichroic at  $D_1$ . The dichroic at  $D_1$  also allows absorption imaging on the D2 line of  $^{40}\text{K}$  (path  $z_2$ ). (b) Path  $z_2$ . This path is used for absorption imaging, and is used for alignment of the 5-degree beam and all three lattice beams. This path is split from  $z_1$  at dichroic  $D_1$ , and has effective magnification of  $\sim 51$ .

# Chapter 5

## Site-Resolved Imaging of $^{40}\text{K}$

In the previous chapter, we have discussed some of the motivations to build a quantum gas microscope for ultracold fermions. We have also described the essential parts of the experimental apparatus. In this chapter, we discuss the technical challenges of performing quantum gas microscopy of fermionic  $^{40}\text{K}$ , and their solutions. Some of the research described in this chapter have been reported in the following publication:

*L. W. Cheuk, M. A. Nichols, M. Okan, T. Gersdorf, V. V. Ramasesh, W. S. Bakr, T. Lompe, and M. W. Zwierlein, “Quantum-Gas Microscope for Fermionic Atoms,” Phys. Rev. Lett. **114**, 193001 (2015)* [22]. Included in Appendix F.

The central feature of quantum gas microscopy is the ability to determine the occupation of every lattice site with high fidelity. One prerequisite for site-resolved imaging is an imaging system that has an imaging resolution on the order of the lattice spacing. How this is realized in our apparatus has been described in Section 4.2. Achieving high imaging resolution, however, is not the only challenge. The other challenge is to obtain enough information from each atom in order to determine its position. In this chapter, we describe some considerations and challenges concerning this aspect of single-site imaging. Some of these issues are particularly problematic for  $^{40}\text{K}$  trapped in an optical lattice formed by 1064 nm light. We will describe how one can circumvent these problems with a specific Raman sideband cooling scheme. With this Raman imaging scheme, we were able to successfully perform site-resolved

imaging of  $^{40}\text{K}$  with high fidelity.

## 5.1 Considerations for Single-Site Imaging

In this section, we discuss some general considerations for site-resolved imaging of ultracold atoms. The first requirement is purely optical. The imaging system must have a resolution on the order of the lattice spacing; this requirement is satisfied with the high-resolution imaging system described in Section 4.2. The second requirement concerns the atoms. In order to determine the position of an atom via imaging, one detects photons scattered off the atoms. In our experiment, we perform fluorescence imaging [102], in which atoms excited by resonant light spontaneously emit photons. By collecting these photons on a camera, the positions of the atoms can be determined.

One undesirable consequence of spontaneous emission, however, is heating caused by photon recoil. If the heating is severe enough that atoms move to different lattice sites during imaging, or gain enough energy to escape the lattice, the imaging will no longer reflect the initial distribution, and the imaging fidelity will suffer. To estimate the magnitude of this effect, consider an atom emitting a photon with wavelength  $\lambda$ . In order to conserve momentum, the atom experiences a recoil of momentum  $\Delta p = \hbar \frac{2\pi}{\lambda}$ . The energy associated with this process is  $E_{\text{res}} = \frac{\hbar^2}{2m} \left( \frac{2\pi}{\lambda} \right)^2$ , which corresponds to a temperature of  $0.4 \mu\text{K}$  for potassium atoms emitting on the D1 or D2 line. It turns out that this recoil temperature is similar to the typical temperature of degenerate samples of ultracold fermions trapped in a lattice. Therefore, one would only be able to scatter a few photons per atom before the sample is destroyed. However, in order to have enough signal-to-noise for high fidelity imaging, one typically needs to detect  $\sim 1000$  photons. Taking into account the 0.20 light collection efficiency of our high-NA imaging system, at least 5000 photons needs to be scattered off each atom. Thus direct fluorescent imaging is not viable.

The first method to improve the situation is to increase the depth of the optical lattice. This has two effects. Firstly, increasing the lattice depth “freezes” the system, since quantum mechanical tunneling becomes suppressed at higher depths. One

therefore has more time to scatter photons before an atom tunnels to a neighboring site. The second effect is that in a deeper trap, one can tolerate more heating before atoms escape. Nevertheless, in our experiment, we are limited to maximum lattice depths of  $200 \mu\text{K}$  in each direction, corresponding to  $\tilde{V}_0 \sim 1200$ . To estimate the number of photons that can be scattered before an atom is heated out of the trap, we associate a momentum scale  $p_{max}$  with the trap depth  $\tilde{V}_0$ , given by

$$p_{max} = \sqrt{2mE_R} \sqrt{\tilde{V}_0} = \frac{\hbar\pi}{a} \sqrt{\tilde{V}_0}, \quad (5.1)$$

where  $a$  is the spacing of the lattice. Assuming that the heating process is diffusive in momentum (this occurs in the case of counter-propagating beams), the total number of photons that can be scattered before an atom is lost is

$$\left( \frac{3p_{max}}{\Delta p} \right)^2 = \frac{9\lambda^2}{4a^2} \tilde{V}_0 \quad (5.2)$$

In the case of a single resonant beam illuminating the atoms, the heating process is no longer diffusive and the situation is worse. The total number of scattered photons is

$$\frac{3p_{max}}{2\Delta p} = \frac{3\lambda}{2a} \sqrt{\tilde{V}_0}. \quad (5.3)$$

At first sight, the number of photons scattered seems sufficient in the first case;  $\sim 5 \times 10^3$  photons can be scattered before the atoms are heated out of the system. Nevertheless, the imaging requirements for quantum gas microscopy are more stringent. For high fidelity imaging, it is not enough for atoms to remain trapped in the lattice; they must in fact remain on the same lattice site during imaging. As the atoms heat up, they are promoted to higher bands, where the tunneling rate between lattice sites can become large on the imaging time-scale. The imaging time, typically  $\sim 1 \text{ s}$ , is chosen as a compromise between collecting enough photons and keeping losses due to background gas. For our lattice depths, this implies that atoms must stay in the bottom few bands in order for tunneling to be negligible.

To estimate what temperature this corresponds to, we approximate each lattice

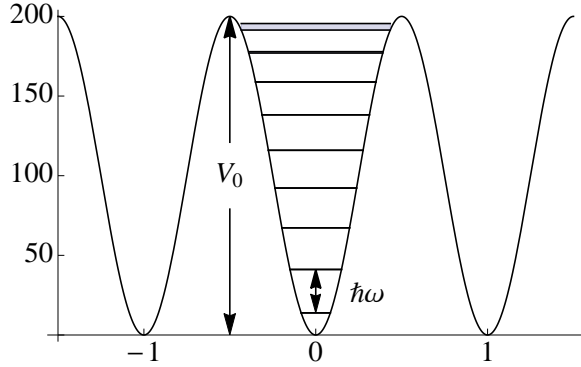
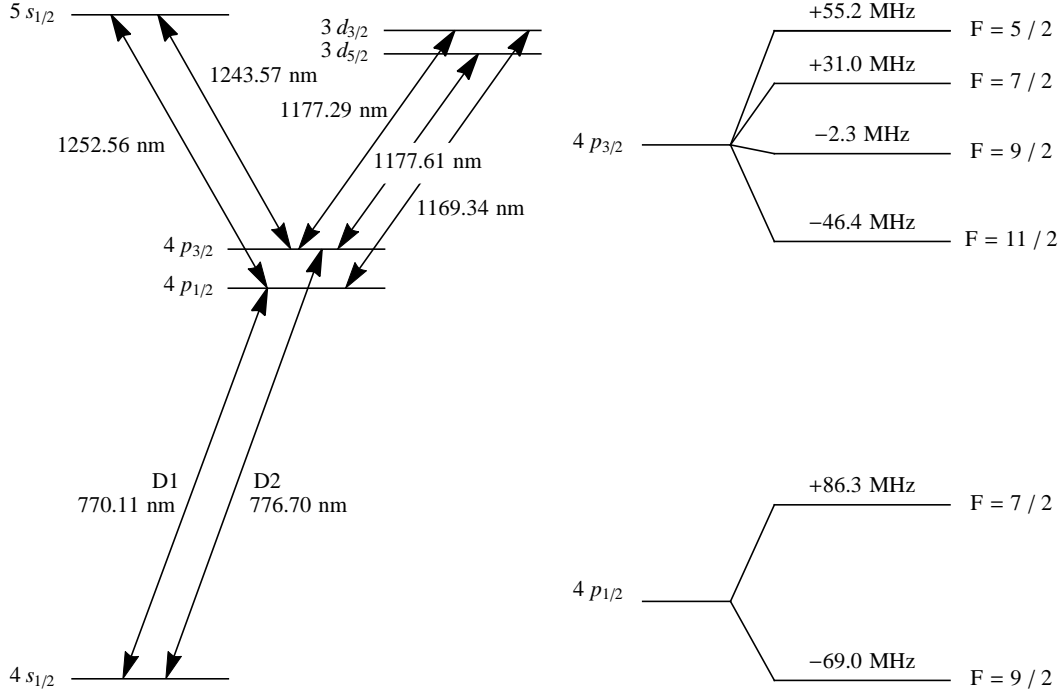


Figure 5-1: Energy levels in a deep lattice. In a deep lattice ( $V_0 \gg E_R$ ), the spacing between the lowest and second lowest bands is approximately given by the  $\hbar\omega$ , where  $\omega = 2\sqrt{\tilde{V}_0 E_R / \hbar}$  is the frequency of the harmonic oscillator that approximates the potential near the minimum of a single lattice well.

site as a harmonic oscillator. In this limit, the harmonic oscillator frequency  $\omega$  corresponds to the bandgaps for the lowest few bands. Recalling that the harmonic oscillator frequency is given by  $\omega = 2\sqrt{\tilde{V}_0 E_R / \hbar}$ , one finds that in the case of  $\sqrt{\tilde{V}_0} \gg 1$  and  $N \sim O(1)$  occupied bands, the energy of the system, relative to the trap depth, is given by  $\eta = 2N/\sqrt{\tilde{V}_0}$ . The number of photons that can be scattered in the balanced and unbalanced beam cases are thus reduced by  $\eta$  and  $\sqrt{\eta}$  respectively. For  $N = 3$ , these factors are  $\sim 1000$  and  $\sim 40$ . This limits the number of scattered photons to a value an order of magnitude lower than required for identifying an atom reliably. Therefore, at experimentally achievable lattice depths, one must cool the atoms while simultaneously scattering photons. This is the main challenge of quantum gas microscopy. Note that this conclusion depends on the mass of the atom, and the imaging resolution of the system, and can thus be different for heavy atoms with transitions at shorter wavelengths [89].

## 5.2 Issues with Imaging $^{40}\text{K}$ in 1064 nm Light

For quantum gas microscopes on bosonic  $^{87}\text{Rb}$ , polarization gradient cooling on the D2 line is used [10, 128], and allows one to scatter up to  $\sim 10^5$  photons while maintaining high imaging fidelities. In the fermionic alkali atoms  $^{40}\text{K}$  and  $^6\text{Li}$ , the excited state hyperfine splittings are smaller than  $^{87}\text{Rb}$ , where the  $F' = 2$  and  $F' = 3$  levels are



(a) Relevant levels and transition wavelengths for the  $4p$  levels of  $^{40}\text{K}$ . Values from [7]. (b) Hyperfine structure of  $4p$  levels in  $^{40}\text{K}$ .

Figure 5-2: Level structure of lowest excited states in  $^{40}\text{K}$ ; Hyperfine structure of  $4p$  levels in  $^{40}\text{K}$ .

split by 193 MHz. In  $^{40}\text{K}$ , the  $F' = 11/2$  and  $F' = 9/2$  levels are split by 45 MHz, about 7 times the natural line width (see Fig. 5-2b); in  $^6\text{Li}$  the situation is worse, with  $F' = 5/2$  and  $F' = 3/2$  split by only 3 MHz, half of the natural linewidth. We chose to use  $^{40}\text{K}$  since the excited state is still resolved, suggesting that polarization gradient cooling could still work, as demonstrated previously in free space [90]. Nevertheless, it turns out that polarization gradient cooling is problematic for  $^{40}\text{K}$  atoms trapped in an optical lattice formed by 1064 nm light. The reason lies in the presence of  $3d_{3/2}$  and  $3d_{5/2}$  states, and to a lesser extent,  $5s_{1/2}$  states (see Fig. 5-2a).

In polarization gradient cooling on the D2 line, one drives transitions between the ground  $4s_{1/2}$  and the excited  $4p_{3/2}$  manifolds. The  $4p_{3/2} \rightarrow 3d_{3/2}$  and  $4p_{3/2} \rightarrow 3d_{5/2}$  transitions both lie at 1177 nm. This implies that the lattice lasers at 1064 nm are detuned only  $\sim 100$  nm to the blue. This produces two undesirable effects. The first is a large AC stark shift of the excited  $4p$  states, which is 5.08 times larger, and

opposite in sign relative to the ground state Stark shift [7]. At the lattice depth for single-site imaging, the Stark shift approaches 60 MHz. The second effect is that the strong Stark shifts lead to mixing between various states in the  $4p_{3/2}$  manifold. When this effect becomes strong, the usual selection rules no longer apply. We discuss these two effects in detail in the following two sections.

### 5.2.1 Anti-Trapping of the $4p$ States

A direct consequence of a large and opposite Stark shift in the excited states ( $4p$ ) is that an atom in the ground state ( $4s_{1/2}$ ) that is initially trapped in a lattice well becomes highly anti-trapped once it is excited. The anti-trapping leads to rapid dispersion of the atomic wave packet, and consequently heating.

To estimate the effect of anti-trapping, we consider a simple model where a two-level atom is trapped in the ground state of a harmonic trap with trap frequency  $\omega$ . In the excited state, the atom experiences an anti-trapping potential  $\bar{V}(x) = -\frac{1}{2}m\bar{\omega}^2x^2$  with anti-trapping frequency  $\bar{\omega}$ . On average, the atom spends a time of  $1/\Gamma$  in the excited state, where  $\Gamma$  is the excited state line width.

The solution for a classical particle in the anti-trapping harmonic potential  $\bar{V}(x)$  has the form of  $x_0 \exp(\pm\bar{\omega}t)$  where  $x_0$  is the starting position and  $t$  is the elapsed time. Therefore one expects that when an atom is excited, the width of the ground state wavepacket increases by a factor of  $\exp(\bar{\omega}/\Gamma)$ . Using the virial theorem, one finds that the energy is proportional to  $\langle x^2 \rangle$ , and thus increases by  $\exp(2\bar{\omega}/\Gamma)$ . At the imaging depth, one finds that a single excitation event is enough to increase the energy of the atom by a factor of 3. One might try to reduce this type of heating by reducing  $\omega$ . If one requires that 5000 scattering events increase the energy by a factor of 3,  $\bar{\omega}$  must be reduced by  $5 \times 10^{-4}$ . Since the anti-trapping frequency is proportional to the square-root of the lattice depth, this corresponds to reducing the lattice depth by  $2 \times 10^{-2}$ . However, at this depth, quantum mechanical tunneling in the lowest band occurs at a rate of  $\sim 1000$ Hz, which restricts the imaging time to be  $\ll 1$  ms.

We are thus in a difficult situation. On one hand, deep lattice depths are required

to keep atoms from moving during imaging, and to relax the temperature requirements during imaging. On the other hand, deep 1064 nm lattices lead to rapid heating for  $^{40}\text{K}$  in the  $4p$  states, which are need to spontaneously scatter photons for imaging. At first sight, it seems that the only solution is to change the wavelength of the lattices. This was not possible in our experiment without major modifications. Nevertheless, as we describe in Section 5.3, the appropriate imaging scheme can circumvent this problem of anti-trapped excited states.

### 5.2.2 Mixing of Excited Hyperfine Levels

In addition to the anti-trapping of the excited  $4p$  states, which is a major issue concerning the motional degrees of freedom, another problem renders polarization gradient cooling on the D2 line ineffective. At the imaging lattice depth, the excited  $4p$  states experience an AC stark shift of 55 MHz, while the hyperfine levels in  $4p_{3/2}$  are spaced by at most  $\sim 50$  MHz. Consequently, the excited  $4p_{3/2}$  states become highly mixed. Even different hyperfine manifolds can be mixed, and  $F$  is no longer a good quantum number. When the total angular momentum  $J = 1/2$ , via the Wigner-Eckart theorem, the effect of a light field can be decomposed into a uniform shift along with an effective magnetic field. In this case, the effective magnetic field is eliminated when the polarization is linear. But for the  $4p_{3/2}$  manifold, where  $J = 3/2$ , one can have tensor light shifts. This implies that even with linear polarizations, different states can be coupled by the tensor light shift. The specific case for  $^{40}\text{K}$  in the presence of 1064 nm light is shown in Fig. 5-10. One can see that at a typical imaging lattice depth of  $h \times 10$  MHz, the usual selection rules, such as  $\Delta F \neq 2$  or  $\Delta m_F \neq 2$ , are no longer valid as  $F$  and  $m_F$  are no longer good quantum numbers. As a result, polarization gradient cooling is expected to be severely affected. Even optical pumping on the D2 line becomes inefficient.

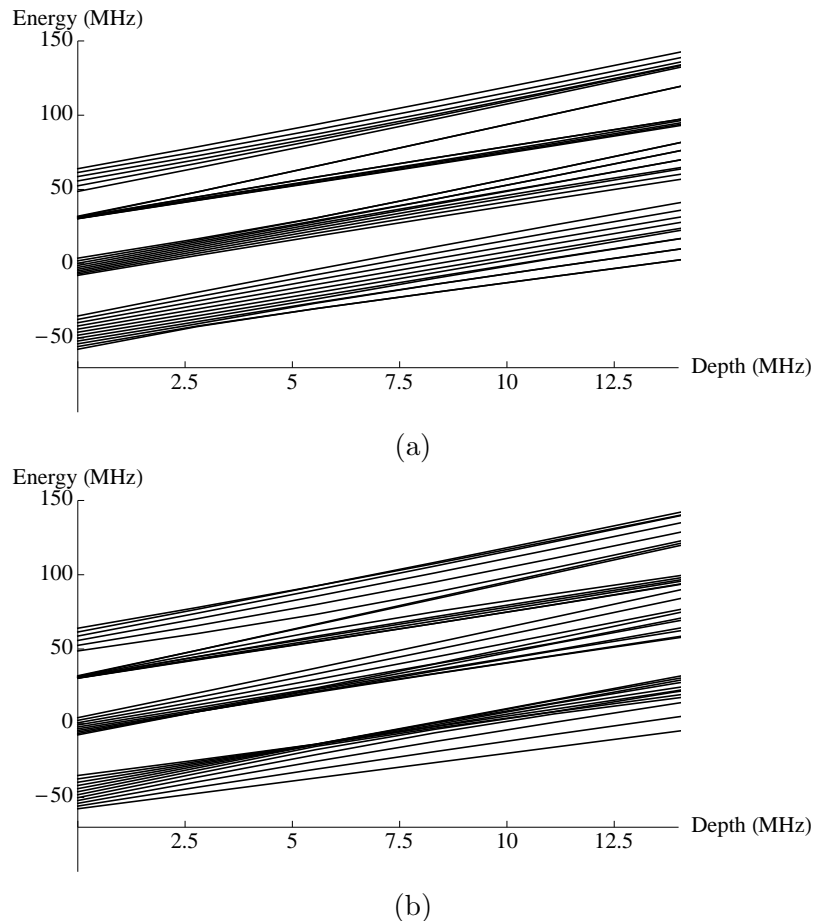


Figure 5-3: Energy diagram of  $4p_{3/2}$  levels in the presence of 1064 nm light. Here, a quantization of 4.0 G is applied to split the Zeeman levels. The horizontal axis is the lattice depth experienced by the  $4s_{1/2}$  state in MHz. The imaging depth corresponds to  $\sim 10$  MHz on the horizontal axis. (a) Linear polarization perpendicular to magnetic field. (b) Linear polarization parallel to magnetic field. The energy levels are computed following [7].

## 5.3 Raman Sideband Cooling

In light of the problems that we encounter for  ${}^{40}\text{K}$  in a 1064 nm lattice, we decided to use Raman sideband cooling as an imaging technique since it allows one to rely less on the anti-trapped excited  $4p$  states. Furthermore, in addition to cooling, Raman sideband cooling also produces spontaneously emitted photons that can be collected for fluorescent imaging. We refer to this scheme as Raman imaging.

Raman sideband cooling was first proposed and realized for ions in the early 1990s [91]. It was subsequently also applied to atoms, directly producing samples with phase space densities approaching unity [141, 71]. In recent years, this technique has been applied as a method of rapid low loss cooling in both bulk and optical tweezer experiments [108, 135, 69]. Nevertheless, before our work, Raman sideband cooling had not been demonstrated for potassium.

### 5.3.1 How Raman Sideband Cooling Works

In order to understand how Raman sideband cooling works, we first consider the simpler scheme of sideband cooling, a technique routinely used in cooling ions. Suppose we have a two-level atom with ground (excited) state  $|g\rangle$  ( $|e\rangle$ ) in a harmonic trap. Further suppose that the ground and excited states experience identical trapping potentials  $V(x) = \frac{1}{2}m\omega^2x^2$ .

In the sideband-resolved regime, where the excited state linewidth  $\Gamma$  is much narrower than the harmonic trapping frequency  $\omega$ , one can selectively drive vibrational-level changing sidebands  $n\omega$  on either side of the carrier transition  $\omega_0$  (see Fig. 5-4b). For example, when one is red-detuned by  $\omega$  relative to the bare transition frequency  $\omega_0$ , the vibrational state is lowered as the atom is transferred into the excited state. Vibration-changing Raman transitions alone, however, do not lead to cooling, as these processes are coherent. In order for cooling to occur, there must be dissipation. For the case of Raman cooling, one must close the cycle after a vibration-lowering transition: the internal state of the atom must be reverted back to the ground state without changing the vibration number. The atom will decay back to the ground

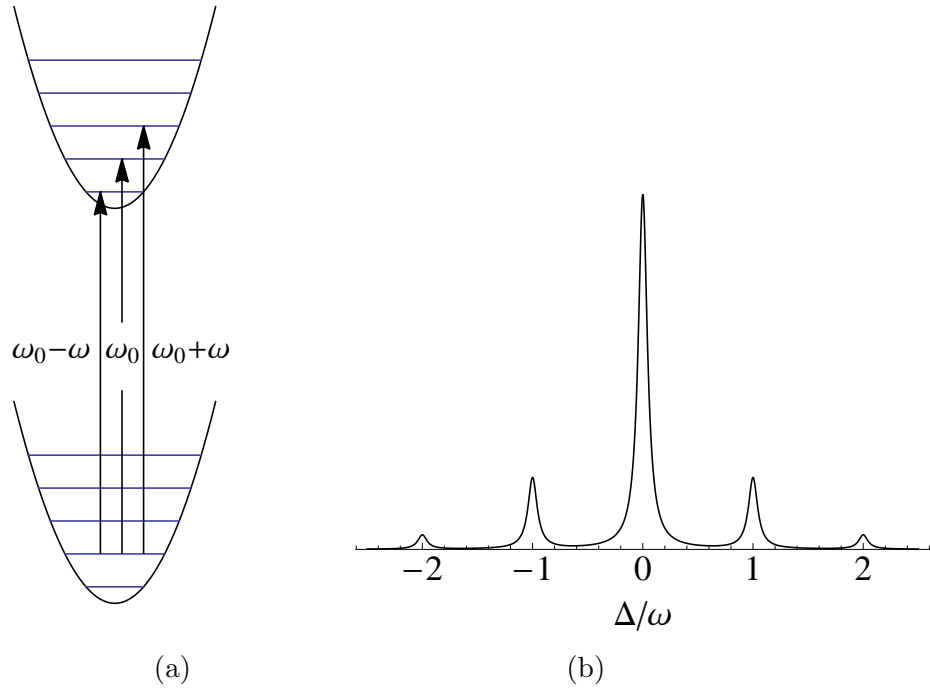


Figure 5-4: The sideband-resolved regime. (a) The vibrational changing transitions are spaced from the carrier frequency  $\omega_0$  by the trap frequency  $\omega$ . Shown are the transitions that change the vibrational number by -1, 0 and 1 respectively. (b) Fluorescence as a function of transition frequency detuning  $\Delta$  from the carrier  $\omega_0$ , normalized to the trap frequency  $\omega$ . When  $\Gamma \ll \omega$ , the sidebands can be resolved. Shown is the case where  $\Gamma = 0.1 \omega$ , with Lamb-Dicke parameter of 0.2, for an atom in vibrational level  $\gg 1$ .

state via spontaneous emission. To ensure that the vibration number is preferentially unchanged, one has to work in the Lamb-Dicke regime, where the wavelength  $\lambda$  of the light driving a transitions is large compared to the harmonic oscillator length  $l = \sqrt{\frac{\hbar}{m\omega}}$ . In this limit, an atom preferentially preserves its vibrational state when it decays from  $|e\rangle$  to  $|g\rangle$  (see Fig. 5-5).

To see why the vibrational number is preferentially unchanged, consider how two vibrational states of the harmonic oscillator are coupled in the presence of light. We only consider the motional part of the atom, and label harmonic oscillator states by  $|n\rangle$ . In the dipole approximation, the atom-light coupling has spatial dependence  $e^{ikx}$ , where  $k$  is the wavevector of the light. In the Lamb-Dicke regime, one can expand

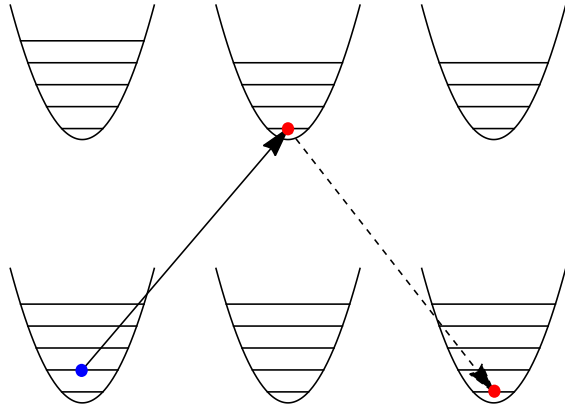


Figure 5-5: Sideband Cooling. An atom starts in  $|g, 1\rangle$ . Light resonant on the  $\omega_0 - \omega$  cooling sideband excites the atom to  $|e, 0\rangle$ . The atom subsequently decays into  $|g, 0\rangle$  preferentially, and its vibrational number remains unchanged. Overall, the energy decreases by  $\hbar\omega$ .

the coupling term as

$$e^{ikx} = 1 + ikx - \frac{k^2 x^2}{2} + \dots \quad (5.4)$$

This is valid since the spatial extent of the wavefunctions  $\langle x^2 \rangle$  is on the order of  $l^2$ , and thus the expansion parameter  $kx$  satisfies  $\langle k^2 x^2 \rangle \ll 1$ . Since different harmonic oscillators states are orthogonal, vibrational changing transitions must originate from terms that contain at least one factor of  $x$ . Recalling that  $\hat{x} = \frac{l}{\sqrt{2}} (a + a^\dagger)$ , where  $a$  ( $a^\dagger$ ) is the lowering (raising) operator, one finds that the matrix elements that couple states differing in vibrational number by  $\Delta n$  are suppressed by  $\eta^{\Delta n}$ , with  $\eta = kl/\sqrt{2}$ .  $\eta$  is known as the Lamb-Dicke parameter, and the Lamb-Dicke regime is defined by  $\eta \ll 1$ .

Unlike in ions, where sideband cooling can be applied, in atoms, one typically cannot reach high enough trap confinement frequencies where the vibrational sidebands are resolved. For example, the  $4p$  states in  $^{40}\text{K}$  have linewidths of  $\Gamma = 2\pi \times 6 \text{ MHz}$ , while at the deepest lattice depths achievable in our experiment, the sideband frequencies are  $\sim 300 \text{ kHz}$ .

Nevertheless, with the use of two-photon Raman transitions, one can easily resolve vibrational sidebands. To see why, consider a two-level system of two hyperfine states

$|a\rangle$  and  $|b\rangle$  in the ground  $4s$  manifold of  $^{40}\text{K}$ . Raman transitions between these two states are driven with the use of two laser beams with frequency  $\omega_1$  and  $\omega_2 = \omega_1 + \delta$ , where  $\delta$  is the detuning and  $\omega_{ba}$  is the bare energy difference between  $|a\rangle$  and  $|b\rangle$ . As discussed in Section 3.2, when  $\omega_1$  and  $\omega_2$  are detuned  $\Delta$  from the  $4s \rightarrow 4p$  transition frequency, the effective two-photon Rabi frequency  $\Omega_2$  is given by

$$\Omega_2 = \frac{\Omega^2}{2\Delta}, \quad (5.5)$$

where  $\Omega$  is the single-photon Rabi frequency. In the limit where  $\Delta \gg \Gamma$ , each beam admixes  $\Omega^2/\Delta^2$  of excited state into the ground states  $|a\rangle$  and  $|b\rangle$ , which implies that the spectral resolution is improved  $\Omega^2/\Delta^2$  relative to the natural line width of  $\Gamma$ . Thus, vibrational transitions with  $\omega \ll \Gamma$  can be resolved, since one can improve the resolution arbitrarily by increasing the two-photon detuning, at the expense of laser power.

Analogous to sideband cooling, one can replace the states  $|g\rangle$  and  $|e\rangle$  with two ground hyperfine states  $|a\rangle$  and  $|b\rangle$ , and replace the single photon vibrational-lowering transition with a two-photon vibrational-lowering transition. A scan of the two-photon detuning  $\delta$  therefore produces an analogous sideband spectrum as shown in Fig. 5-4b. In order to recycle the internal state after removal of one vibrational quantum, sideband cooling relies on spontaneous emission from  $|e\rangle$  to  $|g\rangle$  in the Lamb-Dicke regime. For Raman cooling, one cannot rely on spontaneous emission as both  $|a\rangle$  and  $|b\rangle$  are ground hyperfine states with long lifetimes. Instead, one can perform optical pumping, which transfers atoms from  $|b\rangle$  back to  $|a\rangle$ . This process of lowering the vibrational number via a Raman process and recycling the internal spin state via optical pumping is Raman sideband cooling.

### 5.3.2 What to Do About the Excited States?

The reason we chose to use Raman sideband cooling is that it allows us to avoid the problem of anti-confinement in the  $4p$  states and the mixing of excited  $4p_{3/2}$  states. Alternatively, EIT cooling has also been demonstrated to allow site-resolved

imaging of  $^{40}\text{K}$  [51]. In Raman sideband cooling, the coherent vibration-changing two-photon process can have negligible admixture of the excited states, as long as the two Raman beams are far detuned from single-photon resonance. Whereas the excited state fraction scales as  $1/\Delta^2$ , where  $\Delta$  is the single-photon detuning, the two-photon Rabi frequency scales as  $1/\Delta$ , as long as one is detuned much less than the spin-orbit splitting between  $4p_{3/2}$  and  $4p_{1/2}$ . The effect of the excited states can therefore be eliminated as long as one has sufficient power.

The second ingredient of Raman cooling, optical pumping, must rely on excited states since photons must be spontaneously emitted. From the discussion of mixing of hyperfine states in Section 5.2.2, one sees that for effective optical pumping, one must avoid tensor light shifts. We thus optically pump via the  $4p_{1/2}$  states.

The problem of anti-confinement nevertheless remains even for the  $4p_{1/2}$  manifold. At first sight, anti-confinement seems unavoidable, as spontaneous emission is required for optical pumping. Taking into account that optical pumping typically requires 3 to 10 photons, the estimates in Section 5.2.1 suggest that, for each cooling cycle, the heating due anti-confined excited states will be larger than the cooling of  $\hbar\omega$  by the Raman beams.

The estimates in Section 5.2.1, however, are for the situation when an atom is excited on resonance. The situation is much improved when the optical pumping light is detuned. With detuning, one can suppress the number of atoms that experience heating due to anti-trapping, while still allowing spontaneous emission and therefore optical pumping to proceed. To understand how detuning helps, we introduce the dressed atom picture [26].

Consider a two-level system with ground and excited states  $|g\rangle$  and  $|e\rangle$  separated with energy difference  $\hbar\omega_{eg}$ , in the presence of light detuned by  $\delta \ll \omega_{eg}$  from the resonance. One can describe the combined atom-photon system using the dressed state basis. We first take into account the number of photons  $N$  in the light field by defining basis states  $|g, N\rangle \equiv |g\rangle \otimes |N\rangle$  and  $|e, N\rangle \equiv |e\rangle \otimes |N\rangle$ . Since we are close to resonance ( $\delta \ll \omega_{eg}$ ), pairs of states consisting of  $|g, N\rangle$  and  $|e, N-1\rangle$  are nearly degenerate. In the rotating wave approximation, the light field couples pairs

of states  $|g, N\rangle$  and  $|e, N-1\rangle$  with amplitude  $\hbar\Omega/2$ , where  $\Omega$  is the Rabi frequency. The resulting dressed states  $|G, N\rangle$  and  $|E, N\rangle$  connect to  $|g, N\rangle$  and  $|e, N-1\rangle$  in the limit of  $\Omega \rightarrow 0$ . They can be expressed in the undressed basis  $|g, N\rangle$  and  $|e, N-1\rangle$  as

$$\begin{aligned} |G, N\rangle &= \cos \theta |g, N\rangle + \sin \theta |e, N-1\rangle \\ |E, N\rangle &= -\sin \theta |g, N\rangle + \cos \theta |e, N-1\rangle \end{aligned} \quad (5.6)$$

where  $\tan(2\theta) = -\Omega/\delta$ .

To describe spontaneous emission, we observe that spontaneous emission occurs when  $|e, N\rangle$  decays to  $|g, N+1\rangle$ . Inspection of Eq. (5.6) reveals four possible decay channels:  $|G, N\rangle \rightarrow |G, N-1\rangle$ ,  $|G, N\rangle \rightarrow |E, N-1\rangle$ ,  $|E, N\rangle \rightarrow |G, N-1\rangle$  and  $|E, N\rangle \rightarrow |E, N-1\rangle$ . Denoting the corresponding decay rates by  $\Gamma_{GG}$ ,  $\Gamma_{GE}$ ,  $\Gamma_{EG}$  and  $\Gamma_{EE}$ , one finds that [26]

$$\begin{aligned} \Gamma_{GG} &= \Gamma \sin^2 \theta \cos^2 \theta \\ \Gamma_{GE} &= \Gamma \sin^4 \theta \\ \Gamma_{EG} &= \Gamma \cos^4 \theta \\ \Gamma_{EE} &= \Gamma \sin^2 \theta \cos^2 \theta, \end{aligned} \quad (5.7)$$

where  $\Gamma$  is the excited state linewidth. In the limit of  $|\Omega/\delta| \gg 1$  and  $\delta \gg \Gamma$ ,  $\cos^2 \theta \approx 1$  and  $\sin^2 \theta \approx s \equiv \Omega^2/\delta^2$ . The decay rates in Eq. (5.7) are then  $\Gamma s$ ,  $\Gamma s^2$ ,  $\Gamma$  and  $\Gamma s$  respectively.

We now consider the scenario where the excited state  $|e\rangle$  is anti-trapped, but the ground state  $|g\rangle$  is trapped. At the Stark-shifted resonance, both  $|G, N\rangle$  and  $|E, N\rangle$  states become anti-trapped when  $\Omega \neq 0$ , as shown in Fig. 5-6. However, at large detuning  $\delta \gg \Omega$ ,  $|E, N\rangle$  consists of the bare excited state  $|e\rangle$  admixed with a small amount of  $|g\rangle$ , and is thus anti-trapped. Similarly,  $|G, N\rangle$  is the trapped ground state  $|g\rangle$  admixed with a small amount of anti-trapped excited state  $|e\rangle$ . This is depicted in Fig. 5-7.

The detuning  $\delta$  has two effects. The first concerns the steady state population in

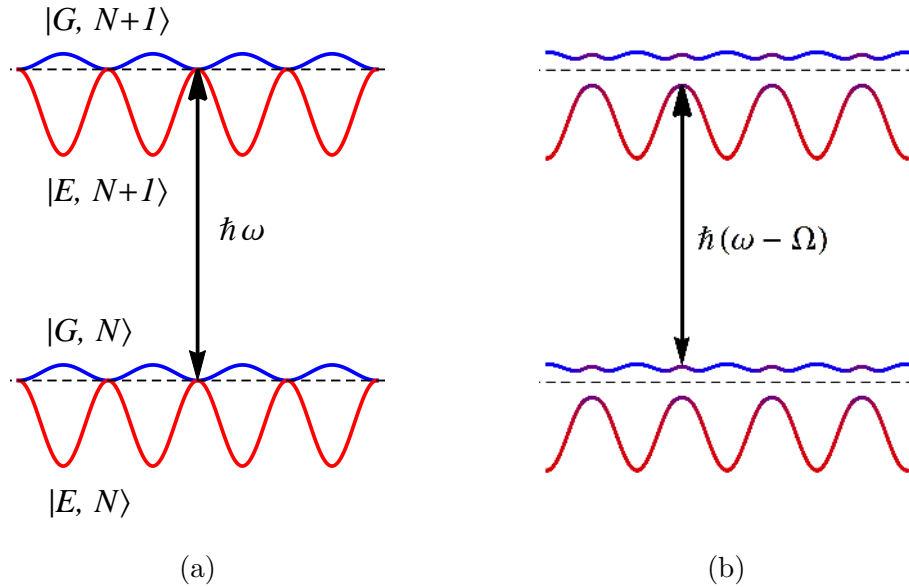


Figure 5-6: Dressed States at Zero Detuning. (a) When  $\Omega = 0$ , the state  $|G, N\rangle$  ( $|E, N\rangle$ ) coincides with  $|g, N\rangle$  ( $|E, N - 1\rangle$ ). Dressed state  $|G, N\rangle$  is predominantly ground state, and is shown in blue, while  $|E, N\rangle$  is shown in red. As shown,  $|g\rangle$  experiences a trapping lattice potential, while  $|e\rangle$  is anti-trapped with 5.5 times the ground state trap depth. The arrow indicates the Stark-shifted resonance. (b) At  $\Omega \neq 0$ , mixing of  $|g, N\rangle$  and  $|e, N - 1\rangle$  states occur. The admixture of  $|g\rangle$  and  $|e\rangle$  is shown by the color of the dressed state, and varies spatially. At the locations where the light is resonant, the dressed states are equal admixtures of  $|g\rangle$  and  $|e\rangle$ , and  $|G, N\rangle$  and  $|E, N\rangle$  forms a doublet that is split by  $\hbar\Omega$ . In this plot,  $\hbar\Omega = 2V_0$ , where  $V_0$  is the lattice depth experienced by the ground state  $|g\rangle$ .

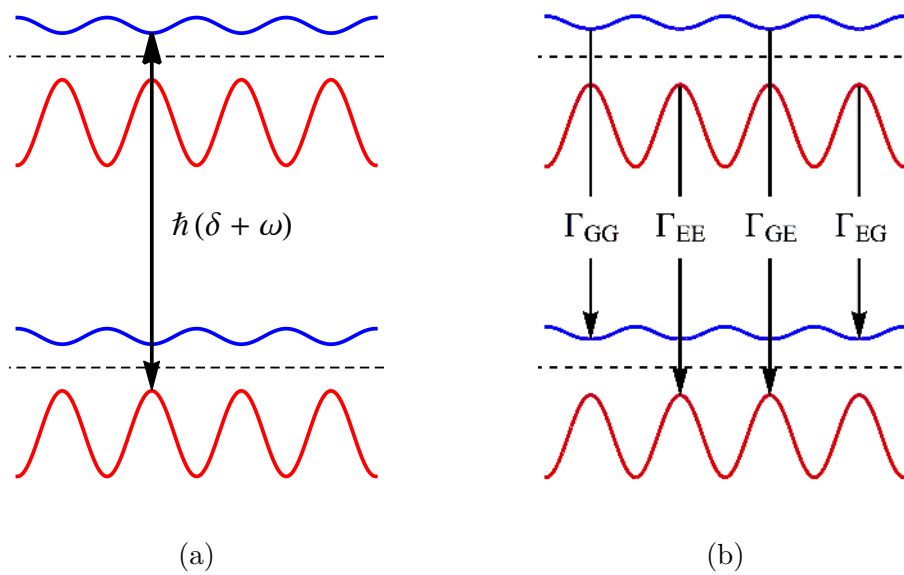


Figure 5-7: Dressed States at Non-Zero Detuning. (a) At  $\Omega = 0$ , the dressed states  $|G, N\rangle$  and  $|E, N\rangle$  are now split by an additional  $\pm\hbar\delta/2$ . (b) Even when  $\Omega \neq 0$ , the admixture of  $|e\rangle$  ( $|g\rangle$ ) into  $|G, N\rangle$  ( $|E, N\rangle$ ) can be small. Shown here is the case for  $\Omega/\delta = 2/3$ . The color indicates the admixture of  $|g\rangle$  (blue) and  $|e\rangle$  (red). When  $\Omega \neq 0$ , four decay channels are possible. These are labeled and indicated by the arrows.

the anti-trapped states  $|E, N\rangle$ . The population in  $|E, N\rangle$  is determined by the ratio  $\Gamma_{GE}/\Gamma_{EG}$ , and is  $s^2$  in the large detuning limit  $s \ll 1$ . The second effect concerns the decay ratios into anti-trapped states  $|E, N\rangle$ . For atoms starting in  $|G, N\rangle$ , the branching ratio into anti-trapped  $|E, N\rangle$  is  $\Gamma_{GE}/\Gamma_{GG} \approx s$ . For atoms starting in  $|E, N\rangle$ , the branching ratio into  $|E, N\rangle$  is  $\Gamma_{EE}/\Gamma_{EG} \approx s$ . Atoms thus preferentially decay into the trapped state  $|G, N\rangle$ .

Therefore, at large detuning, the decay is primarily between two trapped states at a rate given by  $\Gamma_{GG} \approx \Gamma s$ . The excitation rate to an anti-trapped state is suppressed, and is given by  $\Gamma_{GE} \approx \Gamma s^2$ . The effect of anti-trapping can thus be reduced even in the presence of spontaneous emission. If one requires an atom to scatter  $\sim 1 \times 10^4$  photons before entering an anti-trapped state, then one finds  $s \sim 10^{-4}$ , or  $\delta/\Omega \sim 200$ . For  $s \sim 10^{-4}$ , we obtain a spontaneous emission rate  $\sim 4000$  photons per second for  $^{40}\text{K}$ , sufficient for site-resolved fluorescent imaging.

## 5.4 Implementing Raman Imaging of $^{40}\text{K}$

In Section 5.2, we discussed the considerations for performing single-site imaging of  $^{40}\text{K}$ . In Section 5.3, we described how Raman imaging can overcome the issues of anti-trapped excited states and excited state hyperfine mixing. These problems are not specific to  $^{40}\text{K}$ , but are particularly severe for  $^{40}\text{K}$  in the presence of 1064 nm. Here, we describe how single-site imaging of a single 2D layer of  $^{40}\text{K}$  atoms is achieved using Raman sideband cooling in our apparatus.

### 5.4.1 Preparing a Single Layer of $^{40}\text{K}$ Atoms

As described in Section 4.5.1, the trapping potential formed by the 5-degree beam forms a vertical lattice with spacing  $\sim 5\ \mu\text{m}$  along  $\hat{z}$ . Many layers of the lattice can be occupied. The presence of many layers along the imaging axis can lead to a diffuse glow, even when only one layer is within the depth of focus. This can result in decreased signal-to-noise, which makes identifying the occupation of a lattice site more difficult. We therefore first prepare a single layer of atoms. For our initial

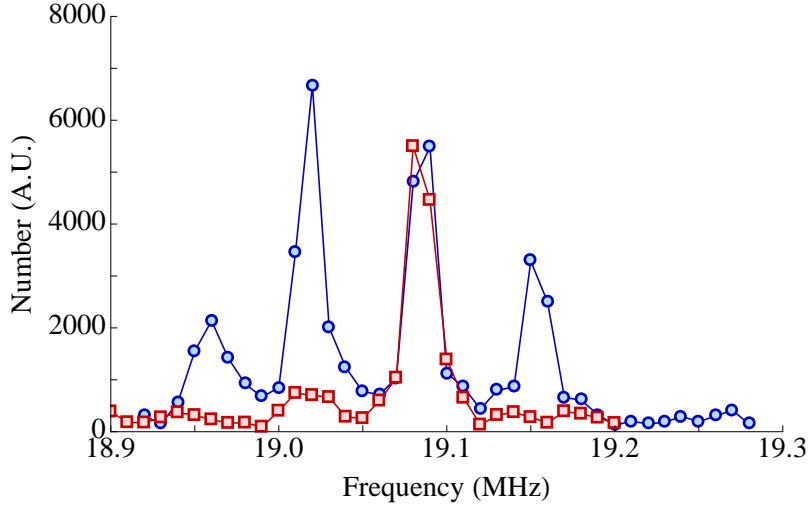


Figure 5-8: “Slicing” spectrum. Shown is the atom number versus microwave frequency (detuning from fixed frequency) for  $|9/2, -9/2\rangle \rightarrow |7/2, -7/2\rangle$  before (blue circles) and after (red squares) slicing.

attempts at single-site imaging, we started with  $\sim 10^6$   $^{40}\text{K}$  atoms at  $\sim 10 \mu\text{K}$  in the hyperfine state  $|F = 9/2, m_F = 9/2\rangle$ , prepared via sympathetic cooling with  $^{23}\text{Na}$  in the plugged quadrupole magnetic trap. The optical plug is then switched off and current is run through the Feshbach coils to produce a magnetic field along  $\hat{z}$ . This shifts the center of the quadrupole trap, which is initially located  $\sim 9$  mm below the substrate. The center is moved upwards in 50 ms to the surface of the substrate. The 5-degree beam, described in Section 4.5.1, is subsequently ramped up in 5 ms to trap atoms, before they are lost from collisions with the substrate. The magnetic trap is subsequently ramped down. An RF sweep then changes the hyperfine state from  $|9/2, 9/2\rangle$  to  $|9/2, -9/2\rangle$ . Since the 5-degree beam is reflected off the surface at  $5.8^\circ$ , it forms a vertical lattice with spacing  $5.3 \mu\text{m}$ . The vertical size of the 5-degree beam allows four layers to be loaded.

In order to select one layer, we use a “slicing” technique that relies on a layer-dependent magnetic field [128]. By applying 50 A of current along the curvature coils run in anti-Helmholtz configuration, we produce a magnetic field gradient of 45 G/cm along the vertical  $\hat{z}$  direction at an offset field of 40 G. This results in an inter-layer frequency difference of 35 kHz on the  $|9/2, -9/2\rangle \rightarrow |7/2, -7/2\rangle$  transition, as shown in Fig. 5-8. In order to have stable enough transition frequencies to select

a single layer, one must stabilize both the magnetic field offset and the gradient. Unfortunately, the experiment is in close proximity ( $\sim 5$  m) to three elevators, which produce time-varying magnetic fields along the vertical direction with a range of  $\pm 20$  mG. Since this is in the same direction as the magnetic field that we apply during "slicing," and the magnitude can shift the layer frequency by more than a layer, we must compensate for these fields. We place a HONEYWELL HMC2003 magnetometer on the chamber,  $\sim 50$  cm above the atoms. This location is chosen for two reasons. The first consideration is that the magnetometer should best reflect the magnetic field contribution of the elevators that the atoms experience, and thus should be placed close to the chamber. The second is that the magnetometer should be in a location where the magnetic field generated by the leads to the coils are less than 2 G, which is the saturation limit of the magnetometer. We feedback on the magnetometer signal, using a pair of coils around the experiment. In order to avoid 60 Hz magnetic noise, the heaters for the  ${}^{40}\text{K}$  oven and 2D MOT, which are  $\sim 50$  cm from the atoms, are switched off using a MOSFET during "slicing." With the ovens switched off, the residual magnetic field noise is  $\sim 1$  mG. Combined with compensation of the elevator fields, the ambient magnetic field is reproducible to a level of  $\pm 2$  mG. The residual magnetic field is determined solely by the current that is run through the curvature coil. This current, produced by a DELTA ELEKTRONIKA SM 18-50 P251 power supply, is measured using a DANFYSIK LEM IT 200-S current transducer. The current from the transducer is converted to a voltage via four high-precision low-drift resistors attached to a heat sink, allowing for accurate current measurements at the  $10^{-5}$  level.

To select a single layer, we apply a 1 ms microwave pulse that sweeps a frequency span of 20 kHz. To minimize the influence of 60 Hz noise on the magnetic field, the start of the pulse is triggered onto a 60 Hz signal obtained from line voltage. The phase of the trigger is set such that the transition frequency is minimally sensitive. The pulse selectively transfers the second layer of atoms to  $|7/2, -7/2\rangle$ . Subsequently, a resonant light pulse on the  $|F = 9/2, m_F = -9/2\rangle \rightarrow |F' = 11/2, m'_F = -11/2\rangle$  cycling transition is applied to remove atoms in the other layers. The  $|7/2, -7/2\rangle$

atoms in the desired layer are then transferred back to  $|9/2, -9/2\rangle$  using a 10 ms pulse sweeping over 80 kHz.

We then produce a  $|9/2, -9/2\rangle$ - $|9/2, -7/2\rangle$  spin mixture via a radio-frequency sweep in order to allow the gas to thermalize. By lowering the power of the 5-degree beam, the atoms are evaporatively cooled. To image the atoms, the lattices beams along the  $\hat{x}$ ,  $\hat{y}$  and  $\hat{z}$  are ramped up and increased to a depth of  $\sim 200 \mu\text{K}$ , where tunneling for atoms in the lowest few bands are negligible during imaging times of  $\sim 1 \text{ s}$ .

### 5.4.2 Raman and Optical Pumping Scheme

While there are many different Raman cooling schemes, such as degenerate sideband cooling [141], we have opted to use a two-level scheme. This is chosen to reduce the number of optical pumping photons required, as optical pumping is the process by which atoms can experience the deleterious effects of 1064 nm light. In order to have an isolated two-level system, we apply a magnetic field of 4.2 G to isolate the microwave transition between state  $|F = 9/2, m_F = -9/2\rangle$  and  $|7/2, -7/2\rangle$  of the ground  $4s_{1/2}$  manifold. At this magnetic field, the various transitions between  $F = 9/2$  and  $F = 7/2$  are spaced by  $> 1 \text{ MHz}$ . The magnetic field is oriented along  $\hat{x}$ , while the two Raman beams propagate along  $\hat{x}$  and  $\hat{y}$  respectively, at an angle of  $10.8^\circ$  relative to the  $x$ - $y$  plane. The polarizations of the two beams are along  $\hat{y}$ , and  $\hat{x}$ , respectively. The Raman beams can thus drive  $|\Delta m_F| = 1$  transitions, up to polarization imperfections. Since the transitions are non-degenerate, one can selectively address only the  $\Delta m_F = +1$  transition by selecting the appropriate two-photon detuning. The Raman beams are detuned  $\sim 50 \text{ GHz}$  red of the D2 line. The light source and the detailed setup for generating the Raman frequencies are described in Appendix B.3. The geometry of the Raman beams also allow coupling to sidebands in all directions, albeit at a weaker strength along  $\hat{z}$  due to the shallow angle. Specifically, the Lamb-Dicke parameters for the Raman beams are 0.17 along  $\hat{x}$  and  $\hat{y}$ , and 0.07 along  $\hat{z}$ .

The second ingredient of Raman cooling is optical pumping. Previously in Sec-

tion 5.3.2, we noted that it is crucial to detune the optical pumping beams when the excited state is anti-confined. It is also important to perform optical pumping on the D1 line ( $4s_{1/2} \rightarrow 4p_{1/2}$ ) since the  $4p_{3/2}$  manifold is susceptible to large tensor light shifts in the presence of the optical lattice. Our optical pumping scheme uses two frequencies, one for  $F$ -pumping and one for  $m_F$ -pumping. We found empirically that it is optimal to have the  $F$ -pumping light detuned by  $-80$  MHz from the Stark-shifted  $F = 7/2 \rightarrow F' = 9/2$  transition, and the  $m_F$ -pumping light detuned by  $-80$  MHz. On the experiment, the optical pumping beams originate from the same fiber, and the polarization of both beams are optimized to minimize admixture of  $\sigma_+$  light. The pumping beams propagate along  $\hat{x}$ , at a shallow angle of  $10.8^\circ$ , and are reflected off the substrate. The beam-size at the substrate is picked to be  $\sim 200 \mu\text{m}$ , as a balance between maintaining uniformity of the pumping beam and minimizing scatter of optical pumping light due to surface roughness of the substrate. Due to the geometry of the beams, there is a small admixture of  $\pi$ -polarized light. This leads to a  $\sim 10^{-2}$  smaller rate along  $\pi$  transitions. For  $F$ -pumping, this is not a major issue. However, for  $m_F$ , pumping light, this can reduce the darkness of the  $|9/2, -9/2\rangle$  state. It is thus preferable to pump on the  $F = 9/2 \rightarrow F' = 7/2$  transition in order to keep  $|9/2, -9/2\rangle$  dark. We rely on the small  $\pi$  admixture to pump atoms out of  $|9/2, -7/2\rangle$ .

### 5.4.3 How to Make Raman Imaging Work

In this section, we outline the steps we took to make Raman imaging work. The first step is to ensure that the atoms are in low enough vibrational bands where Raman cooling is efficient. One must also ensure that the Raman beams can transfer atoms between hyperfine states. These two requirements can be checked by performing Raman spectroscopy. We first calibrate the  $|9/2, -9/2\rangle$  to  $|7/2, -7/2\rangle$  frequency using microwave spectroscopy. Atoms are transferred to  $|7/2, -7/2\rangle$  with a microwave sweep, after which we fluorescent image the remaining  $|9/2, -9/2\rangle$  atoms with a resonant light pulse on  $|9/2, -9/2\rangle \rightarrow |11/2, -11/2\rangle$  transition. The number of atoms is inferred from the amount of fluorescence.

With the transition frequency known, we next performed Raman spectroscopy. After the microwave pulse hides atoms in  $|7/2, -7/2\rangle$ , we apply a reverse sweep to  $|9/2, -9/2\rangle$  using the Raman beams. The two-photon detuning of the Raman beams is swept during the pulse. By adjusting the final evaporation depth, we were able to reach a regime with high sideband asymmetry, indicating that the majority of the atoms were in the lowest vibrational band in along all three axes (See Fig. 5-9). This also provided the frequencies of the sidebands.

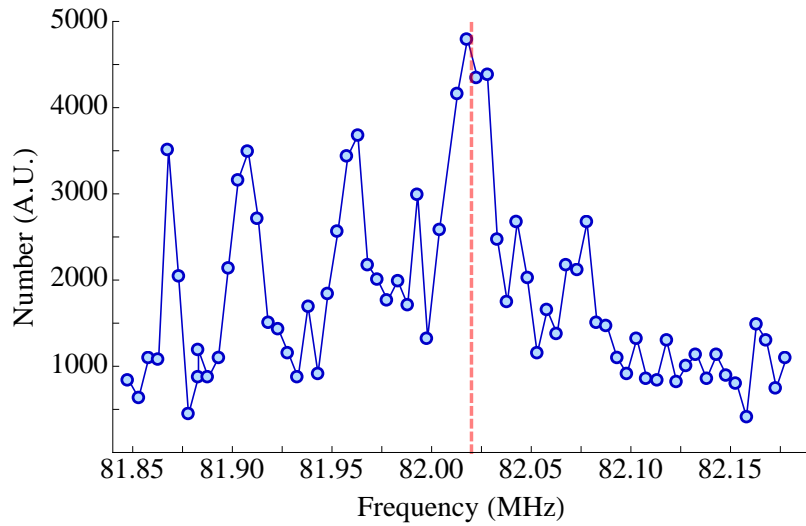


Figure 5-9: Sideband asymmetry measured via Raman spectroscopy. Using a microwave sweep, atoms are initially transferred to  $|7/2, -7/2\rangle$ . We transfer the atoms to  $|9/2, -9/2\rangle$  and measure arrivals via fluorescent imaging with resonant light. The horizontal axis indicates the frequency used for the double-pass AOMs for the Raman beam along  $\hat{x}$ . The carrier transition is indicated by the red arrow. Heating sidebands for the three directions are visible on the left of the carrier; corresponding cooling sidebands are only observed for the  $\hat{z}$  direction.

In order to implement optical pumping, one must first identify the frequencies of the Stark-shifted resonances. To determine the Stark shift, we first prepared atoms in  $F = 9/2$ . When a pulse of D2 light resonant with the  $F = 9/2 \rightarrow F' = 11/2$  transition, the  $9/2 \rightarrow 9/2$  transition, or the  $9/2 \rightarrow 7/2$  transition is applied, atoms are either lost due to heating, or optically pumped into  $F = 7/2$ . The Stark shift can then be obtained by comparing the resonant frequencies with and without lattice, as shown in Fig. 5-10.

The optical pumping beams were subsequently tuned to their respective Stark-

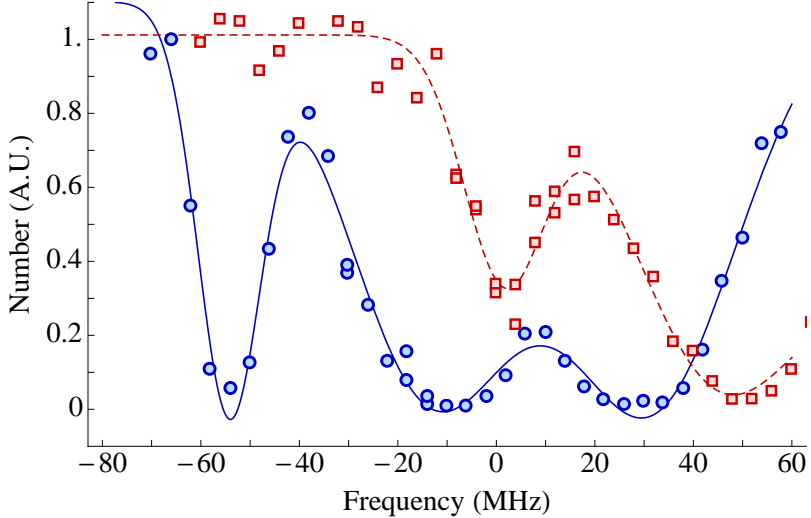


Figure 5-10: Measuring Stark shifts of the D2 transitions. We measure the remaining atom number as a function of the frequency of a resonant light pulse on the D2 line. Shown in blue circles is the measurement without the 1064 nm lattice. From left to right, the three loss features correspond to the  $9/2 \rightarrow 11/2$ ,  $9/2 \rightarrow 9/2$  and  $9/2 \rightarrow 7/2$  transitions respectively. The remaining number measured in the lattice is shown in red squares. Comparison of the resonant features between the two measurements gives a Stark shift of  $\sim 60$  MHz.

shifted resonances. To allow easy scanning of large frequency ranges without significant changes in intensity, the  $F$  and  $m_F$  pumping light was provided by two ECDLs, which were offset-locked to a DBR laser locked to the D1 line. Next, we optimized the polarization of the optical pumping beam to have minimal  $\sigma_+$  admixture. This is non-trivial since the incoming optical pumping beam interferes with its reflection off the substrate. In order to have full control over the polarization, a  $\lambda/2$  and a  $\lambda/4$  waveplate were added to the beam. The angles of the two wave plates were then optimized by the lifetime of  $|9/2, -9/2\rangle$  atoms.

With the sideband frequencies known and the optical pumping frequencies and polarizations found, we attempted Raman sideband cooling. We initially used a pulsed scheme, since it was conceptually easy to understand. In the pulsed scheme, vibrational lowering pulses to address all three directions are applied sequentially, after which a pulse of optical pumping is applied. With optimized pulse parameters, we were able to obtain a first signal of Raman cooling, where we could apply  $\sim 100$  cooling pulses before losses were significant. During this time, the fluorescence

also increased linearly. While this was encouraging, the lifetime with the cooling pulses was only  $\sim 20$  ms, and we were only able to obtain roughly the same number of scattered photons as resonant fluorescent imaging. This corresponded to  $\sim 100$  collected photons.

Adding a detuning of  $\sim +30$  MHz to both the  $F$  and  $m_F$  pumping beams, we were able to extend the lifetime to  $\sim 1000$  cycles. By fixing the number of Raman cycles at  $\sim 10^5$ , we further optimized the intensity and frequencies of the two beams. This provided a lifetime of  $\sim 5 \times 10^4$  cycles, corresponding to a lifetime of 40 s. At this point, the scattering rate was sufficient to detect single atoms.

The next step was to optimize the imaging system. First, one must pick a magnification of the imaging system. As a compromise between signal per pixel and spatial resolution, we chose to image each lattice site to  $3 \times 3$  pixels. Through simulations of the optics system in OSLO, we optimized the imaging system to minimize the spread of the energy density of a point source. The setup of the single-site imaging system was described in Section 4.6 and Section 4.2, and is shown in Fig. 4-10.

One technical consideration in the experiment is background light due to scattering from the substrate. Since the lattice beams, the optical pumping beams and the Raman beams are all reflected off the substrate, roughness of the substrate surface produces a background of scattered light. The lattice light has a wavelength of 1064 nm, far detuned from the D1 and D2 lines of  $^{40}\text{K}$ . It can therefore be easily filtered out. For  $^{40}\text{K}$ , the D1 and D2 lines are split by 3 nm, just enough for interference filters to selectively transmit one of the two wavelengths. Since the optical pumping has to be on the D1 line to avoid tensor light shifts (see Section 5.2.2), we chose to tune the Raman beams close to the D2 line, as mentioned in Section 5.4.2. Note that the majority of spontaneously scattered photons are generated during optical pumping. Only spontaneously scattered photons can be collected by the imaging system, and give information about the locations of the atoms.

After focusing the imaging system, we obtained the first detection of single  $^{40}\text{K}$  atoms, shown in Fig. 5-11. The atom number was measured as a function of imaging time, and a lifetime of 79 s was obtained. While the lifetime of the total number

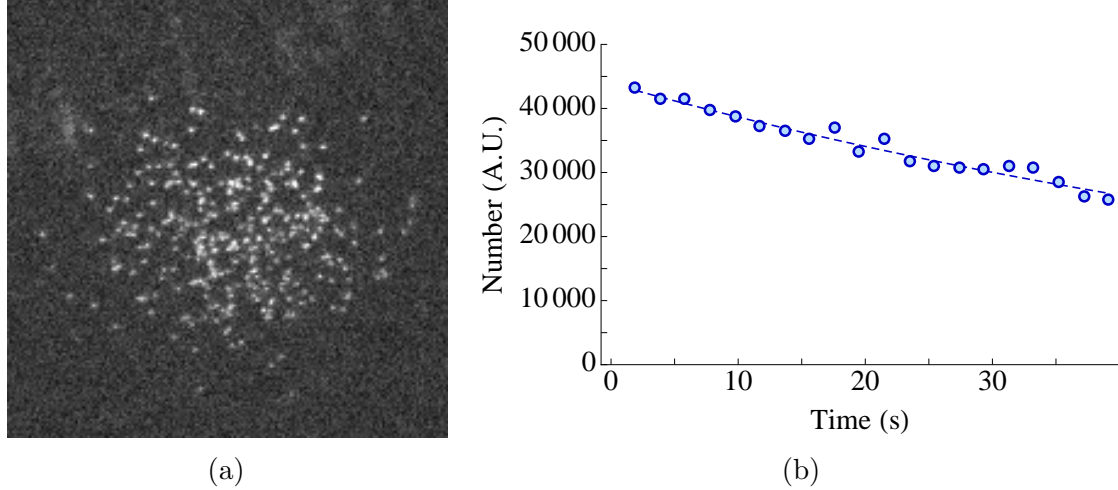


Figure 5-11: First signal of single atoms. (a) Bare image obtained using Raman cooling. (b) Corresponding measurement of total fluorescent photon counts as a function of imaging time show in circles. Shown in dashed is the exponential fit, which gives a time constant of 79 s.

of atoms gives an estimate of the fidelity, it does not directly reveal whether atoms are hopping between sites. For example, if the gas is dilute, and the hopping rate is low enough such that atoms hop but remain in the lattice, hopping will not result in loss. Therefore the net loss rate only provides an upper bound on imaging fidelity. To determine the fidelity, we must next identify occupation of the lattice sites, which will be described in the next section.

## 5.5 Image Reconstruction and Fidelity Estimation

After the imaging system is focused on the atoms, one can proceed to characterize the imaging fidelity by measuring hopping and loss rates during the imaging process. Before this can be done, one must be able to reconstruct images into maps of occupied and unoccupied sites. The necessary steps are outlined in the following sections.

### 5.5.1 Identifying Lattice Axes and Spacings

The first step in image reconstruction is identification of the lattice axes and spacings. We start by imaging a dilute sample, where atoms well-separated. The coordinates

$(x, y)$  along the camera axes of each atom are recorded. We then transform the coordinates  $(x, y)$  to a new set of coordinates  $(x', y')$  via

$$\begin{aligned} x' &= x \cos \theta_y + y \sin \theta_y \\ y' &= -x \sin \theta_y + y \cos \theta_y. \end{aligned} \quad (5.8)$$

The task at hand is to identify  $\theta_x$  and  $\theta_y$  such that  $x'$  and  $y'$  coincides with the  $x$  and  $y$  lattices. Note that  $\theta_x$  need not equal  $\theta_y$ , as the angle between the lattices can differ slightly from  $90^\circ$ . From the list of transformed coordinates  $(x', y')$ , we construct two histograms of all possible differences in  $x'$ , and in  $y'$  respectively. When  $\theta_x$  and  $\theta_y$  are equal to the relative angles of the  $x$  and  $y$  lattice axes, the respective histograms show periodic modulation, as shown in Fig. 5-12b. The lattice spacings can then be precisely determined by identifying the position of the fundamental in the Fourier spectrum, as shown in Fig. 5-12c. The angles are found by fitting the magnitude of the fundamental as a function of  $\theta_x$  and  $\theta_y$ , as shown in Fig. 5-12d.

### 5.5.2 Image Deconvolution

If the imaging resolution is much better than a lattice site, one only needs to identify the axes and spacings. In order to check the imaging resolution, we experimentally determine the point-spread function (PSF) by averaging isolated atoms in sparsely filled images. The measured PSF had a full-width half-max (FWHM) of 640 nm (Fig. 5-13), which is slightly larger than the lattice spacing of 541 nm. In order to resolve occupation for each lattice site, we therefore must perform some additional image processing. In previous bosonic microscopes, an algorithm that minimizes differences between a measured image and an image simulated with the measured PSF was used [9, 144]. We have opted for a simpler deconvolution algorithm that is computationally less intensive. Noting that convolution corresponds to multiplication in Fourier space, deconvolution can simply be carried out by division in Fourier space. The exact imaging processing procedure is described in the following.

We first subtract a “dark” frame, where atoms are removed but the Raman cool-

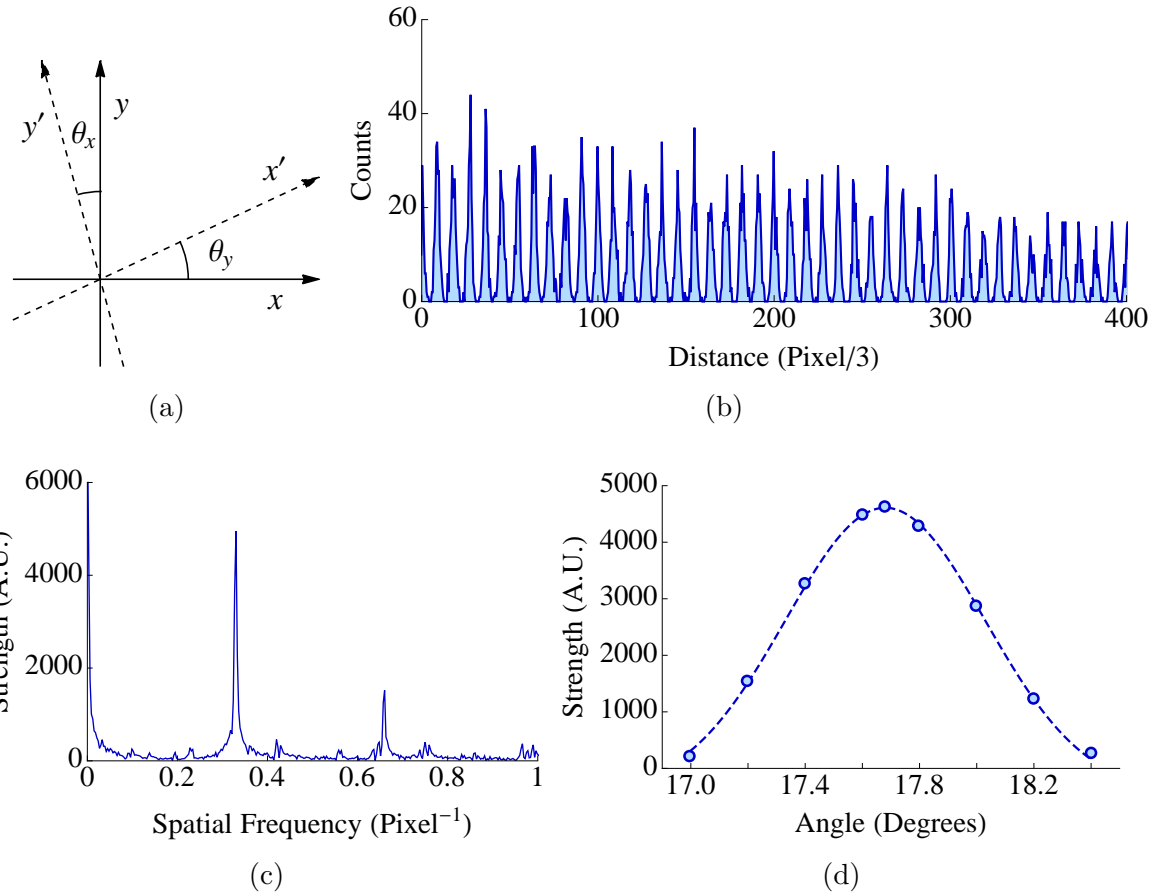


Figure 5-12: Identifying Lattice Axes and Spacings. (a) Diagram showing the coordinate transformation  $(x, y) \rightarrow (x', y')$  described in Section 5.5.1. (b) Histogram of differences in  $x'$  near the optimal angle  $\theta_y$ . (c) Magnitude of the Fourier transform of the difference histogram. The location of the main peak gives the spatial frequency hence the lattice spacing along this direction. (d) Height of the Fourier peak as a function of angle  $\theta_y$ . Shown in dashed is a Gaussian fit; the fitted center gives the optimal  $\theta_y$ .

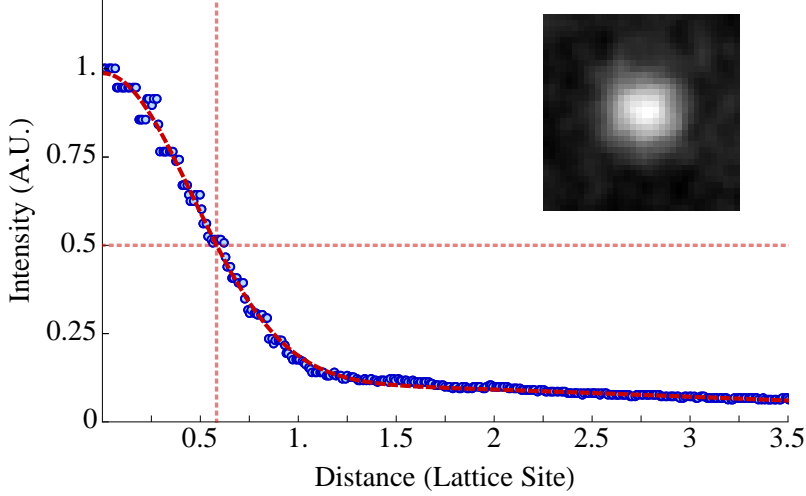


Figure 5-13: Measurement of the point-spread function (PSF). Radially averaged profile of the PSF shown in blue circles. A double Gaussian fit is shown by the red dashed line. The dotted lines indicate the location of the half-width-half-maximum; the corresponding FWHM is 640 nm. Shown in the inset is the PSF, obtained by averaging regions around isolated atoms.

ing beams are on. This is done in order to minimize the effect of optical pumping light scattered from the surface of the substrate. Since the dark frame only has long wavelength intensity modulations, we Fourier filter the dark frame before it is subtracted. The procedure for filtering as follows. From the dark frame  $D(\mathbf{x})$ , we obtain the Fourier transform  $\tilde{D}(\mathbf{q})$ .  $\tilde{D}(\mathbf{q})$  is multiplied by a filtering function  $g(\mathbf{q})$  before an inverse Fourier transform is applied. The filter function  $g(\mathbf{q})$  is given by

$$g(\mathbf{q}) = \frac{1}{1 + (|\mathbf{q}|/q_0)^2}, \quad (5.9)$$

where we pick  $q_0 = 0.0976(\Delta x)^{-1}$ , where  $\Delta x$  is the pixel size and is  $\approx 1/3$  of a lattice site. For these parameters, filtering mostly reduces the noise that is added when the images are re-sampled at a higher resolution.

The subtracted image  $I(\mathbf{x})$  is then deconvoluted by the following steps.

- 1) We Fourier transform the image to obtain  $\tilde{I}(\mathbf{q})$ .
- 2)  $\tilde{I}(\mathbf{q})$  is filtered with a Fermi-Dirac filter to obtain  $\tilde{I}_2(\mathbf{q}) = \tilde{I}(\mathbf{q}) * f(\mathbf{q})$  where  $f(\mathbf{q}) = 1/(\exp[(|\mathbf{q}| - q_0)/q_w] + 1)$ , where  $q_0 \approx 1.5/(\Delta x)$  and  $q_w \sim 0.1$ . Since  $q_0$  is

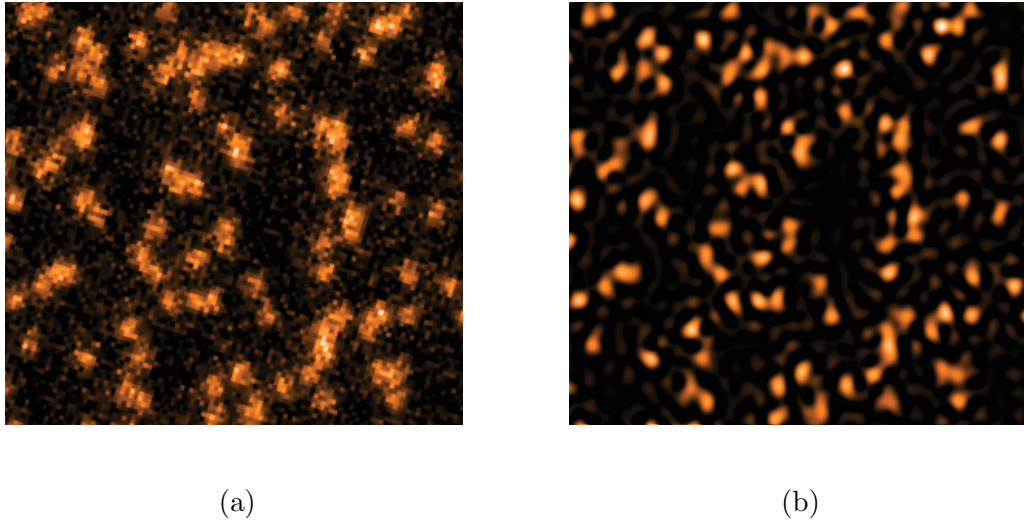


Figure 5-14: Image deconvolution. (a) Image with dark frame subtracted. (b) Subtracted image after deconvolution.

set to be many times the resolution limit of  $\approx 0.3/(\Delta x)$ , it mainly removes noise when the image is resampled by a factor of 3.

3)  $\tilde{P}(\mathbf{q})$  is obtained from the point-spread function  $P(\mathbf{x})$

4) A processed Fourier-transformed signal  $\tilde{I}_3(\mathbf{q})$  is obtained via

$$\tilde{I}_3(\mathbf{q}) = \tilde{I}_2(\mathbf{q}) \frac{\tilde{P}^*(\mathbf{q})}{\tilde{P}^*(\mathbf{q})\tilde{P}(\mathbf{q}) + \epsilon}. \quad (5.10)$$

The constant  $\epsilon$  is set to 0.01. The second factor is used instead of division by  $\tilde{P}(\mathbf{q})$ , since we have limited signal-to-noise. In the presence of noise, division by  $\tilde{P}(\mathbf{q})$  can lead to large amplitudes in regions where  $\tilde{P}(\mathbf{q})$  is small.

5) We reverse Fourier transform  $\tilde{I}_3(\mathbf{q})$  to obtain the deconvoluted image  $I_3(\mathbf{x})$ .

The deconvolution procedure above is also known as Weiner deconvolution in image processing. This is computationally simple since one only needs to perform Fourier transforms and simple algebraic manipulations. An example of deconvolution is shown in Fig. 5-14b.

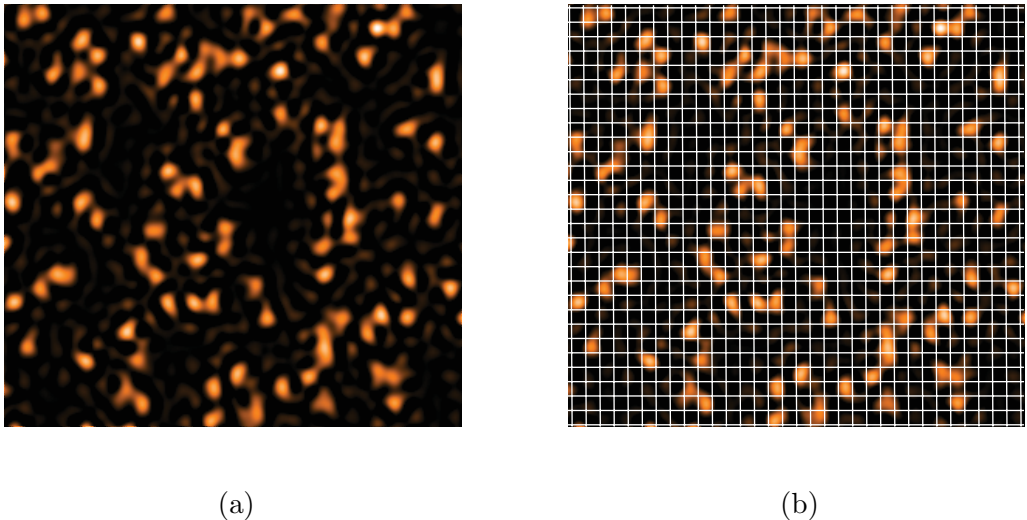


Figure 5-15: Identifying the phases of the lattices (a) Image after deconvolution. (c) Image after deconvolution overlaid with underlying lattice.

### 5.5.3 Identifying the Phases of the Lattices

After deconvolution, the next step is to identify the phase of the lattice along the two directions. We impose a lattice from the previously determined lattice spacings and angles, but vary the offset of each lattice site by  $\approx 1/3$  of a site. At each of the  $9 \times 9$  pairs of offsets, the deconvolved image is binned by the imposed lattice. The number of sites above a certain threshold is recorded. Next, we sum the map along either of the lattice axes, and repeat the resulting 9 points. We fit a sine to the resulting curve, which gives a rough estimate of the phase along each direction. The  $9 \times 9$  map is then shifted by the fitted phase. This roughly centers the maximum onto the center of the  $9 \times 9$  map. We then fit a 2D Gaussian to the map. The center of the Gaussian gives a precise determination of the phase. A deconvolved image overlaid with the lattice is shown in Fig. 5-15.

### 5.5.4 Identifying the Occupation of Lattice Sites

With the offsets of the lattices found, we bin the deconvolved image into each lattice site. A histogram of the counts per bin is then generated. As shown in Fig. 5-16a, the histogram shows a clear bimodal distribution, with one peak centered at zero

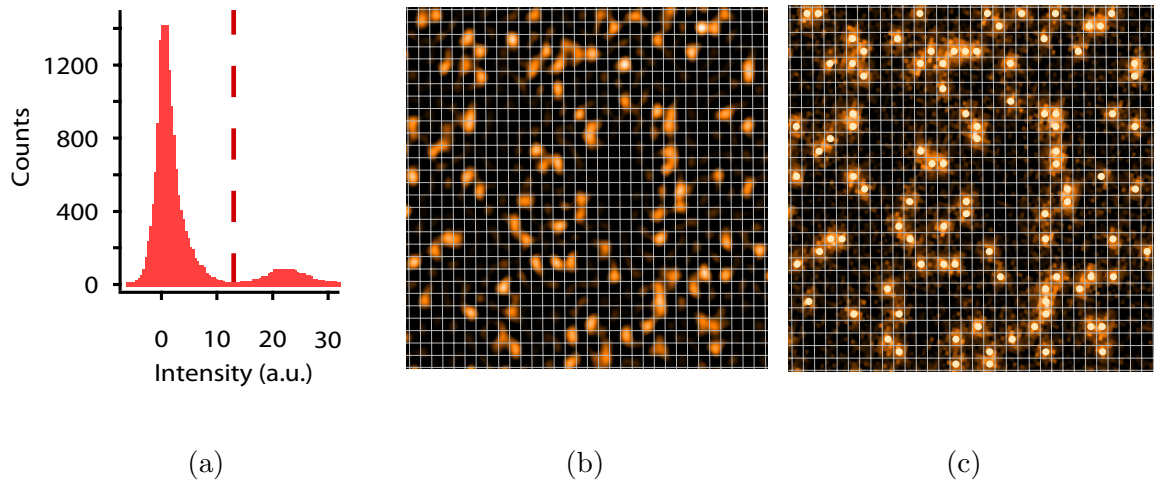


Figure 5-16: Identifying site occupation. (a) Histogram after binning the deconvoluted image into lattice sites. (b) Deconvoluted image overlaid with underlying lattice. (c) Original image overlaid with underlying lattice; sites identified as occupied are marked by circles. Figures reproduced from [22].

corresponding to empty sites, and a second peak corresponding to filled sites. A threshold is set at the minimum between the two peaks, and any site with counts exceeding the threshold is identified as occupied. From simulations with images with a realistic PSF and signal-to-noise, we find the the deconvolution algorithm identifies sites with  $> 99.9\%$  fidelity, for clouds with filling of  $\sim 0.20$ . An example of identifying the occupation of lattice site is shown in Fig. 5-16c.

### 5.5.5 Estimating Image Fidelity

To determine the overall imaging fidelity, we image the same sample multiple times in succession. We set the camera on frame transfer mode. In this mode, half of the pixels are kept in a dark region during each frame. After each frame, the exposed pixels are shifted to the dark region for read-out, while the initial pixels are cleared. This allows one to image in quick succession without waiting for the full read-out time, which is  $\sim 200$  ms when reading out the full imaging area of  $512 \times 512$  pixels.

For each frame, we identify the site occupation as described in Section 5.5.4. For two consecutive frames, if a site that is occupied in the first frame disappears, we

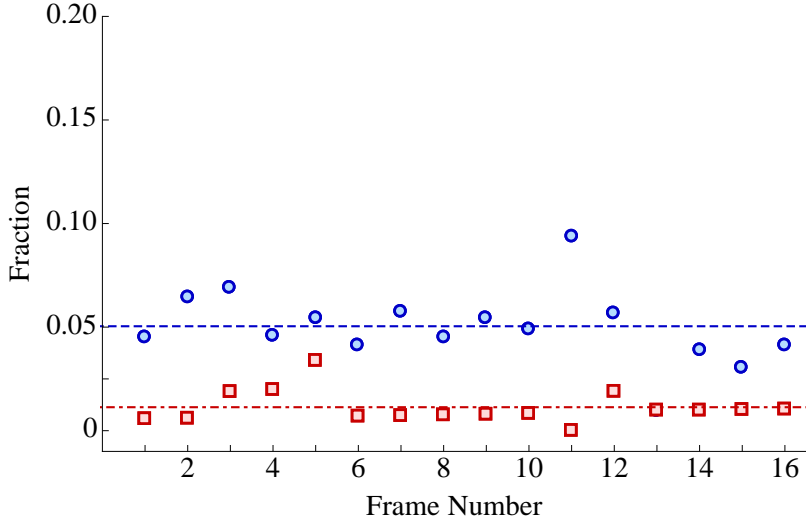


Figure 5-17: Loss rate and hopping rate during imaging. By imaging the same sample multiple times, we obtain loss and hopping fractions, shown in blue circles and red squares respectively. The corresponding averages are shown by blue dashed and red dot-dashed lines. Here, the duration of each frame is 1 second; the loss and hopping rates per second can be directly obtained. To disentangle parity-projected losses due to high fillings, the filling of the sample used to obtain loss and hopping rates is  $\approx 0.2$ . Figure adapted from [22].

identify this as a loss event. If an initially empty site becomes occupied, we identify this as a hopping event. After normalizing to the total number of atoms, we obtain loss and hopping rates. A typical loss rate and hopping rate curve is shown in Fig. 5-17. The net loss rate is the difference between the single site loss rate and the hopping rate. This rate is directly related to the lifetime determination in Section 5.4.3 measured using standard fluorescent imaging. While longer imaging times improve the signal-to-noise for each image, the loss and hopping rates rise proportionally to the imaging time. The optimal imaging time is a balance between reconstruction errors that arise from insufficient signal-to-noise and hopping and losses associated with long imaging times. The optimal image time that allows a fidelity of  $\sim 95\%$  is between 1 and 2 seconds. At these image times, the loss rate is  $\sim 5\%$ , while the hopping rates are  $\sim 1\%$ . Collisions with background gas is expected to account for  $1 - 2\%$  of the losses. An image after optimizing for imaging fidelity is shown in Fig. 5-18

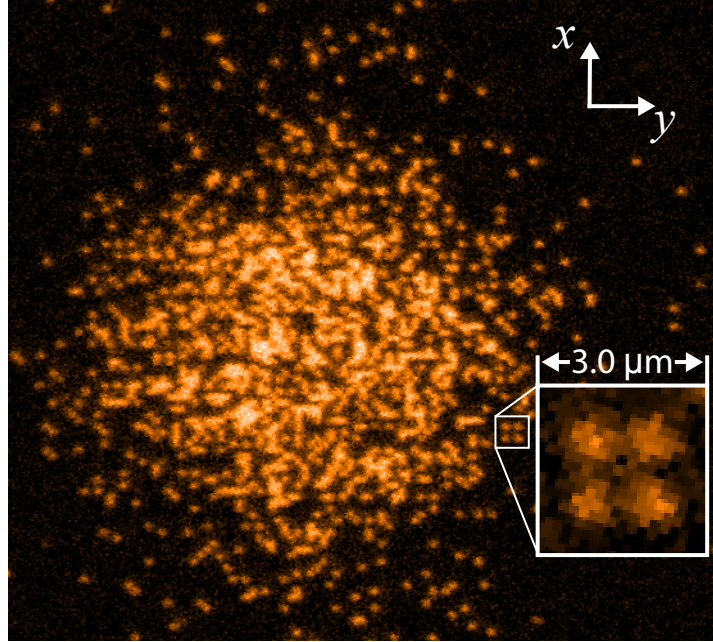


Figure 5-18: Single-Site image after optimization. The inset shows four atoms occupying corners of a  $3 \times 3$  region. Figure reproduced from [22].

### 5.5.6 Bounding Possibility of Density Dependent Losses

A possible imaging issue is density-dependent loss. It is possible that losses can be enhanced when atoms are on neighboring lattice sites. To estimate this effect, we measure the two-point correlation function,  $g^{(2)}(r)$ , as a function of separation distance  $r$ . The  $g^{(2)}$  is defined as

$$g^{(2)}(r) = \frac{\langle n(0)n(r) \rangle}{\langle n \rangle^2} \quad (5.11)$$

If the initial distribution is completely random, one expects  $g^{(2)}(r) = 1$ . This assumption is valid, if the system is at high enough temperatures where the effect of fermion statistics is irrelevant. This is the case for the samples used to characterize imaging.

On a lattice, the distance  $r$  in units of lattice spacing  $a$  is given by  $r = \sqrt{n_x^2 + n_y^2}$ , where  $n_i$  is the separation between two sites along direction  $i$ . On a digitized image, we compute  $g_2(r)$  with the following algorithm. First, we determine the average filling  $\langle n \rangle$ , simply by computing the fraction of filled sites. Next, for every occupied site, we

compute the distances to all other sites within the region of interest. These are added to a histogram  $h$ . For the sites that are filled, we add the distances to a histogram  $h'$ . These histograms can for example be binned with a separation of 1 lattice site. To compute the two-point correlation function, we simply divide each bin in  $h'$  by  $h$ , and normalize by  $\langle n \rangle$ . For dilute high temperature samples produced for optimizing single-site imaging, we find no detectable loss enhancement at short distances of  $\sim 1$  lattice spacing, as shown in Fig. 5-19. In fact, as discussed in Section 2.1.2, at low enough temperatures, where the thermal de Broglie wavelength is larger than the lattice spacing, anti-correlation should appear at short distances. Measurements showing anti-correlations for cold samples will be discussed in Chapter 6.

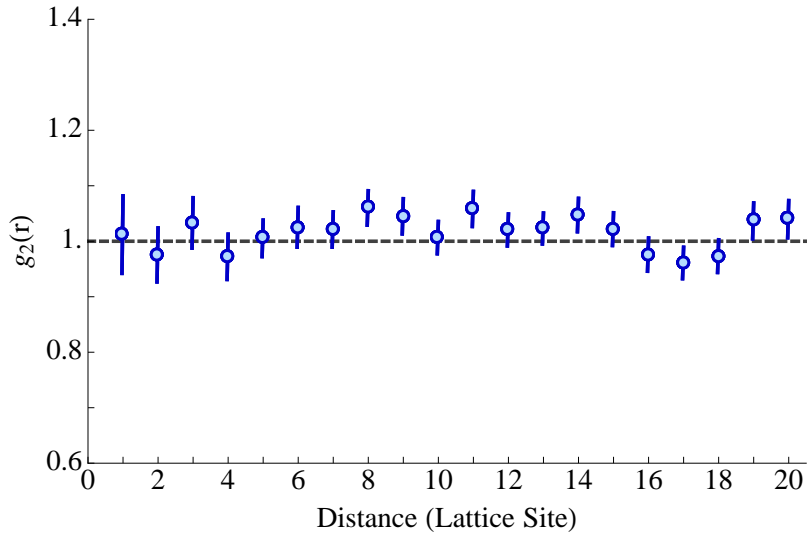


Figure 5-19: Bounding distance-dependent losses with  $g_2(r)$ . Shown in dashed is the uncorrelated value of  $g_2 = 1$ . At low temperatures, one expects that  $g_2(r) < 1$  at short distances, reflecting the Pauli exclusion principle. Correlation measurements showing this Pauli blocking effect is discussed in Chapter 6. Figure adapted from [22].

### 5.5.7 Estimating Raman Cooling Performance

To estimate the performance of our Raman cooling scheme, we infer the ground state population via sideband spectroscopy. We first image the atoms for 3 seconds, and leave the optical pumping light on for  $100\mu\text{s}$  to ensure a large fraction of atoms are in the dark state  $|9/2, -9/2\rangle$ . Subsequently, the  $x$  and  $z$  lattices are lowered to

depths where all sidebands are well-separated. We then apply a 2 ms pulse of Raman light, where the two-photon frequency is swept over 10 kHz. This is followed by a resonant light pulse on the  $|F = 9/2, m_F = -9/2\rangle \rightarrow |F' = 11/2, m'_F = -11/2\rangle$  that removes  $F = 9/2$  atoms. The lattices are then reramped to the imaging depth to image the remaining atoms. Since the Landau-Zener sweeps with the Raman beams are adiabatic, the ratio of the heights of the cooling and the heating sidebands of each axis directly give the fraction of atoms in the motional ground state of that axis (see Fig. 5-20). The product of the ground state fraction of all three axes gives the fraction in the absolute motional ground state. We find that even after imaging, we can achieve a motional ground state population of 72(3)% for  $|9/2, -9/2\rangle$  atoms. Note that the Raman cooling parameters were optimized for imaging fidelity rather than ground state fraction.

The fact that a high ground state population fraction remains even after measurement opens up new possibilities of initializing a many-body system. For example, combining single-site imaging with site-resolved manipulation, one can perform “Maxwell’s demon” type experiments, where the positions of the atoms are rearranged after measurement [143]. Low entropy states and highly out-of-equilibrium states can thus be prepared atom by atom.

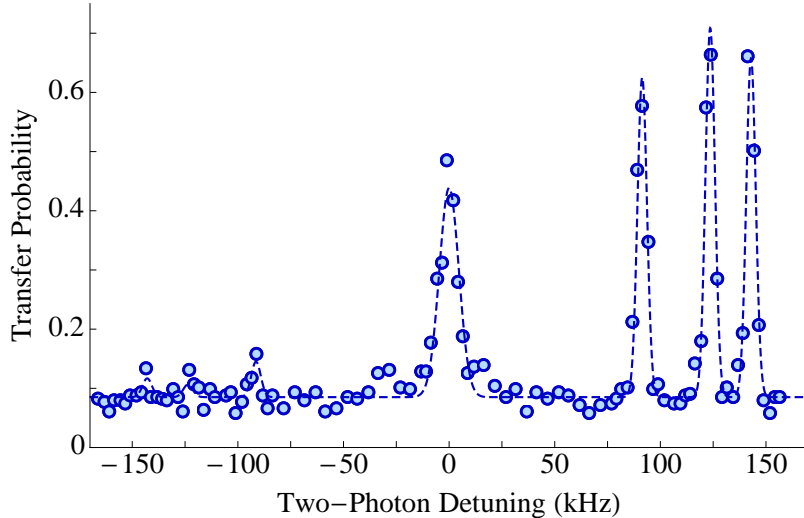


Figure 5-20: Sideband spectra after cooling. The sideband asymmetry indicates a ground state population in  $|9/2, -9/2\rangle$  of 72(3)%, even after imaging. Figure adapted from [22].



# Chapter 6

## Quantum Gas Microscopy of Metals and Insulators

This chapter describes our research on metals, Mott insulators, and band insulators in the Fermi-Hubbard model. The results are summarized in the following publications:

*L. W. Cheuk, M. A. Nichols, K. R. Lawrence, M. Okan, H. Zhang, and M. W. Zwierlein, “Observation of 2D Fermionic Mott Insulators of  $^{40}\text{K}$  with Single-Site Resolution,” *Phys. Rev. Lett.* **114**, 193001 (2016) [21]. Included in Appendix G.*

*L. W. Cheuk, M. A. Nichols, K. R. Lawrence, M. Okan, H. Zhang, E. Khatami, N. Triuedi, T. Paiva, M. Rigol, and M. W. Zwierlein, “Observation of Spatial Charge and Spin Correlations in the 2D Fermi-Hubbard Model,” *Science* **353**, 1260 (2016) [20]. Included in Appendix H.*

In this chapter, we first describe how quantum degenerate gases are produced near the substrate, which allows preparation of Mott and band insulators in our apparatus. We then discuss how to perform thermometry using site-resolved density profiles. We also describe a recent experiment where we utilized the site-resolving ability of the microscope to explore spatial correlations in the Hubbard model. By extending our imaging technique to also resolve the spin of the atoms, we were able to measure correlations in both the spin and charge sectors, which have revealed short-range anti

ferromagnetism, the interaction and Pauli holes, and competition between doublon-holon bunching and Pauli blocking.

## 6.1 Producing Quantum Degenerate Gases Near the Substrate

In Chapter 5, we described how to image fermionic  $^{40}\text{K}$  with single-site resolution with high fidelity. We would like to apply this new ability to study interesting many-body states such as Mott insulators, which occur only when the entropy of the system is sufficiently low. In order to produce such low entropy samples, several additional steps had to be taken. For the atomic samples used to implement single-site imaging, we relied on a magnetic transport scheme described in Section 5.4.1. Atoms were transported magnetically to the substrate and trapped by quickly ramping up the 5-degree beam. This process produced a large amount of heating since it was highly non-adiabatic. In fact, the loading of the 5-degree trap was irreversible; atoms did not survive a time-reversed ramp. The non-adiabatic nature of this scheme was unavoidable since the cloud in the magnetic trap was much larger than the  $\sim 5\text{ }\mu\text{m}$  spacing of the vertical lattice formed by the 5-degree beam. If the 5-degree beam was not ramped up sufficiently quickly, atoms were lost due to contact with the substrate. We briefly explore using a higher magnetic gradient to reduce the cloud size. However, due to geometric constraints, the magnetic trap was not plugged during magnetic transport, which led to short lifetimes due to Majorana losses. The optimal gradient that we found yielded lifetimes of 200 ms, sufficient for a transport time of 50 ms.

### 6.1.1 Moving the Magnetic Trap

In order to transfer more adiabatically into the 5-degree beam, three additional trapping beams are used: a pair of movable ODT beams along  $-\hat{x}$  and  $\hat{y}$ , and an accordion beam. These have been described in Chapter 4. Due to the limited range of move-

ment of the ODT beams, the transport distance had to be minimized. We thus moved the plugged quadrupole trap closer to the surface. We were, however, limited in how far the trap could be moved up. First, one cannot move closer than the initial cloud size prior to evaporation in the magnetic trap, which is on the order of  $\sim 1$  mm, as found experimentally (see Fig. 6-1). The other constraint is the in-vacuum antenna, shown in Fig. 4-2. The top portion of the in-vacuum antenna, formed by two square loops oriented normal to  $\hat{y}$ , is inconveniently located  $\sim 2$  mm below the substrate. Thus, without changing the axis of the optical plug, the center of the magnetic trap could only be moved to  $\sim 2$  mm below the substrate.

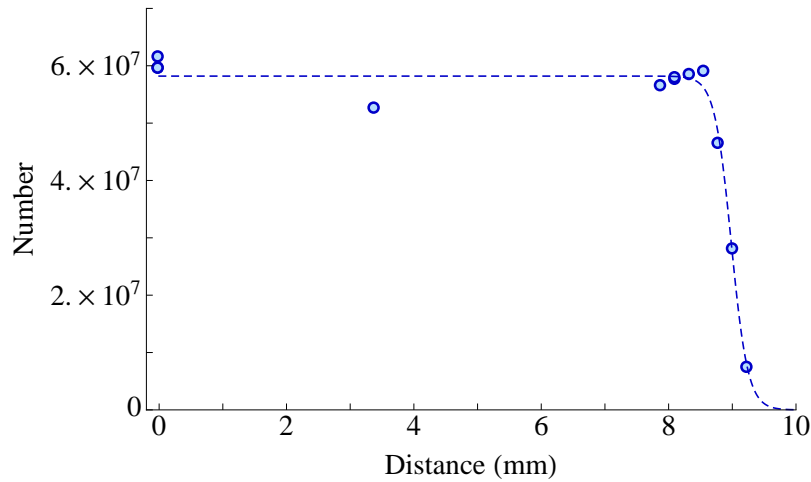


Figure 6-1: Atom number versus magnetic trap position. The magnetic trap position is measured from the vertical center of the chamber.  $^{23}\text{Na}$  atoms are initially held at the vertical center of the chamber. The magnetic trap is moved upwards in 300 ms, held for 350 ms, and moved back in 300 ms for imaging.

In order to move the quadrupole magnetic trap to  $\sim 2$  mm below the substrate, we apply current in the Feshbach coils to shift the magnetic zero. In this configuration, the trap position is no longer determined by geometry alone. Relative noise between the current producing the magnetic gradient and the current producing the offset field causes the trap position to fluctuate in time, which results in heating. Initially, only the Feshbach current was stabilized via feedback. The current for the quadrupole coils was supplied by a Lambda ES-30-500 power supply on current control, without additional stabilization. This current had 60 Hz harmonics that could have amplitudes

as large as  $10^{-2}$ . As a result, rapid heating of the atoms was observed. In fact, the movement of the trap center due to current noise was directly measurable, as shown in Fig. 6-2. To reduce the heating, the current of the quadrupole coils was also stabilized with feedback. Although residual heating due to trap movement was still observable after stabilization, the heating rate was reduced to a tolerable level of  $280\text{ nK/s}$ , as shown in Fig. 6-3.

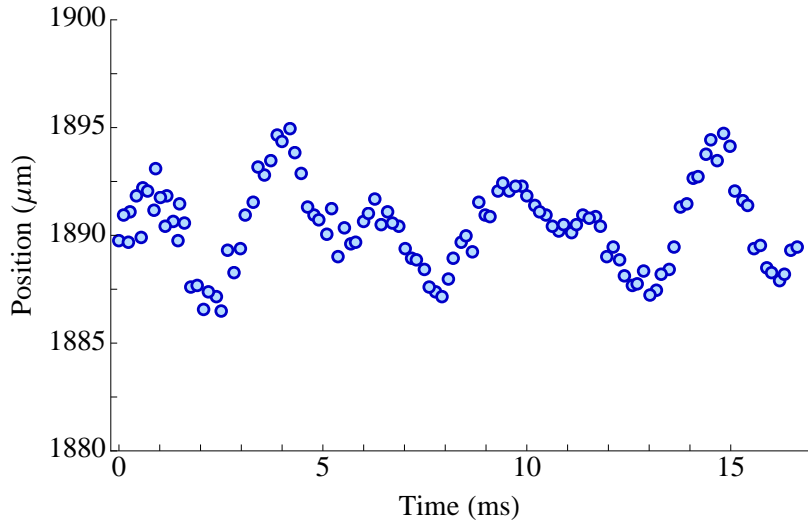


Figure 6-2: Trap position of offset quadrupole magnetic trap measured by in-situ imaging of  $^{23}\text{Na}$  atoms. Here, the current producing the offset field was stabilized, but the current producing the quadrupole magnetic field was not. The timing was triggered to the AC line voltage. Motion of the atoms at 60 Hz harmonics with amplitude of  $\sim 5\text{ }\mu\text{m}$  were observed.

Moving the magnetic trap, however, meant that the optical plug also had to be moved upwards from the vertical center of the chamber by 7.5 mm. Here, it was important to align the plug such that it did not hit the in-vacuum antenna (see Fig. 4-2). In fact, the vacuum pressure rose rapidly when the antenna was hit by the plug beam.

### 6.1.2 A New Transport Scheme

After the magnetic trap was moved to  $\sim 2\text{ mm}$  below the substrate, the next step was to transport the atoms to  $7\text{ }\mu\text{m}$  below the substrate. In order to only load the desired layer of the 5-degree beam, one must compress the cloud to a vertical size of less than

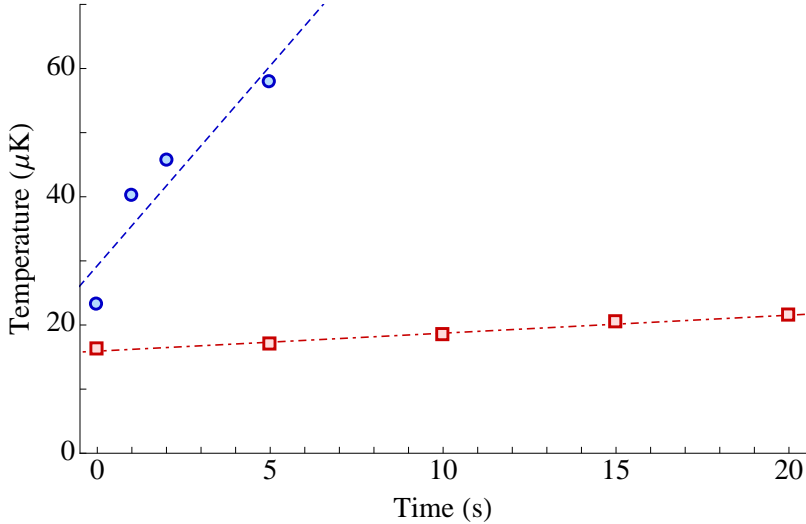


Figure 6-3: Heating rate in offset quadrupole magnetic trap measured via time-of-flight imaging of  $^{23}\text{Na}$  atoms. Shown in red squares is the temperature as a function of wait time, when the currents producing the offset magnetic field and the magnetic gradient were both stabilized. The dashed red line is a linear fit to the data, which gives a heating rate of  $280 \text{ nK/s}$ . Shown in blue circles is the case when a ground loop was intentionally introduced. The dashed blue line is a linear fit to the data, which gives a heating rate of  $6.2 \mu\text{K/s}$ .

the vertical spacing of the layers ( $5 \mu\text{m}$ ) before loading. Because of this small length scale, optical transport is the only viable transport scheme. In our apparatus, optical transport is non-trivial, since any beam that passes close to the substrate will be partially reflected, which would interfere with the incoming beam to form a vertical lattice that inhibits further transport.

In light of these issues, we implemented a two-stage optical transport scheme. The first stage transports atoms from  $\sim 2 \text{ mm}$  below the substrate to  $40 \mu\text{m}$  below the substrate. We load atoms from the magnetic trap into the movable crossed dipole trap formed by two beams along  $-\hat{x}$  and  $\hat{y}$ , as described in Section 4.5.3. Since these two beams have vertical waists of  $40 \mu\text{m}$ , they can be moved to  $\sim 40 \mu\text{m}$  below the substrate before the vertical lattices resulting from the substrate reflections become significant.

As described in Section 4.5.3, the positions of the two ODT beams are controlled by two AODs, whose frequencies can be dynamically changed. When the frequencies are changed, the angles of the beams relative to the  $x$ - $y$  plane remain constant, while

the intersection of the beam with the vertical imaging axis can be tuned from  $\tilde{2}$  mm below the substrate to directly on the surface. Ideally, one would like to use a shallow beam angle in order to maximize the lattice spacing of the vertical lattice formed by the substrate reflection. For the  $x$  beam, the angle of  $1.3^\circ$  was chosen with this in mind. However, along  $\hat{y}$ , such an angle is not possible due to limited optical access. As shown in Fig. 4-2, the in-vacuum antenna prevents shallow angles from being accessible. To avoid hitting the antenna at any point during the transport, the angle of the  $y$  ODT beam is set to  $4.8^\circ$ . Although this is sub-optimal, simulations show that with the appropriate intensity ramps, the transport remains efficient. Although the  $y$  ODT beam does not directly hit the antenna, at high beam powers, we observed a measurable increase of the vacuum pressure at certain points of the transport. We thus limited the power of the  $y$  ODT beam during transport.

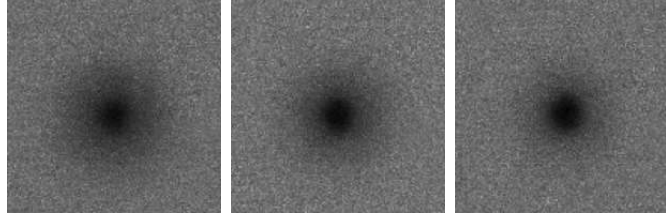


Figure 6-4: <sup>23</sup>Na condensates in the crossed ODT before optical transport. Shown are TOF images of <sup>23</sup>Na atoms in the crossed ODT, imaged along the  $-\hat{y}$  imaging path. The bimodal distribution indicates the presence of a condensate. From left to right, the final trap depth is successively lowered, leading to increasing condensate fractions.

In order to optimize the first stage of optical transport, we used a condensate of <sup>23</sup>Na atoms. <sup>23</sup>Na in  $|2, 2\rangle$  was first evaporated in the offset quadrupole magnetic trap. After the atoms are loaded into the crossed optical dipole trap, a microwave sweep transferred the atoms to  $|1, 1\rangle$ . The ODT depth was then lowered to produce a <sup>23</sup>Na condensate, as shown in Fig. 6-4. Subsequently, the AOD frequencies were ramped linearly in time, and the endpoints for various ramp times were optimized for condensate numbers. While losses during transport were observed, condensates can be moved to  $40\ \mu\text{m}$  below the surface. Optimizing for the final number of condensed <sup>23</sup>Na atoms resulted in a transport time of 1800 ms. Due to the presence of the antenna,

we could only image up to  $\sim 1.7$  mm below the substrate with the  $-\hat{y}$  imaging beam, or up to  $\sim 0.5$  mm below the substrate using the bouncing imaging along  $-\hat{y}$ . As a result, we could not directly image the region from  $\sim 0.5$  mm to  $\sim 1.7$  mm below the surface. Nevertheless, by using the fact that the condensate drops due to gravity, for longer expansion times, atoms could be observed as they drop into view below  $\sim 1.7$  mm, even when they were moved up to  $160\ \mu\text{m}$  from the substrate (Fig. 6-5c).

In order to move the atoms closer than  $40\ \mu\text{m}$  from the surface, we implemented a second stage of optical transport with the accordion beam. The accordion beam is aligned to reflect from the center of the substrate, and its incident angle can be dynamically tuned with a galvo mirror. As described in Section 4.5.2, this beam propagates along  $-\hat{x}$ , and its angle relative to the  $x$ - $y$  plane is tuned from  $1.2^\circ$  to  $5.2^\circ$ . At  $\sim 1.2^\circ$ , the second layer of the vertical lattice formed by the accordion beam occurs at  $\sim 40\ \mu\text{m}$ , while at  $\sim 5.2^\circ$ , the second layer is moved up to  $\sim 8\ \mu\text{m}$ , and sufficiently overlapped with the second layer of the 5-degree beam. At the initial angle, the lattice spacing is large, allowing a large fraction of the atoms to be loaded into a single layer. By adiabatically increasing the accordion angle, the atoms are simultaneously compressed vertically, and moved upwards to substrate. One issue with this transport scheme is that the accordion beam provides little confinement along  $\hat{x}$ . Thus, during the accordion transport, the  $y$  ODT beam is kept on at low powers. Although this produces a competing vertical lattice, simulations show that for a range of intensities, transport is not inhibited and remains efficient. With some optimization, we were able to produce condensates in the accordion, as shown in Fig. 6-6.

After the final stage of optical transport with the accordion, we transfer the atoms into the 5-degree beam. After optimization, we were able to obtain  $^{23}\text{Na}$  condensates in the 5-degree beam, as shown in Fig. 6-7. To confirm that atoms have been transferred to the right layer of the 5-degree beam, we switched from  $^{23}\text{Na}$  to  $^{40}\text{K}$ . Using the same transport scheme,  $^{40}\text{K}$  atoms were loaded into the 5-degree beam, and “slicing” spectroscopy was performed. By comparing the slicing response with the previously measured slicing frequency of the second layer, we were able to verify that only the

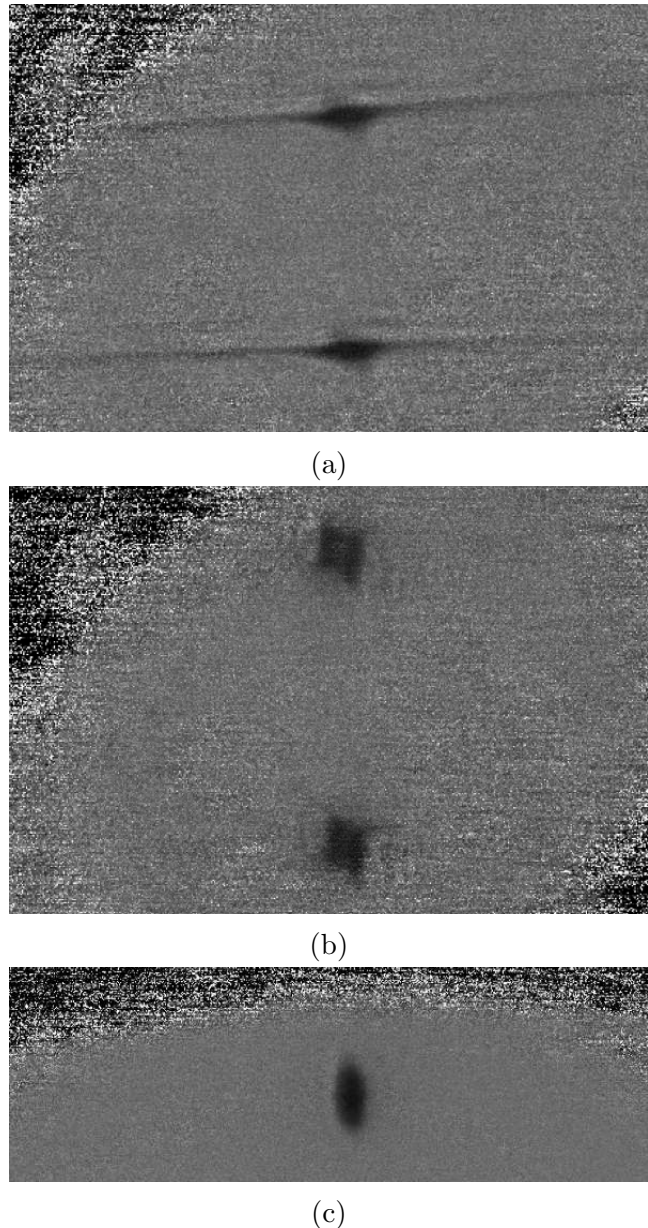


Figure 6-5:  $^{23}\text{Na}$  condensate after transport with the crossed ODT to  $160\ \mu\text{m}$  below substrate. (a) In-situ image of the condensate imaged along the  $-\hat{y}$  bouncing imaging path. (b) Image of the condensate along the  $\hat{y}$  “bouncing” imaging path after 4.5 ms time-of-flight. (c) Condensate falling into view of the  $-\hat{y}$  imaging path after 17.5 ms of TOF. The top edge of the field-of-view is limited by the in-vacuum antenna.

second layer was loaded, as shown in Fig. 6-8.

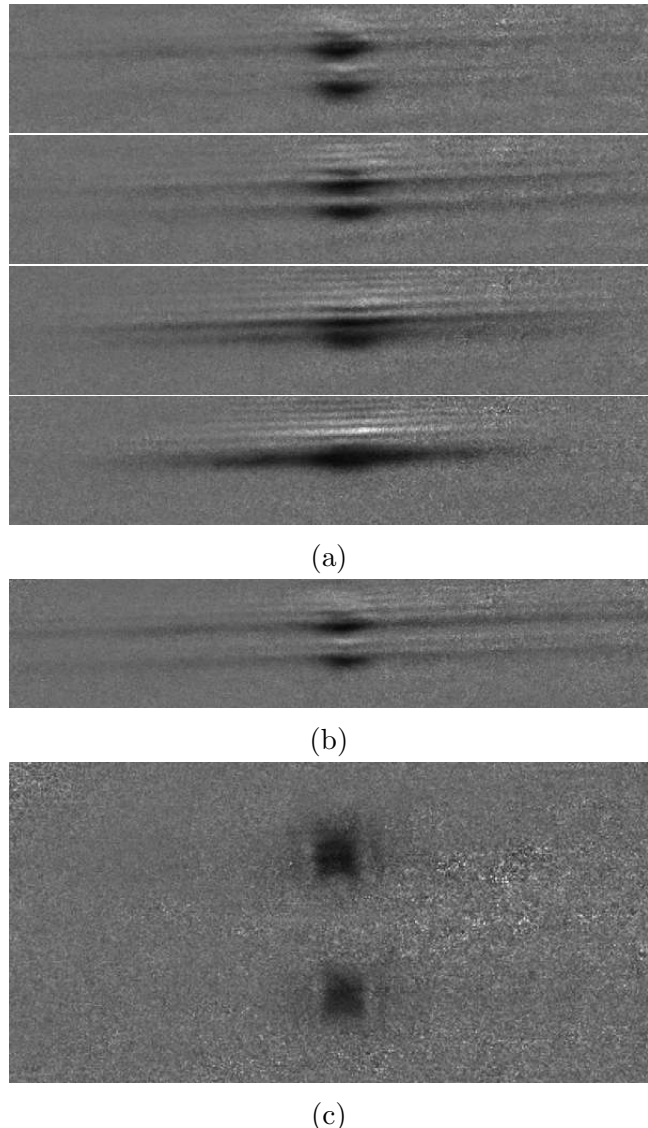


Figure 6-6: Transport using the accordion beam. The  $^{23}\text{Na}$  atoms were first loaded into the second antinode of the vertical lattice formed by the accordion beam. We set the angle of the accordion beam such that the second anti-node is positioned  $40\text{ }\mu\text{m}$  below the substrate. Atoms are then imaged along the  $-\hat{y}$  bouncing imaging axis, which produces two mirror images due to the reflection from the substrate. The midpoint between the two mirror images corresponds to the surface of the substrate. (a) The angle of the galvo mirror is ramped to different values corresponding to different distances below the substrate. From top to bottom, the locations of the atoms are  $40\text{ }\mu\text{m}$ ,  $26\text{ }\mu\text{m}$ ,  $16\text{ }\mu\text{m}$ , and  $7.3\text{ }\mu\text{m}$  from the substrate respectively. (b) After ramping to  $7.3\text{ }\mu\text{m}$ , the galvo mirror angle is unramped to the initial position, where the second anti-node is  $40\text{ }\mu\text{m}$  away. (c) Shown is a TOF image of atoms forming a condensate after being transported to  $7\text{ }\mu\text{m}$  below the surface and subsequently back to their initial location  $40\text{ }\mu\text{m}$  below the substrate in 400 ms.

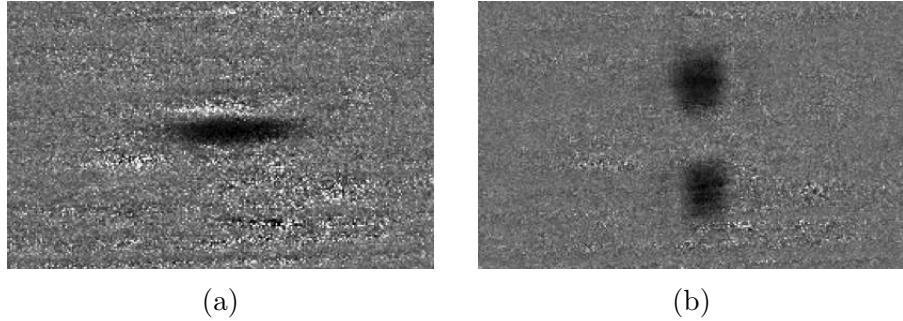


Figure 6-7:  $^{23}\text{Na}$  condensate in 5-degree beam after optical transport. After the atoms are compressed and moved upwards to  $\sim 7\text{ }\mu\text{m}$  from the surface, they are transferred into the 5-degree beam. (a) In-situ image of  $^{23}\text{Na}$  atoms loaded into the second layer of the 5-degree beam,  $7\text{ }\mu\text{m}$  from the substrate. The imaging path here is the  $y$  bouncing imaging path. Along this path, the imaging resolution is not high enough to resolve the two mirror images, when the atoms are closer than  $\sim 10\mu\text{m}$  from the surface. (b) After 4.5 ms of TOF, a bimodal distribution is observed, indicating the presence of a condensate after the entire optical transport process.

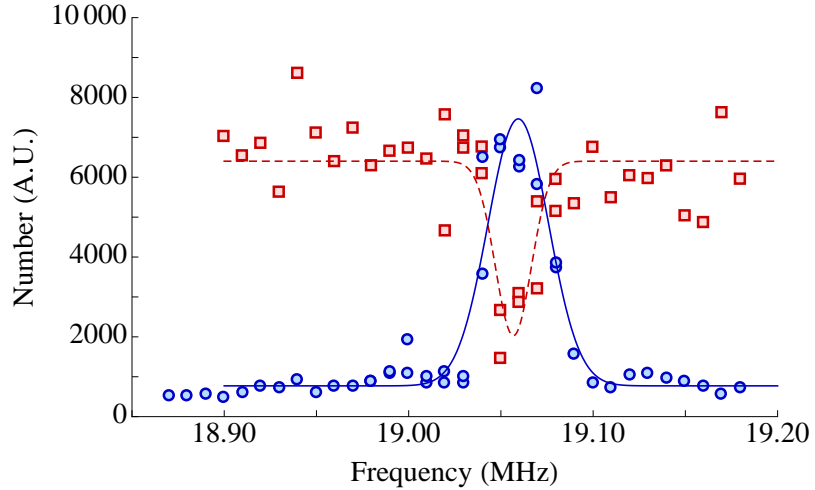


Figure 6-8: Slicing spectrum in 5-degree beam after loading  $^{40}\text{K}$  from the accordion beam. Shown in red squares is a slicing spectrum of  $^{40}\text{K}$  after transfer into the 5-degree beam. A microwave sweep transfers atoms into  $F = 7/2$ , which are subsequently lost due to collisions with remaining  $F = 9/2$  atoms. Shown in blue circles is a slicing spectrum obtained with magnetic transport and direct transfer into the 5-degree beam, after the second layer has been selected. Atoms are predominantly transferred from the the accordion to the second layer of the 5-degree beam.

### 6.1.3 Evaporation of a Single Layer

Although we could transport  $^{23}\text{Na}$  BECs at  $7\text{ }\mu\text{m}$ , creating a gas quantum degenerate fermions proved more difficult. Since the transport process causes heating, we decided

to only partially cool  ${}^{40}\text{K}$  before the ODT transport. Further evaporation is performed after the atoms are moved near the substrate, which recools the atoms after they are heated during transport. A final stage of evaporation is also needed in order to reach appropriate system sizes of  $\sim 1000$  atoms. A transport sequence similar to that used for  ${}^{23}\text{Na}$  allows  $\sim 10^5$  atoms to be transferred into a single layer of the accordion and moved to  $7\ \mu\text{m}$  below the substrate. At the end of the two-stage optical transport, the atoms are held vertically by the accordion beam and transversely by both the  $y$  ODT beam and the dimple beam, which was described in Section 4.5.4. At this point, an initial stage of evaporation is performed by lowering the power of the accordion beam. The powers of the accordion beam and the  $y$  ODT beam are subsequently ramped down, while the 5-degree beam is ramped up. At this point, the atoms are confined in all directions by the 5-degree beam, which has sufficient trapping along  $\hat{x}$ , the direction of propagation. Although the 5-degree beam is sufficient to trap the atoms on its own, evaporation in this beam is not efficient due to the low confinement along the propagation direction. We thus evaporate in a trap formed by a combination of the 5-degree beam and the dimple beam.

One important aspect of evaporation is that atoms must be able to leave the trap. For a 2D layer, it is easiest for atoms to escape radially in the  $x$ - $y$  plane, as the vertical direction is tightly confining. We thus chose to apply a magnetic gradient in the  $x$ - $y$  plane. This is done by applying current in the bias field coil along  $\hat{x}$ , which also produces a magnetic field gradient along  $\hat{x}$  in addition to a bias field. By lowering the powers of the dimple and the 5-degree beams simultaneously, we were able to produce quantum degenerate samples of 2-component Fermi gases.

## 6.2 Site-resolved Profiles of Metals and Insulators

With the new transport scheme and evaporation in the dimple trap, we were able to produce low entropy samples for quantum gas microscopy. In order to access the different states of the Fermi-Hubbard model, one needs to tune both the interaction parameter  $U/t$  and the chemical potential  $\mu$ . As discussed in Section 2.2.1, Feshbach

resonances can be used to tune the *s*-wave scattering length  $a$ , and consequently the interaction energy  $U$ . Alternatively, one can increase the relative effect of interactions by reducing the tunneling amplitude  $t$ , which can be suppressed by increasing the lattice depth. In principle, the lattice depth also tunes the interaction parameter  $U$  due to modification of the Wannier functions. The main effect of changing the lattice depth, however, is in changing  $t$ , which can be varied over many orders of magnitude. For the studies described here, the parameter  $U/t$  was tuned using the lattice depth.

In order to tune the chemical potential, we make use of the fact that the system is trapped. Under the local density approximation, this leads to a spatially varying local chemical potential through the sample, with the trap center attaining the highest local  $\mu$ . Thus, low values of  $\mu$  can always be reached at the edges of the trap. To tune the maximum value of  $\mu$  at the center of the trap, we use the dimple beam to vary the radial confinement. By increasing the power of the dimple beam, the radial confinement is increased, and a higher maximum chemical potential can be reached.

As described in Section 2.3.2, the three prototypical states in the Fermi-Hubbard model are the metal, the band insulator, and the Mott insulator. The latter two have signatures that are particularly suited for site-resolved detection with a microscope. In a band insulator, the occupation of each lattice site is exactly two, while in a Mott insulator, it approaches unity in the limit of large  $U/t$ , as doublons become energetically forbidden. These two insulating states are realized with different parameters. The band insulator occurs when the chemical potential is higher than any energy scale ( $\mu \gg U, t, T$ ), but still smaller than the bandgap, in order to remain in the single-band limit. The Mott insulator on the other hand is reached when the interaction energy  $U$  becomes much larger than all energy scales except the bandgap,  $U \gg t, T$ , and the system is at half-filling. Experimentally, one can observe band insulators in the center of the trap at high radial confinements, and moderate values  $U/t$ . To access the Mott insulator, one again needs a relatively large radial confinement in order to obtain a chemical potential corresponding to half-filling. Additionally, in order to suppress doublons, it is beneficial to use a high value of  $U/t$ , which can be achieved experimentally at deeper lattice depths ( $\tilde{V}_0 > 8$ ). Outside of these two regimes, one

generically observes a metallic state.

By tuning the lattice depth along with the intensity of the dimple beam, we were able to observe metals, band insulators and Mott insulators with single-site resolution through the microscope, as shown in Fig. 6-9. Using the deconvolution algorithm described in Section 5.5, we can identify the occupation of each lattice site, which we then use to generate site-resolved profiles, as shown in Fig. 6-9. From these profiles, one finds that when the interactions are strong ( $U \gg t$ ), double occupancies are suppressed, and when the global chemical potential is sufficiently high, a large portion of the system contains exactly one atom per site, as one would expect for a Mott insulator. When the global chemical potential is raised by increasing the radial confinement, the imaged profiles show a dark central region. This is consistent with the formation of a band-insulating region in the center of the trap, which contains doubly occupied sites. These sites appear dark since our imaging suffers from parity-projection. When two atoms reside in a single lattice well, they are both lost quickly due to light-assisted collisions during imaging. In other words, the measured signal reveals only the parity of the site occupation.

Before we describe how we quantitatively characterize the site-resolved profiles, we describe a few properties of this parity-projected signal. As we will show, the parity-projected signal for spin-1/2 fermions is in fact the magnitude squared of the local magnetic moment on a site. This originates from the fact that for a spin-1/2 system, one can have at most two atoms on a single site, due to the Pauli exclusion principle. Note that this is not true even for a single-component Bose gas, since the occupation of a site is unbounded.

### 6.2.1 The Local Moment and Its Properties

To understand why the parity-projected signal directly measures the magnitude of the local magnetic moment, we first observe that for spin-1/2 fermions, the parity-projected density can be described by the operator

$$\hat{n}_i - 2\hat{d}_i, \quad (6.1)$$

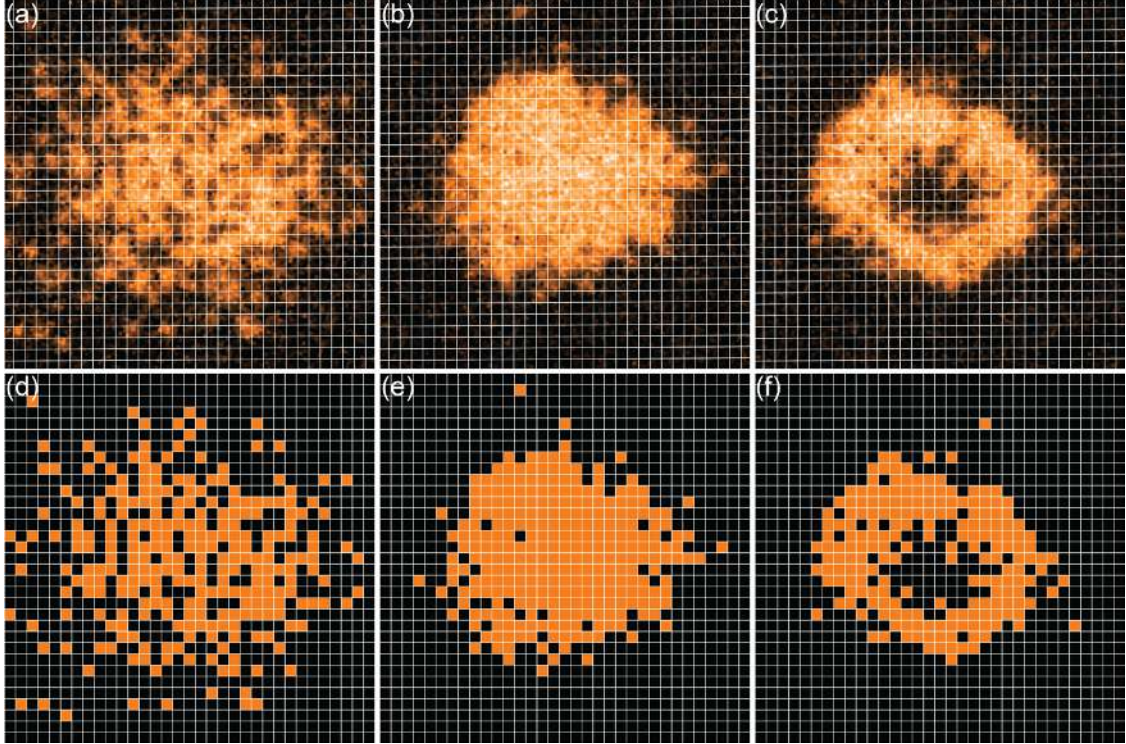


Figure 6-9: Site-resolved images of metals and insulators. Shown in (a), (b) and (c) are site-resolved images of  $^{40}\text{K}$  atoms trapped in a 2D square lattice. (d), (e) and (f) are the corresponding reconstructed site occupations. In (a,d),  $U/8t = 0.33$ ,  $\mu_0/U = 0.52$ , and  $k_B T/U = 1.46$ . A metallic state is observed. In (b,e),  $U/8t = 12.3$ ,  $\mu_0/U = 0.46$ , and  $k_B T/U = 0.09$ . A Mott insulator is observed. In (c,f),  $U/8t = 2.6$ ,  $\mu_0/U = 1.43$ , and  $k_B T/U = 0.18$ . A band insulating region is observed in the center of the trap. Here,  $\mu_0$  denotes the chemical potential in the center of the trap. Temperatures and chemical potentials are obtained from fits of the radially averaged profiles to NLCE data for the metallic and band-insulating cases, and from a fit to HTSE data for the Mott-insulating case. Figures reproduced from [21].

where  $\hat{n}_i = \hat{n}_{\uparrow,i} + \hat{n}_{\downarrow,i}$ , and  $\hat{d}_i = \hat{n}_{\uparrow,i}\hat{n}_{\downarrow,i}$ . Since  $(\hat{n}_{\sigma,i})^2 = \hat{n}_{\sigma,i}$  for fermions, we can rewrite this as

$$\hat{n}_{\uparrow,i} + \hat{n}_{\downarrow,i} - 2\hat{d}_i = (\hat{n}_{\uparrow,i} - \hat{n}_{\downarrow,i})^2 = \hat{m}_{z,i}^2. \quad (6.2)$$

where  $\hat{m}_{z,i}^2$  is the magnitude squared of the local magnetic moment, also known as the local moment.

When there are well-formed local moments, one can approximately describe the system with an effective spin model. For example, in the Fermi-Hubbard model, magnetic moments are well-formed when  $U \gg 8t$ . In this limit, the charge degree of

freedom is frozen, and one can describe the spin degrees of freedom by the Heisenberg model. To quantify whether or not local magnetic moments are well-formed, one can examine the quantity

$$\langle \hat{m}_{z,i}^2, \hat{m}_{z,i}^2 \rangle_C = \langle \hat{m}_{z,i}^4 \rangle - \langle \hat{m}_{z,i}^2 \rangle^2, \quad (6.3)$$

which measures the quantum projection noise of the observable  $\hat{m}_{z,i}^2$ . The operator  $\langle \hat{m}_{z,i}^4 \rangle$  can be written as

$$\begin{aligned} \hat{m}_{z,i}^4 &= \left( \hat{n}_{\uparrow,i} + \hat{n}_{\downarrow,i} - 2\hat{d}_i \right)^2 \\ &= \hat{n}_{\uparrow,i}^2 + \hat{n}_{\downarrow,i}^2 + 4\hat{d}_i^2 + 2\hat{n}_{\uparrow,i}\hat{n}_{\downarrow,i} - 4\hat{d}_i\hat{n}_{\uparrow,i} - 4\hat{d}_i\hat{n}_{\downarrow,i} \\ &= \hat{n}_{\uparrow,i} + \hat{n}_{\downarrow,i} + 4\hat{d}_i + 2\hat{d}_i - 4\hat{d}_i - 4\hat{d}_i \\ &= \hat{n}_{\uparrow,i} + \hat{n}_{\downarrow,i} - 2\hat{d}_i = \hat{m}_{z,i}^2. \end{aligned} \quad (6.4)$$

We thus obtain the operator identity  $\hat{m}_{z,i}^4 = \hat{m}_{z,i}^2$ . The quantum projection noise is therefore given by  $\langle \hat{m}_{z,i}^2 \rangle (1 - \langle \hat{m}_{z,i}^2 \rangle)$  and is zero when  $\langle \hat{m}_{z,i}^2 \rangle$  is either 0 or 1. More generally, the operator identity indicates that measurements of any observable that is constructed out of the local parity-projected density  $\hat{m}_{z,i}^2$  will not yield any additional information.

### 6.2.2 Thermometry Using Site-Resolved Images

To quantitatively analyze the site-resolved profiles, we note that the atoms are trapped in a potential  $V(\mathbf{r})$ , which can be approximated by a radially symmetric harmonic potential  $V(r) = \frac{1}{2}m\omega^2r^2$ . Under the local density approximation, one defines spatially varying local chemical potential  $\mu(r) = \mu_0 - V(r)$ , where  $\mu_0$  is the global chemical potential. Thus, because of the trapping potential, different states can coexist within the same sample. For example, when  $\mu_0$  is large enough, the center of the trap can be band-insulating, while the outer edges, which are at lower densities, are metallic. Since the trap is radially symmetric, the resulting local moment profiles are also radially symmetric. Radial averaging of reconstructed profiles thus provides  $\langle \hat{m}_z^2(r) \rangle$ , which can then be related to the local chemical potential  $\mu(r)$ . In principle, one can

deduce the temperature by fitting  $\langle \hat{m}_z^2(r) \rangle$  to theory, provided that theory is available. In the atomic limit of  $U/8t \gg 1$  and  $k_B T/t \gg 1$ , one can use the high-temperature series expansion described in Section 2.3.3. For moderate interaction strengths of  $U/8t \sim 1$ , NLCE data gives reliable results down to temperatures of  $k_B T/t \sim 0.6$  for all fillings.

In order to perform thermometry, one must first determine the Hubbard parameters  $U$  and  $t$ . To calibrate  $t$ , the depth of each lattice is measured through modulation spectroscopy. In modulation spectroscopy, we determine the resonant frequencies of exciting atoms to higher bands when modulating the lattice intensity. We observe an increased width of the sample when the modulation frequency is resonant with inter-band transitions. Comparing the measured resonance frequencies with a band structure calculation then allows one to calibrate the lattice depth  $V_0$  for each direction. The Hubbard parameter  $t$  can then be computed from the lattice depth  $V_0$  as described in Section 2.1.2. Note that for a Fermi gas, a large number of quasi-momentum states in the lowest band are occupied. This leads to broadening of the resonances, as shown in Fig. 6-10.

To obtain  $U$ , we first prepare Mott insulators in the atomic limit ( $U/(8t) \gg 1$ ), where almost every site has a single atom. We then modulate the intensity of either of the lattice beams along  $\hat{x}$  or  $\hat{y}$ . In the atomic limit, a doubly occupied site requires an additional energy  $U$  compared to a singly occupied site (see Fig. 6-11a). Since lattice modulation modulates the tunneling amplitude, one can induce tunneling of a spin  $\sigma$  atom to a neighboring site with a spin  $-\sigma$  atom. In order to conserve energy, the transfer occurs only if the modulation frequency equals  $U/h$ . As shown in Fig. 6-11b, when this occurs, we observe a reduction in the parity-projected density, which indicates that doublons have been created. The typical energy of  $U$  is  $\sim h \times 1 \text{ kHz}$ , which is separated by roughly an order of magnitude from the band excitation frequencies at typical lattice depths. We note, however, that this method of calibrating  $U$  is reliable only when  $U/t \gg 1$  is large, since the resonance condition of  $\nu = U/h$  is broadened, due to tunneling, by an amount  $t/h$ . At smaller values of  $U/t$ , we thus determine  $U$  through a band structure calculation using the calibrated

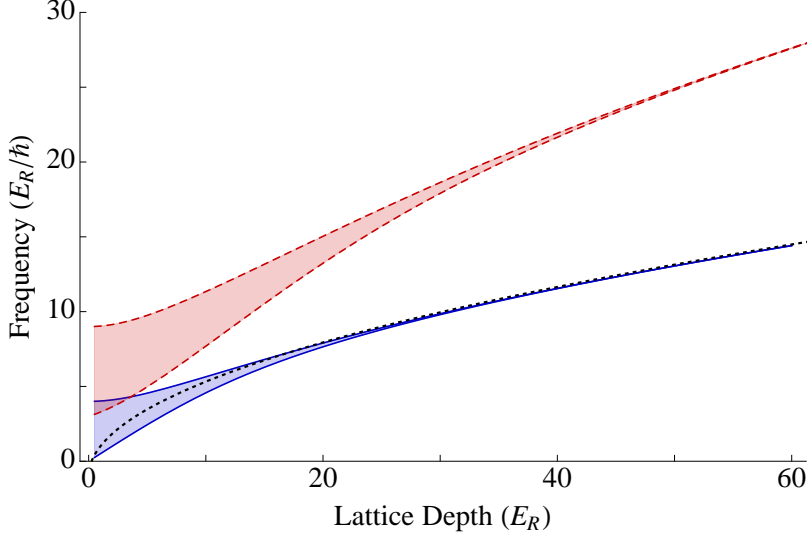


Figure 6-10: Band transition frequencies as a function of lattice depth. Shown in solid blue lines are the maximum and minimum transition frequencies versus lattice depth for transfer of atoms to the first excited band. In red dashed lines are the corresponding frequencies for transfer of atoms to the second excited band. Also shown, using the black dot-dashed line, is the harmonic approximation. The harmonic approximation  $\Delta E = \hbar\omega = 2E_R\sqrt{\tilde{V}_0}$  is corrected by the first order perturbation shift of  $-E_R$ . Note that for a Fermi gas, a large fraction of quasi-momentum states are occupied, which implies that the responses will cover the frequency range between the maximum and the minimum. It thus becomes difficult to calibrate the lattice at low depths. One can calibrate the lattice at higher depths where this is less of an issue, and subsequently scale the depth according to the lattice beam intensities. One also observes that although the transitions to the first excited band are suppressed at large depths, they have a smaller frequency spread. We therefore use these transitions for lattice calibration at intermediate depths.

lattice depths.

Using the calibrated values of  $U$  and  $t$ , we then fit the radially averaged profiles to NLCE theory, with  $T$ ,  $\mu_0$  and  $\omega$  as free parameters. We find good agreement between the observed profiles and theory, an example of which is shown in Fig. 6-12b. An alternative measurement of the degeneracy, rather than temperature, is the entropy per particle. Although we cannot directly measure the entropy, by using the fitted temperatures and chemical potentials, and assuming the validity of the local density approximation, we can use theory to extract the entropy profile of the sample. As shown in Fig. 6-12d, the entropy per site in the band-insulating region is suppressed, indicating that the number of available states is reduced.

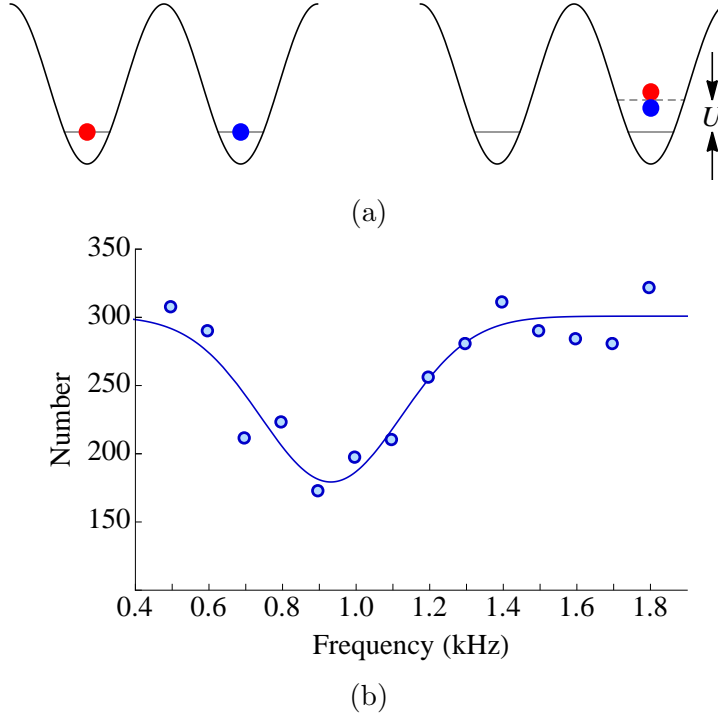


Figure 6-11: Calibrating  $U$  via lattice modulation. (a) In the atomic limit where  $U/t \gg 1$ , the system is well-described by the occupation number of each lattice site. A double occupancy costs an additional energy of  $U$ . Therefore, in order for lattice modulation to drive a spin  $\sigma$  atom onto a neighboring site with a spin  $-\sigma$  atom, the modulation frequency must equal  $U/h$ . Note that the response is broadened by  $t/h$ , corresponding to the width of the upper Hubbard band. (b) A typical modulation spectrum. Here,  $\tilde{V}_0 = 10$  and the scattering length is at the background value of  $a = 174a_0$  [120].

Earlier, we discussed some properties of the local moment, since it is the signal that we directly observe. One conclusion that we found was that the variance in the local moment is related to its average value, and therefore does not yield additional information. This can be checked experimentally by measuring the fluctuations of the moment two separate ways. The first way is to make use of the property that the variance of the local moment is precisely the quantum projection noise given by Eq. (6.3). The variance can thus be obtained from the average local moment via  $\langle \hat{m}_{z,i}^2 \rangle (1 - \langle \hat{m}_{z,i}^2 \rangle)$ . The second way to determine the fluctuations is to rely on the radial symmetry of the system to directly compute the variance of the measured moments at a given radius. Although the radial symmetry is only approximate, we find that the variance obtained using the two different methods agree, in accordance

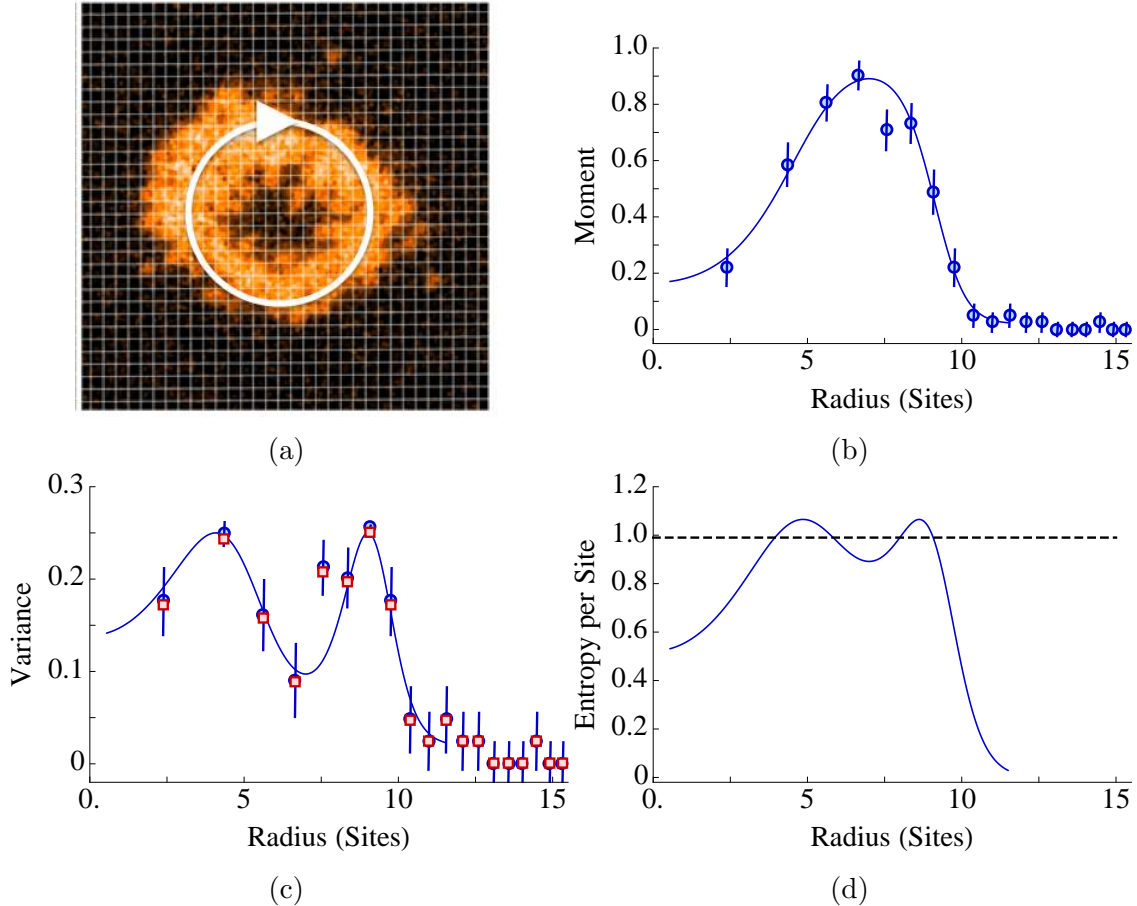


Figure 6-12: Radially averaged profile of a sample with coexisting metallic, Mott insulating and band-insulating regions. The Hubbard parameters are  $U/8t = 2.6(1)$ . (a) The bare image overlaid with the underlying lattice; a radial averaging contour is shown schematically. (b) The radially averaged local moment versus radius. Shown in the solid blue line is a fit of to profile to NLCE data. The fit yields a global chemical potential of  $\mu_0 \approx 1.4U$  and a temperature of  $k_B T/t = 3.7$ . (c) Variance of the local moment. Shown in blue circles is the experimentally measured variance, which assumes that sites at equal radii are equivalent. Shown in red squares is the variance computed from the average moment. The error bars for the second method are not shown. (d) Entropy per site as a function of radius, obtained from NLCE theory using the fitted parameters. The average entropy per particle,  $0.99(6) k_B$ , is shown by the dashed black line.

with the operator identity  $\hat{m}_{z,i}^4 = \hat{m}_{z,i}^2$ .

One can determine the global chemical potential  $\mu_0$  by fitting the measured profiles to theory. For the parity-projected signal, the particle-hole transformation discussed in Section 2.3 allows one further simplification, as long as the filling in the trap center

exceeds  $\langle \hat{n}_i \rangle = 1$ . Consider the local moment under a particle-hole transformation:

$$\begin{aligned}
\hat{m}_{z,i}^2 &= \hat{n}_{\uparrow,i} + \hat{n}_{\downarrow,i} - 2\hat{d}_i \rightarrow 2 - (\hat{n}_{\uparrow,i} + \hat{n}_{\downarrow,i}) - 2(1 - \hat{n}_{\uparrow,i})(1 - \hat{n}_{\downarrow,i}) \\
&\rightarrow 2 - (\hat{n}_{\uparrow,i} + \hat{n}_{\downarrow,i}) - 2(1 - \hat{n}_{\uparrow,i} - \hat{n}_{\downarrow,i}) - 2\hat{d}_i \\
&\rightarrow \hat{n}_{\uparrow,i} + \hat{n}_{\downarrow,i} - 2\hat{d}_i = \hat{m}_{z,i}^2.
\end{aligned} \tag{6.5}$$

We find that the local moment is invariant under a particle-hole transformation, which implies that the moment must be symmetric about  $\mu = U/2$ . Therefore, in a trapped system where  $\mu > U/2$  in the trap center, the location of the maximum moment determines where the local chemical potential  $\mu(r) = U/2$ . This also corresponds to the half-filling point. One can thus identify the half-filling point from the local moment, without having measured the total density directly.

We also note that since the peak value of  $\langle \hat{m}_z^2 \rangle$  occurs at half-filling, it can be used as an independent thermometer. This method of thermometry, however, has two disadvantages. One drawback of using the moment is that  $\langle \hat{m}_z^2 \rangle$  saturates when  $k_B T \approx U$  as the charge degrees of freedom become frozen, and is increasingly insensitive at lower temperatures. Another disadvantage is that unless the interactions are sufficiently strong,  $\langle \hat{m}_z^2 \rangle$  can be a multi-valued function of temperature [103]. In particular, for a fixed  $U/t$ , certain values of  $\langle \hat{m}_z^2 \rangle$  at half-filling can correspond to two different temperatures.

To understand the non-monotonic behavior of the local moment as a function of temperature, we examine how the formation of moments affects the kinetic and interaction energies. In the atomic limit ( $U \gg t$ ), the formation of local moments is favored. To lowest order in  $t$ , the interaction energy  $U$  suppresses double occupancies, while the tunneling energy  $t$  favors delocalization of particles and thus suppresses the formation of local moments. This suggests that, starting at  $k_B T \gg U$ , the local moment increases as the temperature is lowered towards  $k_B T \sim U$ . At lower temperatures, one must take into account effects from super-exchange, which lower the energy per nearest-neighbor pair by  $\sim 4t^2/U$ . Since the super-exchange energy is maximized with well-formed moments, super-exchange also favors the formation of

local moments, and therefore competes with the kinetic energy, which favors reduction of local moments. Since the kinetic energy is  $\sim t$ , the ratio of these two competing terms is  $\propto (4U/t)^2$ . At second order in  $t/U$ , local moments are favored at strong interactions, while delocalization is favored at lower interactions. Consequently, for moderate interactions, at the half-filling point  $\langle \hat{n}_i \rangle = 1$ , the local moment first rises as the temperature increases before decreasing again at high temperatures. The two relevant temperature scales where these changes occur are  $k_B T \sim t^2/U$  and  $k_B T \sim U$ . At high temperatures where  $k_B T \gg U$ , a single site has equal probabilities of being empty, filled with either an  $\uparrow$  or  $\downarrow$  atom, or doubly occupied. Thus at sufficiently high temperatures,  $\langle m_z^2 \rangle = 0.5$ .

### 6.3 Charge and Spin Correlations in the Fermi-Hubbard Model

One unique capability of quantum gas microscopes is their ability to directly measure spatial correlations down to a separation of a single lattice site. In this section, we describe measurements of both spin and charge correlations in the Fermi-Hubbard model as a function of filling. In the language of electronic systems, varying the filling away from half-filling ( $n = 1$ ) translates to doping the system with electrons or holes. The Hubbard model, while simple in form, is not solved except for several limited cases, one of these being the case of half-filling, where at low temperatures, the system is a Mott insulator with anti-ferromagnetic order. The complete phase diagram is not known precisely, since the model remains unsolved due to the “fermion sign problem.” Nevertheless, generically, strongly correlated materials display a variety of phases in close proximity to the Mott insulating phase. For example, in high- $T_c$  cuprates, an unconventional  $d$ -wave superconducting phase, a pseudo-gap phase, and a “stripe” phase, can all occur upon doping of a Mott insulator [83, 28].

To emphasize the competition between the kinetic energy and the interaction energy, we study the regime in which they are of similar sizes. Note that the kinetic

term favors delocalization, and can be diagonalized in a basis of delocalized Bloch waves. On the other hand, the interaction energy contains only on-site terms and is diagonalized by localized states. We therefore focus on the case of  $U/t \sim 8$  for the 2D square lattice, where these two terms are of the same order.

### 6.3.1 How to Measure Spin Correlations

As discussed previously, Raman imaging is not spin-sensitive, and measures the parity-projected site occupations. In order to access spin correlations, one must therefore implement a spin-sensitive detection scheme. In this section, we describe how this can be accomplished. We first define the spin correlator  $\langle \hat{S}_{z,i}, \hat{S}_{z,j} \rangle_C$ :

$$\langle \hat{S}_{z,i}, \hat{S}_{z,j} \rangle_C = \frac{1}{4} \sum_{\sigma} (\langle \hat{n}_{\sigma,i}, \hat{n}_{\sigma j} \rangle_C - \langle \hat{n}_{\sigma,i}, \hat{n}_{-\sigma j} \rangle_C), \quad (6.6)$$

where  $\hat{S}_{z,i} = \frac{1}{2}(\hat{n}_{\uparrow,i} - \hat{n}_{\downarrow,i})$ .

Although we cannot determine the spin of the atoms using the signal obtained via Raman imaging, we can remove one spin state before imaging the atoms. During this spin-selective removal process, doublons are also lost. The measured signal after spin removal is thus described by the operator

$$\hat{p}_{\sigma,i} = \hat{n}_{\sigma,i} - \hat{d}_i, \quad (6.7)$$

when atoms of spin  $-\sigma$  are removed. The spatial correlations of the spin-removed signal are then given by

$$\langle \hat{p}_{\sigma,i}, \hat{p}_{\sigma,j} \rangle_C = \langle \hat{n}_{\sigma,i}, \hat{n}_{\sigma,j} \rangle_C - \langle \hat{n}_{\sigma,i}, \hat{d}_j \rangle_C + \langle \hat{d}_i, \hat{d}_j \rangle_C \quad (6.8)$$

We can compare this to the moment-moment correlator  $\langle \hat{m}_{z,i}^2, \hat{m}_{z,j}^2 \rangle_C$ , which is given by

$$\langle \hat{m}_{z,i}^2, \hat{m}_{z,j}^2 \rangle_C = \langle \hat{n}_i, \hat{n}_j \rangle_C + 4\langle \hat{d}_i, \hat{d}_j \rangle_C - 2\langle \hat{n}_i, \hat{d}_j \rangle_C - 2\langle \hat{d}_i, \hat{n}_j \rangle_C. \quad (6.9)$$

In order to remove the  $\langle \hat{d}_i, \hat{d}_j \rangle_C$  term, one can use the combination

$$2 \sum_{\sigma} \langle \hat{p}_{\sigma,i}, \hat{p}_{\sigma,j} \rangle_C - \langle \hat{m}_{z,i}^2, \hat{m}_{z,j}^2 \rangle_C. \quad (6.10)$$

Conveniently, all other terms containing  $\hat{d}_i$  are also cancelled, and this combination is in fact proportional to the spin correlator  $\langle \hat{S}_{z,i}, \hat{S}_{z,j} \rangle_C$ :

$$\begin{aligned} 2 \sum_{\sigma} \langle \hat{p}_{\sigma,i}, \hat{p}_{\sigma,j} \rangle_C - \langle \hat{m}_{z,i}^2, \hat{m}_{z,j}^2 \rangle_C &= 2 \sum_{\sigma} \langle \hat{n}_{\sigma,i}, \hat{n}_{\sigma,j} \rangle_C - \langle \hat{n}_i, \hat{n}_j \rangle_C \\ &= \sum_{\sigma} [\langle \hat{n}_{\sigma,i}, \hat{n}_{\sigma,j} \rangle_C - \langle \hat{n}_{\sigma,i}, \hat{n}_{-\sigma,j} \rangle_C] \\ &= 4 \langle \hat{S}_{z,i}, \hat{S}_{z,j} \rangle_C \end{aligned} \quad (6.11)$$

This implies that separately averaged correlation maps from two spin-removed  $\hat{p}_{\sigma,i}$  images, combined with the averaged correlation map obtained from the local moment  $\hat{m}_{z,i}^2$  images, gives the spin correlator. The validity of this approach relies on the fact that doublons are removed when we remove one spin state  $\sigma$ . This can be verified by measuring the effect of spin removal on band insulator images. The mechanisms behind this type of spin imaging will not be discussed here, and we defer an in-depth discussion to future dissertations.

To quantify the spin correlations, we define the spin correlator at a separation of one lattice site  $C_s(1)$ :

$$C_s(1) = \sum_{j \in \text{nn}_i} \langle \hat{S}_{z,i}^2, \hat{S}_{z,j}^2 \rangle_C. \quad (6.12)$$

Using the described spin-imaging procedure, we can obtain radially averaged profiles of the  $C_s(1)$ . A way to produce theory-independent curves is to plot the measured  $C_s(1)$  versus the average measured moment, as shown in Fig. 6-13a. We observe that, at a separation of one site, the spin correlations are negative, suggesting the presence of antiferromagnetic correlations. Nevertheless, one must keep in mind that the non-interacting Fermi gas on a square lattice also displays negative correlations at a distance of one site, as discussed in Section 2.1.1. In the case of the non-interacting gas, this is simply a manifestation of Pauli-blocking. Therefore, to demonstrate the

effects of interactions, we must compare the measured correlations with those of the non-interacting Fermi gas. As shown in Fig. 6-13b, a comparison does indicate that at lower temperatures, the measured correlations are enhanced, confirming the presence of a short-range, effective anti-ferromagnetic interaction.

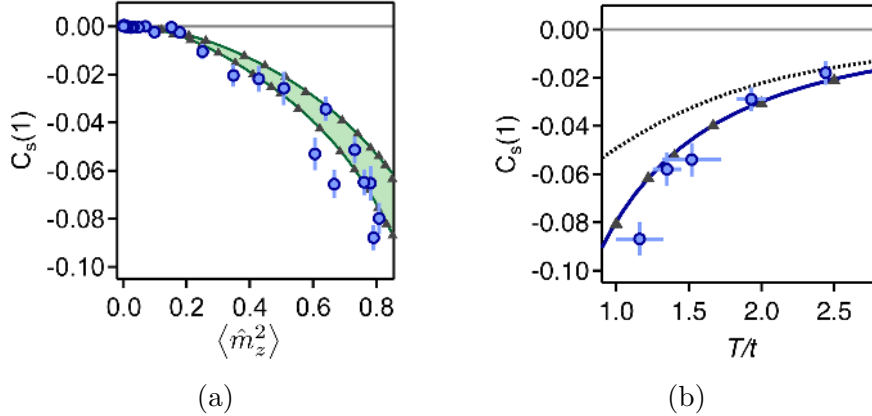


Figure 6-13: Nearest-neighbor spin correlator  $C_s(1)$ . (a)  $C_s(1)$  as a function of the moment  $\langle \hat{m}_{z,i}^2 \rangle$  at  $U/t = 7.2$ . For comparison, NLCE results are shown by the green lines while DQMC results are shown by the gray triangles, for two temperatures  $k_B T/t = 0.89$  and  $1.22$ . (b)  $C_s(1)$  as a function of temperature  $k_B T/t$ . The results for the non-interacting gas is shown by the gray dotted line. The solid blue line shows NLCE results, while the gray triangles show DQMC results. Figures reproduced from [20].

Since the density of the trapped sample monotonically increases from the edges of the trap towards the center, we can apply the local density approximation to obtain the values of the correlators at different chemical potentials  $\mu$ . As shown in Fig. 6-13a, we find that as the moment decreases, the spin correlator  $C_s(1)$  also weakens monotonically. With the help of NLCE and DQMC calculations, we can convert the moment into a filling. In the language of electronic systems, we observe a weakening antiferromagnetic correlations as the system is doped away from half-filling.

### 6.3.2 Charge Correlations as a Function of Filling

Although the observed negative spin correlations at separation of one site were not unexpected, the measured correlations in the charge sector revealed some rather unexpected features. Specifically, the moment-moment correlator at a separation of one

site,  $C_m(1)$ , which we define as

$$C_m(1) = \frac{1}{4} \sum_{j \in \text{nn}_i} \langle \hat{m}_{z,i}^2, \hat{m}_{z,j}^2 \rangle_C, \quad (6.13)$$

displayed a change in sign. Note that  $C_m(1)$  is a type of charge correlator, as it is not sensitive to spin.

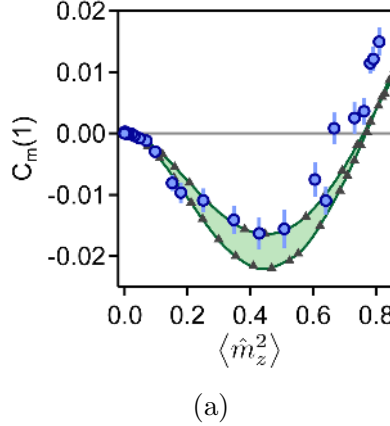


Figure 6-14: Nearest-neighbor moment correlator  $C_m(1)$  as a function of moment  $\langle \hat{m}_{z,i}^2 \rangle$  at  $U/t = 7.2$ . For comparison, NLCE results are shown by the green lines while DQMC results are shown by the gray triangles, for two temperatures  $k_B T/t = 0.89$  and  $1.22$ . A sign changed is observed around  $\langle \hat{m}_{z,i}^2 \rangle = 0.7$ . Figure from [20].

Naively, one might expect that as we dope the system away from half-filling, charge correlations should weaken as the sample becomes dilute. However, as shown in Fig. 6-14, we observe that, as a function of moment (and hence filling),  $C_m(1)$  is non-monotonic, and in fact changes sign at a local moment of  $\sim 0.7$ . At low values of the moment, corresponding to low fillings,  $C_m(1)$  is negative and becomes more negative as the filling is increased, until a filling of  $\sim 0.25$ . It then increases as a function of filling, changing sign and eventually becoming slightly positive near half-filling. This behavior is in stark contrast to that of the spin correlator  $C_s(1)$ , which weakens monotonically away from half-filling, as shown in Fig. 6-13a.

In order to understand how this non-monotonic behavior arises, we first consider the low filling limit, where the doublon fraction is low. Here, one can make the approximation that  $\langle \hat{m}_{z,i}^2 \rangle \approx \langle \hat{n}_i \rangle$ . Thus moment-moment correlations are simply

density-density correlations at low filling. As discussed in Section 2.1.1, Pauli-blocking leads to negative density correlations even in the non-interacting Fermi gas. Repulsive interactions should only enhance this effective repulsion, making the correlations more negative. In order more clearly see this effect, we normalize the correlator  $C_m(1)$  by the average value of the local moment to obtain the correlation function  $g_2(1)$ , which is defined by

$$g_2(1) = \frac{C_m(1)}{\langle \hat{m}_{z,i}^2 \rangle \langle \hat{m}_{z,j}^2 \rangle}. \quad (6.14)$$

Normalized in this fashion, we find that  $g_2(1)$  monotonically decreases as the filling is lowered, as shown in Fig. 6-15a. Comparing the result with the non-interacting case, we find that repulsive interactions enhance the negative correlations.

One way to interpret this behavior at low fillings is to note that  $g_2(1)$ , as a function of decreasing density, can be roughly thought as a measure of the density correlation function  $g_2(k_{Fr})$  of a Fermi gas at increasingly shorter distances  $k_{Fr}$ . That is, measuring  $g_2(1)$  as one lowers the filling is roughly equivalent to measuring  $k_{Fr}$  at shorter and shorter distances, as  $k_F$  decreases with density, while  $r$  is fixed at a separation of one site. More specifically, for a free 2D Fermi gas with half a particle per lattice site,  $k_F = \sqrt{2\pi}/a \propto \sqrt{n}$ . One can thus read off  $g_2(1)$  as a function of filling from Fig. 2-1 in Section 2.1.1. One can therefore interpret the negative correlations at low fillings as the first direct observation of an interaction-enhanced Pauli hole.

To understand the opposite limit of half-filling, where  $\langle \hat{n}_i \rangle = 1$ , it is useful to consider the various contributions to the moment-moment correlator. Near half-filling, one can no longer make the assumption that the doublon fraction is low. In fact, as we shall see, the doublons play an important role. To clarify the various different contributions, we define the hole operator  $\hat{h}_{\sigma,i} = 1 - \hat{n}_{\sigma,i}$ . Physically, this is motivated by the fact that, near half-filling, the charge degree of freedom is essentially frozen, as the majority of sites are filled with one particle, and interactions suppress the occurrence of doublons. It is thus convenient to think of the system as a mobile gas of holes and doublons. While we cannot image the density directly to observe holes themselves, we can define a similar observable, the anti-moment, described by

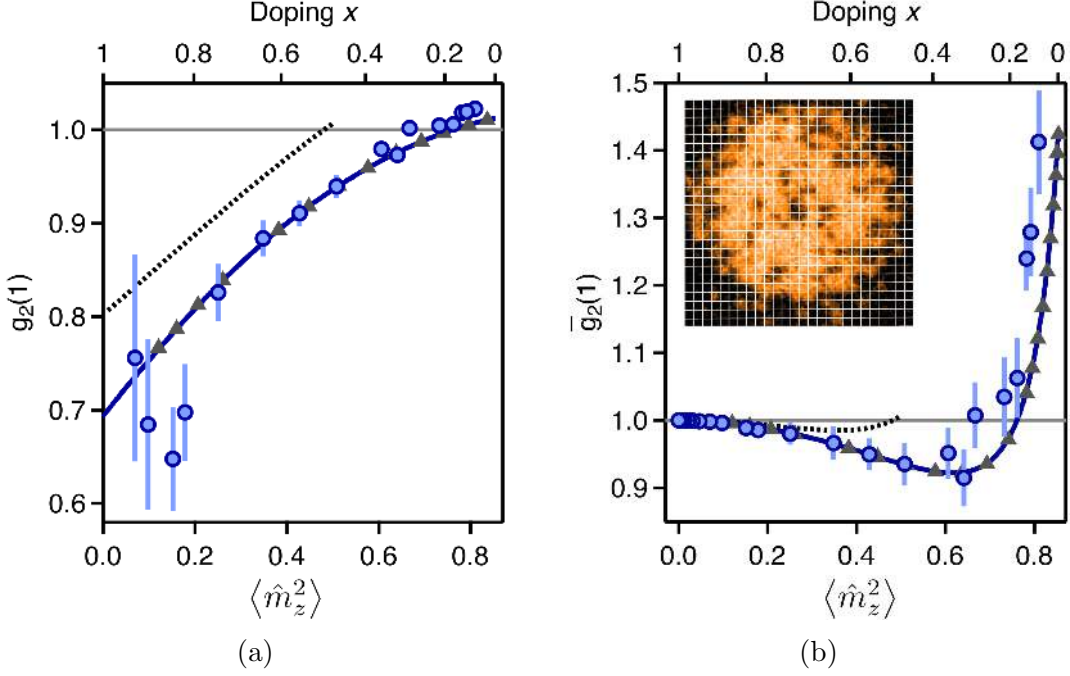


Figure 6-15:  $g_2(1)$  and  $\bar{g}_2(1)$  as a function of doping. (a) Shown is  $g_2(1)$ , the 2-point correlation function for moments at a separation of one lattice site, as a function of moment and filling. Shown in dashed is the result for the non-interacting Fermi gas as a function of filling. The suppression at low fillings can be interpreted as a direct observation of an interaction-enhanced Pauli hole. (b) Shown is  $\bar{g}_2(1)$ , the 2-point correlation function for anti-moments at a separation of one lattice site, as a function of moment and filling.  $\bar{g}_2(1)$  emphasizes the bunching property of anti-moments near half-filling. Shown in the inset is an exemplary image that shows pairs of neighboring anti-moments, which arise due to doublon-holon bunching near half-filling. Figures reproduced from [20].

the operator  $1 - \hat{m}_z^2$ . This operator directly measures the empty sites after parity-projection, and is small near half-filling.

Having defined the anti-moment, we first note that the anti-moment spatial correlator  $\langle (1 - \hat{m}_{z,i}^2)(1 - \hat{m}_{z,j}^2) \rangle_C$  is equal to the moment spatial correlator  $\langle \hat{m}_{z,i}^2 \hat{m}_{z,j}^2 \rangle_C$ . We can define an analogous  $g_2$  function of the anti-moments by normalizing  $C_m(1)$  with the anti-moment density. This function  $\bar{g}_2(r)$  at a separation of one site is then

$$\bar{g}_2(1) = \frac{\langle \hat{m}_{z,i}^2, \hat{m}_{z,j}^2 \rangle_C}{\langle 1 - \hat{m}_{z,i}^2 \rangle \langle 1 - \hat{m}_{z,i}^2 \rangle}, \quad (6.15)$$

where we restrict to nearest neighbor pairs  $i, j$ . This quantity is shown in Fig. 6-15b

as a function of the measured moment. One observes a large enhancement of  $\bar{g}_2(1)$  above unity near half-filling, indicating that the anti-moments strongly bunch.

Keeping in mind that anti-moments can be either holes or doublons, we separate the moment-moment correlator into its various components.

$$\langle \hat{m}_{z,i}^2, \hat{m}_{z,j}^2 \rangle_C = \langle \hat{h}_i \hat{h}_j \rangle_C + 4\langle \hat{d}_i \hat{d}_j \rangle_C + 2\langle \hat{d}_i \hat{h}_j \rangle_C + 2\langle \hat{h}_i \hat{d}_j \rangle_C. \quad (6.16)$$

From the Pauli exclusion principle, we expect the first two terms to be negative. Repulsive interactions only enhance the negative correlations. Therefore, the positive correlations observed near half-filling must arise from the last two terms. This is confirmed by NLCE and QMC calculations, as shown in Fig. 6-16. Since the last two terms describe correlations between holes and doublons and are positive, doublon-holon must bunch together.

To understand why doublons and holes bunch, we first consider the large  $U/t$  limit. Earlier, we described an effective antiferromagnetic interaction arising from virtual tunneling to high energy states that contain a nearest-neighbor doublon-holon pair. Second order perturbation theory gave an energy reduction of  $4t^2/U$  when the neighboring spins are anti-aligned. In addition to computing the energy shift, one can examine the the perturbed wavefunction. The wavefunction must contain an admixture of virtual doublon-holon states, with an amplitude of  $2t/U$ . This implies that if one observes anti-ferromagnetic interactions, one should simultaneously observe a small admixture  $4t^2/U$  of a doublon-hole pair. In other words, nearest-neighbor anti-ferromagnetic correlations go hand-in-hand with nearest-neighbor doublon-holon correlations. The sign change in the moment-moment correlator  $\langle \hat{m}_{z,i}^2, \hat{m}_{z,j}^2 \rangle_C$  as a function of filling thus reflects the competition between effective repulsion due to an interaction-enhanced Pauli hole and effective doublon-holon attraction that arise from superexchange.

Although the non-monotonic behavior of the nearest-neighbor moment-moment correlator was initially unexpected, in retrospect, its origins are clear. The moment-moment correlator highlights the effect of doubles on the formation of local magnetic

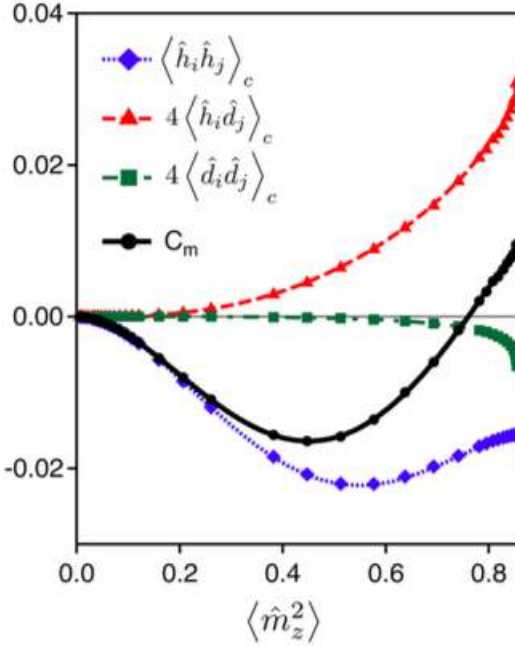


Figure 6-16: Various contributions to the nearest-neighbor moment-moment correlator  $C_m(1)$ . As expected, the holon-holon correlator  $\langle \hat{h}_i \hat{h}_j \rangle$  and the doublon-doublon correlator  $\langle \hat{d}_i \hat{d}_j \rangle$  are both negative, due to Pauli blocking and repulsive interactions. However, the doublon-holon correlator  $\langle \hat{h}_i \hat{d}_j \rangle$  is positive due to super-exchange. Figure reproduced from [20].

moments. The correlator also suggests that doubles can have important physical consequences. This can, for example, affect how charge is transported. By comparing with predictions made by approximate models where doubles are projected out, further studies could shed light on the roles of doublons in the Hubbard model.

### 6.3.3 The Double Well at Half-Filling: a Toy Model

We conclude this chapter with a discussion of the double well at half-filling, i.e. the half-filled two-site Hubbard model. This model is exactly solvable, and can elucidate some simple concepts that carry over to larger systems. We first consider the case where we have exactly one  $\uparrow$  particle and one  $\downarrow$  particle. The system is spin-balanced and at half-filled. In order to write down a representation of the Hamiltonian, we use the following basis:

$$\begin{aligned}
 |\uparrow\downarrow, 0\rangle &= c_{\uparrow,1}^\dagger c_{\downarrow,1}^\dagger |\text{vac}\rangle \\
 |0, \uparrow\downarrow\rangle &= c_{\uparrow,2}^\dagger c_{\downarrow,2}^\dagger |\text{vac}\rangle \\
 |\uparrow, \downarrow\rangle &= c_{\uparrow,1}^\dagger c_{\downarrow,2}^\dagger |\text{vac}\rangle \\
 |\downarrow, \uparrow\rangle &= c_{\downarrow,1}^\dagger c_{\uparrow,2}^\dagger |\text{vac}\rangle,
 \end{aligned} \tag{6.17}$$

where  $|\text{vac}\rangle$  is the vacuum state. Note that the ordering of the fermion operators is important. In this basis, the matrix representation of the two-site Hubbard model is then

$$\hat{H} = \begin{pmatrix} U & 0 & -t & t \\ 0 & U & -t & t \\ -t & -t & 0 & 0 \\ t & t & 0 & 0 \end{pmatrix}, \tag{6.18}$$

which can be diagonalized. The spectrum, ordered from lowest to highest in energy, consists of energies

$$\begin{aligned}
 E_- &= \frac{U}{2} - \frac{1}{2}\sqrt{16t^2 + U^2} \\
 E_z &= 0 \\
 E_U &= U \\
 E_+ &= \frac{U}{2} + \frac{1}{2}\sqrt{16t^2 + U^2}.
 \end{aligned} \tag{6.19}$$

The corresponding eigenvalues are

$$\begin{aligned}
|-\rangle &= \cos \theta \frac{1}{\sqrt{2}} (|\uparrow, \downarrow\rangle - |\downarrow, \uparrow\rangle) + \sin \theta \frac{1}{\sqrt{2}} (|\uparrow\downarrow, 0\rangle + |0, \uparrow\downarrow\rangle) \\
|z\rangle &= \frac{1}{\sqrt{2}} (|\uparrow, \downarrow\rangle + |\downarrow, \uparrow\rangle) \\
|U\rangle &= \frac{1}{\sqrt{2}} (|\uparrow\downarrow, 0\rangle - |0, \uparrow\downarrow\rangle) \\
|+\rangle &= \cos \theta \frac{1}{\sqrt{2}} (|\uparrow\downarrow, 0\rangle + |0, \uparrow\downarrow\rangle) - \sin \theta \frac{1}{\sqrt{2}} (|\uparrow, \downarrow\rangle - |\downarrow, \uparrow\rangle), \tag{6.20}
\end{aligned}$$

where  $\tan \theta = 4t/(U + \sqrt{16t^2 + U^2})$ . In the limit of  $U \gg t$ ,  $E_- \rightarrow -4t^2/U$  and  $E_+ \rightarrow 4t^2/U$ . This indicates that the ground state, which is a spin singlet, is lower in energy by  $4t^2/U$  from the next state, as expected from super-exchange. Furthermore, one observes that in this limit,  $\theta \approx 2t/U$ , which implies that the ground state wavefunction  $|-\rangle$  has a  $4t^2/U^2$  doublon-holon states  $|0, \uparrow\downarrow\rangle$  and  $|\uparrow\downarrow, 0\rangle$ . This was mentioned in the previous section as the origin of doublon-holon bunching.

One might notice that the low energy states  $|-\rangle$  and  $|z\rangle$  both have  $\langle \hat{S}_{z,1} \hat{S}_{z,2} \rangle = -1/4$ . At first sight, this might seem puzzling, as we had argued earlier that antiferromagnetic spin correlations are enhanced for the ground state. A more subtle issue concerns the SU(2) symmetry of the Hubbard Hamiltonian. By symmetry,  $\langle \hat{S}_{z,1} \hat{S}_{z,2} \rangle = \langle \hat{S}_{x,1} \hat{S}_{x,2} \rangle = \langle \hat{S}_{y,1} \hat{S}_{y,2} \rangle$ . However, in the present case, under a global spin rotation described by the unitary transformation

$$\begin{aligned}
\hat{c}_{\uparrow,i} &\rightarrow \frac{1}{\sqrt{2}} (\hat{c}_{\uparrow,i} + \hat{c}_{\downarrow,i}) \\
\hat{c}_{\downarrow,i} &\rightarrow \frac{1}{\sqrt{2}} (-\hat{c}_{\uparrow,i} + \hat{c}_{\downarrow,i}), \tag{6.21}
\end{aligned}$$

the state  $|-\rangle$  remains unchanged, while  $|z\rangle \rightarrow \frac{1}{\sqrt{2}} (|\uparrow, \uparrow\rangle + |\downarrow, \downarrow\rangle)$  and  $\langle z | \hat{S}_{z,1} \hat{S}_{z,2} | z \rangle$  becomes positive.

The resolution to these two issues is that SU(2) symmetry is broken when we imposed the condition of having exactly one  $\uparrow$  and one  $\downarrow$  particle. Under global spin rotations,  $\hat{n}_{\sigma,i}$  is not invariant; only the total number operator  $\hat{n}_{\uparrow,i} + \hat{n}_{\downarrow,i}$  remains invariant. To preserve SU(2), we thus relax these constraints, and only require that

the system be at half-filling, i.e.  $(\hat{n}_{\downarrow,i} + \hat{n}_{\uparrow,i})|\psi\rangle = |\psi\rangle$ .

The Hilbert space is now enlarged by two spin-polarized states at  $E = 0$ , given by

$$\begin{aligned} |\uparrow, \uparrow\rangle &= c_{\uparrow,1}^\dagger c_{\uparrow,2}^\dagger |\text{vac}\rangle \\ |\downarrow, \downarrow\rangle &= c_{\uparrow,1}^\dagger c_{\downarrow,2}^\dagger |\text{vac}\rangle, \end{aligned} \quad (6.22)$$

which do not couple to the other states at half-filling. There are now three degenerate states at  $E = E_z$ :  $|z\rangle$ ,  $|\uparrow, \uparrow\rangle$  and  $|\downarrow, \downarrow\rangle$ . Averaged over these three degenerate states, one finds that while  $\langle S_{z,1} \rangle = \langle S_{z,2} \rangle = 0$ ,  $\langle S_{z,1} S_{z,2} \rangle = 1/12$ , giving  $\langle S_{z,1} S_{z,2} \rangle_C = 1/12$ . In this enlarged space, we find that the average spin correlators  $\langle S_{z,1} S_{z,2} \rangle_C$  for each energy are  $-1/4 + |\mathcal{O}(t^2/U^2)|$ ,  $1/12$ ,  $0$  and  $-|\mathcal{O}(t^2/U^2)|$  respectively. We thus find that the lowest energy state is a nearest-neighbor singlet with  $\langle S_{z,1} S_{z,2} \rangle_C < 0$ . The next states in energy are split by super-exchange, and are spin triplet states with  $\langle S_{z,1} S_{z,2} \rangle_C > 0$ . Even higher in energy are states separated by  $\sim U$ , the Hubbard gap. These results now respect the global SU(2) symmetry. Note that for the two-site model, due to the smallness of the system, SU(2) symmetry is strongly violated when the spin populations are fixed separately.

At first glance, the two-site model cannot capture the physics away from half-filling, since the only fillings that can be accessed for the balanced system are half-filling, the empty vacuum state, and the fully filled band insulator. The latter two cases can be mapped onto one another by a particle-hole transformation, as discussed in Section 2.3. To obtain qualitative predictions away from half-filling, we can interpolate to fillings between vacuum and half-filling by relaxing the requirement of fixed total number, i.e. using the grand canonical ensemble. This is similar in spirit to how SU(2) symmetry is recovered previously when one works in the grand canonical ensemble for each spin species. Working in the grand canonical ensemble allows one to relate the doublon-holon correlator to the strength of spin correlations away from half-filling by using results of the two-site model. One can obtain qualitative predictions for nearest-neighbor correlations that arise in a square lattice, where a single site is shared among four nearest-neighbor pairs. For example, one finds that for nearest-

neighbors  $i, j$ ,  $\langle \hat{h}_i \hat{d}_j \rangle_C = -\tan^2 \theta C_s(1) \approx -16(t^2/U^2)C_s(1)$ , at  $T = 0$ . Note that we have made use of the fact that for the two-site model, spin correlations and doublon-holon correlations are absent for the vacuum state, the band-insulating state and states with an odd-number of particles. Analogous results can be obtained for finite temperature by taking into account higher energy states. In fact, this approximate calculation using two-site results is equivalent to using the smallest cluster in NLCE, and should qualitatively capture short-range correlations at high temperatures, as one moves away from the atomic limit.



# Chapter 7

## Summary and Outlook

In the previous chapters, I have described two areas of research that were covered during my PhD, namely spin-orbit coupling of fermions and quantum gas microscopy of the Fermi-Hubbard model. Here, we provide a brief summary of the results, and an outlook on future research directions for the fermionic quantum gas microscope.

In the case of spin-orbit coupling, we have described several motivations, including the prospect of topologically protected quantum computation in the case of *p*-wave superfluids, which may arise in spin-orbit coupled *s*-wave superfluids. We showed how a specific experimental scheme using internal hyperfine states and Raman lasers can realize spin-orbit coupling in 1D with a transverse Zeeman field, which is relevant for creating Majorana zero modes in 1D wires. We presented a technique, similar to ARPES, that allows for the direct measurement of spinful dispersions and the direct observation of the spin-orbit gap.

Although separately, spin-orbit coupling and *s*-wave superfluidity have been realized with fermionic  ${}^6\text{Li}$  atoms, combining the two is problematic for  ${}^6\text{Li}$ .  ${}^6\text{Li}$  suffers from a relatively high amount of heating due to spontaneous emission. Nevertheless, in Section 3.4, we suggested some possible ways to extend the lifetime, which can potentially allow one to observe interesting many-body states. Alternatively, one could implement other spin-orbit coupling schemes, or use a different atom for which the problem of spontaneous emission is much reduced.

The second area of research discussed in this thesis was quantum gas microscopy of

the Fermi-Hubbard model. The prospect of better understanding the Hubbard model, a prototypical strongly correlated model, has spurred intense experimental interest. Within the past two years, six fermion microscopes have been realized worldwide, both for  ${}^6\text{Li}$  and  ${}^{40}\text{K}$ . In addition to our group [22, 21], several other groups have also demonstrated successful high-fidelity imaging [51, 106, 98, 33], and have realized low-entropy samples in the Hubbard regime [98, 45, 17]. The arrival of fermionic quantum gas microscopes has already led to new results on magnetic and charge correlations in both 1D and 2D [107, 20, 15, 17, 58]. With the possibility of manipulating optical potentials through the microscope, and the ability of detecting small systems as small as a single site, samples where the magnetic correlation length approaches the system size have been realized [87].

We have recently added the ability to project arbitrary optical potentials through the microscope. Similar to the case of bosonic microscopes, this will open up the possibility to perform many new types of experiments, ranging from quantum walks to thermalization studies in isolated systems [112, 70]. The ability to create localized perturbations could allow one to measure response functions in the space and time domain, complementary to the usual frequency-momentum responses [76]. With precise control over optical potentials, one could also prepare identical copies of many-body states, which can enable the measurement of quantities such as the entanglement entropy of a system [110], an idea which has been demonstrated in bosonic microscopes [64, 70].

Another exciting possibility offered by custom optical potentials is the preparation of low entropy samples [59, 11]. For example, by tailoring the optical potential to create large metallic regions while retaining a small region near  $n = 1$ , one can obtain small lightly-doped samples at much lower temperatures, as has been recently demonstrated with  ${}^6\text{Li}$  [87]. This type of entropy rearrangement is similar in spirit to nuclear demagnetization cooling. Here, entropy is moved to regions of low density, where charge degrees of freedom are available.

One key feature of ultracold experiments is that the systems are clean and isolated, allowing coherent dynamics to persist. This is especially advantageous for non-

equilibrium experiments such as quantum quenches, where some parameter of the Hamiltonian is suddenly modified. Combined with the ability to control the spatial distribution of the initial state, one can explore, in a well-controlled manner, issues such as the fate of a single hole in a Mott insulator. More generally, one could measure transport properties of the Fermi-Hubbard model [113] by applying a gradient either optically or magnetically. This could potentially reveal the atypical transport phenomena observed in the cuprates [83]. For example, one might be able to observe anomalous resistivity, atypical scaling of the AC conductivity at high frequencies [122], or a sign change of the thermopower as the system is doped [104]. This would allow one to directly connect microscopic correlations obtained via site-resolved measurements, with macroscopic responses, even far out of the linear response regime. For example, if a striped phase, observed in some cuprates, were to emerge upon doping, one could explore consequences on either spin or charge transport [101].

Current experiments have only explored a small portion of parameter space in the Hubbard model, with most experiments focused on the repulsive and spin-balanced cases. Beyond this regime, one can for example study how spin imbalance affects the system, as explored recently [17]. In the context of real systems, this corresponds to a purely Zeeman field without a Lorentz force. With the use of a Feshbach resonance, one can also change the sign of the interaction and explore the attractive Hubbard model. Although there is a direct one-to-one mapping with the repulsive model, certain observables could be detected more easily on the attractive side. Another interesting avenue lies in the exploration of higher spin systems. In  ${}^{40}\text{K}$ , one can prepare a stable 3-component mixture in the bulk, even without a lattice. This can allow one to simulate a spin-1 Hubbard model on a square lattice, which could have novel magnetic phases not found in spin-1/2 systems [118]. In  ${}^{40}\text{K}$ , away from any Feshbach resonances, the interactions between different spin states are approximately equal, allowing the possibility of creating  $\text{SU}(N)$  systems. In a lattice, systems with  $N > 3$  can have enhanced stability, since 3-body processes are highly suppressed due to the Hubbard gap and the band gap. In  $\text{SU}(N)$  systems, many novel phases are predicted to emerge even on a square lattice. For example, staggered flux phases

[60] and topological spin liquids [56, 55] with fractional quasi-particles have been predicted. This could be another avenue towards realizing topological phases. Rather than using engineered dispersion relations or breaking time-reversal symmetry in order to realize topologically non-trivial states, topological phases naturally “emerge” out of strong correlations. Fractional particles that look nothing like the underlying bare particles could also emerge in these phases. Both the appearance of toplogical phases and fractional particles in strongly correlated systems highlight the notion of emergence, a notion that lies at the heart of many-body physics.

In conclusion, the unprecedented level of control offered by quantum gas microscopes promises the possibility for many new types of experiments on dynamics and correlations in Hubbard-type fermionic systems. Such systems could ultimately reveal new emergent phenomena and provide new perspectives on strongly correlated materials.

# Appendix A

## Coils and Magnetic Fields for $^{40}\text{K}$ Quantum Gas Microscope

This appendix contains information on how various magnetic fields are generated in the quantum gas microscope apparatus.

In addition to coils for the slower, slower compensation and 2D MOT, which are not described here, there are six coils that are relevant for this thesis. Three of these are used to generate low magnetic fields along the three directions  $\hat{x}$ ,  $\hat{y}$  and  $\hat{z}$ . All three are used for fine positioning of the quadrupole magnetic trap, and can be used to zero ambient magnetic fields. The coils along  $\hat{y}$  are powered by a DELTA ELECTRONIKA SM 18-50 power supply in current control mode. The coils along  $\hat{z}$  are powered by an AGILENT E3614A power supply. The coils along  $\hat{x}$  are used during optical pumping after MOT loading, during Raman imaging, and also during evaporation near the substrate. In order to rapidly switch on a field along  $\hat{x}$  for optical pumping, the coils along  $\hat{x}$  are powered by a SORENSEN DLM 20-30 power supply except during MOT loading, where they are powered by an AGILENT E3614A power supply. The coils are switched between these two sources using MOSFETs.

The other three coils, namely the Feshbach coils, the MOT coils and the curvature coils, were described in Chapter 4. Four power supplies are shared among these three coils. Table A.1 lists the various power supplies used, which coils they can be connected to, and their functions.

Function	Power Supply	Coil	Configuration
$^{23}\text{Na}$ MOT	FB	MOT	Anti-Helmholtz
$^{23}\text{Na}$ Catch	Magcatch	MOT	Anti-Helmholtz
$^{40}\text{K}$ MOT	Magcatch	MOT	Anti-Helmholtz
$^{40}\text{K}$ Catch	Magcatch	MOT	Anti-Helmholtz
Plugged Trap	FB	FB	Helmholtz
	Curvature	Curvature	Anti-Helmholtz
Feshbach Field	FB	FB	Helmholtz
“Slicing”	Slicer	Curvature	Anti-Helmholtz

Table A.1: List of power supplies and coils, their functions, and their configurations. The power supplies labeled FB, Magcatch, Curvature, and Slicer are DELTA ELEKTRONIKA SM 30-200 P167, DELTA ELEKTRONIKA SM66-AR-110, LAMBDA ESS-30-500 and DELTA ELEKTRONIKA SM 18-220 power supplies respectively. As described in Section 5.4.1 and Section 6.1.1, the current of the FB power supply is measured with a DANFYSIK LEM IT 200-S current transducer and stabilized. The current of the Slicer power supply is also stabilized with DANFYSIK LEM IT 200-S. The current of the Curvature supply is stabilized with a DANISENSE DS600IDSA current transducer. The Magcatch power supply is not actively stabilized. Other than the Slicer, which is switched using MOSFETs, the other connections are switched using IGBTs.

In addition to the listed coils, there are 8 other coils originally designed as cloverleaf coils for a Ioffe-Pritchard trap. These are not relevant for this thesis.

For convenience, the gradients and field calibrations for the curvature and Feshbach coils, obtained from a magnetic coil simulation, are included in Table A.2.

Quantity	$z$ Location (mm)	Value
FB field	9.5	2.196 G/A
FB field	7.5	2.184 G/A
FB gradient along $\hat{z}$	9.5	-0.0668 G/cm · A
FB gradient along $\hat{z}$	7.5	-0.0511 G/cm · A
Curvature gradient along $\hat{z}$	9.5	0.9344 G/cm · A
Curvature gradient along $\hat{z}$	7.5	0.9186 G/cm · A

Table A.2: Magnetic field and gradient calibrations for Feshbach and Curvature coils, obtained from a simulation. The  $z$  values of 9.5 and 7.5 correspond roughly to the locations of the atoms at the surface of the substrate, and in the quadrupole magnetic trap respectively.



## Appendix B

# Laser Systems for $^{40}\text{K}$ Quantum Gas Microscope

This appendix contains the laser systems used in the quantum gas microscope apparatus.

There are a total of 20 fibers that carry light from the  $^{40}\text{K}$  and  $^{23}\text{Na}$  laser systems to the experiment. These are given in Table B.1. There are a total of 7 fibers that carry 1064 nm light to the experiment for trapping and transport. There is 1 fiber that carries incoherent 830 nm light to the experiment for the “dimple” trap. This setup is simple and has been described in Chapter 4. In this appendix, we focus on the first two cases.

The following are details of how the various beams are related to the different fibers and light sources. This complements the description of some of the beams in Chapter 4. The  $^{23}\text{Na}$  and  $^{40}\text{K}$  MOT light are combined with dichroic mirrors on the experiment. The side MOT beams are in the  $x$ - $y$  plane. The  $^{23}\text{Na}$  MOT (side) beams are split with a  $1 \times 4$  fiber coupler and takes one fiber input. The  $^{40}\text{K}$  MOT (side) beams come from a  $4 \times 4$  fiber coupler that takes up to four fiber inputs. Only two inputs are used, one for cooling light, and one for repumping light. The  $^{40}\text{K}$  2D MOT repumping and cooling light are sent to the experiment in two separate fibers. They are combined on the experiment. The 2D MOT push beam is sent via one fiber. Both repumping and cooling light are combined before the fiber input for the push

beam. The optical pumping beams for  $^{23}\text{Na}$  and  $^{40}\text{K}$  are combined with beamsplitters and dichroic mirrors on the experiment. They are sent to the experiment with 3 separate fibers, and are sent into the vacuum chamber along  $\hat{x}$ . The three fibers carry  $F$ -pumping light for Na,  $m_F$ -pumping light for Na, and  $m_F$ -pumping light for K.  $F$ -pumping for K is carried out using the MOT repumping beams.

For imaging, the  $y$ -imaging beam originates from one fiber, and carries both  $^{23}\text{Na}$  and  $^{40}\text{K}$  D2 imaging light. This can be used to image K and Na at low magnetic fields. The  $x$  bouncing imaging,  $y$  bouncing imaging, and  $z$  imaging fibers carry  $^{23}\text{Na}$  light, and  $^{40}\text{K}$  D2 imaging light from a separate source. The separate source allows imaging of  $^{40}\text{K}$  at arbitrary magnetic fields.

For the 1064 nm trapping and transport beams, the light ultimately originates from a MEPHISTO laser that is amplified via three NUFERN 50W fiber amplifiers. The  $x$ ,  $y$  movable ODT beams and  $y$ -lattice beam originate from one Nufern; the  $z$ -lattice, accordion beam and 5-degree beam originate from a second Nufern; the  $x$ -lattice light is generated by a third Nufern.

In the subsequent sections, we include schematics of how the different sources of light are derived.

## B.1 $^{40}\text{K}$ Laser System

This section contains the schematics for the laser system used to cool and image  $^{40}\text{K}$ . The transitions are near the D2 line of  $^{40}\text{K}$ . The source of the light is an ECDL locked to the D2 line of  $^{39}\text{K}$ , as shown in Fig. B-2. Some of the light is split off as a frequency reference for a separate D2 imaging system, shown in Fig. B-3. The rest is amplified with a tapered amplifier and sent via a fiber to the main laser table, as shown in Fig. B-1.

Fiber	Function	Direction
$^{23}\text{Na}$ MOT (side)	MOT light; split via a $1 \times 4$ fiber splitter	$\pm \hat{x}', \pm \hat{y}'$
$^{23}\text{Na}$ MOT (bottom)	Retro-reflected vertical MOT light	$\hat{z}$
$^{23}\text{Na}$ Slower	Slowing light	Slower Axis
$^{23}\text{Na}$ Dark Spot	$F = 1$ repumping light	$\hat{x}''$
$^{40}\text{K}$ MOT (side)	MOT cooling light; combined and split via a $4 \times 4$ fiber splitter	$\pm \hat{x}', \pm \hat{y}'$
$^{40}\text{K}$ MOT Repump (side)	MOT repumper light; combined and split via a $4 \times 4$ fiber splitter	$\pm \hat{x}', \pm \hat{y}'$
$^{40}\text{K}$ MOT (bottom)	Retro-reflected vertical MOT light	$\hat{z}$
$^{40}\text{K}$ 2D MOT	2D MOT cooling light	$\pm \hat{x}', \pm \hat{z}$
$^{40}\text{K}$ 2D MOT Repump	2D MOT repumping light	$\pm \hat{x}', \pm \hat{z}$
$^{40}\text{K}$ 2D MOT Push	2D MOT push light	$-\hat{x}''$
$^{23}\text{Na}$ $F = 1$ Optical Pumping	$F$ -pumping for $^{23}\text{Na}$	$\hat{x}$
$^{23}\text{Na}$ $F = 2$ Optical Pumping	$m_F$ -pumping for $^{23}\text{Na}$	$\hat{x}$
$^{40}\text{K}$ Optical Pumping	$m_F$ -pumping for $^{40}\text{K}$	$\hat{x}$
$y$ -imaging	$^{23}\text{Na}$ and $^{40}\text{K}$ imaging along $\hat{y}$	$\hat{y}$
$z$ -imaging	$^{23}\text{Na}$ and $^{40}\text{K}$ imaging along $\hat{z}$	$\hat{z}$
$x$ bouncing imaging	$^{23}\text{Na}$ and $^{40}\text{K}$ bouncing imaging along $\hat{x}$	$\hat{x}$
$y$ bouncing imaging	$^{23}\text{Na}$ and $^{40}\text{K}$ bouncing imaging along $\hat{y}$	$\hat{y}$
$x$ -Raman	Raman light along $-\hat{x}$	$-\hat{x}$
$y$ -Raman	Raman light $-\hat{y}$	$-\hat{y}$
D1 optical pumping	Raman imaging D1 pumping light along $-\hat{x}$	$-\hat{x}$

Table B.1: List of fibers that bring  $^{23}\text{Na}$  and/or  $^{40}\text{K}$  light to the experiment, their functions, and the directions of the corresponding beams that enter the chamber.

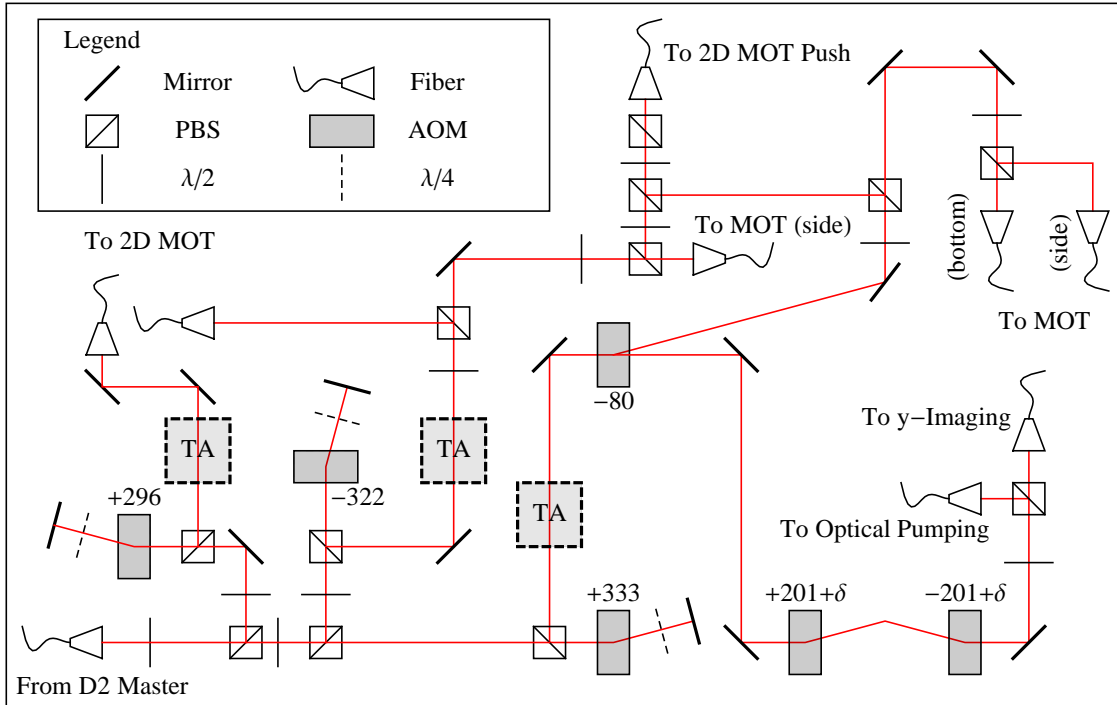


Figure B-1: Main laser table for  $^{40}\text{K}$  D2 Light. The  $y$ -imaging light is combined with  $^{23}\text{Na}$  D2 imaging light from the  $F = 2$  (B) output with a dichroic mirror, before being sent to the experiment with a single fiber. Frequencies are in MHz.

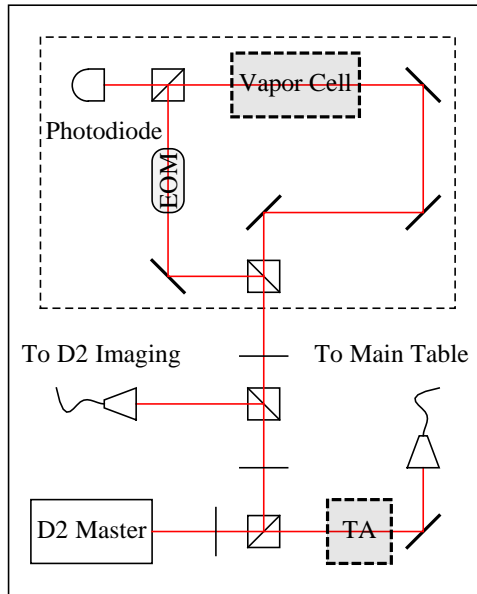


Figure B-2: Sub-system for  $^{40}\text{K}$  master laser. The master laser is locked to the cross-over feature of the D2 line of  $^{39}\text{K}$  via modulation transfer spectroscopy. Frequencies are in MHz.

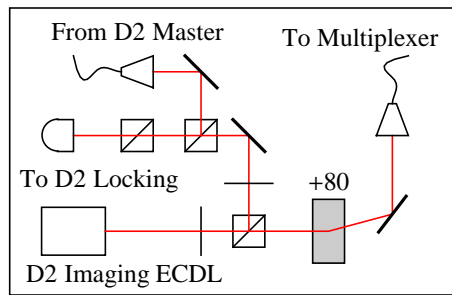


Figure B-3: Sub-system for D2 imaging laser. The D2 imaging laser is offset-locked to the D2 master laser. Frequencies are in MHz. The multiplexer combines  $^{40}\text{K}$  D2 imaging light with  $^{23}\text{Na}$  imaging light, and has outputs to the bouncing imaging and vertical imaging paths.

## B.2 $^{23}\text{Na}$ Laser System

This section contains the laser table layout for light used to image and cool  $^{23}\text{K}$ . The light source is a MPB COMMUNICATIONS FIBER AMPLIFIER that amplifies light from a 1178 nm seed laser (TOPTICA DL-PRO). It produces 1.3 W of frequency-doubled 589 nm light. The main laser table and the locking sub-system is shown in Fig. B-4 and Fig. B-5 respectively.

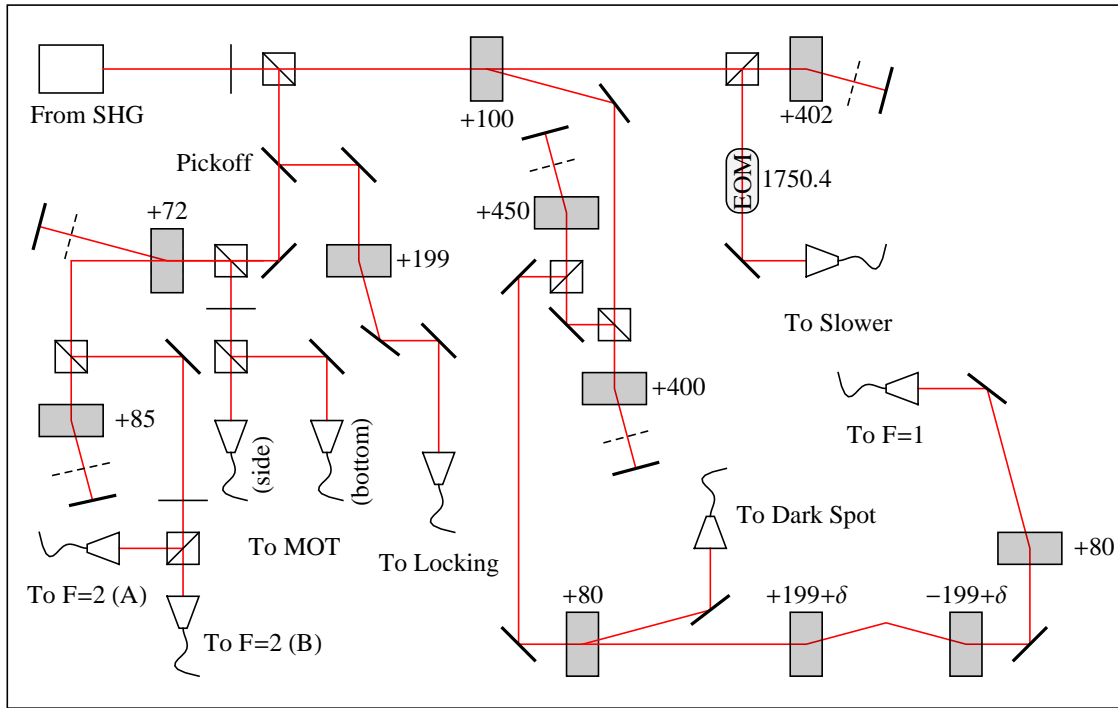


Figure B-4: Main laser table for  $^{23}\text{Na}$  D2 light. Frequencies are in MHz. The  $F = 2$  (A) is sent to the optical pumping axis along  $\hat{x}$ , while the  $F = 2$  (B) is sent to both the  $y$  imaging axis, and a free-space multiplexer that combines with  $^{40}\text{K}$  D2 imaging light. The outputs of the multiplexer are sent to the  $x$  and  $y$  bouncing imaging paths, and also to the vertical imaging path along  $\hat{z}$ . A single fiber brings the  $y$ -imaging light to the experiment.

## B.3 Raman Imaging Laser System

This section contains the schematics for the laser system for light used to Raman image  $^{40}\text{K}$ . Raman imaging requires two sources of light, one for optical pumping,

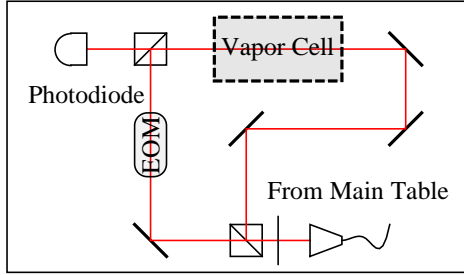


Figure B-5: Locking sub-system for  $^{23}\text{Na}$ . The master laser is locked to the  $F = 2 \rightarrow F' = 3$  feature of the D2 line of  $^{23}\text{Na}$  via modulation transfer spectroscopy.

and one for Raman transfer. The optical pumping light is derived from two ECDLs (TOPTICA DL-PRO) offset-locked to a DBR laser (PHOTODIGM PH770DBR), as shown in Fig. B-6. The DBR laser serves as a frequency reference, and is locked to the cross-over feature of the  $^{39}\text{K}$  D1 line, as shown in Fig. B-7. For the Raman light, we use a M SQUARED SOLSTiS Ti-Saph laser pumped by a LIGHTHOUSE PHOTONICS SPROUT DPSS 532 nm laser. The light is detuned  $\sim 50$  GHz to the red of the D2 line. The two Raman frequencies are generated with AOMs, as shown in Fig. B-8. Conversion of photodiode beat frequencies to transition frequencies on  $^{40}\text{K}$  D1 line are shown in Table B.2.

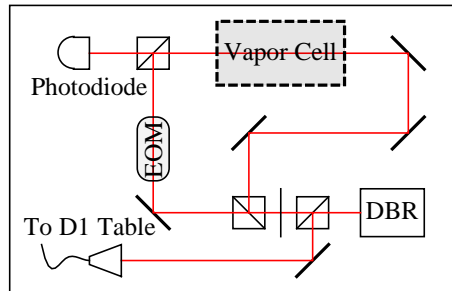


Figure B-6: Laser system for D1 light for  $^{40}\text{K}$ . The two ECDLs are offset-locked to the D1 master laser. The final beamsplitter and waveplate before the fiber can be used to inject light from the Ti-Saph laser that provides the Raman light. This can be used for alignment of the optical pumping path. Frequencies are in MHz.

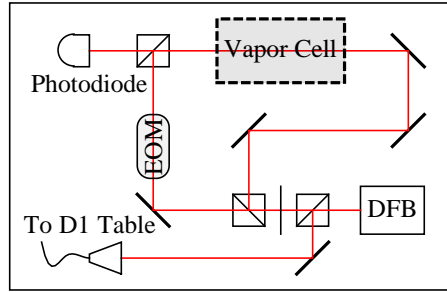


Figure B-7: Sub-system for D1 master laser. The master laser is a DBR laser locked to the highest frequency cross-over feature of the D1 line of  $^{39}\text{K}$  via modulation transfer spectroscopy. Frequencies are in MHz.

Light	Frequency relative to $^{39}\text{K}$ D1 line center	Zeeman shift at 4.2 G	AOM shift	DBR lock point relative to $^{39}\text{K}$ D1 line center	Beat Frequency
$F$ -pump ( $ 7/2, -7/2\rangle \rightarrow  9/2, -9/2\rangle$ )	-657.7	-6.1	+80	+78.5	-822.3
$m_F$ -pump ( $ 9/2, -9/2\rangle \rightarrow  7/2, -7/2\rangle$ )	+783.4	+7.4	+80	+78.5	+632.3

Table B.2: D1 Locking Frequencies. Frequencies are in MHz. This does not take into account the Stark shift from the lattices, which shifts all transitions by  $\approx 60$  MHz to the blue at the imaging depth.

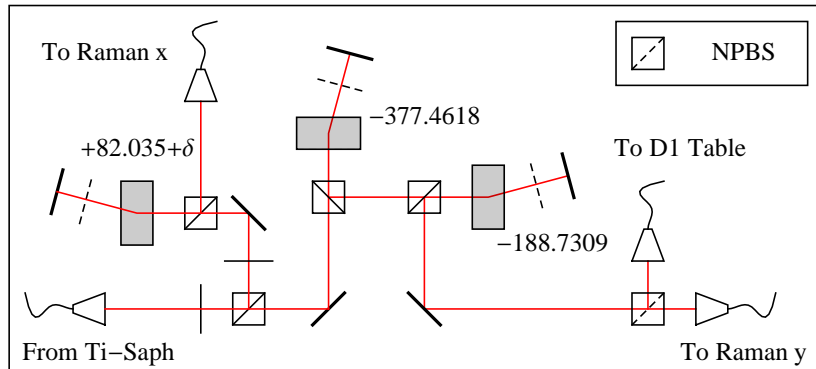


Figure B-8: Laser system for Raman light for  $^{40}\text{K}$ . The light is detuned  $\sim 50$  GHz to the red of the  $^{40}\text{K}$  D2 line.  $\delta$  denotes the detuning from the carrier transition at the Raman imaging magnetic field of 4.2 G. Frequencies are in MHz.

## B.4 1064 nm Laser System

The 1064 nm beams include the  $x$ ,  $y$ , and  $z$  lattices, the 5-degree beam, the movable  $x-y$  ODTs and the accordion beam. These beams originate from three 50W NUFERN fiber amplifiers seeded by a single COHERENT MEPHISTO laser. The details of how these various beams are obtained from the three amplifiers are illustrated in Fig. B-9.

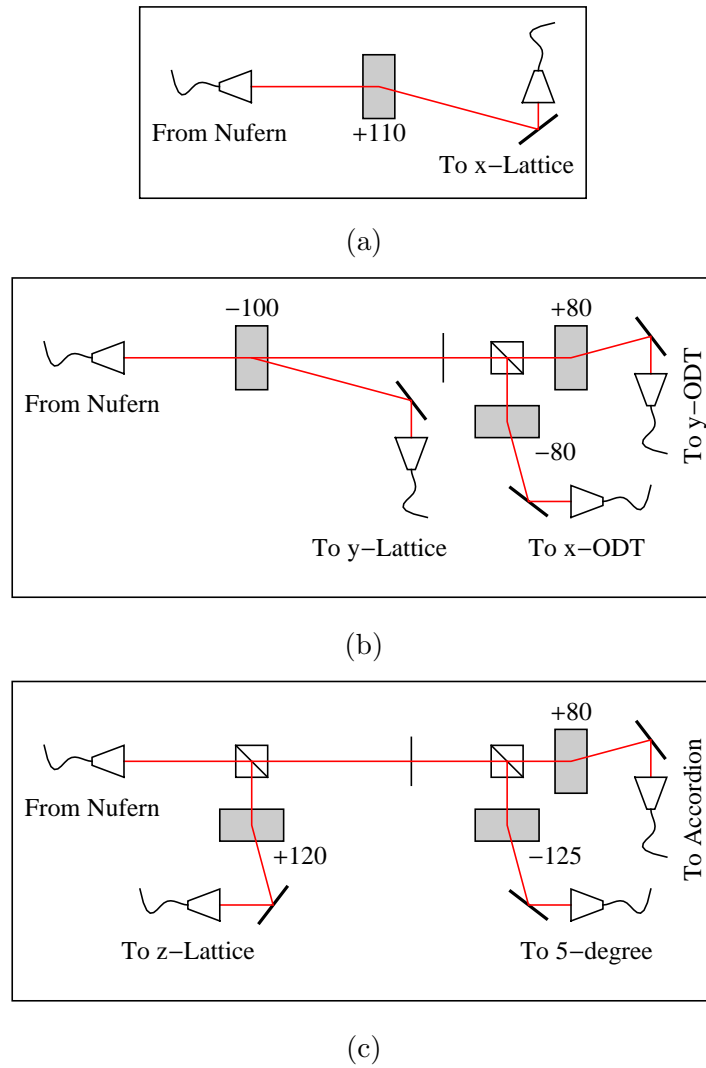


Figure B-9: 1064 nm laser system schematics.



# Appendix C

## $^{40}\text{K}$ Feshbach Resonances

This appendix contains a list of Feshbach resonances computed using multi-channel quantum defect theory (MQDT) [19, 123]. In Table C.2, resonances from 20 G to 550 G in the  $l = 0$  ( $s$ -wave) and  $l = 1$  ( $p$ -wave) channels are listed, for  $M_F \leq 0$ . For  $l = 0$ , resonances in the lowest channel are computed for all  $M_F \leq 0$ . For  $M_F = 0$ , where many experimental measurements are available for the higher energy channels, the second and third lowest channels for  $l = 0$  are computed. For  $l = 1$ , the lowest channel is computed for odd  $M_F$  and the lowest two channels are computed for even  $M_F$ , for  $M_F \leq -5$ . Dipolar coupling terms are not included. Some of the resonances have been observed, most have not. The two predicted resonances that we have observed for the first time are an  $s$ -wave resonance between  $|9/2, -7/2\rangle$  and  $|9/2, -5/2\rangle$  at  $\sim 230$  G and a  $p$ -wave resonance for the same states at  $\sim 218$  G. We also provide an improved preliminary measurement of the  $s$ -wave resonance between  $|9/2, -7/2\rangle$  and  $|9/2, -5/2\rangle$  near  $\sim 174$  G [120]. Our improved measurement gives center of  $174.3(1)$  G and width of  $7.7(5)$  G. We defer a discussion of the measurement to future dissertations.

To determine whether a spin mixture experiences any  $p$ -wave resonances that could overlap with a specific  $s$ -wave resonance, one can follow the steps listed below.

- 1) Determine  $M_F$ . For example, the mixture  $|9/2, -7/2\rangle$  and  $|9/2, -5/2\rangle$  has  $M_F = -6$ . The mixture  $|9/2, -9/2\rangle$  and  $|9/2, -5/2\rangle$  has  $M_F = -7$ .

- 2a) If  $M_F$  is odd, relevant  $l = 1$  resonances are the second lowest channel  $l = 1$  resonances for  $M_F$ , and the lowest channel resonances for  $M_F - 2$  and  $M_F + 2$ . For example, for the  $|9/2, -9/2\rangle - |9/2, -5/2\rangle$  mixture, one needs to consider the lowest channel  $l = 1$  resonances for  $M_F = -7$ ,  $M_F = -9$  and  $M_F = -5$ . The relevant resonances are at 219.4 G for  $|9/2, -9/2\rangle$  and  $|9/2, -5/2\rangle$ , and at 234.6 G and 246.4 G for  $|9/2, -5/2\rangle$  ( $M_F = -5$ ). There are no resonances for  $M_F = -9$ .
- 2b) If  $M_F$  is even, relevant  $l = 1$  resonances are the first lowest  $l = 1$  channels for  $M_F$ ,  $M_F - 1$  and  $M_F + 1$ . For example, for the  $|9/2, -7/2\rangle - |9/2, -5/2\rangle$  mixture, one needs to consider the lowest channel  $l = 1$  resonances for  $M_F = -6$  and  $M_F = -7$  and  $M_F = -5$ . The relevant resonances are at 218.2 G for  $|9/2, -7/2\rangle$  and  $|9/2, -5/2\rangle$ , at 199.8 G for  $|9/2, -7/2\rangle$  ( $M_F = -7$ ), and two resonances at 234.6 G and 246.4 G for  $|9/2, -5/2\rangle$  ( $M_F = -5$ ).

$M_F$	States ( $m_{F,1}, m_{F,2}$ )	$l$	Positon (Theory)	Width (Theory)	Position (Exp.)	Width (Exp.)
-8	(-9/2, -7/2)	0	202.9	7.1	202.1 [120]	7.0(2) [120]
-7	(-9/2, -5/2)	0	225.8	7.4	224.2 [120]	9.7(6) [120]
	(-7/2, -7/2)	1	199.763	$5 \times 10^{-5}$	$\sim 198.8$ [120]	-
	(-9/2, -5/2)	1	219.352	21.6	215(5) [126]	-
-6	(-7/2, -5/2)	0	175.0	9.3	$\sim 174$ [120]	$\sim 7$ [120]
		0	229.6	8.6	Observed	-
		0	448.7	0.9	-	-
	(-7/2, -5/2)	1	218.2149	$2.5 \times 10^{-3}$	Observed	-
	(-9/2, -3/2)	1	240.09	39.3	-	-
-5	(-7/2, -3/2)	0	169.6	1.0	168.5(0.4) [126]	-
		0	261.4	12.4	260.3(0.6) [126]	-
		0	367.3	1.0	-	-
	(-5/2, -5/2)	1	234.613	$6.1 \times 10^{-3}$	-	-

		1	246.403	$5.8 \times 10^{-3}$	245.3(0.5) [126]	-
	(-7/2, -3/2)	1	159.094	10	-	-
		1	248.1356	$3.1 \times 10^{-3}$	-	-
-4	(-5/2, -3/2)	0	178.9	11.1	-	-
		0	256.0	17.4	-	-
		0	372.6	0.2	-	-
		0	451.4	1.4	-	-
	(-5/2, -3/2)	1	263.669	$4.3 \times 10^{-2}$	-	-
-3	(-5/2, -1/2)	0	26.6	0.06	-	-
		0	42.4	0.3	-	-
		0	117.0	0.02	-	-
		0	184.0	0.07	-	-
		0	313.6	20.8	-	-
		0	413.0	1.0	-	-
	(-3/2, -3/2)	1	288.747	0.012	-	-
		1	312.9487	0.011	-	-
-2	(-3/2, -1/2)	0	38.25	0.32	-	-
		0	138.57	0.15	-	-
		0	220.25	1.6	-	-
		0	293.5	35.4	-	-
		0	449.3	0.8	-	-
		0	491.36	0.2	-	-
	(-3/2, -1/2)	1	339.644	$6.1 \times 10^{-3}$	-	-
		1	399.2423	$3.1 \times 10^{-4}$	-	-
-1	(-3/2, +1/2)	0	48.35	0.38	-	-
		0	115.51	1.45	-	-
		0	147.40	0.04	-	-
		0	204.7	1.3	-	-

		0	404.1	19.5	-	-
		0	506.06	1.1	-	-
	(-1/2, -1/2)	1	374.829	0.018	373(2) [78]	2 [78]
		1	420.047	$1.8 \times 10^{-3}$	-	-
		1	530.326	$2.6 \times 10^{-7}$	-	-
0	(-1/2, +1/2)	0	31.1	0.25	31(4) [78]	5 [78]
		0	53.6	0.4	53(4) [78]	5 [78]
		0	87.5	0.4	88(4) [78]	5 [78]
		0	145.45	0.02	-	-
		0	247.3	1.8	146(0.8) [78]	4 [78]
		0	390.4	37.1	389.5(0.1) [78]	5.5 [78]
	(-1/2, -1/2)	1	76.2256	$2.6 \times 10^{-3}$	-	-
		1	465.310	$6 \times 10^{-3}$	-	-
		1	554.045	$9 \times 10^{-5}$	-	-

Table C.1: List of Feshbach resonances of  ${}^{40}\text{K}$ . Magnetic fields are in Gauss.  $l = 0$  resonances in the lowest channel are computed for  $M_F \leq 0$ . For  $l = 1$ , the lowest channel is computed for odd  $M_F$  and the lowest two channels are computed for even  $M_F$ , for  $M_F \leq -5$ .

$M_F$	States ( $m_{F,1}, m_{F,2}$ )	$l$	Positon (Theory)	Width (Theory)	Position (Exp.)	Width (Exp.)
0	(-3/2, +3/2)	0	31.6427	0.169	31(4) [78]	6 [78]
		0	55.7361	0.0957	53(4) [78]	4 [78]
		0	94.3052	1.90	95(4) [78]	23 [78]
		0	99.0565	0.004	-	-
		0	121.227	0.121	-	-
		0	181.818	2.841	182(4) [78]	12 [78]
		0	512.78	22.5	-	-
		0	630.717	1.78	-	-

		0	766.234	0.002	-	-
	(-5/2, +5/2)	0	32.6	0.6	31(4) [78]	6 [78]
		0	62	2	61(4) [78]	21[78]
		0	94.5	2	-	-
		0	112.162	0.02	-	-
		0	157.2	1	-	-
		0	647	8	-	-
		0	786.1	0.5	-	-

Table C.2: Higher channel  $l = 0$  Feshbach resonances for  $M_F = 0$ . Shown are the Feshbach resonances between 20 G and 800 G for the second and third lowest channels for  $M_F = 0$ . Magnetic fields are in Gauss.

A plot showing the lowest channel  $l = 0, 1$  resonances and the second lowest  $l = 1$  resonances for  $M_F \leq -5$  is shown in Fig. C-1. From the discussion of  $p$ -wave resonances, it is clear that the  $\sim 174$  G  $s$ -wave resonance for the  $|9/2, -7/2\rangle$ - $|9/2, -5/2\rangle$  mixture is the only  $s$ -wave resonance that is unaffected by nearby  $p$ -wave resonances on the repulsive side.

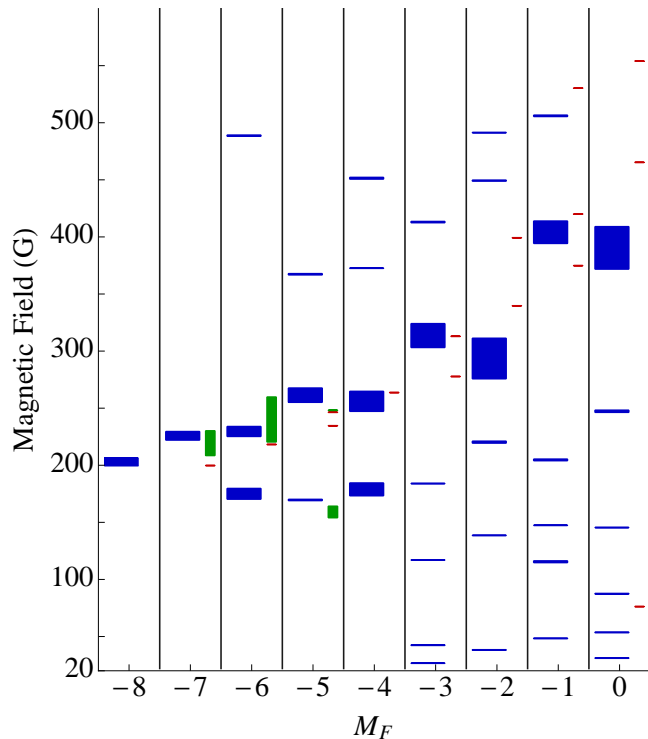


Figure C-1: Some Feshbach resonances of  ${}^{40}\text{K}$ . The positions and widths of Feshbach resonances for  $M_F \leq 0$ . The lowest channel  $l = 0, 1$  resonances are shown in blue and dark red, respectively; the second lowest channel  $l = 1$  resonances for  $M_F \leq -4$  are shown in green. The  $l = 1$  resonance widths are for a collision energy of  $1 \mu\text{K}$  above threshold. Widths less than  $0.1 \text{ G}$  are shown as  $0.1 \text{ G}$ .

## Appendix D

# Evolution of Fermion Pairing from Three to Two Dimensions

This appendix contains a reprint of the following paper [131]:

A. T. Sommer, L. W. Cheuk, M. J. H. Ku, W. S. Bakr, and M. W. Zwierlein,,  
“Evolution of Fermion Pairing from Three to Two Dimensions,” Phys. Rev. Lett.  
**108**, 045302 (2012).

## Evolution of Fermion Pairing from Three to Two Dimensions

Ariel T. Sommer, Lawrence W. Cheuk, Mark J. H. Ku, Waseem S. Bakr, and Martin W. Zwierlein

Department of Physics, MIT-Harvard Center for Ultracold Atoms, and Research Laboratory of Electronics, MIT,  
 Cambridge, Massachusetts 02139, USA

(Received 13 October 2011; published 23 January 2012)

We follow the evolution of fermion pairing in the dimensional crossover from three-dimensional to two-dimensional as a strongly interacting Fermi gas of  $^6\text{Li}$  atoms becomes confined to a stack of two-dimensional layers formed by a one-dimensional optical lattice. Decreasing the dimensionality leads to the opening of a gap in radio-frequency spectra, even on the Bardeen-Cooper-Schrieffer side of a Feshbach resonance. The measured binding energy of fermion pairs closely follows the theoretical two-body binding energy and, in the two-dimensional limit, the zero-temperature mean-field Bose-Einstein-condensation to Bardeen-Cooper-Schrieffer crossover theory.

DOI: 10.1103/PhysRevLett.108.045302

PACS numbers: 67.85.-d, 03.75.Lm, 05.30.Fk, 32.30.Bv

Interacting fermions in coupled two-dimensional (2D) layers present unique physical phenomena and are central to the description of unconventional superconductivity in high-transition-temperature cuprates [1] and layered organic conductors [2]. Experiments on ultracold gases of fermionic atoms have allowed access to the crossover from Bose-Einstein condensation (BEC) of tightly bound fermion pairs to Bardeen-Cooper-Schrieffer (BCS) superfluidity of long-range Cooper pairs in three spatial dimensions [3,4] and, more recently, the confinement of interacting Fermi gases to two spatial dimensions [5–9]. A fermionic superfluid loaded into a periodic potential should form stacks of two-dimensional superfluids with tunable interlayer coupling [10–13], an ideal model for Josephson-coupled quasi-2D superconductors [1,14]. For deep potentials in the regime of uncoupled 2D layers, increasing the temperature of the gas is expected to destroy superfluidity through the Berezinskii-Kosterlitz-Thouless mechanism [15–17], while more exotic multiplane vortex loop excitations are predicted for a three-dimensional (3D) anisotropic BCS superfluid near the critical point [18].

In this Letter, we study fermion pairing across the crossover from 3D to 2D in a periodic potential of increasing depth. To form a bound state in 3D, the attraction between two particles in a vacuum must exceed a certain threshold. However, if the two particles interact in the presence of a Fermi sea, the Cooper mechanism allows pairing for arbitrarily weak interactions [19]. In 2D, even two particles in a vacuum can bind for arbitrarily weak interactions. Surprisingly, the mean-field theory of the BEC-BCS crossover in 2D predicts that the binding energy of fermion pairs in the many-body system is identical to the two-body binding energy  $E_b$  [20]. Indeed, to break a pair and remove one pairing partner from the system costs an energy [21]  $E_{b,\text{MF}} = \sqrt{\mu^2 + \Delta^2} - \mu$  within mean-field theory, where  $\mu$  is the chemical potential and  $\Delta$  is the pairing gap. In 2D, one finds [20]  $\mu = E_F - E_b/2$  and  $\Delta^2 = 2E_F E_b$ , where  $E_F$  is the Fermi energy, and thus  $E_{b,\text{MF}} = E_b$ ; i.e., the

many-body and two-body binding energies are predicted to be identical throughout the BEC-BCS crossover.

We realize a system that is tunable from 3D to 2D with a gas of ultracold fermionic  $^6\text{Li}$  atoms trapped in an optical trap and a standing-wave optical lattice. The lattice produces a periodic potential along the  $z$  direction,

$$V(z) = V_0 \sin^2(\pi z/d), \quad (1)$$

with depth  $V_0$  and lattice spacing  $d = 532$  nm. Together with the optical trap, the lattice interpolates between the 3D and 2D limits. It gradually freezes out motion along one dimension and confines particles in increasingly uncoupled layers. Features characteristic of the 2D system appear as the strength of the periodic potential is increased. The threshold for pairing is reduced, allowing pairs to form for weaker attractive interactions than in the 3D system. The effective mass of particles increases along the confined direction, and the center of mass and relative degrees of freedom of an atom pair become coupled [11]. For a deep potential that suppresses interlayer tunneling, the system is an array of uncoupled two-dimensional layers. Here, the center of mass and relative motion decouple and fermion pairs form for the weakest interatomic attraction [11,22,23].

In the experiment, the appearance of bound fermion pairs is revealed using radio-frequency (rf) spectroscopy. The atomic gas consists of an equal mixture of  $^6\text{Li}$  atoms in the first and third hyperfine states (denoted as  $|1\rangle$  and  $|3\rangle$ ), chosen to minimize final-state interaction effects in the rf spectra [24]. Interactions between atoms in states  $|1\rangle$  and  $|3\rangle$  are greatly enhanced by a broad Feshbach resonance at 690.4(5) G [25]. An rf pulse is applied to transfer atoms from one of the initial hyperfine states to the unoccupied second hyperfine state (denoted as  $|2\rangle$ ). In previous work on rf spectroscopy of  $^{40}\text{K}$  fermions in a deep one-dimensional (1D) lattice [8], an rf pulse transferred atoms from an initially weakly interacting state into a strongly interacting spin state, likely producing polarons [26]. In

our Letter, the initial state is the strongly interacting, largely paired Fermi gas in equilibrium, and the final state is weakly interacting.

An asymmetric dissociation peak (the bound-to-free transition) in the rf spectrum indicates the presence of fermion pairs. For two-particle binding, the pair dissociation line shape in the 3D and 2D limits is proportional to  $\rho(h\nu - E_b)/\nu^2$ , with  $\rho$  the free-particle density of states and  $\nu = \pm(\nu_{\text{rf}} - \nu_{\text{hf}})$  the offset of the rf frequency  $\nu_{\text{rf}}$  from the hyperfine splitting  $\nu_{\text{hf}}$  (plus symbol:  $|1\rangle \rightarrow |2\rangle$  transition; minus symbol:  $|3\rangle \rightarrow |2\rangle$  transition). This form can be obtained from Fermi's golden rule and the bound-state wave function in momentum space; see also Refs. [21,27]. In 2D, the expected dissociation line shape is then proportional to

$$I(\nu) \propto \frac{\theta(h\nu - E_b)}{\nu^2}. \quad (2)$$

In addition to the pairing peak, at finite temperature one expects a peak in the rf spectrum due to unbound atoms (the free-to-free transition). A narrow bound-to-bound transition can also be driven at an offset frequency  $\nu_{bb} = (E_b - E'_b)/h$  that transfers one spin state of the initial bound pair with binding energy  $E_b$  into a bound state of  $|2\rangle$  with  $|1\rangle$  or  $|3\rangle$ , of binding energy  $E'_b$ . For a  $|1\rangle - |3\rangle$  mixture near the Feshbach resonance,  $E_b \ll E'_b$  [24], so the bound-to-bound peak is well-separated from the bound-to-free and free-to-free peaks. As very recently calculated [28], final-state interactions and the anomalous nature of scattering in 2D introduce an additional factor of  $\frac{\ln^2(E_b/E'_b)}{\ln^2[(h\nu - E_b)/E'_b] + \pi^2}$  into Eq. (2), causing a rounding off of the sharp peak expected from the step function.

In a 1D lattice, the binding energy for two-body pairs is determined by the lattice spacing  $d$ , the depth  $V_0$ , and the 3D scattering length  $a$ . In the 2D limit  $V_0 \gg E_R$ , with recoil energy  $E_R = \frac{\hbar^2\pi^2}{2md^2}$ , the scattering properties of the gas are completely determined by  $E_b$  [22,23]. In that limit, the lattice wells can be approximated as harmonic traps with level spacing  $\hbar\omega_z = 2\sqrt{V_0 E_R}$  and harmonic oscillator length  $l_z = \sqrt{\frac{\hbar}{m\omega_z}}$ . In a many-particle system in 2D, the ratio of the binding energy to the Fermi energy determines the strength of interactions. The 2D scattering amplitude  $f(E_F) = \frac{2\pi}{-\ln(k_F a_{2D}) + i\pi/2}$  for collisions with energy  $E_F$  is parametrized by  $\ln(k_F a_{2D})$ , where  $k_F = \sqrt{2mE_F}/\hbar$  and  $a_{2D} = \hbar/\sqrt{mE_b}$ . It is large when  $|\ln(k_F a_{2D})| \lesssim 1$  [22,23], corresponding to the strong-coupling regime [28,29]. The BEC side of the BEC-BCS crossover corresponds to negative values of  $\ln(k_F a_{2D})$ , while the BCS side corresponds to positive values [20].

The experimental sequence proceeds as follows. An ultracold gas of  ${}^6\text{Li}$  is produced by sympathetic cooling with  ${}^{23}\text{Na}$  as described previously [21]. The  ${}^6\text{Li}$  atoms are transferred from a magnetic trap to an optical dipole trap (wavelength 1064 nm, waist 120  $\mu\text{m}$ ), with axial harmonic

confinement (frequency 22.8 Hz) provided by magnetic field curvature. With  ${}^6\text{Li}$  polarized in state  $|1\rangle$ , the magnetic bias field is raised to 568 G, and an equal mixture of hyperfine states  $|1\rangle$  and  $|3\rangle$  is created using a 50% rf transfer from  $|1\rangle$  to  $|2\rangle$  followed by a full transfer from  $|2\rangle$  to  $|3\rangle$ . The field is then raised to the final value, and evaporative cooling is applied by lowering the depth of the optical dipole trap, resulting in a fermion pair condensate with typically  $5 \times 10^5$  atoms per spin state. The lattice is then ramped up over 100 ms. The retro-reflected lattice beam (wavelength 1064 nm) is at an angle of 0.5 degrees from the optical dipole trap beam, enough to selectively reflect only the lattice beam. The depth of the lattice is calibrated using Kapitza-Dirac diffraction of a  ${}^{23}\text{Na}$  BEC and a  ${}^6\text{Li}_2$  molecular BEC and by lattice modulation spectroscopy on the  ${}^6\text{Li}$  cloud. The magnetic field and hyperfine splitting are calibrated using rf spectroscopy on spin-polarized clouds. After loading the lattice, the rf pulse is applied for a duration of typically 1 ms. Images of state  $|2\rangle$  and either  $|1\rangle$  or  $|3\rangle$  are recorded in each run of the experiment.

To ensure loading into the first Bloch band, the Fermi energy and temperature of the cloud are kept below the second band. The 2D Fermi energy  $E_F^{2D} = \frac{2\pi\hbar^2 n}{m}$ , with  $n$  the 2D density per spin state, is typically  $h \times 10$  kHz. The bottom of the second band is at least one recoil energy  $E_R = h \times 29.3$  kHz above the bottom of the first band in shallow lattices and up to about  $h \times 300$  kHz for the deepest lattices. The temperature is estimated to be on the order of the Fermi energy.

Rf spectra are recorded for various lattice depths and interaction strengths. Figure 1 shows examples of spectra over a range of lattice depths at the 3D Feshbach resonance and on the BCS side of the resonance at 721 G, where fermion pairing in 3D is a purely many-body effect. At the lowest lattice depths, the spectra show only a single peak, shifted to positive offset frequencies due to many-body interactions. This is similar to the case without a lattice [24,30]; to discern a peak due to fermion pairs from a peak due to unbound atoms would require locally resolved rf spectroscopy of imbalanced Fermi gases [30]. However, as the lattice depth is raised, the single peak splits into two and a clear pairing gap emerges. The narrow peak at zero offset is the free-to-free transition, and the asymmetric peak at positive offset is the pair dissociation spectrum. The pair spectrum, especially on resonance, shows a sharp threshold and a long tail corresponding to dissociation of fermion pairs into free atoms with nonzero kinetic energy.

Binding energies are determined from the offset frequency of the pairing threshold. Although the line shape in Eq. (2) jumps discontinuously from zero to its maximum value, the spectra are observed to be broadened. This is to a large part due to the logarithmic corrections [28] noted above, which predict a gradual rise at the threshold  $h\nu = E_b$ , and a spectral peak that is slightly shifted from

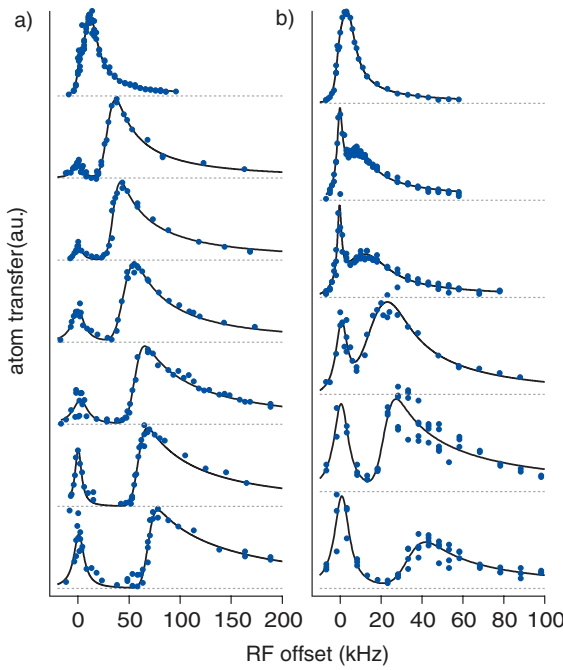


FIG. 1 (color online). Evolution of fermion pairing in the 3D-to-2D crossover in a one-dimensional optical lattice, observed via rf spectroscopy. Shown is the transferred atom number versus rf offset frequency relative to the atomic hyperfine splitting. (a) Spectra at the Feshbach resonance at 690.7(1) G with  $d/a = -0.01(4)$ . Lattice depths from top to bottom in units of  $E_R$ : 1.84(3), 4.8(2), 6.1(2), 9.9(4), 12.2(4), 18.6(7), and 19.5(7). (b) Spectra on the BCS side at 720.7(1) G,  $d/a = -1.15(2)$ . Lattice depths in units of  $E_R$ : 2.75(5), 4.13(7), 4.8(1), 6.0(2), 10.3(2), and 18.1(4).

$E_b$ . We include possible additional broadening by convolving the theoretical line shape, including the logarithmic correction, with a Gaussian function of width  $w_m$ . The parameters  $E_b$  and  $w_m$  are determined by a least-squares fit to the measured spectrum. Typical spectra have  $w_m$  of 5 kHz, consistent with our estimates of broadening based on collisions and three-body losses. The Fourier broadening is 1 kHz. Power broadening is about 5 kHz on the free-to-free transition and less than 1 kHz on the bound-to-free transition due to the reduced wave function overlap. Inclusion of the logarithmic correction is found to be necessary in order for the fit function to reproduce the observed behavior of the high-frequency tail. The final-state binding energy used in the logarithmic correction for fitting is obtained from spectra where both a bound-to-bound and a bound-to-free peak were measured. At low lattice depths, the 2D form for the paired spectrum should differ from the exact shape that interpolates between the 3D and 2D limits. In the case where the shape of the spectrum is given by the 3D limit, fitting to the 2D form overestimates the binding energy by 8%.

Figure 2 shows the measured binding energies as function of  $V_0/E_R$  for several interaction strengths. The binding

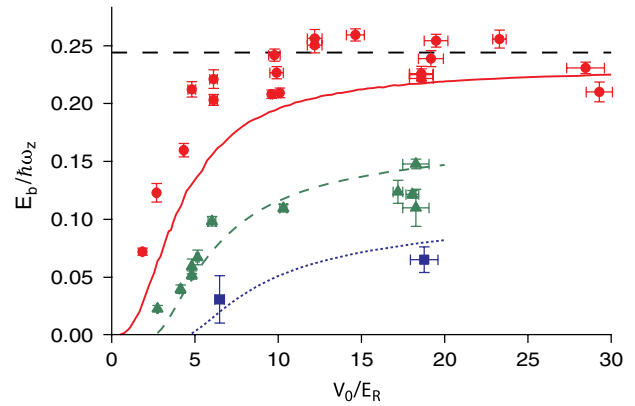


FIG. 2 (color online). Binding energy  $E_b$  versus lattice depth  $V_0$  at several values of the 3D scattering length  $a$ .  $E_b$  is normalized via the lattice frequency  $\omega_z$ . Red circles: results from spectra at 690.7(1) G and  $d/a = -0.01(4)$ . Green triangles: 720.7(1) G,  $d/a = -1.15(2)$ . Blue squares: 800.1(1) G,  $d/a = -2.69(1)$ . Curves show predictions from Orso *et al.* [11]. Horizontal black dashed line: harmonic approximation result for  $1/a = 0$ .

energies are normalized by  $\hbar\omega_z \equiv 2\sqrt{V_0 E_R}$ , which equals the level spacing in the harmonic approximation to the lattice potential. The measured binding energies grow with increasing lattice depth and agree reasonably well with theoretical predictions for two-body bound pairs in a 1D lattice [11]. The binding energy at the 3D resonance approaches a constant multiple of  $\hbar\omega_z$  as the lattice depth increases, as expected from the 2D limit [22,23]. Figure 3(a) compares the binding energies measured in lattices deeper than  $17E_R$  to predictions in the harmonic quasi-2D limit [22,23]. At the 3D Feshbach resonance, we find  $E_b = 0.232(16)\hbar\omega_z$  for deep lattices. The error bar refers to the standard error on the mean. This value is close to the harmonic confinement result of  $0.244\hbar\omega_z$  [23]. The exact calculation [11] predicts a constant downward shift of the binding energy by  $0.2E_R$  for deep lattices due to the anharmonicity of the sinusoidal potential. For  $V_0$  of about  $20E_R$ , this gives a prediction of  $0.22\hbar\omega_z$ , also close to the measured value.

Figure 3(b) shows the binding energy measured in deep lattices normalized by the exact two-body result [11] versus the many-body interaction parameter  $\ln(k_F a_{2D})$ . Overall, the binding energies are close to the two-body value, even in the strong-coupling regime for  $|\ln(k_F a_{2D})| < 1$ , as predicted by zero-temperature mean-field theory [20]. The data show a slight downward deviation for the strongest coupling. At fixed reduced temperature  $T/T_F$ , the relationship should be universal. It will thus be interesting to see in future work whether the binding energy depends significantly on temperature.

The bound-to-bound transition is seen in Fig. 4 as a narrow peak at negative offset frequencies. In the regime where  $E_b$  can be found from the pair dissociation spectrum,

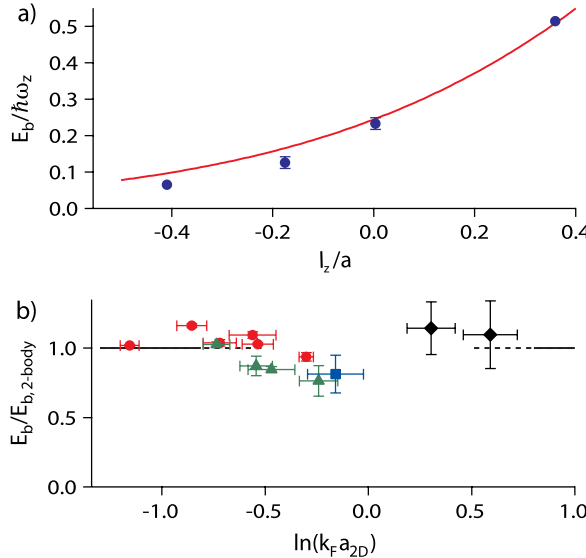


FIG. 3 (color online). (a) Binding energy of fermion pairs versus interaction strength  $l_z/a$  for deep lattices ( $V_0 > 17E_R$ ). Solid curve: theoretical prediction in the 2D harmonic limit [22,23]. (b) Ratio of the measured binding energy to the two-body result [11] versus  $\ln(k_F a_{2D})$  for  $V_0 > 17E_R$ . Black diamonds: binding energy determined from the bound-to-bound transition with resonant final-state interactions. Other data symbols: see Fig. 2. Horizontal line: zero-temperature mean-field theory [20].

the bound-to-bound peak position directly yields the binding energy in the final state  $E'_b$ . For example, the spectrum in Fig. 4(a), taken at the 3D  $|1\rangle - |3\rangle$  resonance at 690.7(1) G and  $V_0/E_R = 9.59(7)$ , gives  $E'_b/E_R = 18.0(1)$  at a final-state interaction of  $d/a' = 8.41(2)$ . Likewise, the spectrum in Fig. 4(b) at  $V_0/E_R = 26.1(4)$  and a magnetic field of 751.1(1) G, where  $d/a' = 2.55(1)$ , gives  $E'_b/E_R = 5.3(1)$ . An independent measurement for  $d/a = 2.55(2)$  using the bound-to-free spectrum at 653.55 G yields  $E_b/E_R = 5.25(2)$ , showing that bound-to-bound transitions correctly indicate binding energies.

The BCS side of the 2D BEC-BCS crossover is reached in Fig. 4(c) by increasing the number of atoms to increase  $E_F$  and increasing the magnetic field to reach a lower binding energy. In Fig. 4(c), the central Fermi energy is  $\hbar \times 43(6)$  kHz and  $T/T_F = 0.5(2)$ . The magnetic field is set to 834.4(1) G, where  $d/a = -3.06(1)$ , and the final-state interactions between  $|1\rangle$  and  $|2\rangle$  are resonant, with  $d/a' = -0.01(3)$ . The lattice depth is  $V_0/E_R = 26.4(3)$ . Thus, we know that  $E'_b = 0.232(16)\hbar\omega_z = 2.4(2)E_R$  at this lattice depth. From the bound-to-bound transition in Fig. 4(c), we can then directly determine the binding energy of  $|1\rangle - |3\rangle$  fermion pairs to be  $E_b/E_R = 0.9(2)$ . The theoretical prediction [11] for two-body binding gives  $E_b/E_R = 0.82(1)$ . The measured binding energy gives a many-body interaction parameter of  $\ln(k_F a_{2D}) = 0.6(1)$ , on the BCS side but within the strongly interacting regime, where one expects many-body effects beyond mean-field

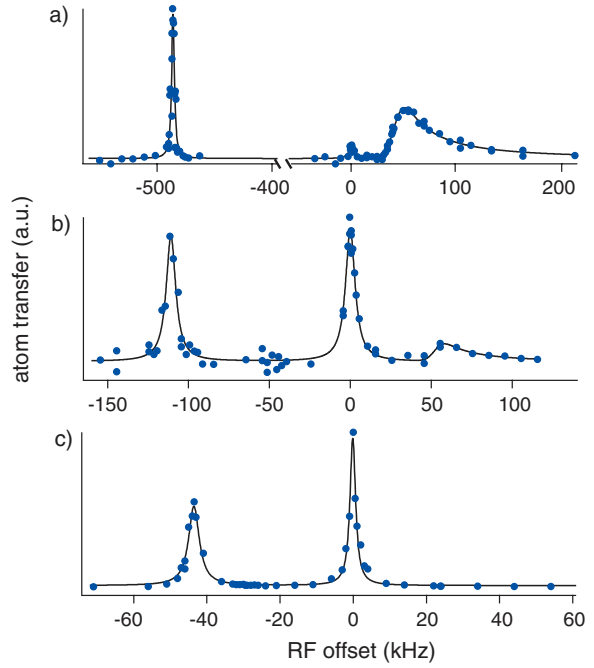


FIG. 4 (color online). Spectra including the bound-to-bound transition, a narrow peak at negative rf offset. Shown are spectra at magnetic fields of (a) 690.7(1) G, (b) 751.1(1) G, and (c) 834.4(1). The interaction parameters  $d/a$  are (a)  $-0.01(4)$ , (b)  $-1.91(1)$ , and (c)  $-3.06(1)$ . Lattice depths in units of  $E_R$  are (a)  $9.59(7)$ , (b)  $26.1(4)$ , and (c)  $26.4(3)$ . The bound-to-free transition is not visible in (c). The transfer is from  $|1\rangle$  to  $|2\rangle$  in (a) and (b) and from  $|3\rangle$  to  $|2\rangle$  in (c).

BEC-BCS theory [26,29]. It is therefore interesting that the measured binding energy is close to the expected two-body binding energy to much better than the Fermi energy, as predicted by mean-field theory [20].

In conclusion, we have measured the binding energy of fermion pairs along the crossover from 3D to 2D in a one-dimensional optical lattice. Measurements were performed at several lattice depths and scattering lengths, allowing quantitative comparison with theoretical predictions. Considering the fact that the gas is a strongly interacting many-body system, the close agreement with two-body theory is surprising, especially in the strong-coupling regime. While mean-field BEC-BCS theory in 2D predicts this behavior [20], it misses other important features of the many-body system, most strikingly the interaction between fermion pairs [13]. Superfluidity in a one-dimensional lattice will be an exciting topic for future studies. Stacks of weakly coupled, superfluid 2D layers would constitute a basic model of the geometry found in high-temperature superconductors.

The authors would like to thank G. Orso for providing his code to calculate binding energies and M. Köhl and W. Zwerger for stimulating discussions. This work was supported by the NSF, AFOSR-MURI, ARO-MURI, ONR, DARPA YFA, a grant from the Army Research Office with

funding from the DARPA OLE program, the David and Lucile Packard Foundation, and the Alfred P. Sloan Foundation.

- [1] M. Tinkham, *Introduction to Superconductivity* (Dover, Mineola, NY, 2004), 2nd ed., p. 318.
- [2] J. Singleton and C. Mielke, *Contemp. Phys.* **43**, 63 (2002).
- [3] *Ultracold Fermi Gases*, Proceedings of the International School of Physics “Enrico Fermi,” Course CLXIV, edited by M. Inguscio, W. Ketterle, and C. Salomon (Elsevier, Amsterdam, 2008).
- [4] S. Giorgini, L. P. Pitaevskii, and S. Stringari, *Rev. Mod. Phys.* **80**, 1215 (2008).
- [5] K. Günter, T. Stöferle, H. Moritz, M. Köhl, and T. Esslinger, *Phys. Rev. Lett.* **95**, 230401 (2005).
- [6] X. Du, Y. Zhang, and J. E. Thomas, *Phys. Rev. Lett.* **102**, 250402 (2009).
- [7] K. Martiyanov, V. Makhlov, and A. Turlapov, *Phys. Rev. Lett.* **105**, 030404 (2010).
- [8] B. Fröhlich, M. Feld, E. Vogt, M. Koschorreck, W. Zwerger, and M. Köhl, *Phys. Rev. Lett.* **106**, 105301 (2011).
- [9] P. Dyke, E. D. Kuhnle, S. Whitlock, H. Hu, M. Mark, S. Hoinka, M. Lingham, P. Hannaford, and C. J. Vale, *Phys. Rev. Lett.* **106**, 105304 (2011).
- [10] G. Orso and G. V. Shlyapnikov, *Phys. Rev. Lett.* **95**, 260402 (2005).
- [11] G. Orso, L. P. Pitaevskii, S. Stringari, and M. Wouters, *Phys. Rev. Lett.* **95**, 060402 (2005).
- [12] L. Salasnich, *Phys. Rev. A* **76**, 015601 (2007).
- [13] W. Zhang, G.-D. Lin, and L.-M. Duan, *Phys. Rev. A* **77**, 063613 (2008).
- [14] S. T. Ruggiero, T. W. Barbee, and M. R. Beasley, *Phys. Rev. Lett.* **45**, 1299 (1980).
- [15] J. M. Kosterlitz and D. Thouless, *J. Phys. C* **5**, L124 (1972).
- [16] D. S. Petrov, M. A. Baranov, and G. V. Shlyapnikov, *Phys. Rev. A* **67**, 031601 (2003).
- [17] W. Zhang, G.-D. Lin, and L.-M. Duan, *Phys. Rev. A* **78**, 043617 (2008).
- [18] M. Iskin and C. A. R. Sá de Melo, *Phys. Rev. Lett.* **103**, 165301 (2009).
- [19] L. N. Cooper, *Phys. Rev.* **104**, 1189 (1956).
- [20] M. Randeria, J.-M. Duan, and L. Y. Shieh, *Phys. Rev. Lett.* **62**, 981 (1989).
- [21] W. Ketterle and M. Zwierlein, *Riv. Nuovo Cimento Soc. Ital. Fis.* **31**, 247 (2008).
- [22] D. S. Petrov and G. V. Shlyapnikov, *Phys. Rev. A* **64**, 012706 (2001).
- [23] I. Bloch, J. Dalibard, and W. Zwerger, *Rev. Mod. Phys.* **80**, 885 (2008).
- [24] C. Schunck, Y. Shin, A. Schirotzek, and W. Ketterle, *Nature (London)* **454**, 739 (2008).
- [25] M. Bartenstein, A. Altmeyer, S. Riedl, R. Geursen, S. Jochim, C. Chin, J. H. Denschlag, R. Grimm, A. Simoni, E. Tiesinga, C. J. Williams, and P. S. Julienne, *Phys. Rev. Lett.* **94**, 103201 (2005).
- [26] V. Pietila, D. Pekker, Y. Nishida, and E. Demler, [arXiv:1110.0494](https://arxiv.org/abs/1110.0494).
- [27] C. Chin and P. S. Julienne, *Phys. Rev. A* **71**, 012713 (2005).
- [28] C. Langmack, M. Barth, W. Zwerger, and E. Braaten, [arXiv:1111.0999](https://arxiv.org/abs/1111.0999).
- [29] G. Bertaina and S. Giorgini, *Phys. Rev. Lett.* **106**, 110403 (2011).
- [30] A. Schirotzek, Y.-i. Shin, C. H. Schunck, and W. Ketterle, *Phys. Rev. Lett.* **101**, 140403 (2008).

## Appendix E

# Spin-Injection Spectroscopy of a Spin-Orbit Coupled Fermi Gas

This appendix contains a reprint of the following paper [23]:

L. W. Cheuk, A. T. Sommer, Z. Hadzibabic, T. Yefsah, W. S. Bakr, and M. W. Zwierlein, “Spin-Injection Spectroscopy of a Spin-Orbit Coupled Fermi Gas,” *Phys. Rev. Lett.* **109**, 095302 (2012).



## Spin-Injection Spectroscopy of a Spin-Orbit Coupled Fermi Gas

Lawrence W. Cheuk,<sup>1</sup> Ariel T. Sommer,<sup>1</sup> Zoran Hadzibabic,<sup>1,2</sup> Tarik Yefsah,<sup>1</sup> Waseem S. Bakr,<sup>1</sup> and Martin W. Zwierlein<sup>1</sup>

<sup>1</sup>*Department of Physics, MIT-Harvard Center for Ultracold Atoms, and Research Laboratory of Electronics,  
MIT, Cambridge, Massachusetts 02139, USA*

<sup>2</sup>*Cavendish Laboratory, University of Cambridge, J. J. Thomson Avenue, Cambridge CB3 0HE, United Kingdom*

(Received 25 June 2012; published 27 August 2012)

The coupling of the spin of electrons to their motional state lies at the heart of recently discovered topological phases of matter. Here we create and detect spin-orbit coupling in an atomic Fermi gas, a highly controllable form of quantum degenerate matter. We directly reveal the spin-orbit gap via spin-injection spectroscopy, which characterizes the energy-momentum dispersion and spin composition of the quantum states. For energies within the spin-orbit gap, the system acts as a spin diode. We also create a spin-orbit coupled lattice and probe its spinful band structure, which features additional spin gaps and a fully gapped spectrum. In the presence of *s*-wave interactions, such systems should display induced *p*-wave pairing, topological superfluidity, and Majorana edge states.

DOI: 10.1103/PhysRevLett.109.095302

PACS numbers: 67.85.Lm, 03.65.Vf, 03.65.Wj, 03.75.Ss

Spin-orbit coupling is responsible for a variety of phenomena, from the fine structure of atomic spectra to the spin Hall effect, topological edge states, and, in the presence of interactions, the predicted phenomenon of topological superconductivity [1,2]. In electronic systems, spin-orbit coupling arises from the relativistic transformation of electric fields into magnetic fields in a moving reference frame. In the reference frame of an electron moving with wave vector  $\mathbf{k}$  in an electric field, the motional magnetic field couples to the electron spin through the magnetic dipole interaction. In a two-dimensional semiconductor heterostructure, the electric field can arise from structure or bulk inversion asymmetry [3], leading to magnetic fields of the form  $\mathbf{B}^{(R)} = \alpha(-k_y, k_x, 0)$  or  $\mathbf{B}^{(D)} = \beta(k_y, k_x, 0)$ , respectively known as the Rashba [4] and Dresselhaus [5] contributions. Including a possible momentum-independent Zeeman field  $\mathbf{B}^{(Z)} = (0, B_y^{(Z)}, B_z^{(Z)})$ , the Hamiltonian of the electron takes the form

$$\mathcal{H} = \frac{\hbar^2 k^2}{2m} - \frac{g\mu_B}{\hbar} \mathbf{S} \cdot (\mathbf{B}^{(D)} + \mathbf{B}^{(R)} + \mathbf{B}^{(Z)}), \quad (1)$$

where  $g$  is the electron  $g$  factor,  $\mu_B$  is the Bohr magneton, and  $\mathbf{S}$  is the electron spin.

The energy-momentum dispersion and the associated spin texture of the Hamiltonian in Eq. (1) are shown in Fig. 1(a) for  $B_y^{(Z)} = 0$  and  $\alpha = \beta$ . In the absence of a perpendicular Zeeman field  $B_z^{(Z)}$ , the spectrum consists of the parabolic free particle dispersions for the two spin states that are shifted relative to each other in  $k$  space owing to the spin-orbit interaction. For a nonzero field  $B_z^{(Z)}$ , a gap opens in the spectrum. This gap, known as the spin-orbit gap, has been recently observed in one-dimensional quantum wires [6,7]. The two energy bands are spinful in the sense that the spin of an atom is locked to its momentum.

In this work, we engineer the Hamiltonian in Eq. (1) with equal Rashba and Dresselhaus strengths in an optically trapped, degenerate gas of fermionic lithium atoms via Raman dressing of atomic hyperfine states [8,9]. Raman fields have previously been used to generate spin-orbit coupling and gauge fields in pioneering work on Bose-Einstein condensates [10–12] and, recently, spin-orbit coupling in Fermi gases [13]. Here, we directly measure the spinful band structure of Eq. (1), as well as the rich band structure of a spin-orbit coupled lattice. For this, we introduce spin-injection spectroscopy, which is capable of completely characterizing the quantum states of spin-orbit coupled fermions, including the energy-momentum dispersion and the associated spin texture. By tracing the evolution of quantum states in the Brillouin zone, this method can be extended to directly measure topological invariants, such as the Chern number in a two-dimensional system [1,2,14].

Spin-orbit coupling is generated by using a pair of laser beams that connects the second and third lowest hyperfine levels in  ${}^6\text{Li}$ , labeled  $|\downarrow\rangle$  and  $|\uparrow\rangle$ , via a two-photon Raman transition, as shown in Figs. 1(b) and 1(c). The Raman process imparts momentum  $\hbar Q\hat{x}$  to an atom while changing its spin from  $|\downarrow\rangle$  to  $|\uparrow\rangle$  and momentum  $-\hbar Q\hat{x}$  while changing the spin from  $|\uparrow\rangle$  to  $|\downarrow\rangle$ . Defining a quasimomentum  $q = k_x + \frac{Q}{2}$  for spin  $|\downarrow\rangle$  and  $q = k_x - \frac{Q}{2}$  for spin  $|\uparrow\rangle$ , one obtains the Hamiltonian of the form given in Eq. (1) [10]. In this mapping,  $B_z^{(Z)} = \hbar\Omega_R/g\mu_B$ , where  $\Omega_R$  is the two-photon Rabi frequency,  $B_y^{(Z)} = \hbar\delta/g\mu_B$ , where  $\delta$  is the two-photon detuning, and  $\alpha = \beta = \frac{\hbar^2 Q}{2mg\mu_B}$ . In addition to providing spin-orbit coupling, the Raman beams lead to spontaneous photon scattering. For our experimental setup, the spontaneous scattering rate is  $\sim 240$  times smaller than  $\Omega_R$ , slow enough to permit accurate spin-injection spectroscopy (see Supplemental Material [15]).

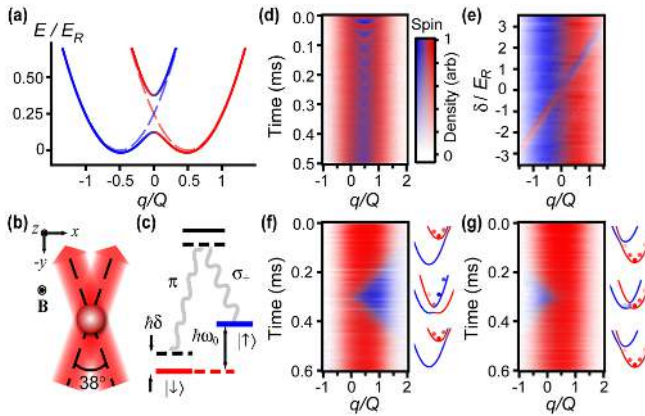


FIG. 1 (color online). Realization of spin-orbit coupling in an atomic Fermi gas. (a) Energy bands as a function of quasimomentum  $q$  for Raman coupling strength of  $\hbar\Omega_R = 0.25E_R$  and  $\hbar\delta = 0E_R$ . Energy bands for  $\hbar\Omega_R = \hbar\delta = 0E_R$  are shown with dashed lines. Color indicates spin composition of the states. (b) A pair of Raman beams at  $\pm 19^\circ$  relative to the  $\hat{y}$  axis couples states  $|\downarrow, k_x = q\rangle$  and  $|\uparrow, k_x = q + Q\rangle$ . A bias magnetic field  $\mathbf{B}$  in the  $\hat{z}$  direction provides the quantization axis. (c) Energy level diagram of states coupled by the Raman fields:  $\hbar\delta$  is the two-photon detuning. The hyperfine interaction splits  $|\uparrow\rangle$  and  $|\downarrow\rangle$  by  $\hbar\omega_0$ , and the relevant polarization components are  $\pi$  and  $\sigma_+$ . (d) Momentum-dependent Rabi oscillations for  $\hbar\Omega_R = 0.71(2)E_R$  and  $\hbar\delta = -0.25(1)E_R$ . Atoms are prepared in  $|\downarrow\rangle$  (red) and are subsequently projected into a superposition of eigenstates as the Raman field is pulsed on. (e) A  $\pi$  pulse for the resonant momentum class is applied at different  $\hbar\delta$  for  $\hbar\Omega_R = 0.035(5)E_R$ . (f),(g) Adiabatic loading and unloading of atoms into the upper (lower) band with  $\hbar\Omega_R = 0.53(5)E_R$ . The Raman beams are turned on with  $\delta = \mp 8.5\Omega_R$ , which is then swept linearly to  $\delta = 0$  and back at a rate of  $|\dot{\delta}| = 0.27(5)\Omega_R^2$ .

We sympathetically cool  ${}^6\text{Li}$  atoms with  ${}^{23}\text{Na}$  in a magnetic trap down to a temperature of  $T < 0.1T_F$ , where  $T_F$  is the Fermi temperature [16]. After removal of Na atoms, the Li atoms are transferred into an optical dipole trap formed by two orthogonal 1064 nm beams. To separate the atomic hyperfine levels, we apply a magnetic field of 11.6 G. At this field, the interactions between states  $|\uparrow\rangle$  and  $|\downarrow\rangle$  (scattering length  $20a_0$ ) are negligible in the experiment.

When the spin-orbit gap is opened suddenly, an atom prepared in the state  $|\downarrow, k_x = q - Q/2\rangle$  oscillates between  $|\downarrow, k_x = q - Q/2\rangle$  and  $|\uparrow, k_x = q + Q/2\rangle$  with a momentum-dependent frequency  $\Delta(q)/\hbar$ , where  $\Delta(q)$  is the energy difference between the bands at quasimomentum  $q$ . Such Rabi oscillations correspond to Larmor precession of the pseudospin in the effective magnetic field  $\mathbf{B}^{(\text{SO})} = \mathbf{B}^{(\text{D})} + \mathbf{B}^{(\text{R})} + \mathbf{B}^{(\text{Z})}$ . We have observed these oscillations by starting with atoms in  $|\downarrow\rangle$ , pulsing on the Raman field for a variable duration  $\tau$ , and imaging the atoms spin-selectively after time-of-flight expansion from the trap. Time-of-flight maps momentum to real space, allowing direct momentum resolution of the spin

populations. As a function of pulse duration, we observe oscillations of the spin polarization with momentum-dependent frequencies, as shown in Fig. 1(d). Since our Fermi gas occupies a large range of momentum states with near-unity occupation, each image at a given pulse duration  $\tau$  contains information for a large range of momenta  $q$ . The observation of momentum-dependent oscillations demonstrates the presence of a spin-orbit gap and shows that the atomic system is coherent over many cycles. To highlight the momentum selectivity of this process, we prepare an equal mixture of atoms in states  $|\uparrow\rangle$  and  $|\downarrow\rangle$  and pulse on the Raman fields for a time  $t = \pi/\Omega_R$  for different two-photon detunings  $\delta$ . This inverts the spin for atoms with momentum  $q$  where  $\Delta(q)$  is minimal and equals  $\hbar\Omega_R$ . The resonant momentum class depends linearly on  $\delta$  due to the Doppler shift  $\propto k_x Q$ , as shown in Fig. 1(e).

Instead of pulsing on the Raman field and projecting the initial state into a superposition of states in the two bands, one can introduce the spin-orbit gap adiabatically with respect to band populations. This is achieved by starting with a spin-polarized Fermi gas and sweeping the two-photon detuning  $\delta$  from an initial value  $\delta_i$  to a final detuning  $\delta_f$ . The magnitude of the initial detuning  $|\delta_i|$  is much larger than the two-photon recoil energy  $E_R = \hbar^2 Q^2 / 2m$ , so that the effective Zeeman field is almost entirely parallel with the spins. Depending on the direction of the sweep, this loads atoms into either the upper or the lower dressed band. We interrupt the sweep at various times and image the spin-momentum distribution. This reveals that the spin texture follows the effective Zeeman field. We verify that the process is reversible by sweeping the detuning back to  $\delta_i$  and observing that full spin polarization is restored, as shown in Figs. 1(f) and 1(g).

Having demonstrated the ability to engineer spin-orbit coupling in a Fermi gas, we introduce a general approach to measure the eigenstates and energies of fermions at each quasimomentum  $q$  and thus resolve the band structure and the spin texture of spin-orbit coupled atomic systems. Our approach yields similar information to spin and angle-resolved photoemission spectroscopy (spin-ARPES), a powerful technique recently developed in condensed matter physics [17]. Spin-ARPES is particularly useful for studying magnetic and quantum spin Hall materials; it has been used, for example, to directly measure topological quantum numbers in the  $\text{Bi}_{1-x}\text{Sb}_x$  series, revealing the presence of topological order and chiral properties [18].

Our spectroscopic technique uses radio frequency (rf) spin injection of atoms from a free Fermi gas into an empty spin-orbit coupled system using photons of a known energy, as shown in Fig. 2(a). After injection, the momentum and spin of the injected atoms are analyzed by using time of flight [19] combined with spin-resolved detection. Atoms are initially loaded into one of two free “reservoir” atomic states  $|\downarrow\rangle_R$  and  $|\uparrow\rangle_R$ , for which we use the first and fourth lowest hyperfine states of  ${}^6\text{Li}$ . State  $|\downarrow\rangle_R$  can be

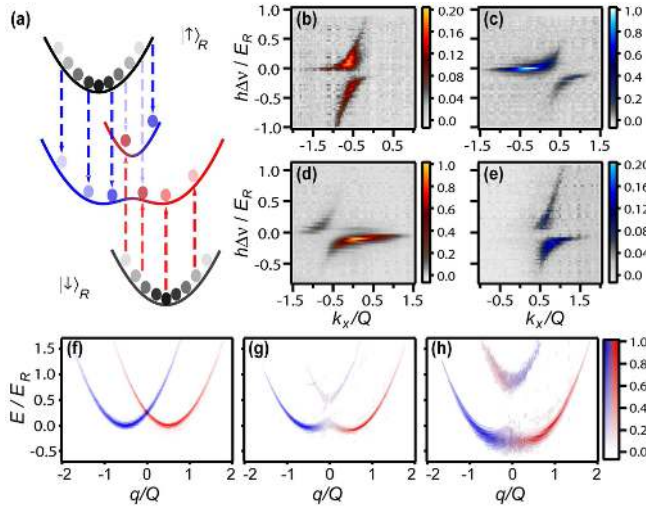


FIG. 2 (color online). Spin-injection spectroscopy. (a) An rf pulse injects atoms from the reservoir states (shown in black)  $|\uparrow\rangle_R$  and  $|\downarrow\rangle_R$  into the spin-orbit coupled system (shown in red and blue). Injection occurs when the rf photon energy equals the energy difference between the reservoir state and the spin-orbit coupled state at quasimomentum  $q$ . (b),(c) Spin-resolved  $|\downarrow\rangle$  and  $|\uparrow\rangle$  spectra, respectively, when transferring out of  $|\uparrow\rangle_R$ . Here,  $\hbar\Omega_R = 0.43(5)E_R$  and  $\hbar\delta = 0.00(3)E_R$ . (d),(e) Spin-resolved  $|\downarrow\rangle$  and  $|\uparrow\rangle$  spectra, respectively, when transferring out of  $|\downarrow\rangle_R$  for the same Raman strength  $\hbar\Omega_R$ . (f), (g), and (h) The reconstructed spinful dispersions for  $\hbar\delta = 0.00(3)E_R$  and  $\hbar\Omega_R = 0E_R$ ,  $\hbar\Omega_R = 0.43(5)E_R$ , and  $\hbar\Omega_R = 0.9(1)E_R$ , respectively.

coupled via rf to the state  $|\downarrow\rangle$ , as this connects the first and second lowest hyperfine states. Similarly, an atom in state  $|\uparrow\rangle_R$  can be transferred to  $|\uparrow\rangle$ . rf spin injection does not impart momentum to the atom and occurs when the frequency of the rf pulse matches the energy difference between the spin-orbit coupled bands and the initial reservoir state, as shown in Fig. 2(a). Spin injection from  $|\downarrow\rangle_R$  ( $|\uparrow\rangle_R$ ) populates mostly the region of the spin-orbit coupled bands with a strong admixture of  $|\downarrow\rangle$  ( $|\uparrow\rangle$ ) states. Thus, the use of two reservoir states allows us to measure both the  $|\downarrow\rangle$ -rich and the  $|\uparrow\rangle$ -rich parts of the spin-orbit coupled bands. Following the injection process, the Raman beams are switched off, and the atoms are simultaneously released from the trap. By counting the number of atoms of a given spin and momentum as a function of injection energy after time of flight, we determine the dispersion of the spin-orbit coupled bands along with their spin texture. Note that, while spin-ARPES and previous momentum-resolved spectroscopic techniques in ultracold atoms probe the occupied states of a given system, our spin-injection method probes the unoccupied states. In the case of fermionic superfluids, this would reveal the excited branch of the quasiparticle dispersion.

The topological characteristics of the bands, which are encoded in the eigenstates, can be extracted from the spin and momentum composition. For our spin-orbit system with  $\delta = 0$ , the spin of the eigenstates is confined to the

$y$ - $z$  plane on the Bloch sphere, because the effective magnetic field has no  $\hat{x}$  component. More general couplings may not restrict the spin to a great circle on the Bloch sphere, in which case at least two spin components must be measured for a complete characterization of the bands. This can be achieved by rotating the different spin components onto the measurement basis with an rf pulse.

Applying spin-injection spectroscopy, we have measured the band structure of the equal-part Rashba-Dresselhaus Hamiltonian at  $\delta = 0$  for several  $\Omega_R$ . Figures 2(b)–2(e) show spin- and momentum-resolved spin-injection spectra obtained with atoms starting in the  $|\uparrow\rangle_R$  reservoir (top row) and starting in the  $|\downarrow\rangle_R$  reservoir (bottom row), for the case  $\hbar\Omega_R = 0.43(5)E_R$  and  $\delta = 0$ . The  $(q, \uparrow) \leftrightarrow (-q, \downarrow)$  symmetry of the system can be seen in the spectra in Fig. 2. The energy at each quasimomentum is found by adding the energy injected into the system by the rf pulse to the initial kinetic energy of the free particle in the reservoir. Figures 2(f)–2(h) show the dispersion and spin texture of the bands obtained from the data. As  $\Omega_R$  is increased, we observe the opening of a spin-orbit gap at  $q = 0$ . The spin composition of the bands evolves from purely  $|\uparrow\rangle$  or  $|\downarrow\rangle$  away from the spin-orbit gap to a mixture of the two spin states in the vicinity of the spin-orbit gap, where the spin states are resonantly coupled.

A Fermi gas with the above dispersion has a spinful semimetallic behavior when the Fermi energy lies within the spin-orbit gap. When the Fermi energy is outside the spin-orbit gap, there is a fourfold degeneracy of states at the Fermi surface. Inside the gap, however, the degeneracy is halved. Furthermore, propagation of spin up particles at the Fermi energy can occur only in the positive  $q$  direction, while spin down fermions can propagate only in the opposite direction. For energies within the gap, the system thus acts as a spin-current diode.

An even richer band structure involving multiple spinful bands separated by fully insulating gaps can arise in the presence of a periodic lattice potential. This has been realized for Bose-Einstein condensates by adding rf coupling between the Raman-coupled states  $|\uparrow\rangle$  and  $|\downarrow\rangle$  [20]. Using a similar method, we create a spinful lattice for ultracold fermions and use spin-injection spectroscopy to probe the resulting spinful band structure. The combined Raman-rf coupling scheme is shown in Fig. 3(a). The Raman field couples the states  $|\downarrow, k_x = q\rangle$  and  $|\uparrow, k_x = q + Q\rangle$  with strength  $\Omega_R$ , whereas the rf field couples the states  $|\downarrow, k_x = q\rangle$  and  $|\uparrow, k_x = q\rangle$  with strength  $\Omega_{RF}$ . As a result, the set of coupled states for a given quasimomentum  $q$ , shown in the repeated Brillouin scheme in Fig. 3(b), is  $|\sigma, k_x = q + nQ\rangle$  for integer  $n$  and  $\sigma = \uparrow, \downarrow$ . The lowest four bands are degenerate at the band center  $q = 0$  when  $\Omega_R = \Omega_{RF} = 0$ . The Raman field splits the degeneracy between the first and fourth bands, leaving the other two degenerate. The remaining degeneracy, which is a Dirac point, is removed with the addition of the rf field. Thus,

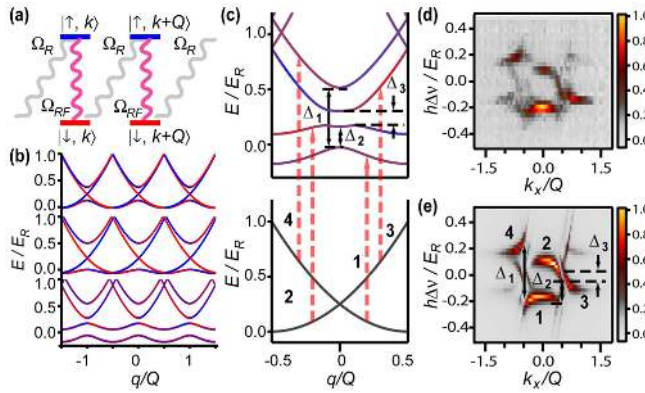


FIG. 3 (color online). Creating and probing a spin-orbit coupled lattice. (a) The addition of a radio frequency field allows momentum transfer of any multiple of  $Q$ , producing a spinful lattice band structure. (b) The band structure of the Raman-rf system in the repeated zone scheme. Band structures from top to bottom correspond to  $\hbar\Omega_{\text{RF}} = 0$  and  $\hbar\Omega_R = 0.25E_R$ ,  $\hbar\Omega_R = 0.5E_R$  and  $\hbar\Omega_{\text{RF}} = 0$ , and  $\hbar\Omega_R = 0.5E_R$  and  $\hbar\Omega_{\text{RF}} = 0.25E_R$ . In the bottommost band, all degeneracies are lifted. (c) Spin injection from free particle bands to spinful lattice bands, starting from  $|\downarrow\rangle_R$ . Transitions near zero rf detuning ( $\hbar\Delta\nu \sim 0$ ) that give rise to dominant spectral features are identified. (d) Experimental spectrum of the Raman-rf system with  $\hbar\Omega_R = 0.40(5)E_R$  and  $\hbar\Omega_{\text{RF}} = 0.28(2)E_R$  in the spin  $|\downarrow\rangle$  channel after injection from reservoir  $|\downarrow\rangle_R$ . (e) Theoretical spectra corresponding to (d). Features corresponding to the gaps and transitions identified in (c) are labeled.

when the system is filled up to the top of the second band, it is an insulator. Furthermore, when  $\Omega_{\text{RF}}$  is large enough, a band gap also opens between the first and second bands.

Figure 3(d) shows the  $|\downarrow\rangle$  channel of the spin-injection spectra, measured with fermions initially in reservoir state  $|\downarrow\rangle_R$ . Spectra with injection from  $|\downarrow\rangle_R$  is sufficient to reconstruct the full band structure given the  $(q, \uparrow) \leftrightarrow (-q, \downarrow)$  symmetry of the Hamiltonian. The transitions between the reservoir and the spin-orbit coupled bands for  $\hbar\Omega_R = 0.40(5)E_R$  and  $\hbar\Omega_{\text{RF}} = 0.28(2)E_R$  are shown in Fig. 3(c). The experimental spectrum in Fig. 3(d) is compared to the theoretically calculated spectrum, shown in Fig. 3(e). The spectrum exhibits four prominent features separated by three energy gaps, labeled  $\Delta_1$ ,  $\Delta_2$ , and  $\Delta_3$  in Fig. 3(e). The gaps giving rise to these features are shown on the band structure in Fig. 3(c). The gap  $\Delta_1$  is opened by the spin-orbit coupling, while  $\Delta_2$  is opened by a direct rf coupling, and  $\Delta_3$  is opened by a second-order process that involves both the rf and Raman fields, explaining its smallness. We have explored the Raman-rf system for a range of coupling strengths as shown in the spectra in Figs. 4(a) and 4(b). With a careful choice of the Raman-rf coupling strengths, spinful flat bands can be realized (see Supplemental Material, Fig. S3 [15]), where interactions should play a dominant role [21].

To illustrate how the energy bands along with the corresponding eigenstates can be extracted, we reconstruct the

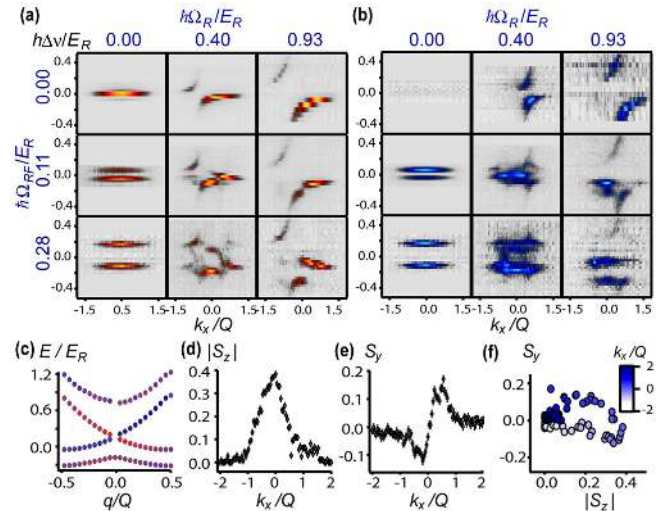


FIG. 4 (color online). Evolution of spin-textured energy bands of a spin-orbit coupled lattice. (a),(b) Experimental Raman-rf spin-injection spectra for injection from  $|\downarrow\rangle_R$  for channels  $|\downarrow\rangle$  and  $|\uparrow\rangle$ , respectively. The color map used is the same as Figs. 2(b) and 2(e) after rescaling to the maximum intensity. Interaction effects between  $|\uparrow\rangle$  with  $|\downarrow\rangle_R$  (see Fig. S4) makes only the dominant features resolvable in  $|\uparrow\rangle$ , while finer features are visible in  $|\downarrow\rangle$ . (c) Reconstructed band structure for  $\hbar\Omega_R = 0.93(7)E_R$  and  $\hbar\Omega_{\text{RF}} = 0.28(2)E_R$ . Color indicates the spin texture. (d)–(f) Experimentally measured spin components  $S_y$  and  $|S_z|$  as a function of momentum  $k_x$  for the lattice wave functions corresponding to the bottommost band in (c).

energy bands along with the spin texture for  $\hbar\Omega_R = 0.93(7)E_R$  and  $\hbar\Omega_{\text{RF}} = 0.28(2)E_R$ , as shown in Fig. 4(c). The energies of the bands are obtained from the resonant frequencies in the spin-injection spectra, while the spin composition  $S_{y,z}$  is extracted from the relative weights of the signal in the two spin channels (see Supplemental Material [15]). In Figs. 4(d)–4(f), we show the extracted value of  $S_y(k_x)$  and  $|S_z(k_x)|$  for the bottommost band when  $\hbar\Omega_R = 0.93(7)E_R$  and  $\hbar\Omega_{\text{RF}} = 0.28(2)E_R$ . For more general spin-orbit Hamiltonians involving  $\sigma_x$ , one can extract the phase between all three components of  $\vec{S}(k_x)$  with additional rf pulses and fully characterize the eigenstate for the corresponding quasimomentum  $q$ . The topology of the band, encoded in the evolution of its eigenstates across the Brillouin zone, can thus be measured.

In summary, we have created and directly probed a spin-orbit gap in a Fermi gas of ultracold atoms and realized a fully gapped band structure allowing for spinful flat bands. We introduced spin-injection spectroscopy to characterize the spin-textured energy-momentum dispersion. We further show that spin-injection spectroscopy allows reconstruction of eigenstates in a spinful lattice system. Extensions of this method can reveal the nontrivial topology of bands in more general spin-orbit coupled systems [22], opening a path to probing topological insulators with ultracold atoms. Similar spectroscopic techniques should

allow the demonstration of effective *p*-wave interactions in a single component spin-orbit coupled Fermi gas, either near an *s*-wave Feshbach resonance or for flat bands as realized here. In these systems, interactions may lead to BCS pairing in a *p*-wave channel and, in a two-dimensional Fermi gas with pure Rashba coupling, to  $p_x + ip_y$  pairing and chiral superfluidity [23,24].

This work was supported by the NSF, a grant from the Army Research Office with funding from the DARPA OLE program, ARO-MURI on Atomtronics, AFOSR-MURI, ONR YIP, DARPA YFA, an AFOSR PECASE, and the David and Lucile Packard Foundation. Z. H. acknowledges funding from EPSRC under Grant No. EP/I010580/1.

- [1] M. Z. Hasan and C. L. Kane, *Rev. Mod. Phys.* **82**, 3045 (2010).
- [2] X.-L. Qi and S.-C. Zhang, *Rev. Mod. Phys.* **83**, 1057 (2011).
- [3] R. Winkler, *Spin-Orbit Coupling Effects in Two-Dimensional Electron and Hole Systems*, Springer Tracts Mod. Phys. Vol. 191 (Springer, Berlin, 2003).
- [4] Y. A. Bychkov and E. I. Rashba, *J. Phys. C* **17**, 6039 (1984).
- [5] G. Dresselhaus, *Phys. Rev.* **100**, 580 (1955).
- [6] C. H. L. Quay, T. L. Hughes, J. A. Sulpizio, L. N. Pfeiffer, K. W. Baldwin, K. W. West, D. Goldhaber-Gordon, and R. de Picciotto, *Nature Phys.* **6**, 336 (2010).
- [7] S. Nadj-Perge, V. S. Pribiag, J. W. G. van den Berg, K. Zuo, S. R. Plissard, E. P. A. M. Bakkers, S. M. Frolov, and L. P. Kouwenhoven, *Phys. Rev. Lett.* **108**, 166801 (2012).
- [8] X.-J. Liu, M. F. Borunda, X. Liu, and J. Sinova, *Phys. Rev. Lett.* **102**, 046402 (2009).
- [9] J. Dalibard, F. Gerbier, G. Juzeliūnas, and P. Öhberg, *Rev. Mod. Phys.* **83**, 1523 (2011).
- [10] Y.-J. Lin, Jiménez-García, and I. B. Spielman, *Nature (London)* **471**, 83 (2011).
- [11] Y.-J. Lin, R. L. Compton, Jiménez-García, J. V. Porto, and I. B. Spielman, *Nature (London)* **462**, 628 (2009).
- [12] M. Aidelberger, M. Atala, S. Nascimbéne, S. Trotzky, Y.-A. Chen, and I. Bloch, *Phys. Rev. Lett.* **107**, 255301 (2011).
- [13] P. Wang, Z.-Q. Yu, Z. Fu, J. Miao, L. Huang, S. Chai, H. Zhai, and J. Zhang, preceding Letter, *Phys. Rev. Lett.* **109**, 095301 (2012).
- [14] E. Zhao, N. Bray-Ali, C. J. Williams, I. B. Spielman, and I. I. Satija, *Phys. Rev. A* **84**, 063629 (2011).
- [15] See Supplemental Material at <http://link.aps.org/supplemental/10.1103/PhysRevLett.109.095302> for details of the experimental setup and data analysis.
- [16] Z. Hadzibabic, S. Gupta, C. A. Stan, C. H. Schunck, M. W. Zwierlein, K. Dieckmann, and W. Ketterle, *Phys. Rev. Lett.* **91**, 160401 (2003).
- [17] M. Hoesch, T. Greber, V. N. Petrov, M. Muntwiler, M. Hengsberger, W. Auwarter, and J. Osterwalder, *J. Electron Spectrosc. Relat. Phenom.* **124**, 263 (2002).
- [18] D. Hsieh, Y. Xia, L. Wray, D. Qian, A. Pal, J. H. Dil, J. Osterwalder, F. Meier, G. Bihlmayer, C. L. Kane, Y. S. Hor, R. J. Cava, and M. Z. Hasan, *Science* **323**, 919 (2009).
- [19] J. T. Stewart, J. P. Gaebler, and D. S. Jin, *Nature (London)* **454**, 744 (2008).
- [20] K. Jiménez-García, L. J. LeBlanc, R. A. Williams, M. C. Beeler, A. R. Perry, and I. B. Spielman, *Phys. Rev. Lett.* **108**, 225303 (2012).
- [21] K. Sun, Z. Gu, H. Katsura, and S. Das Sarma, *Phys. Rev. Lett.* **106**, 236803 (2011).
- [22] J. D. Sau, R. Sensarma, S. Powell, I. B. Spielman, and S. Das Sarma, *Phys. Rev. B* **83**, 140510 (2011).
- [23] R. A. Williams, L. J. LeBlanc, K. Jiménez-García, M. C. Beeler, A. R. Perry, W. D. Phillips, and I. B. Spielman, *Science* **335**, 314 (2011).
- [24] C. Zhang, S. Tewari, R. M. Lutchyn, and S. Das Sarma, *Phys. Rev. Lett.* **101**, 160401 (2008).

## Appendix F

# Quantum-Gas Microscope for Fermionic Atoms

This appendix contains a reprint of the following paper [22]:

L. W. Cheuk, M. A. Nichols, M. Okan, T. Gersdorf, V. V. Ramasesh, W. S. Bakr, T. Lompe, and M. W. Zwierlein, “Quantum-Gas Microscope for Fermionic Atoms,” Phys. Rev. Lett. **114**, 193001 (2015).



## Quantum-Gas Microscope for Fermionic Atoms

Lawrence W. Cheuk, Matthew A. Nichols, Melih Okan, Thomas Gersdorf, Vinay V. Ramasesh,  
Waseem S. Bakr, Thomas Lompe, and Martin W. Zwierlein

Department of Physics, MIT-Harvard Center for Ultracold Atoms and Research Laboratory of Electronics,  
MIT, Cambridge, Massachusetts 02139, USA

(Received 30 March 2015; published 13 May 2015)

We realize a quantum-gas microscope for fermionic  $^{40}\text{K}$  atoms trapped in an optical lattice, which allows one to probe strongly correlated fermions at the single-atom level. We combine 3D Raman sideband cooling with high-resolution optics to simultaneously cool and image individual atoms with single-lattice-site resolution at a detection fidelity above 95%. The imaging process leaves the atoms predominantly in the 3D motional ground state of their respective lattice sites, inviting the implementation of a Maxwell's demon to assemble low-entropy many-body states. Single-site-resolved imaging of fermions enables the direct observation of magnetic order, time-resolved measurements of the spread of particle correlations, and the detection of many-fermion entanglement.

DOI: 10.1103/PhysRevLett.114.193001

PACS numbers: 37.10.De, 03.75.Ss, 37.10.Jk, 67.85.Lm

The collective behavior of fermionic particles governs the structure of the elements, the workings of high-temperature superconductors and colossal magnetoresistance materials, and the properties of nuclear matter. Yet our understanding of strongly interacting Fermi systems is limited, due in part to the antisymmetry requirement on the many-fermion wave function and the resulting “fermion sign problem” [1]. In recent years, ultracold atomic quantum gases have enabled quantitative experimental tests of theories of strongly interacting fermions [2–5]. In particular, fermions trapped in optical lattices can directly simulate the physics of electrons in a crystalline solid, shedding light on novel physical phenomena in materials with strong electron correlations. A major effort is devoted to the realization of the Fermi-Hubbard model at low entropies, believed to capture the essential aspects of high- $T_c$  superconductivity [6–12]. For bosonic atoms, a new set of experimental probes ideally suited for the observation of magnetic order and correlations has become available with the advent of quantum-gas microscopes [13–15], enabling high-resolution imaging of Hubbard-type lattice systems at the single-atom level. They allowed the direct observation of spatial structures and ordering in the Bose-Hubbard model [14,16] and of the intricate correlations and dynamics in these systems [17,18]. A longstanding goal has been to realize such a quantum-gas microscope for fermionic atoms. This would enable the direct probing and control at the single-lattice-site level of strongly correlated fermion systems, in particular the Fermi-Hubbard model, in regimes that cannot be described by current theories. These prospects have sparked significant experimental efforts to realize site-resolved, high-fidelity imaging of ultracold fermions, but this goal has so far remained elusive.

In the present work, we realize a quantum-gas microscope for fermionic  $^{40}\text{K}$  atoms by combining 3D Raman

sideband cooling with a high-resolution imaging system. The imaging setup incorporates a hemispherical solid immersion lens optically contacted to the vacuum window [Fig. 1(a)]. In combination with a microscope objective with numerical aperture (NA) of 0.60, the system achieves an enhanced NA of 0.87 while eliminating aberrations that would arise from a planar vacuum window. In order to keep the atoms localized while performing fluorescence imaging, one must simultaneously cool them in order to mitigate the heating from spontaneously emitted imaging photons. Previous microscope experiments in Hubbard-type lattices [13–15] cool via optical molasses. In contrast, we employ 3D Raman sideband cooling [19–27], in which Raman transitions on vibration-lowering sidebands are combined with optical pumping to provide cooling. Our method therefore not only achieves site-resolved imaging, but also

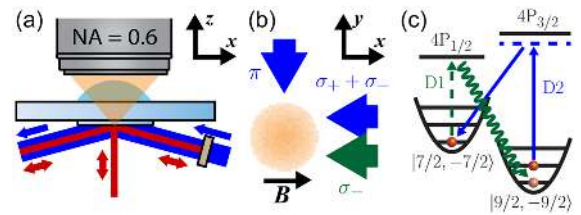


FIG. 1 (color online). (a) High-resolution imaging setup. A solid immersion lens is formed by a spherical cap and a superpolished substrate contacted on either side of the vacuum window. Using an objective with  $\text{NA} = 0.60$ , the system achieves an effective  $\text{NA} = 0.87$ . The substrate reflects 1064-nm light while transmitting  $D_1$  and  $D_2$  light of  $^{40}\text{K}$ . The lattice beams are shown in red; the optical pumping and  $x$  Raman beams are shown in blue. (b) Top view of Raman beams (blue) and optical pumping beam (green). (c) Raman cooling scheme. The Raman beams detuned near the  $D_2$  line (solid blue) drive vibration-lowering transitions. The optical  $F$ -pumping beam (dashed green) is tuned to the  $D_1$  line. Not shown is the  $m_F$ -pumping beam.

leaves a large fraction of the atoms [72(3)%] in the 3D motional ground state of each lattice site. This opens up prospects for the preparation of low-entropy many-body states, by measuring the atoms' initial positions and rearranging them into the desired configuration [28].

Raman sideband cooling has previously been used to cool  $^{87}\text{Rb}$  and  $^{133}\text{Cs}$  atoms in lattices and in optical tweezers to large ground-state populations [20–27]. Here, we realize continuous Raman sideband cooling of  $^{40}\text{K}$  using two states from the ground hyperfine manifolds,  $|a\rangle = |F = 9/2, m_F = -9/2\rangle$  and  $|b\rangle = |7/2, -7/2\rangle$ , which form an approximate two-level system. To make  $|a\rangle$  and  $|b\rangle$  nondegenerate with other hyperfine states, and to provide a quantization axis for optical pumping, we apply a bias field of 4.2 G along the  $x$  direction [Fig. 1(b)]. A pair of Raman beams collinear with  $x$  and  $y$  lattice beams, but not retroreflected, drives vibration-lowering Raman transitions from  $|a\rangle$  to  $|b\rangle$  [Fig. 1(c)]. The Raman lasers are detuned  $-41$  GHz from the  $D_2$  transition. The optical pumping is performed on the  $D_1$  transition, 3 nm away from the  $D_2$  line, allowing us to filter out stray Raman light while transmitting atomic fluorescence. The optical pumping light contains two frequencies, one to remove atoms from the  $F = 7/2$  manifold ( $F$  pumping), and the other to remove atoms from all states  $|F = 9/2, m_F\rangle$  with  $m_F \neq -9/2$  ( $m_F$  pumping). By collecting the photons that are spontaneously scattered during this optical pumping process, we can image the atoms without using additional resonant light.

To prepare a cold cloud of fermionic atoms under the microscope,  $^{40}\text{K}$  is first sympathetically cooled with  $^{23}\text{Na}$  in a plugged magnetic quadrupole trap [29], centered  $\sim 9$  mm below a superpolished substrate that forms the bottom of the solid immersion lens. After removal of  $^{23}\text{Na}$ , the cloud of  $\sim 1 \times 10^6$   $^{40}\text{K}$  atoms is magnetically transported to the substrate and trapped in a vertical lattice formed by a 1064-nm laser beam reflected off the substrate at an angle of  $5.9^\circ$ . A single layer  $7.8 \mu\text{m}$  from the surface can be selected using a radiofrequency sweep in a vertical magnetic gradient followed by a resonant light pulse that removes atoms in the remaining layers. Next, we prepare a 50:50 mixture of  $|9/2, -9/2\rangle$  and  $|9/2, -7/2\rangle$  to allow thermalization, and transfer the atoms to a vertical ( $z$  direction) 1064-nm beam, forming a lattice along  $z$  with a spacing of 532 nm [Fig. 1(a)]. After evaporating by lowering the power of the  $z$  lattice, the  $z$  depth is increased to  $180 \mu\text{K}$ . We simultaneously ramp up two additional 1064-nm beams [Fig. 1(a)] reflected off the substrate at  $10.8^\circ$  and retroreflected. These form a lattice in the horizontal plane with a spacing of 541 nm [30].

During imaging, the atoms are trapped in a deep lattice, where the potential at each lattice site can be approximated by a harmonic well with vibrational frequency  $\omega$ . At our imaging depth, the vibrational frequencies for the three axes are  $(\omega_x, \omega_y, \omega_z) = 2\pi \times (280, 300, 260)$  kHz,

corresponding to lattice depths of  $220 \mu\text{K}$ ,  $250 \mu\text{K}$ , and  $190 \mu\text{K}$ , respectively. The Rabi coupling for transitions that change the vibrational number by 1 is proportional to the Lamb-Dicke parameter,  $\eta = \Delta ka$ , where  $a = \sqrt{\hbar/2m\omega}$  is the harmonic oscillator length and  $\hbar\Delta k$  is the momentum transfer due to the Raman beams. Along our lattice directions,  $\Delta k_x = 8.0 \mu\text{m}^{-1}$ ,  $\Delta k_y = 8.0 \mu\text{m}^{-1}$ , and  $\Delta k_z = 3.1 \mu\text{m}^{-1}$ , yielding Lamb-Dicke parameters of 0.17 for  $x$  and  $y$ , and 0.068 for  $z$ . The polarizations of both Raman beams are linear and parallel to the substrate [Fig. 1(b)], in order to avoid differential effective magnetic fields between  $|a\rangle$  and  $|b\rangle$  originating from vector light shifts that would arise for circularly polarized light. The Raman beam along the  $y$  axis contains a single frequency, whereas the Raman beam along the  $x$  axis contains three frequencies, allowing us to address the cooling sidebands of the three directions simultaneously. The resulting two-photon detunings from the bare  $|a\rangle \rightarrow |b\rangle$  transition are 400 kHz, 450 kHz, and 360 kHz for cooling along  $x$ ,  $y$ , and  $z$ , respectively. These frequencies compensate for differential Stark shifts that arise in the presence of optical pumping light. The  $x$  Raman beam intensities of the three frequency components are  $0.79 \text{ W/cm}^2$ ,  $0.47 \text{ W/cm}^2$ , and  $0.49 \text{ W/cm}^2$ , respectively; the intensity of the  $y$  Raman beam is  $2.0 \text{ W/cm}^2$ .

In addition to these Raman beams, optical pumping light is present to complete the cooling cycle. During optical pumping, atoms enter electronically excited states, and preferentially decay into the desired state. Typically, the excited states experience an antitrapping potential when the ground-state experiences a trapping potential. For our 1064-nm lattice, the anti-trapping potential for the atoms in the  $4P_{1/2}$  states is 5.4 times stronger than the trapping potential for atoms in the  $4S_{1/2}$  states, due to the  $4P_{1/2} \rightarrow 3D_{3/2}$  transition at 1169 nm. This strong antitrapping would lead to heating and diffusion of atoms through the lattice during imaging.

A solution to this problem is to detune the optical pumping light away from resonance. This reduces the population in the antitrapping states and favors transitions into trapping states. To understand this, we model the optical pumping process using a driven two-level system whose excited state is coupled to a dark state  $|D\rangle$  via spontaneous emission. In this system, the bare states experience spatially dependent light shifts due to the optical lattice formed by the 1064-nm beams, as illustrated in Fig. 2. The states dressed by the optical pumping light are labeled  $|g, N\rangle$  and  $|e, N\rangle$ , and are superpositions of the bare electronic ground state with  $N$  photons and the bare excited state with  $N - 1$  photons [Fig. 2(a); see Supplemental Material [31]]. In the presence of resonant pumping light, neither of the dressed states is trapping [Fig. 2(b)], which leads to heating.

However, at large detunings  $\delta \gg \Omega$ , where  $\Omega$  is the Rabi frequency, one dressed state becomes trapping. Furthermore, spontaneous decay among the dressed states

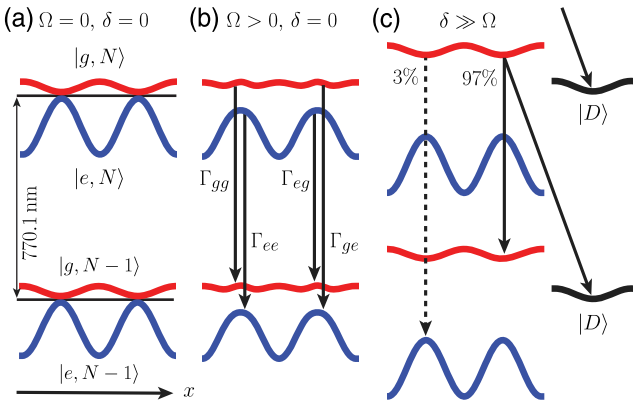


FIG. 2 (color online). (a) Electronic ground ( $|g, N\rangle$ ) and excited ( $|e, N\rangle$ ) states dressed by optical pumping photons. (b) On resonance, all dressed states are equally populated and experience an antitrapping potential. The four decay channels between the dressed states are equal. (c) The dressed states with  $\Omega/\delta = 0.175$ , shown with the dark state  $|D\rangle$ . Only a small fraction  $\Omega^4/\delta^4$  of the steady-state population resides in antitrapping states. For the atoms in the trapping state, the branching ratios between trapping transitions (solid arrows) and antitrapping transitions (dashed arrow) are shown.

favors population in the trapping states. Specifically, the decay rates  $\Gamma_{eg}$ ,  $\Gamma_{ee}$ ,  $\Gamma_{gg}$ , and  $\Gamma_{ge}$ , defined in Fig. 2(b), are proportional to 1,  $s$ ,  $s$ , and  $s^2$ , respectively, where  $s = \Omega^2/(4\delta^2)$ . The ratio of the antitrapped population to the trapped population is suppressed, because in steady state, it is given by  $\Gamma_{ge}/\Gamma_{eg}$  which scales as  $s^2$ . Another benefit of large detunings involves the state  $|D\rangle = |9/2, -9/2\rangle$  into which atoms are optically pumped [Fig. 2(c)]. This state is dark to the optical pumping light, and hence has no excited state admixture; consequently, it experiences a trapping potential. Atoms in trapping states  $|g, N\rangle$  decay preferentially into trapping states or  $|D\rangle$ , since

the ratio of antitrapping transitions to dark state transitions scales as  $\Gamma_{ge}/\Gamma_{gg} = s$ , which is small at large  $\delta$ .

In light of these considerations, we detune the hyperfine-changing ( $F$ ) pumping light  $-80$  MHz from the Stark-shifted  $F = 7/2 \rightarrow F' = 9/2$  transition and the Zeeman-level ( $m_F$ ) pumping light  $-80$  MHz from the Stark-shifted  $F = 9/2 \rightarrow F' = 7/2$  transition. The optical pumping beam copropagates with the  $x$  Raman beam, and has its polarization optimized for minimal  $\sigma_+$  admixture. The  $F$  and  $m_F$  components have intensities of  $5.8$  mW/cm $^2$  and  $1.6$  mW/cm $^2$ , respectively; the Lamb-Dicke parameters for optical pumping are  $\sim 0.18$  for all directions.

This Raman cooling scheme allows us to collect fluorescence while keeping the atoms confined to their lattice sites [Fig. 3(a)]. Furthermore, we find that atoms are cooled predominantly into their motional ground state. Indeed, Raman spectroscopy after cooling reveals vibrational ground-state populations of  $0.92(2)$ ,  $0.92(2)$ , and  $0.85(2)$  along  $x$ ,  $y$ , and  $z$ , respectively [Fig. 3(b)]. This corresponds to a 3D ground-state population of  $72(3)\%$ . Note that parameters are optimized for imaging fidelity rather than for a large ground-state population. We measure a fluorescence rate of  $\sim 5000$  photons/(atoms) with a lifetime of  $\sim 30$  s. With a photon collection and detection efficiency of  $20\%$ , about  $1000$  photons per atom can be collected in an exposure time of  $1$  s, which is sufficient to detect single atoms with high fidelity. Since the system is in steady state, the cooling rate is equal to the heating rate, which can be estimated by the number of scattered photons and the Lamb-Dicke parameter. This gives a cooling rate of  $\sim 2$   $\mu\text{K}/\text{ms}$ .

To verify that we can resolve individual lattice sites, we measure the point spread function (PSF) of our imaging system using isolated atoms from sparsely populated images. The measured PSF has a full width half maximum (FWHM) of  $640$  nm [Fig. 4(a)]. Images are deconvolved

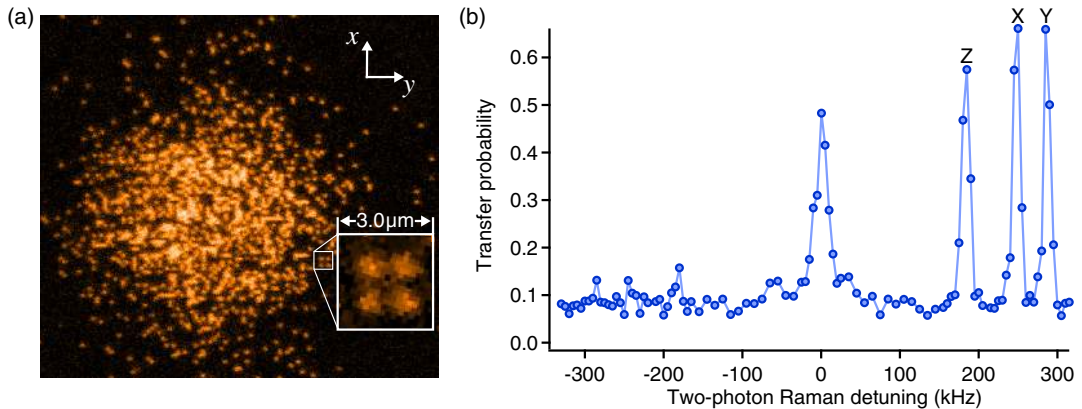


FIG. 3 (color online). (a) Site-resolved imaging of fermionic atoms on a densely filled 541-nm-period optical lattice, with an exposure time of  $2$  s; one can clearly discern the lattice structure and individual atoms. (b) Raman spectrum after cooling. The lattice depths are chosen such that the vibrational sidebands are well resolved. The heating sidebands for the three lattice axes are labeled  $Z$ ,  $X$ , and  $Y$ . We observe a large sideband asymmetry, from which we extract a 3D ground-state occupation of  $72(3)\%$  [19].

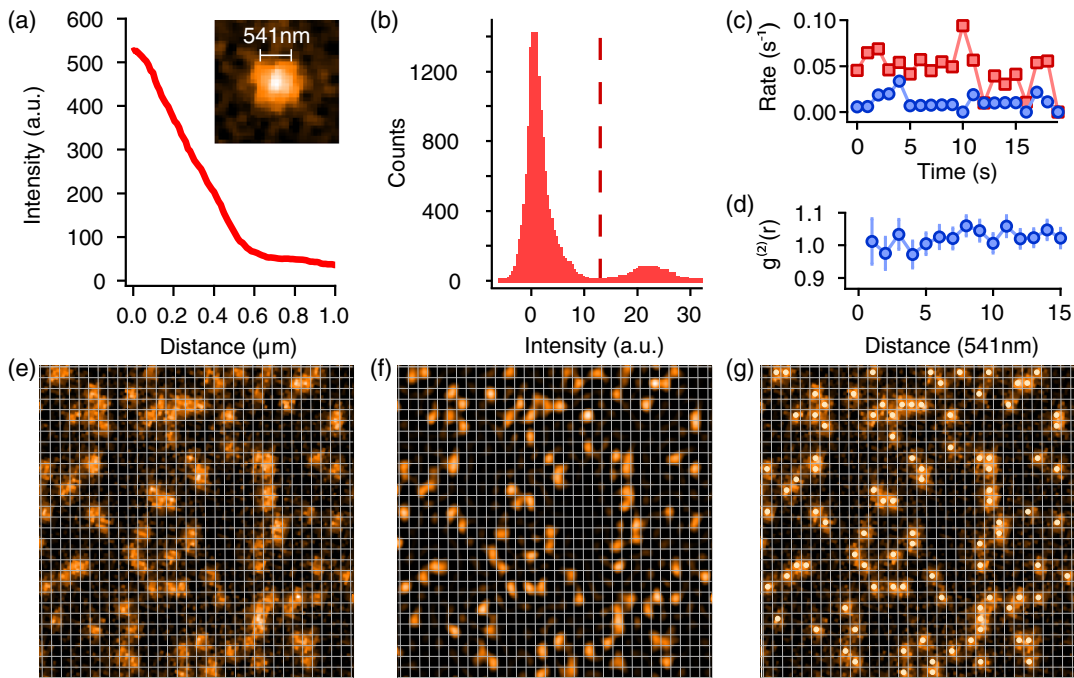


FIG. 4 (color online). (a) Radially averaged PSF extracted from isolated atoms; the FWHM is 640 nm. (b) Intensity histogram after binning the deconvolved images by lattice site. The threshold for reconstruction is shown by the dashed line. (c) Loss and hopping rates, shown in red squares and blue circles, respectively, as extracted from 20 consecutive 1-s exposures. (d) Correlation measurement  $g^{(2)}(r)$  of a thermal cloud with filling of 0.19, showing the absence of distance-dependent loss. (e) Image of sparsely filled lattice with grid lines showing lattice spacing and orientation. The exposure time is 1 s. (f),(g) The same image after deconvolution and with the filled sites identified.

with the PSF to achieve sublattice-site resolution. From such images, we also extract the lattice axes and spacings necessary to reconstruct the atomic distribution. Binning the intensity of the deconvolved image by lattice site reveals a clear bimodal distribution [Fig. 4(b)], which is used to determine whether a site is filled [Figs. 4(e), 4(f), 4(g)]. This bimodality gives a reconstruction error of  $<1\%$ .

An important aspect of quantum-gas microscopy is the fidelity of the imaging process, which can be characterized by hopping and loss rates. To this end, we take a series of images of the same atomic cloud and observe changes in the site occupations between images. Sites that are empty but become occupied in a subsequent image are counted as hopping events; sites that become empty are counted as loss events. The Raman cooling parameters are optimized for low hopping and loss rates while maintaining a fixed level of fluorescence. For optimized parameters, we achieve loss rates of  $<4.8 \pm 0.2\%$  and hopping rates of  $<1.2 \pm 0.2\%$  for 1-s exposures of clouds with fillings between 0.10 and 0.20 [Fig. 4(c)]. These rates, which include reconstruction errors, give a detection fidelity of  $>95\%$  for sparse clouds. At higher fillings, hopping events lead to loss of additional atoms in doubly occupied sites due to light-assisted collisions. However, even for unity filling, we estimate the imaging fidelity to still be  $>94\%$ , because of the low hopping rate.

To ensure that the imaging does not cause additional losses for neighboring atoms, one can measure the 2-point correlation function  $g^{(2)}(r) = \langle n(x)n(x+r) \rangle / \langle n \rangle^2$  of thermal clouds, since distance-dependent loss will produce anticorrelations at short distances. For a dilute thermal cloud with a filling of 0.19, one  $29 \times 32$  site image gives  $g^{(2)}(r) = 1.00(7)$  for distances from  $r = 1$  to 10 lattice spacings, indicating that the imaging does not cause significant distance-dependent loss [Fig. 4(d)].

In conclusion, we have realized high-fidelity site-resolved imaging of  $^{40}\text{K}$  fermionic atoms in a Hubbard-type optical lattice by combining 3D Raman sideband cooling with high-resolution photon collection. In contrast to existing boson microscopes, the technique leaves atoms predominantly in the absolute 3D ground state of a given lattice site. This opens up new ways to assemble low-entropy Fermi-Hubbard systems atom by atom [28,32,33]. Combining site-resolved imaging with on-site-manipulation would allow one to deterministically create localized excitations and follow their time evolution [18]. Finally, the presence of  $^{23}\text{Na}$  in our system invites the realization of a quantum-gas microscope for ultracold fermionic NaK molecules [34], which have been proposed as a new resource for quantum information processing and quantum simulation of lattice models with long-range dipolar interactions.

We would like to thank Katherine Lawrence for experimental assistance and critical readings of the manuscript, and the Greiner group and Vladan Vuletić for fruitful discussions. This work was supported by the NSF, AFOSR-PECASE, AFOSR-MURI on Exotic Phases of Matter, ARO-MURI on Atomtronics, ONR, a grant from the Army Research Office with funding from the DARPA OLE program, and the David and Lucile Packard Foundation.

*Note added.*—Recently, single-site-imaging for fermionic atoms has also been reported for  $^{40}\text{K}$  and  $^6\text{Li}$  [35,36].

- [1] E. Y. Loh, J. E. Gubernatis, R. T. Scalettar, S. R. White, D. J. Scalapino, and R. L. Sugar, *Phys. Rev. B* **41**, 9301 (1990).
- [2] Ultracold Fermi Gases, *Proceedings of the International School of Physics “Enrico Fermi”*, edited by M. Inguscio, W. Ketterle, and C. Salomon, Course CLXIV (IOS Press, Amsterdam, 2008).
- [3] I. Bloch, J. Dalibard, and W. Zwerger, *Rev. Mod. Phys.* **80**, 885 (2008).
- [4] *The BCS-BEC Crossover and the Unitary Fermi Gas*, Vol. 836, edited by Q. Zwerger (Springer, New York, 2011).
- [5] M. W. Zwierlein, in *Novel Superfluids*, Vol. 2, edited by K.-H. Bennemann and J. B. Ketterson (Oxford University Press, Oxford, 2014).
- [6] T. Esslinger, *Annu. Rev. Condens. Matter Phys.* **1**, 129 (2010).
- [7] J. Chin, D. Miller, Y. Liu, C. Stan, W. Setiawan, C. Sanner, K. Xu, and W. Ketterle, *Nature (London)* **443**, 961 (2006).
- [8] R. Jördens, N. Strohmaier, K. Günter, H. Moritz, and T. Esslinger, *Nature (London)* **455**, 204 (2008).
- [9] U. Schneider, L. Hackermüller, S. Will, T. Best, I. Bloch, T. A. Costi, R. W. Helmes, D. Rasch, and A. Rosch, *Science* **322**, 1520 (2008).
- [10] D. Greif, T. Uehlinger, G. Jotzu, L. Tarruell, and T. Esslinger, *Science* **340**, 1307 (2013).
- [11] J. Imriška, M. Iazzi, L. Wang, E. Gull, D. Greif, T. Uehlinger, G. Jotzu, L. Tarruell, T. Esslinger, and M. Troyer, *Phys. Rev. Lett.* **112**, 115301 (2014).
- [12] R. A. Hart, P. M. Duarte, T. L. Yang, X. X. Liu, T. Paiva, E. Khatami, R. Scalettar, N. Trivedi, D. A. Huse, and R. G. Hulet, *Nature (London)* **519**, 211 (2015).
- [13] W. S. Bakr, J. I. Gillen, A. Peng, S. Fölling, and M. Greiner, *Nature (London)* **462**, 74 (2009).
- [14] J. F. Sherson, C. Weitenberg, M. Endres, M. Cheneau, I. Bloch, and S. Kuhr, *Nature (London)* **467**, 68 (2010).
- [15] M. Miranda, R. Inoue, Y. Okuyama, A. Nakamoto, and M. Kozuma, [arXiv:1410.5189](https://arxiv.org/abs/1410.5189).
- [16] W. S. Bakr, A. Peng, M. E. Tai, R. Ma, J. Simon, J. I. Gillen, S. Fölling, L. Pollet, and M. Greiner, *Science* **329**, 547 (2010).
- [17] M. Endres, M. Cheneau, T. Fukuhara, C. Weitenberg, P. Schauß, C. Gross, L. Mazza, M. C. Banuls, L. Pollet, I. Bloch, and S. Kuhr, *Science* **334**, 200 (2011).
- [18] M. Cheneau, P. Barmettler, D. Poletti, M. Endres, P. Schauß, T. Fukuhara, C. Gross, I. Bloch, C. Kollath, and S. Kuhr, *Nature (London)* **481**, 484 (2012).
- [19] C. Monroe, D. M. Meekhof, B. E. King, S. R. Jefferts, W. M. Itano, D. J. Wineland, and P. Gould, *Phys. Rev. Lett.* **75**, 4011 (1995).
- [20] S. E. Hamann, D. L. Haycock, G. Klose, P. H. Pax, I. H. Deutsch, and P. S. Jessen, *Phys. Rev. Lett.* **80**, 4149 (1998).
- [21] V. Vuletić, C. Chin, A. J. Kerman, and S. Chu, *Phys. Rev. Lett.* **81**, 5768 (1998).
- [22] A. J. Kerman, V. Vuletić, C. Chin, and S. Chu, *Phys. Rev. Lett.* **84**, 439 (2000).
- [23] D.-J. Han, S. Wolf, S. Oliver, C. McCormick, M. T. DePue, and D. S. Weiss, *Phys. Rev. Lett.* **85**, 724 (2000).
- [24] K. D. Nelson, X. Li, and D. S. Weiss, *Nat. Phys.* **3**, 556 (2007).
- [25] A. M. Kaufman, B. J. Lester, and C. A. Regal, *Phys. Rev. X* **2**, 041014 (2012).
- [26] Y. S. Patil, S. Chakram, L. M. Aycock, and M. Vengalattore, *Phys. Rev. A* **90**, 033422 (2014).
- [27] J. D. Thompson, T. G. Tiecke, A. S. Zibrov, V. Vuletić, and M. D. Lukin, *Phys. Rev. Lett.* **110**, 133001 (2013).
- [28] D. S. Weiss, J. Vala, A. V. Thapliyal, S. Myrgren, U. Vazirani, and K. B. Whaley, *Phys. Rev. A* **70**, 040302 (2004).
- [29] J. W. Park, C.-H. Wu, I. Santiago, T. G. Tiecke, S. Will, P. Ahmadi, and M. W. Zwierlein, *Phys. Rev. A* **85**, 051602 (2012).
- [30] For characterization of the imaging, preparation of a single layer is not necessary since the  $x$  and  $y$  lattice depths, Raman coupling, and optical pumping intensities are sufficiently different such that only the desired layer is imaged.
- [31] See Supplemental Material at <http://link.aps.org/supplemental/10.1103/PhysRevLett.114.193001> for details.
- [32] S. Murmann, A. Bergschneider, V. M. Klinkhamer, G. Zürn, T. Lompe, and S. Jochim, *Phys. Rev. Lett.* **114**, 080402 (2015).
- [33] A. M. Kaufman, B. J. Lester, C. M. Reynolds, M. L. Wall, M. Foss-Feig, K. R. A. Hazzard, A. M. Rey, and C. A. Regal, *Science* **345**, 306 (2014).
- [34] J. W. Park, S. A. Will, and M. W. Zwierlein, [arXiv:1505.00473](https://arxiv.org/abs/1505.00473).
- [35] E. Haller, J. Hudson, A. Kelly, D. A. Cotta, B. Peaudecerf, G. D. Bruce, and S. Kuhr, [arXiv:1503.02005](https://arxiv.org/abs/1503.02005).
- [36] M. F. Parsons, F. Huber, A. Mazurenko, C. S. Chiu, W. Setiawan, K. Wooley-Brown, S. Blatt, and M. Greiner, [arXiv:1504.04397](https://arxiv.org/abs/1504.04397).

## Appendix G

# Observation of 2D Fermionic Mott Insulators of $^{40}\text{K}$ with Single-Site Resolution

This appendix contains a reprint of the following paper [21]:

L. W. Cheuk, M. A. Nichols, K. R. Lawrence, M. Okan, H. Zhang, and M. W. Zwierlein, “Observation of 2D Fermionic Mott Insulators of  $^{40}\text{K}$  with Single-Site Resolution,” *Phys. Rev. Lett.* **114**, 193001 (2016).



## Observation of 2D Fermionic Mott Insulators of $^{40}\text{K}$ with Single-Site Resolution

Lawrence W. Cheuk, Matthew A. Nichols, Katherine R. Lawrence, Melih Okan, Hao Zhang, and Martin W. Zwierlein

*Department of Physics, MIT-Harvard Center for Ultracold Atoms, and Research Laboratory of Electronics,  
MIT, Cambridge, Massachusetts 02139, USA*

(Received 31 March 2016; published 10 June 2016)

We report on the site-resolved observation of characteristic states of the two-dimensional repulsive Fermi-Hubbard model, using ultracold  $^{40}\text{K}$  atoms in an optical lattice. By varying the tunneling, interaction strength, and external confinement, we realize metallic, Mott-insulating, and band-insulating states. We directly measure the local moment, which quantifies the degree of on-site magnetization, as a function of temperature and chemical potential. Entropies per particle as low as  $0.99(6)k_B$  indicate that nearest-neighbor antiferromagnetic correlations should be detectable using spin-sensitive imaging.

DOI: 10.1103/PhysRevLett.116.235301

Strongly correlated fermions present a fundamental challenge to many-body physics, as no general method exists to predict what phenomena will emerge [1]. Ultracold gases of fermionic atoms have shown promise as a clean, highly controllable platform for studying such systems [2,3]. One prominent example is the realization of strongly coupled fermionic superfluids, enabled by the enhanced interactions that arise near a Feshbach resonance [4,5]. Another class of strongly correlated systems well suited for simulation with ultracold atoms is lattice models, in which the kinetic and interaction energies can be set to comparable strengths [3,6]. One such model is the Fermi-Hubbard model, believed to capture the essential aspects of high-temperature superconductivity [7,8].

The realization of the Fermi-Hubbard model at low entropies has been a longstanding goal in ultracold atom experiments. Mott-insulating behavior has been observed in three dimensions (3D) via reduction of double occupancies and compressibility [9–12]. Short-range antiferromagnetic correlations above the Néel temperature were observed via Bragg scattering and dimerized lattices [13–15]. Recently, the equation of state of the Fermi-Hubbard model has been measured in two dimensions (2D) for spin 1/2 and in 3D for higher spin values [16,17]. However, these experiments relied on conventional imaging techniques that do not allow site-resolved measurements of microscopic quantities.

Such microscopic measurements first became possible in bosonic systems through the development of quantum gas microscopes with single-site resolution, and have enabled studies of ordering, spatial structures, and correlations in the Bose-Hubbard model [18–21]. Recently, the ability to perform single-site imaging has been extended to the two workhorse fermionic isotopes of alkali atoms,  $^6\text{Li}$  and  $^{40}\text{K}$  [22–26]. While  $^6\text{Li}$  has faster lattice dynamics due to its smaller mass,  $^{40}\text{K}$  features a larger fine structure splitting, which is beneficial for implementing spin-dependent potentials and spin-orbit coupling.

After initial demonstrations of site-resolved imaging of nondegenerate Fermi gases, the goal has been to apply

these imaging techniques to low-entropy degenerate gases in order to study quantum many-body phenomena. Within the past few months, Pauli blocking was directly observed in a spin-polarized gas of  $^6\text{Li}$  [26], and the metallic, Mott-insulating, and band-insulating states of the 2D Fermi-Hubbard model have been directly detected, both in  $^6\text{Li}$  [27], and, as reported in this paper, in  $^{40}\text{K}$ . In this Letter, we also demonstrate the formation of local moments at half filling as the temperature is lowered.

Our system is described by the single-band 2D Hubbard Hamiltonian with two spin states on a square lattice,

$$\hat{H} = -t \sum_{\langle i,j \rangle, \sigma} (\hat{c}_{i\sigma} \hat{c}_{j\sigma}^\dagger + \text{H.c.}) + U \sum_i \hat{n}_{i\uparrow} \hat{n}_{i\downarrow} + \sum_{i, \sigma} (V_i - \mu_0) \hat{n}_{i\sigma},$$

where  $\hat{c}_{i\sigma}$  ( $\hat{c}_{i\sigma}^\dagger$ ) is the fermion annihilation (creation) operator for spin  $\sigma = \{\uparrow, \downarrow\}$  on site  $i$ ,  $\hat{n}_{i\sigma} = \hat{c}_{i,\sigma}^\dagger \hat{c}_{i,\sigma}$  is the number operator on site  $i$ , and angle brackets indicate summation over nearest neighbors.  $U$  and  $t$  denote the on-site interaction energy and nearest-neighbor hopping amplitude, respectively, while  $\mu_0$  is the chemical potential and  $V_i$  is the on-site energy due to the overall trapping potential. The trapping potential is approximated by  $V_i = \frac{1}{2} m \omega^2 d_i^2 a^2$ , where  $m$  is the atomic mass,  $\omega$  is the global trapping frequency,  $d_i$  is the distance in lattice sites from the center of the trap, and  $a$  is the lattice spacing.

Despite the simplicity of the Hamiltonian, this model is theoretically intractable and has been solved only in special cases. At weak interactions ( $U/8t < 1$ ) or when the average filling is well below unity, the system is metallic. If the chemical potential is high enough to fill all available states, the system becomes a band insulator, with two opposite-spin atoms per site. At strong interactions ( $U/8t \gg 1$ ) and at half filling, another insulating state, the Mott insulator, appears when the temperature  $k_B T \ll U$ . At temperatures well below the superexchange scale of  $4t^2/U$ , long-range antiferromagnetic correlations arise. It is conjectured that  $d$ -wave superconductivity emerges upon doping a magnetically ordered

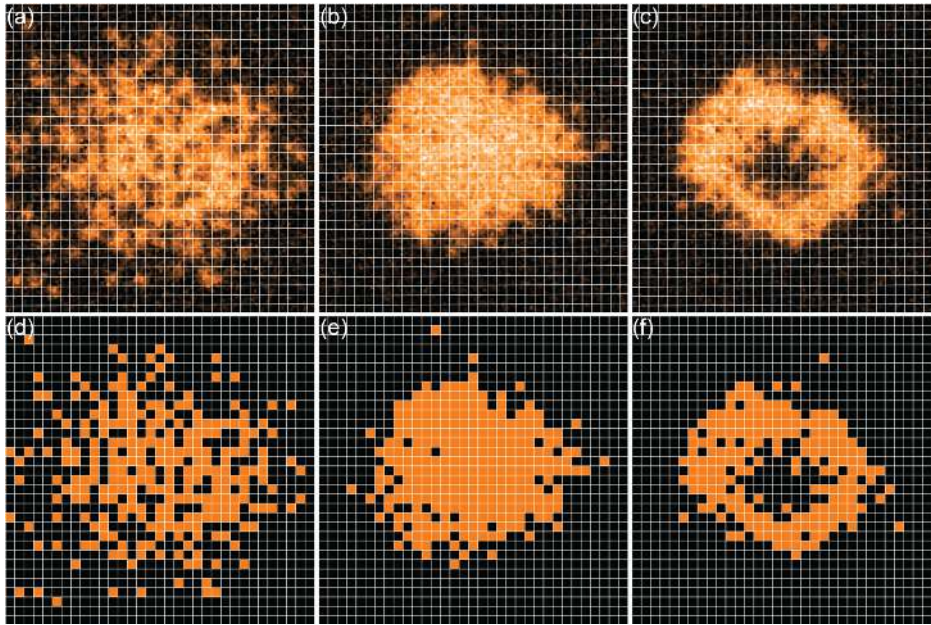


FIG. 1. Metallic, Mott-insulating, and band-insulating states under the quantum gas microscope: observed fluorescence images, showing (a) the metallic state, with  $\mu_0/h = 280(40)$  Hz,  $\omega = 2\pi \times 111(3)$  Hz, and  $U/8\bar{t} = 0.33(4)$  with  $U/h = 540(60)$  Hz; (b) the Mott-insulating state, with  $\mu_0/h = 624(22)$  Hz,  $\omega = 2\pi \times 115(3)$  Hz, and  $U/8\bar{t} = 12.3(8)$  with  $U/h = 1350(50)$  Hz; and (c) the band-insulating state, with  $\mu_0/h = 1450(40)$  Hz,  $\omega = 2\pi \times 181(3)$  Hz, and  $U/8\bar{t} = 2.6(1)$  with  $U/h = 1007(40)$  Hz. [(d)–(f)] Reconstructed detected site occupations corresponding to (a)–(c), respectively.

Mott insulator [7,8]. Within the local density approximation (LDA), the overall harmonic confining potential leads to a spatially varying local chemical potential, and thus metallic, Mott-insulating, and band-insulating states can coexist within the same sample [28,29].

To realize this model, we begin by sympathetically cooling  $^{40}\text{K}$  atoms with  $^{23}\text{Na}$  atoms in a magnetic trap. The  $^{40}\text{K}$  atoms are then transferred into an optical dipole trap, and an equal mixture of hyperfine states  $|F = 9/2, m_F = -9/2\rangle$  and  $|9/2, -7/2\rangle$  is created. After evaporation and transport, we obtain a highly oblate layer of  $\sim 300$   $^{40}\text{K}$  atoms in the  $x$ - $y$  plane  $7\ \mu\text{m}$  underneath the imaging system. Subsequently, we ramp up a square optical lattice in the  $x$ - $y$  plane, with lattice spacing  $a = 541$  nm, to a depth of either  $6E_R$ ,  $12E_R$ , or  $18E_R$ , where  $E_R = (\hbar^2/2m)(\pi/a)^2$ . The laser beams that create the  $x$ - $y$  lattice also interfere to form a lattice along  $z$  with  $3\ \mu\text{m}$  spacing, where only one layer is populated. We use the lattice depth to tune the Hubbard parameters  $t$  and  $U$ , without utilizing any Feshbach resonances. For this work, the magnetic field is set to 4.5 G, where the scattering length is  $170a_0$ ,  $a_0$  being the Bohr radius. While the lattice is ramped up, the radial confinement within the plane is brought to the desired value. For imaging, the lattice depth is quickly increased to  $\sim 1000E_R$ , while an additional lattice along the  $z$  direction with spacing 532 nm is also applied.

We detect the occupation on each lattice site using Raman sideband cooling, which cools the atoms while scattering enough photons to produce a fluorescence image [22]. This imaging technique, combined with an image reconstruction algorithm, allows us to determine the occupation of a given lattice site with a measured imaging fidelity of 95%. Because pairs of atoms residing on the same site are lost during imaging due to light-assisted collisions [30], only the parity of the occupation is detected. Additionally, this imaging

method does not distinguish between the two spin states. The average detected occupation at site  $i$  is thus given by  $n_{\text{det}}(i) = \langle \hat{n}_{\text{det}}(i) \rangle$ , where  $\hat{n}_{\text{det}}(i) = \hat{n}_{i\uparrow} + \hat{n}_{i\downarrow} - 2\hat{n}_{i\uparrow}\hat{n}_{i\downarrow}$ .

We directly observe the metallic, Mott-insulating, and band-insulating states using three configurations of lattice depths and radial confinements. The three different samples are prepared identically until the 2D lattice ramp, where both the depth of the lattice and the radial confinement are adjusted. In Fig. 1 we show the site-resolved fluorescence images and the reconstructed detected site occupations. In Fig. 2 we show profiles of the corresponding radially averaged parity-projected densities  $n_{\text{det}}$  and their variances. The Mott-insulating and band-insulating states are both expected to show suppressed variance in  $n_{\text{det}}$ . In particular, the variance is suppressed in Mott-insulating regions due to the charge gap, which is  $U$  at half filling; in the band-insulating regions, it is suppressed instead by Pauli blocking. In the metallic regions the variance is not suppressed, and in the case of half filling it equals 0.25, since a site is equally likely to be empty, doubly occupied, or singly occupied by an atom of either spin state. The variance can either be directly measured, or obtained via  $\langle \hat{n}_{\text{det}}^2 \rangle - \langle \hat{n}_{\text{det}} \rangle^2 = n_{\text{det}}(1 - n_{\text{det}})$ . This is due to the operator identity  $\hat{n}_{i\sigma}^2 = \hat{n}_{i\sigma}$  for fermions, which implies  $\langle \hat{n}_{\text{det}}^2 \rangle = \langle \hat{n}_{\text{det}} \rangle$ , and more generally all moments of  $n_{\text{det}}$  can be found from  $n_{\text{det}}$  itself.

The metallic state, with peak occupation 0.7 and peak variance  $\sim 0.25$ , is shown in Figs. 1(a), 1(d), 2(a), and 2(d). Here, the lattice depth is  $6E_R$  and the radial confinement is  $\omega = 2\pi \times 111(3)$  Hz. This corresponds to  $U/8\bar{t} = 0.33(4)$ , where  $\bar{t} = \sqrt{t_x t_y}$  is the mean hopping amplitude, with  $t_x$  ( $t_y$ ) being the mean hopping amplitude along the  $x$  ( $y$ ) direction [39]. In order to observe the Mott insulator, shown in Figs. 1(b), 1(e), 2(b), and 2(e), we increase the interaction to  $U/8\bar{t} = 12.3(8)$  by increasing the lattice depth to  $18E_R$

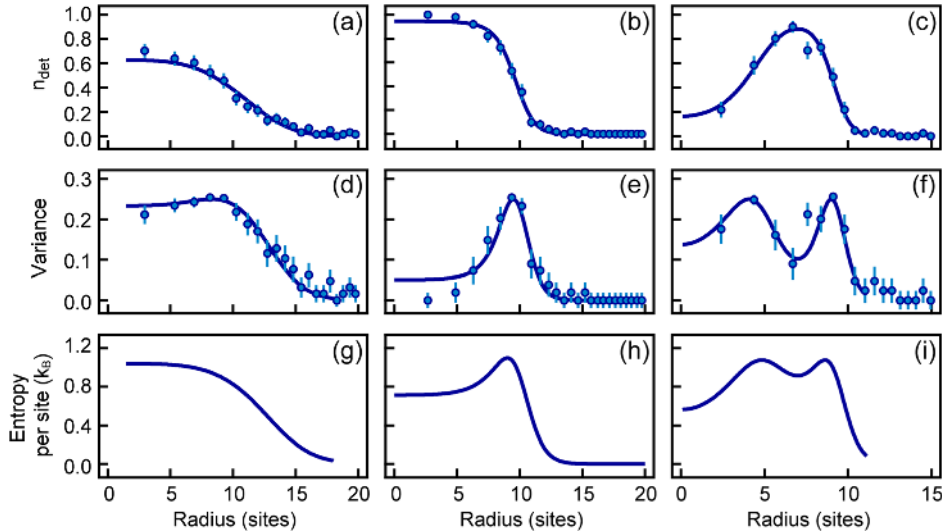


FIG. 2. Radially averaged detected site occupation [(a)–(c)], variance [(d)–(f)], and entropy [(g)–(i)], with theoretical curves. [(a), (d), and (g)] Metallic state, with  $\mu_0/h = 280$  (40) Hz and  $k_B T/U = 1.46(18)$ ; average entropy per particle  $S/N = 1.7(1)k_B$ . [(b), (e), and (h)] Mott-insulating central region, with  $\mu_0/h = 624$  (22) Hz and  $k_B T/U = 0.09(1)$ ;  $S/N = 1.23(6)k_B$ . [(c), (f), and (i)] Band-insulating center and Mott-insulating annular region, with  $\mu_0/h = 1450$  (40) Hz and  $k_B T/U = 0.18(2)$ ;  $S/N = 0.99(6)k_B$ . The profiles were fitted to numerical linked cluster expansion (NLCE) data with  $U/\bar{t} = 3$  for (a), (d), and (g) and to high-temperature series expansion (HTSE) for (b), (e), and (h). For (c), (f), and (i), profiles were fitted to NLCE data with  $U/\bar{t} = 21$ , shown in solid.

and the trap confinement to  $\omega = 2\pi \times 115$  (3) Hz. The detected site occupation flattens to 0.98(2) at the trap center, with a corresponding variance less than 0.03. To observe the band insulator, shown in Figs. 1(c), 1(f), 2(c), and 2(f), we

increase the global chemical potential, by increasing the trap confinement to  $\omega = 2\pi \times 181$  (3) Hz, while reducing the interaction to  $U/8\bar{t} = 2.6(1)$ , by lowering the lattice depth to  $12E_R$ . At the center the detected density is depleted and the

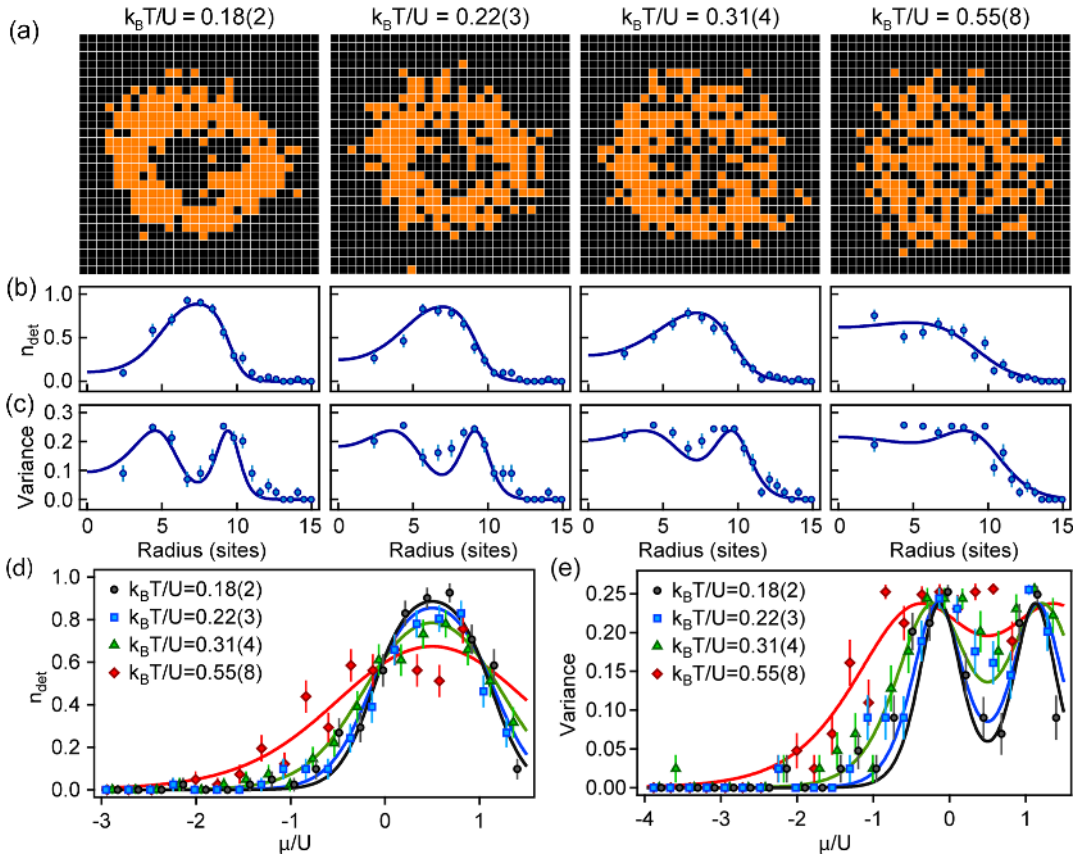


FIG. 3. Heating of Mott and band insulators. (a) Site-resolved images, (b) density profiles, and (c) variances for temperatures  $k_B T/U = 0.18(2)$ ,  $0.22(3)$ ,  $0.31(4)$ ,  $0.55(8)$  (left to right) at fixed  $U/8\bar{t} = 2.6(1)$  and  $\omega = 2\pi \times 183$  (3) Hz, with fitted curves from HTSE (solid). [(d) and (e)] Radially averaged observed filling and variance, respectively, for all four temperature values as a function of chemical potential, calculated from the fitted global chemical potential.

variance is suppressed, indicating a band-insulating region with two atoms per site. Because of the varying local chemical potential across the trap, a surrounding Mott-insulating annular region is also visible. The metallic regions that border the insulating regions are clearly evidenced by the increased variance.

To characterize the atomic clouds, we fit the radially averaged parity-projected density  $n_{\text{det}}$  to the equation of state of the spin-balanced Hubbard model obtained either through NLCE data [31], for  $U/8\bar{t} = 0.33(4), 2.6(1)$ , or from the HTSE in  $\bar{t}/k_B T$  [32], for  $U/8\bar{t} = 12.3(8)$ . From these fits, we extract temperatures of  $k_B T/U = 0.55(9), 0.09(1), 0.18(2)$  for the three configurations shown in Figs. 2(a), 2(d), and 2(g); 2(b), 2(e), and 2(h); and 2(c), 2(f), and 2(i), respectively. From the fits, we deduce the local entropy per site, shown in Figs. 2(g)–2(i), and the trap-averaged entropy per particle. These curves illustrate redistribution of entropy between the different regions of the trap. There is a local reduction of entropy in the Mott and band-insulating regions, with a corresponding increase of entropy in the metallic rings. Additionally, we observe that the average entropy per particle is  $1.7(1)k_B$ ,  $1.23(6)k_B$ , and  $0.99(6)k_B$  for the three configurations.

In order to explore the effects of temperature, we heat samples at  $U/8\bar{t} = 2.6(1)$  and confinement of  $\omega = 2\pi \times 181(3)$  Hz by varying the hold time in the lattice up to 3 s. In Fig. 3(a), we show the reconstructed site occupations for four temperatures from  $k_B T/U = 0.18(2)$  to  $0.55(8)$ . As the temperature increases, singly occupied sites are created in the band-insulating region as  $k_B T$  approaches  $\mu_0$ , while double occupancies and holes appear in the Mott-insulating region as  $k_B T$  approaches  $U$ . The radially averaged density profiles, shown in Fig. 3(b), are fitted with HTSE to extract the temperature and chemical potential. In Fig. 3(c), we show the measured variance for the samples from Fig. 3(a). The variance is suppressed in insulating regions at low temperatures, but approaches 0.25 throughout the sample at high temperatures. To extract trap-independent properties, we use the fitted value of  $\mu_0$  and the trap frequency  $\omega$  to determine the local chemical potential  $\mu = \mu_0 - \frac{1}{2}m\omega^2 d_i^2 a^2$ . Under the LDA, the local properties are equivalent to those of a homogeneous system at the same chemical potential. Radial profiles can then be converted to profiles with varying  $\mu/U$ , as shown in Figs. 3(d) and 3(e) for the site occupation and variance, respectively.

While the detected site occupation  $n_{\text{det}}$  does not allow one to obtain the total density  $\langle \hat{n}_\downarrow + \hat{n}_\uparrow \rangle$  or the double occupancy  $\langle \hat{n}_\downarrow \hat{n}_\uparrow \rangle$  separately, it directly gives the local moment  $\langle m_z^2 \rangle = \langle (\hat{n}_\uparrow - \hat{n}_\downarrow)^2 \rangle = \langle \hat{n}_\uparrow + \hat{n}_\downarrow - 2\hat{n}_\uparrow \hat{n}_\downarrow \rangle = \langle \hat{n}_{\text{det}} \rangle$  [33]. In the strong coupling limit  $U \gg t$  and at half filling, as the temperature is lowered below  $\sim U$ , the local moment is expected to approach unity as the system enters the Mott-insulating state. At even lower temperatures, near the superexchange scale  $t^2/U$ , the moment is expected to slightly decrease, signaling reduced localization as magnetic

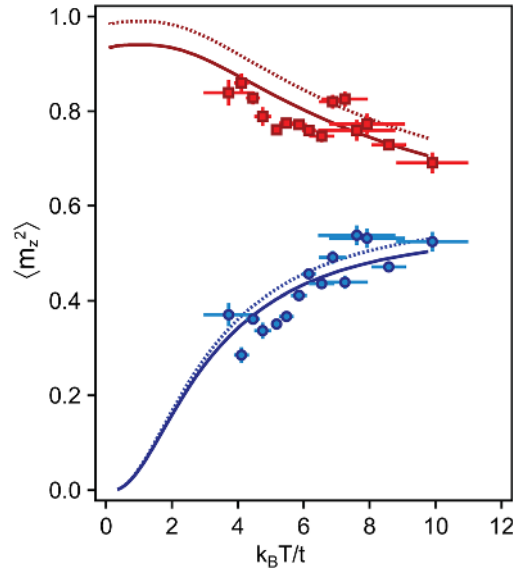


FIG. 4. Local moment  $\langle m_z^2 \rangle$  as a function of temperature at  $U/8\bar{t} = 2.6(1)$  for  $\mu/U = 0.5$  (red squares) and  $\mu/U = -0.25$  (blue circles). The local moments are extracted from 117 samples. For each sample, the temperature and global chemical potential are determined by fitting to HTSE in the outer regions where  $n_{\text{det}} < 0.25$ . NLCE data at  $U/t = 21$  with and without adjustment for imaging fidelity are shown in solid and dotted lines, respectively.

interactions become important [34]. The moment, directly given by  $n_{\text{det}}$ , can thus show signatures of superexchange, albeit at temperatures lower than those accessed in the current work. In Fig. 4, we show the local moment at half filling ( $\mu = U/2$ ) as a function of temperatures for the same parameters as in Fig. 3. To determine the half-filling point, the detected occupation is fitted to HTSE in the outer regions of the sample where  $n_{\text{det}} < 0.25$ , from which we extract the temperature and global chemical potential  $\mu_0$ . At half filling, a measurement of the local moment also yields the double occupancy via  $\langle \hat{n}_\uparrow \hat{n}_\downarrow \rangle = (1 - \langle m_z^2 \rangle)/2$ . We also show the measured temperature dependence of the moment at  $\mu = -U/4$ . Note that  $\langle m_z^2 \rangle$  is symmetric about  $\mu = U/2$ , a consequence of the particle-hole symmetry of the Fermi-Hubbard model on a bipartite lattice. Thus, the behavior of the moment versus temperature at  $\mu = -U/4$  is representative of the metallic regions both below and above half filling. After correction for imaging fidelity, the data for both values of  $\mu$  are consistent with the NLCE predictions.

In summary, we have directly observed with single-site resolution the Mott-insulating, band-insulating, and metallic states of the 2D Hubbard model using fermionic  $^{40}\text{K}$  in an optical lattice. We measure entropies as low as  $0.99(6)k_B$  per particle, indicating that short-range antiferromagnetic spin correlations should be present [31,35,36]. The Mott insulator provides a well-controlled initial state for further studies, such as the properties of one-dimensional Hubbard chains and dynamics of magnetic

polarons [8,37]. Additionally, the presence of  $^{23}\text{Na}$  in our system, combined with the recently demonstrated creation of ground state  $^{23}\text{Na}^{40}\text{K}$  molecules [38], opens the possibility to study lattice models with long-range and anisotropic interactions at the single-site level.

The authors thank David Reens and Thomas Lompe for experimental support, and Zoran Hadzibabic for a critical reading of the manuscript. This work was supported by the NSF, AFOSR-PECASE, AFOSR-MURI on Exotic Phases of Matter, ARO-MURI on Atomtronics, a grant from the Army Research Office with funding from the DARPA OLE program, and the David and Lucile Packard Foundation. K. R. L. was supported by the Fannie and John Hertz Foundation and the NSF GRFP. M. A. N. was supported by the DoD through the NDSEG Fellowship Program.

- [1] M. Troyer and U.-J. Wiese, *Phys. Rev. Lett.* **94**, 170201 (2005).
- [2] *Proceedings of the International School of Physics “Enrico Fermi,” Course CLXIV, Varenna, 2006*, edited by M. Inguscio, W. Ketterle, and C. Salomon (IOS Press, Amsterdam, 2008).
- [3] I. Bloch, J. Dalibard, and W. Zwerger, *Rev. Mod. Phys.* **80**, 885 (2008).
- [4] *The BCS-BEC Crossover and the Unitary Fermi Gas*, edited by W. Zwerger (Springer, New York, 2011), Vol. 836.
- [5] M. W. Zwierlein, in *Novel Superfluids*, edited by K.-H. Bennemann and J. B. Ketterson (Oxford University Press, Oxford, 2014), Vol. 2.
- [6] T. Esslinger, *Annu. Rev. Condens. Matter Phys.* **1**, 129 (2010).
- [7] P. W. Anderson, *Science* **235**, 1196 (1987).
- [8] P. A. Lee, N. Nagaosa, and X.-G. Wen, *Rev. Mod. Phys.* **78**, 17 (2006).
- [9] R. Jördens, N. Strohmaier, K. Günter, H. Moritz, and T. Esslinger, *Nature (London)* **455**, 204 (2008).
- [10] U. Schneider, L. Hackermüller, S. Will, T. Best, I. Bloch, T. A. Costi, R. W. Helmes, D. Rasch, and A. Rosch, *Science* **322**, 1520 (2008).
- [11] S. Taie, R. Yamazaki, S. Sugawa, and Y. Takahashi, *Nat. Phys.* **8**, 825 (2012).
- [12] P. M. Duarte, R. A. Hart, T.-L. Yang, X. Liu, T. Paiva, E. Khatami, R. T. Scalettar, N. Trivedi, and R. G. Hulet, *Phys. Rev. Lett.* **114**, 070403 (2015).
- [13] D. Greif, T. Uehlinger, G. Jotzu, L. Tarruell, and T. Esslinger, *Science* **340**, 1307 (2013).
- [14] R. A. Hart, P. M. Duarte, T.-L. Yang, X. Liu, T. Paiva, E. Khatami, R. T. Scalettar, N. Trivedi, D. A. Huse, and R. G. Hulet, *Nature (London)* **519**, 211 (2015).
- [15] D. Greif, G. Jotzu, M. Messer, R. Desbuquois, and T. Esslinger, *Phys. Rev. Lett.* **115**, 260401 (2015).
- [16] E. Cocchi, L. A. Miller, J. H. Drewes, M. Koschorreck, D. Pertot, F. Brennecke, and M. Köhl, *Phys. Rev. Lett.* **116**, 175301 (2016).
- [17] C. Hofrichter, L. Riegger, F. Scazza, M. Höfer, D. R. Fernandes, I. Bloch, and S. Fölling, [arXiv:1511.07287](https://arxiv.org/abs/1511.07287) [Phys. Rev. X (to be published)].
- [18] W. S. Bakr, A. Peng, M. E. Tai, R. Ma, J. Simon, J. I. Gillen, S. Fölling, L. Pollet, and M. Greiner, *Science* **329**, 547 (2010).
- [19] J. F. Sherson, C. Weitenberg, M. Endres, M. Cheneau, I. Bloch, and S. Kuhr, *Nature (London)* **467**, 68 (2010).
- [20] M. Endres, M. Cheneau, T. Fukuhara, C. Weitenberg, P. Schauß, C. Gross, L. Mazza, M. C. Banuls, L. Pollet, I. Bloch, and S. Kuhr, *Science* **334**, 200 (2011).
- [21] M. Cheneau, P. Barmettler, D. Poletti, M. Endres, P. Schauß, T. Fukuhara, C. Gross, I. Bloch, C. Kollath, and S. Kuhr, *Nature (London)* **481**, 484 (2012).
- [22] L. W. Cheuk, M. A. Nichols, M. Okan, T. Gersdorf, V. V. Ramasesh, W. S. Bakr, T. Lompe, and M. W. Zwierlein, *Phys. Rev. Lett.* **114**, 193001 (2015).
- [23] E. Haller, J. Hudson, A. Kelly, D. A. Cotta, B. Peaudecerf, G. D. Bruce, and S. Kuhr, *Nat. Phys.* **11**, 738 (2015).
- [24] M. F. Parsons, F. Huber, A. Masurenko, C. S. Chiu, W. Setiawan, K. Wooley-Brown, S. Blatt, and M. Greiner, *Phys. Rev. Lett.* **114**, 213002 (2015).
- [25] G. J. A. Edge, R. Anderson, D. Jervis, D. C. McKay, R. Day, S. Trotzky, and J. H. Thywissen, *Phys. Rev. A* **92**, 063406 (2015).
- [26] A. Omran, M. Boll, T. A. Hilker, K. Kleinlein, G. Salomon, I. Bloch, and C. Gross, *Phys. Rev. Lett.* **115**, 263001 (2015).
- [27] D. Greif, M. F. Parsons, A. Masurenko, C. S. Chiu, S. Blatt, F. Huber, G. Ji, and M. Greiner, *Science* **351**, 953 (2016).
- [28] V. W. Scarola, L. Pollet, J. Oitmaa, and M. Troyer, *Phys. Rev. Lett.* **102**, 135302 (2009).
- [29] T. Paiva, R. Scalettar, M. Randeria, and N. Trivedi, *Phys. Rev. Lett.* **104**, 066406 (2010).
- [30] M. T. DePue, C. McCormick, S. L. Winoto, S. Oliver, and D. S. Weiss, *Phys. Rev. Lett.* **82**, 2262 (1999).
- [31] E. Khatami and M. Rigol, *Phys. Rev. A* **84**, 053611 (2011).
- [32] J. Oitmaa, C. Hamer, and W. Zheng, *Series Expansion Methods for Strongly Interacting Lattice Models* (Cambridge University Press, Cambridge, 2006).
- [33] J. E. Hirsch, *Phys. Rev. B* **31**, 4403 (1985).
- [34] T. Paiva, R. T. Scalettar, C. Huscroft, and A. K. McMahan, *Phys. Rev. B* **63**, 125116 (2001).
- [35] J. P. F. LeBlanc and E. Gull, *Phys. Rev. B* **88**, 155108 (2013).
- [36] S. Chiesa, C. N. Varney, M. Rigol, and R. T. Scalettar, *Phys. Rev. Lett.* **106**, 035301 (2011).
- [37] C. Weitenberg, M. Endres, J. F. Sherson, M. Cheneau, P. Schausz, T. Fukuhara, I. Bloch, and S. Kuhr, *Nature (London)* **471**, 319 (2011).
- [38] J. W. Park, S. A. Will, and M. W. Zwierlein, *Phys. Rev. Lett.* **114**, 205302 (2015).
- [39] See Supplemental Material <http://link.aps.org/supplemental/10.1103/PhysRevLett.116.235301> for determination of Hubbard parameters.

## Appendix H

# Observation of Spatial Charge and Spin Correlations in the 2D Fermi-Hubbard Model

This appendix contains a reprint of the following paper [20]:

L. W. Cheuk, M. A. Nichols, K. R. Lawrence, M. Okan, H. Zhang, E. Khatami, N. Trivedi, T. Paiva, M. Rigol, and M. W. Zwierlein, “Observation of Spatial Charge and Spin Correlations in the 2D Fermi-Hubbard Model,” *Science* **353**, 1260 (2016).

also in two dimensions. Realization of the paradigmatic quantum phase transition from such an artificial valence bond solid to a Heisenberg antiferromagnet (41) therefore seems within reach of present experiments.

Recently, we became aware of similar experimental results in two dimensions (42, 43).

## REFERENCES AND NOTES

1. P. W. Anderson, *Science* **235**, 1196–1198 (1987).
2. K. L. Hur, T. M. Rice, *Ann. Phys.* **324**, 1452–1515 (2009).
3. A. Auerbach, *Interacting Electrons and Quantum Magnetism* (Springer Science & Business Media, 1994).
4. T. Giamarchi, *Quantum Physics in One Dimension* (Clarendon, 2004).
5. T. Esslinger, *Ann. Rev. Condens. Matter Phys.* **1**, 129–152 (2010).
6. R. Jördens, N. Strohmaier, K. Günther, H. Moritz, T. Esslinger, *Nature* **455**, 204–207 (2008).
7. U. Schneider et al., *Science* **322**, 1520–1525 (2008).
8. R. Jördens et al., *Phys. Rev. Lett.* **104**, 180401 (2010).
9. S. Taie, R. Yamazaki, S. Sugawa, Y. Takahashi, *Nat. Phys.* **8**, 825–830 (2012).
10. P. M. Duarte et al., *Phys. Rev. Lett.* **114**, 070403 (2015).
11. D. Greif et al., *Science* **351**, 953–957 (2016).
12. L. W. Cheuk et al., *Phys. Rev. Lett.* **116**, 235301 (2016).
13. C. Hofrichter et al., *Phys. Rev. X* **6**, 021030 (2016).
14. E. Coccia et al., *Phys. Rev. Lett.* **116**, 175301 (2016).
15. S. Trotzky, Y.-A. Chen, U. Schnorrberger, P. Cheinet, I. Bloch, *Phys. Rev. Lett.* **105**, 265303 (2010).
16. D. Greif, T. Uehlinger, G. Jotzu, L. Tarruell, T. Esslinger, *Science* **340**, 1307–1310 (2013).
17. D. Greif, G. Jotzu, M. Messer, R. Desbuquois, T. Esslinger, *Phys. Rev. Lett.* **115**, 260401 (2015).
18. R. A. Hart et al., *Nature* **519**, 211–214 (2015).
19. S. Murmann et al., *Phys. Rev. Lett.* **115**, 215301 (2015).
20. L. W. Cheuk et al., *Phys. Rev. Lett.* **114**, 193001 (2015).
21. M. F. Parsons et al., *Phys. Rev. Lett.* **114**, 213002 (2015).
22. E. Haller et al., *Nat. Phys.* **11**, 738–742 (2015).
23. G. J. A. Edge et al., *Phys. Rev. A* **92**, 063406 (2015).
24. A. Omran et al., *Phys. Rev. Lett.* **115**, 263001 (2015).
25. G. Zürn et al., *Phys. Rev. Lett.* **110**, 135301 (2013).
26. J. Sirker, A. Klümper, *Phys. Rev. B* **66**, 245102 (2002).
27. E. V. Gorelik et al., *Phys. Rev. A* **85**, 061602 (2012).
28. B. Scialla et al., *Phys. Rev. A* **88**, 063629 (2013).
29. F. H. L. Essler, H. Frahm, F. Göhmann, A. Klümper, V. E. Korepin, *The One-Dimensional Hubbard Model* (Cambridge Univ. Press, 2005).
30. Supplementary text is available as supplementary materials on Science Online.
31. J. Seby-Straley, M. Anderlini, P. Jessen, J. Porto, *Phys. Rev. A* **73**, 033605 (2006).
32. S. Fölling et al., *Nature* **448**, 1029–1032 (2007).
33. F. Werner, O. Parcollet, A. Georges, S. R. Hassan, *Phys. Rev. Lett.* **95**, 056401 (2005).
34. R. Olf, F. Fang, G. E. Marti, A. MacRae, D. M. Stamper-Kurn, *Nat. Phys.* **11**, 720–723 (2015).
35. J.-S. Bernier et al., *Phys. Rev. A* **79**, 061601 (2009).
36. T.-L. Ho, Q. Zhou, *Proc. Natl. Acad. Sci. U.S.A.* **106**, 6916–6920 (2009).
37. A. M. Rey et al., *Europhys. Lett.* **87**, 60001 (2009).
38. S. Trebst, U. Schollwöck, M. Troyer, P. Zoller, *Phys. Rev. Lett.* **96**, 250402 (2006).
39. S. Nascimbène et al., *Phys. Rev. Lett.* **108**, 205301 (2012).
40. M. Lubasch, V. Murg, U. Schneider, J. I. Cirac, M.-C. Bañuls, *Phys. Rev. Lett.* **107**, 165301 (2011).
41. T. Senthil, A. Vishwanath, L. Balents, S. Sachdev, M. P. A. Fisher, *Science* **303**, 1490–1494 (2004).
42. M. F. Parsons et al., *Science* **353**, 1253–1256 (2016).
43. L. W. Cheuk et al., *Science* **353**, 1260–1264 (2016).

## ACKNOWLEDGMENTS

We acknowledge help by K. Kleinlein and M. Lohse during the setup of the experiment and financial support by Max-Planck-Gesellschaft and the European Union [Ultracold Quantum Matter (UQUAM) and Quantum Simulation of Many-Body Physics in Ultracold Gases (QUSIMGAS)]. The data that support the plots

within this paper and other findings of this study are available from the corresponding author upon reasonable request.

## SUPPLEMENTARY MATERIALS

[www.sciencemag.org/content/353/6305/1257/suppl/DC1](http://www.sciencemag.org/content/353/6305/1257/suppl/DC1)  
Supplementary Text  
Figs. S1 to S5  
Table S1  
References (44–51)  
17 May 2016; accepted 18 August 2016  
10.1126/science.aag1635

## QUANTUM SIMULATION

# Observation of spatial charge and spin correlations in the 2D Fermi-Hubbard model

**Lawrence W. Cheuk,<sup>1\*</sup> Matthew A. Nichols,<sup>1\*</sup> Katherine R. Lawrence,<sup>1</sup> Melih Okan,<sup>1</sup> Hao Zhang,<sup>1</sup> Ehsan Khatami,<sup>2</sup> Nandini Trivedi,<sup>3</sup> Thereza Paiva,<sup>4</sup> Marcos Rigol,<sup>5</sup> Martin W. Zwierlein<sup>1†</sup>**

Strong electron correlations lie at the origin of high-temperature superconductivity. Its essence is believed to be captured by the Fermi-Hubbard model of repulsively interacting fermions on a lattice. Here we report on the site-resolved observation of charge and spin correlations in the two-dimensional (2D) Fermi-Hubbard model realized with ultracold atoms. Antiferromagnetic spin correlations are maximal at half-filling and weaken monotonically upon doping. At large doping, nearest-neighbor correlations between singly charged sites are negative, revealing the formation of a correlation hole, the suppressed probability of finding two fermions near each other. As the doping is reduced, the correlations become positive, signaling strong bunching of doublons and holes, in agreement with numerical calculations. The dynamics of the doublon-hole correlations should play an important role for transport in the Fermi-Hubbard model.

**A** central question in the study of cuprate high-temperature superconductors is how spin and charge correlations give rise to the wealth of observed phenomena. Antiferromagnetic order present in the absence of doping quickly gives way to superconductivity upon doping with holes or electrons (1), suggesting the viewpoint of competing phases. On the other hand, antiferromagnetic correlations can also occur in the form of singlet bonds between neighboring sites. In fact, it has been proposed (2) that superconductivity could result, upon doping a Mott insulator, from the condensation of such resonating valence bonds. It has also been argued (1) that the pseudogap and “strange metal” regions are supported by a liquid of spin-singlets. This argument has spurred the simultaneous examination of nearest-neighbor spin and charge correlations, which might reveal the underlying mechanisms of pairing and transport.

In recent years, ultracold atomic gases have been established as pristine quantum simulators of strongly correlated many-body systems (3–5). The Fermi-Hubbard model is of special importance, thanks to its paradigmatic role for the study of high-critical temperature cuprates. At low temperatures and away from half-filling, solving the Fermi-Hubbard model theoretically

is very challenging because of the fermion sign problem. Central properties of Fermi-Hubbard physics—from the reduction of double occupancy (6, 7) and of compressibility (8, 9) as the repulsion is increased, to short-range antiferromagnetic correlations (10–12) and the equation of state (9, 13, 14)—have been observed in ultracold atom experiments. The recently developed Fermi gas microscopes (13, 15–19) have led to the direct observation of two-dimensional (2D) fermionic Mott insulators, band insulators, and metals with single-atom, single-site-resolved detection (20, 21). The strength of this technique, however, is on full display when single-site detection is used to directly measure correlations in the gas, as has been achieved with bosons (22–24).

<sup>1</sup>Department of Physics, MIT-Harvard Center for Ultracold Atoms, and Research Laboratory of Electronics, Massachusetts Institute of Technology (MIT), Cambridge, MA 02139, USA.

<sup>2</sup>Department of Physics and Astronomy, San José State University, San José, CA 95192, USA. <sup>3</sup>Department of Physics, The Ohio State University, Columbus, OH 43210, USA. <sup>4</sup>Instituto de Física, Universidade Federal do Rio de Janeiro, Caixa Postal 68.528, 21941-972 Rio de Janeiro, RJ, Brazil. <sup>5</sup>Department of Physics, The Pennsylvania State University, University Park, PA 16802, USA.

\*These authors contributed equally to this work. †Corresponding author. Email: zwierlein@mit.edu

In our study, we used a Fermi gas microscope of  $^{40}\text{K}$  atoms to directly observe charge and spin correlations in the 2D Fermi-Hubbard model (15, 21). Spin correlations displaying antiferromagnetic behavior have also been observed very recently with fermionic  $^{6}\text{Li}$  in one (25) and two (26) dimensions. We employ the local resolution to simultaneously obtain correlations in the entire range from zero doping (half-filling) to full doping (zero filling), as the density varies in the underlying trapping potential. The microscope measures the parity-projected density on a given lattice site—that is, doubly occupied sites (doublons) appear empty. For a two-spin mixture of fermions in the lowest band of the optical lattice, the parity-projected density is described by the magnetic moment operator (27)  $\hat{m}_{z,i}^2 = (\hat{n}_{\uparrow,i} - \hat{n}_{\downarrow,i})^2$ , where  $\hat{n}_{\sigma,i} = \hat{c}_{\sigma,i}^\dagger \hat{c}_{\sigma,i}$  is the number operator and  $\hat{c}_{\sigma,i}$  ( $\hat{c}_{\sigma,i}^\dagger$ ) are fermion annihilation (creation) operators for spin  $\sigma = \uparrow, \downarrow$  on site  $i$ . Many repeated measurements yield the average local moment on each site (Fig. 1, A and D), which is a thermodynamic quantity that quantifies the interaction energy. This is evident when one rewrites the interaction energy term  $U\hat{n}_{\uparrow,i}\hat{n}_{\downarrow,i}$  as  $\frac{U}{2}(\hat{n}_{\uparrow,i} + \hat{n}_{\downarrow,i} - \hat{m}_{z,i}^2)$ . The Fermi-Hubbard Hamiltonian can be written in terms of local moments as

$$\hat{H} = -t \sum_{\langle i,j \rangle, \sigma} (\hat{c}_{\sigma,i}^\dagger \hat{c}_{\sigma,j} + \text{h.c.}) - \frac{U}{2} \sum_i \hat{m}_{z,i}^2 - \mu \sum_i (\hat{n}_{\uparrow,i} + \hat{n}_{\downarrow,i}) \quad (1)$$

which is a form that highlights the particle-hole symmetry of the Hamiltonian. Here,  $\langle i,j \rangle$  denotes nearest-neighbor sites  $i$  and  $j$ ,  $t$  is the nearest-neighbor hopping amplitude,  $U$  is the on-site interaction energy, and  $\mu$  is the chemical potential. At moderate temperatures and depending on the fillings  $n_i = \langle \hat{n}_{\uparrow,i} + \hat{n}_{\downarrow,i} \rangle$ , this model can yield metallic, band insulating, or Mott insulating states. At half-filling ( $n_i = 1$ ) and at temperatures below the superexchange scale  $4t^2/U$ , quasi-long-range antiferromagnetic correlations arise. For a fixed temperature, these correlations are expected to be maximal when  $U \approx 8t$ , where the interaction energy equals the single-particle bandwidth. Upon doping, a pseudogap phase emerges; at even lower temperatures, one expects a d-wave superconducting state (1). Although the superexchange scale is about a factor of 2 lower than the temperatures achieved here, site-resolved detection of short-range correlations should already reveal precursory signs of physics at this energy scale.

Figure 1A shows a typical measurement of the site-resolved average local magnetic moment from ~90 individual experimental realizations at  $U/t = 7.2(1)$ . Atoms are confined in a radially symmetric trapping potential. Under the local density approximation, this results in a varying local chemical potential and, thus, a spatially varying filling  $n$  throughout the sample. We prepared samples where the maximum filling, which occurs in the center of the trap, lies above  $n = 1$ . From radially averaged profiles (Fig. 1D), the half-filling point is identified as the radial position where the moment reaches its maximum. This follows from the

particle-hole symmetry of the moment operator  $\hat{m}_{z,i}^2$ , a property that holds for all of its averages and cumulants (27).

Because the local moment satisfies the operator identity  $(\hat{m}_{z,i}^2)^2 = \hat{m}_{z,i}^2$ , fluctuations of the local moment do not yield additional information.

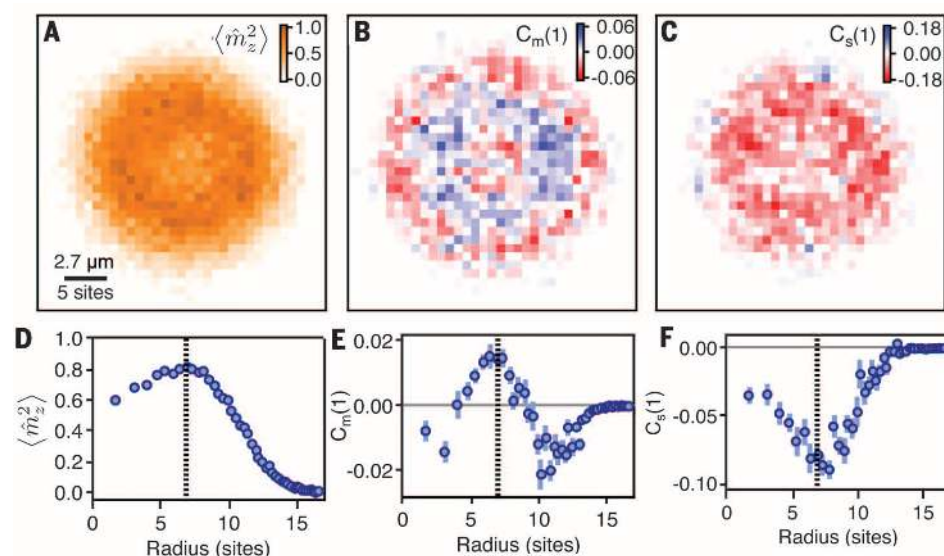


**Fig. 1. Local moment and nearest-neighbor charge and spin correlations.** An ultracold atom realization of the Fermi-Hubbard model for  $U/t = 7.2(1)$  is shown. (A to C) Local moment, nearest-neighbor moment correlator, and nearest-neighbor spin correlator, respectively, as functions of position, averaged over ~90 shots. The spatial variations reflect the varying local doping due to the underlying trapping potential. (D to F) Radial averages of (A), (B), and (C), respectively. The half-filling point is marked by vertical dotted lines.

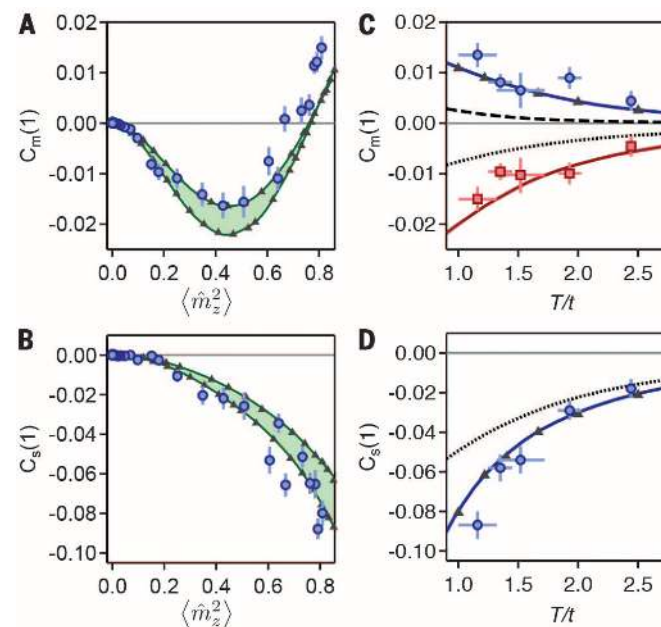


**Fig. 2. Spin and moment correlators as functions of doping and temperature for  $U/t = 7.2(1)$ .** (A and B) Nearest-neighbor moment correlator [ $C_m(1)$ ] (A) and spin correlator [ $C_s(1)$ ] (B) as functions of the local moment, denoted by blue circles. Results from NLCE (and DQMC) for temperatures  $T/t = 0.89$  and  $1.22$  are shown in green lines (and gray triangles), with the intermediate temperature range indicated by green shading. (C) The maximum and minimum of the moment correlator as functions of temperature are denoted by blue circles and red squares, respectively. Corresponding results are obtained from NLCE (solid blue line and solid red line, respectively), for the noninteracting gas (black dashed and dotted lines, respectively), and from DQMC for the correlator at half-filling (gray triangles). (D) Nearest-neighbor spin correlator at half-filling as a function of temperature (blue circles). Solid blue line, NLCE results; gray triangles, DQMC results; black dotted line, noninteracting gas. For all graphs, theory curves are not adjusted for the experimental imaging fidelity of 95%.

However, correlations of the moment between different sites do (27). We experimentally measured the moment correlator at a separation of one site,  $C_m(1)$ , defined as

$$C_m(1) = \frac{1}{4} \sum_{j \in \text{nn}_i} \left( \langle \hat{m}_{z,i}^2 \hat{m}_{z,j}^2 \rangle - \langle \hat{m}_{z,i}^2 \rangle \langle \hat{m}_{z,j}^2 \rangle \right) \quad (2)$$

where the sum is over all four nearest neighbors. The locally resolved correlator  $C_m(1)$  at each site  $i$  and its radial average are shown in Fig. 1, B and E, respectively.  $C_m(1)$  displays nonmonotonic behavior, changing sign as the filling is lowered.

The local moment correlator, however, is not sensitive to the sign of the spin  $S_{z,i} = \frac{1}{2}(\hat{n}_{\uparrow,i} - \hat{n}_{\downarrow,i})$ . One important spin-sensitive correlator is  $\langle \hat{S}_{z,i} \hat{S}_{z,j} \rangle$ , which can reveal antiferromagnetic ordering, expected to occur at half-filling and at low temperatures. This correlator can be expressed as  $\frac{1}{2} \sum_{\sigma} \langle \hat{p}_{\sigma,i} \hat{p}_{\sigma,j} \rangle - \frac{1}{4} \langle \hat{m}_{z,i}^2 \hat{m}_{z,j}^2 \rangle$  (28), where  $\hat{p}_{\sigma,i} = \hat{n}_{\sigma,i} - \hat{n}_{\uparrow,i} \hat{n}_{\downarrow,i}$ , which we measured by removing one spin state via resonant light, before imaging. All terms can be obtained experimentally in separate runs and are averaged separately. Analogous to the nearest-neighbor moment correlator  $C_m(1)$ , we define the nearest-neighbor spin correlator at site  $i$

$$C_s(1) = \sum_{j \in \text{nn}_i} \left( \langle \hat{S}_{z,i} \hat{S}_{z,j} \rangle - \langle \hat{S}_{z,i} \rangle \langle \hat{S}_{z,j} \rangle \right) \quad (3)$$

Figure 1, C and F, show the locally resolved nearest-neighbor spin correlation  $C_s(1)$  and its corresponding radial average, respectively. The fact that  $C_s(1)$  is negative suggests antiferromagnetic correlations, as expected (29–31). However, even without interactions, Pauli-blocking of like spins suppresses  $C_s(1)$ . One can see this by noting

that  $C_s(1)$  contains density correlations of either spin species separately  $[\langle \hat{n}_{\sigma,i} \hat{n}_{\sigma,j} \rangle - \langle \hat{n}_{\sigma,i} \rangle^2]$ , which are negative even for the noninteracting gas thanks to Pauli suppression. For the lowest temperatures reached, we observed a maximum absolute spin correlation of about a factor of 2 larger than that of a noninteracting Fermi gas.

Figure 2, A and B, show the nearest-neighbor moment and spin correlations versus the measured local moment  $\langle \hat{m}_z^2 \rangle$ . This representation allows for comparison with theory under minimal assumptions. As a thermodynamic quantity, the moment can replace the role of the chemical potential  $\mu$ . All thermodynamic variables can then be viewed as functions of the local moment, the spin correlation at half-filling,  $U$ , and  $t$ . In fact, the local spin correlation at half-filling is itself a thermometer that does not require any fit (32). Also shown in Fig. 2, A and B, are numerical linked-cluster expansion (NLCE) (33) and determinantal quantum Monte Carlo (DQMC) (34) calculations (28), which display similar behavior as the experimental data. Note that there are no free parameters; the temperature  $T/t = 1.16(16)$  is obtained from the spin correlation at half-filling.

As expected, the antiferromagnetic spin correlations are maximum at half-filling and decrease in absolute value with increased doping. Moment correlations instead are negative at low to intermediate fillings, crossing zero around a moment of 0.75 (doping  $\approx 0.21$ ) before turning positive toward half-filling. This implies that moments change their character from effectively repulsive (antibunching) to effectively attractive (bunching). The antibunching and bunching behaviors in the moments, as well as the antiferromagnetic spin correlations, become more pronounced as the temperature is lowered. Figure 2C shows the moment

correlation at half-filling (maximum positive value), as well as its minimum value versus temperature. The spin correlator at half-filling (minimum value) (Fig. 2D) displays a similar temperature dependence, reaching  $-0.09$  at the lowest temperatures in our experiment. This is about 30% of the maximum spin correlation expected for the spin- $\frac{1}{2}$  Heisenberg model at zero temperature in two dimensions (35).

To interpret the moment correlations, one may recast them in terms of the two-point correlator

$$g_2(r) = \frac{\langle \hat{m}_z^2(r) \hat{m}_z^2(0) \rangle}{\langle \hat{m}_z^2(r) \rangle \langle \hat{m}_z^2(0) \rangle} \quad (4)$$

which measures the probability of finding two moments a distance  $r$  from each other. In the absence of correlations,  $g_2 = 1$ . At low filling, for which the doublon density is negligible and the moment  $\langle \hat{m}_z^2 \rangle = \langle \hat{n} \rangle - 2\langle \hat{n}_{\uparrow} \hat{n}_{\downarrow} \rangle \approx n$  is essentially the density,  $g_2(r)$  measures density correlations. These are nontrivial even for the spin-polarized noninteracting Fermi gas, where fermion statistics lead to anticorrelations at short distances, reflecting the fact that two fermions cannot occupy the same site. This leads to Pauli suppression of  $g_2$  that persists to a distance on the order of the average interparticle spacing, a feature known as the Pauli hole. Although implications of this fermion antibunching have been observed in the suppression of density fluctuations (36, 37) and momentum space correlations (38, 39), the real space suppression  $g_2(r)$  has not been observed in situ before. In a noninteracting two-spin mixture, the anticorrelations are halved, as only two identical fermions experience the Pauli hole. However, repulsive interactions between opposite spins also suppress  $g_2(r)$ , leading to a combined Pauli and correlation hole.

In Fig. 3A, we show the directly measured  $g_2(1)$  as a function of moment at an intermediate interaction of  $U/t = 7.2$ . The strong suppression of  $g_2(1)$  at low fillings (large interparticle spacing) is observed and is stronger than Pauli suppression alone, reflecting short-range anticorrelations due to repulsive interactions. The data are well described by NLCE and DQMC calculations (Fig. 3A).

Whereas  $g_2(r)$  measures the probability of finding two moments a distance  $r$  from each other, near half-filling, where  $\langle \hat{m}_z^2 \rangle \sim 1$ , the correlations arise mainly from sites where the moment is zero (i.e., sites with holes and doublons). The number of holes and doublons, which appear empty after imaging, is given by  $\langle 1 - \hat{m}_z^2 \rangle$ . The corresponding two-point correlation function  $\bar{g}_2(r)$  of these antimoments is thus

$$\bar{g}_2(r) = \frac{\langle (1 - \hat{m}_z^2(r))(1 - \hat{m}_z^2(0)) \rangle}{\langle 1 - \hat{m}_z^2(r) \rangle \langle 1 - \hat{m}_z^2(0) \rangle} \quad (5)$$

In Fig. 3B, we show that  $\bar{g}_2(1)$  is strongly enhanced near half-filling beyond the uncorrelated value of 1.  $\bar{g}_2(1)$  thus reveals the strong bunching of holes and doublons. There are three contributions

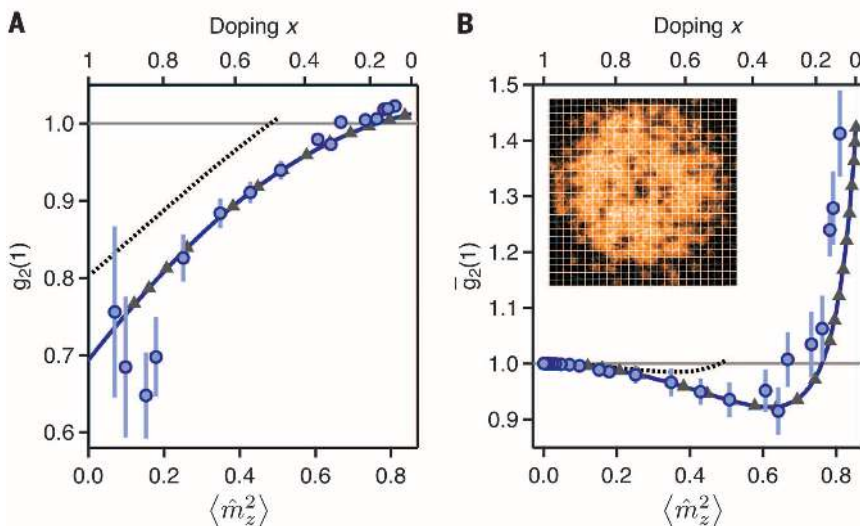


**Fig. 3. Two-point correlation functions.**  $g_2$  is the correlation function for moments and  $\bar{g}_2$  for antimoments at a separation of one lattice site for  $U/t = 7.2(1)$ . (A)  $g_2(1)$  for moments. (B)  $\bar{g}_2(1)$  for antimoments. Blue circles, experimental data; blue solid line, NLCE theory; gray triangles, DQMC theory. Both NLCE and DQMC calculations are performed at  $T/t = 1.22$ , and neither are adjusted for the experimental imaging fidelity of 95%. Black dotted lines, noninteracting gas. The doping  $x$  as a function of local moment is determined from NLCE theory at  $T/t = 1.22$ , without adjustment for imaging fidelity. (Inset) Typical image showing neighboring antimoments (imaged holes) near half-filling.

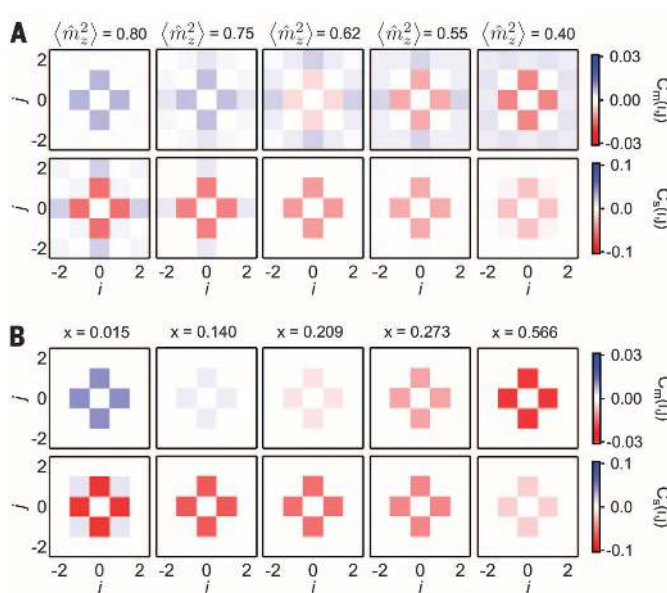
**Fig. 4. Spin and moment correlations as functions of distance and doping.** (A) Moment and spin correlations for  $U/t = 7.2(1)$  are shown in the top and bottom rows, respectively, at various values of the local moment. Correlation values are averaged over symmetric points. The moment correlator  $C_m(0,1)$  changes sign near a local moment of  $\langle \hat{m}_z^2 \rangle \approx 0.75$ . The anticorrelation of spins  $C_s(0,1)$  is observed to weaken upon increasing doping (decreasing moment). In contrast, the next-nearest-neighbor spin correlator  $C_s(1,1)$  changes from positive at zero doping to negative at large doping.

(B) Moment and spin correlations obtained from DQMC theory for  $U/t = 7.2(1)$  and  $T/t = 1.00$  are shown in the top and bottom rows, respectively, at various values of doping  $x$ . The nonzero value of the moment and spin correlators at distance  $(i,j) = (0,0)$  are omitted for clarity. They are both local quantities determined by the value of the moment. NLCE and DQMC results for the correlators at all distances shown are in good agreement (28).

to  $\bar{g}_2(1)$ : correlations between pairs of holes, between pairs of doublons, and between holes and doublons. One expects neighboring holes and neighboring doublons to show negative correlations due to Pauli suppression and strong repulsion. Hence, the bunching behavior must originate from positive correlations between neighboring doublon-hole pairs. This expectation is confirmed by NLCE and DQMC calculations (28).

The strong doublon-hole correlation near half-filling in the presence of antiferromagnetic correlations can be qualitatively captured by a simple two-site Hubbard model, experimentally realized in (40). In the strongly interacting limit ( $U \gg t$ ), the doublon density vanishes and the ground state is a spin singlet. However, at intermediate interaction strengths, tunneling admixes a doublon-hole pair into the ground state wave function, with an amplitude  $\sim t/U$ . Thus, short-range singlet correlations at moderate  $U/t$  occur naturally together with nearest-neighbor doublon-hole correlations.

At a separation of one lattice site, we have revealed the competition between the combined Pauli- and interaction-driven repulsion of singly occupied sites and the effective attraction of doublons and holes, which manifests itself in a sign change of the correlator. The ability of the microscope to measure at a site-resolved level also allows investigation of longer-distance correlations. In Fig. 4, A and B, we show the moment and spin correlations  $C_m(i,j)$  and  $C_s(i,j)$ , respectively, as a function of separation distance  $i\hat{x} + j\hat{y}$ . Near half-filling, even at the temperatures of this graph ( $T/t \approx 1.2$ ), antiferromagnetic spin correlations beyond the next neighbor are visible. With increased doping, they give way to a more isotro-



pic negative spin correlation. For example,  $C_s(1,1)$  changes sign from positive at half-filling to negative at large dopings. This resembles the effect of Pauli suppression that is already present for non-interacting fermions. For the moment correlator, we clearly observe the sign change of  $C_m(1,0)$  at a doping of  $x \approx 0.21$  and that the correlations do not extend substantially beyond one site.

The measurement of nonlocal moment correlations also results in direct access to the associated potential energy fluctuations ( $\Delta E_{\text{pot}}$ ). From the Fermi-Hubbard Hamiltonian in Eq. 1, we find that

$$\begin{aligned} \Delta E_{\text{pot}}^2 &= \frac{1}{4} U^2 \left( \langle \hat{M}^2 \rangle - \langle \hat{M} \rangle^2 \right) \\ &= \frac{1}{4} U^2 \sum_{ij} \left( \langle \hat{m}_{z,i}^2 \hat{m}_{z,j}^2 \rangle - \langle \hat{m}_{z,i}^2 \rangle \langle \hat{m}_{z,j}^2 \rangle \right) \end{aligned} \quad (6)$$

where  $\hat{M} = \sum_i \hat{m}_{z,i}^2$  is the total moment operator. At half-filling, the contribution to the fluctuations from the nearest-neighbor moment correlations is thus  $U^2 C_m(1) \approx 0.8t^2$  for  $T/t \approx 1$  and  $U/t = 7.2(1)$ . This suggests that doublon-hole correlations can arise from coherent tunneling of particles bound in spin singlets.

Away from half-filling, both NLCE and DQMC calculations are currently limited to a temperature range around  $T/t \approx 0.5$ , not far below what is reached experimentally in this work. Further reduction in experimental temperatures will provide a valuable benchmark for theoretical techniques, especially away from half-filling, where the sign problem arises. The clear importance of doublon-hole correlations will prompt further studies of their dynamics, especially away from

half-filling, which could elucidate their role for the transport properties of a possible strange metal phase and potential pseudogap behavior.

## REFERENCES AND NOTES

- P. A. Lee, N. Nagaosa, X.-G. Wen, *Rev. Mod. Phys.* **78**, 17–85 (2006).
- P. W. Anderson, *Science* **235**, 1196–1198 (1987).
- M. Inguscio, W. Ketterle, C. Salomon, Eds., *Ultracold Fermi Gases*, Proceedings of the International School of Physics “Enrico Fermi,” Course CLXIV, Varenna, 20 to 30 June 2006 (IOS Press, 2008).
- I. Bloch, J. Dalibard, W. Zwerger, *Rev. Mod. Phys.* **80**, 885–964 (2008).
- T. Esslinger, *Annu. Rev. Condens. Matter Phys.* **1**, 129–152 (2010).
- R. Jördens, N. Strohmaier, K. Gürter, H. Moritz, T. Esslinger, *Nature* **455**, 204–207 (2008).
- S. Taie, R. Yamazaki, S. Sugawa, Y. Takahashi, *Nat. Phys.* **8**, 825–830 (2012).
- U. Schneider et al., *Science* **322**, 1520–1525 (2008).
- P. M. Duarte et al., *Phys. Rev. Lett.* **114**, 070403 (2015).
- D. Greif, T. Uehlinger, G. Jotzu, L. Tarruell, T. Esslinger, *Science* **340**, 1307–1310 (2013).
- R. A. Hart et al., *Nature* **519**, 211–214 (2015).
- D. Greif, G. Jotzu, M. Messer, R. Desbuquois, T. Esslinger, *Phys. Rev. Lett.* **115**, 260401 (2015).
- E. Cocchi et al., *Phys. Rev. Lett.* **116**, 175301 (2016).
- C. Hofrichter et al., *Phys. Rev. X* **6**, 021030 (2016).
- L. W. Cheuk et al., *Phys. Rev. Lett.* **114**, 193001 (2015).
- E. Haller et al., *Nat. Phys.* **11**, 738–742 (2015).
- M. F. Parsons et al., *Phys. Rev. Lett.* **114**, 213002 (2015).
- A. Omran et al., *Phys. Rev. Lett.* **115**, 263001 (2015).
- G. J. A. Edge et al., *Phys. Rev. A* **92**, 063406 (2015).
- D. Greif et al., *Science* **351**, 953–957 (2016).
- L. W. Cheuk et al., *Phys. Rev. Lett.* **116**, 235301 (2016).
- M. Endres et al., *Science* **334**, 200–203 (2011).
- M. Endres et al., *Appl. Phys. B* **113**, 27–39 (2013).
- R. Islam et al., *Nature* **528**, 77–83 (2015).
- M. Böll et al., *Science* **353**, 1257–1260 (2016).
- M. F. Parsons et al., *Science* **353**, 1253–1256 (2016).
- E. Kapit, E. Mueller, *Phys. Rev. A* **82**, 013644 (2010).
- See the supplementary materials on Science Online.
- J. E. Hirsch, *Phys. Rev. B* **31**, 4403–4419 (1985).
- E. Khatami, M. Rigol, *Phys. Rev. A* **84**, 053611 (2011).
- J. P. F. LeBlanc, E. Gull, *Phys. Rev. B* **88**, 155108 (2013).
- M. J. H. Ku, A. T. Sommer, L. W. Cheuk, M. W. Zwierlein, *Science* **355**, 563–567 (2012).
- M. Rigol, T. Bryant, R. P. P. Singh, *Phys. Rev. Lett.* **97**, 187202 (2006).
- R. Blankenbecler, D. J. Scalapino, R. L. Sugar, *Phys. Rev. D Part. Fields* **24**, 2278–2286 (1981).
- T. Paiva, R. Scalettar, M. Randeria, N. Trivedi, *Phys. Rev. Lett.* **104**, 066406 (2010).
- C. Sanner et al., *Phys. Rev. Lett.* **105**, 040402 (2010).
- T. Müller et al., *Phys. Rev. Lett.* **105**, 040401 (2010).
- T. Rom et al., *Nature* **444**, 733–736 (2006).
- T. Jeltes et al., *Nature* **445**, 402–405 (2007).
- S. Murmann et al., *Phys. Rev. Lett.* **114**, 080402 (2015).

## ACKNOWLEDGMENTS

We thank S. Todadri, M. Randeria, and M. Greiner and his research group for fruitful discussions. This work was supported by the NSF, an Air Force Office of Scientific Research Presidential Early Career

Award for Scientists and Engineers and Multidisciplinary University Research Initiative (MURI) on Exotic Quantum Phases, an Army Research Office MURI on Atomtronics, and the David and Lucile Packard Foundation. M.A.N. was supported by the U.S. Department of Defense through the National Defense Science and Engineering Graduate Fellowship Program. K.R.L. was supported by the Fannie and John Hertz Foundation and the NSF Graduate Research Fellowship Program. N.T. acknowledges funding from

NSF Division of Materials Research grant 1309461 and partial support by a grant from the Simons Foundation (343227) and thanks S. Todadri for hospitality at MIT during her sabbatical. T.P. acknowledges support from Brazilian National Council for Scientific and Technological Development, Fundação de Amparo à Pesquisa do Estado do Rio de Janeiro, and Instituto Nacional de Ciência e Tecnologia on Quantum Information. M.R. was supported by the U.S. Office of Naval Research.

## SUPPLEMENTARY MATERIALS

[www.sciencemag.org/content/353/6305/1260/suppl/DC1](http://www.sciencemag.org/content/353/6305/1260/suppl/DC1)  
Supplementary Text  
Figs. S1 to S6  
References (41–47)

10 June 2016; accepted 18 August 2016  
10.1126/science.aag3349

## POLYMER SCIENCE

# Quantifying the impact of molecular defects on polymer network elasticity

Mingjiang Zhong,<sup>1,2\*</sup> Rui Wang,<sup>2\*</sup> Ken Kawamoto,<sup>1\*</sup>  
Bradley D. Olsen,<sup>2†</sup> Jeremiah A. Johnson<sup>1†</sup>

Elasticity, one of the most important properties of a soft material, is difficult to quantify in polymer networks because of the presence of topological molecular defects in these materials. Furthermore, the impact of these defects on bulk elasticity is unknown. We used rheology, disassembly spectrometry, and simulations to measure the shear elastic modulus and count the numbers of topological “loop” defects of various order in a series of polymer hydrogels, and then used these data to evaluate the classical phantom and affine network theories of elasticity. The results led to a real elastic network theory (RENT) that describes how loop defects affect bulk elasticity. Given knowledge of the loop fractions, RENT provides predictions of the shear elastic modulus that are consistent with experimental observations.

**M**olecular defects fundamentally govern the properties of all real materials (1–3). The language of crystallography has been successfully used to describe defects and to model their impact in materials with a degree of periodicity, such as silicon, steel, block copolymers, and liquid crystals. However, understanding defects in amorphous materials presents a continued challenge. In polymer networks, the relevant defects are largely of a topological nature: The properties of these amorphous materials depend primarily upon the way the molecules in the material are connected. Understanding the correlation between the network topology and properties is one of the greatest outstanding challenges in soft materials.

Polymer networks can have a wide range of shear elastic moduli ( $G'$ ) from  $\sim 10^2$  to  $\sim 10^7$  Pa (4, 5), with different applications requiring moduli across this entire range. Covalent polymer networks are generally formed via kinetically controlled processes; consequently, they possess cyclic topological defects. The classical affine and phantom network theories of network elasticity neglect the presence of such defects (4, 5); they rely on idealized end-linked networks (Fig. 1A) that consider only acyclic tree-like structures, which leads to overestimation of  $G'$  (6, 7). In practice,  $G'$  is frequently calculated according to the equation

$G' = Cv_{\text{eff}}kT$ , where  $kT$  is the thermal energy,  $v_{\text{eff}}$  is the density of elastically effective chains, and  $C$  is a constant that has a value of 1 for the affine network model and  $1 - 2/f$  for the phantom network model (where  $f$  is the functionality of the network junctions). Because polymer networks include elastically defective chains,  $v_{\text{eff}}$  is never known precisely, and thus neither theory is able to accurately fit experimental data; a controversy continues over which theory, if either, is correct. Thus, despite decades of advances in polymer network design, our inability to quantitatively calculate the effects of defects on shear elastic modulus and to measure the corresponding defect densities in real polymer networks precludes quantitative prediction of  $G'$  and validation of the affine and phantom network models (4, 8–12).

To understand how molecular structure affects  $G'$  and to use this knowledge to create a predictive theory of elasticity, it is first necessary to quantify the density of topological defects in a polymer network and to determine the impact of these defects on the mechanical properties of the network. Cyclic defects, created from intrajunction reactions during network formation, are chemically and spectroscopically almost identical to noncyclic junctions, making them difficult to distinguish and quantify (5, 13–16). We have developed symmetric isotopic labeling disassembly spectrometry (SILDAs) as a strategy to precisely count the number of primary loops (Fig. 1B), the simplest topological defects, in polymer networks formed from  $A_2 + B_3$  and  $A_2 + B_4$  reactions (17–20). Furthermore, we have developed Monte Carlo

simulations and kinetic rate theories that show that cyclic defects in these polymer networks are kinetically linked, such that experimental measurement of only the primary loops determines the densities of all higher-order defects including secondary (Fig. 1C) and ternary loops (Fig. 1D) (21). Here, we measured loop fractions and  $G'$  for a series of hydrogels, thus providing quantitative relationships between these parameters. With this information, we examined the classical affine and phantom network theories of elasticity, and we derived a modified phantom network theory—real elastic network theory (RENT)—that accounts for topological molecular defects.

To rigorously determine how molecular topological defects affect elasticity, it is necessary to measure the topological defect density and modulus in the same gel. A class of stable yet chemically degradable gels was developed from bis-azido-terminated polyethylene glycol (PEG) (number-average molecular weight  $M_n = 4600$ , dispersity index  $D = 1.02$ ) polymers with non-labeled or isotopically labeled segments near their chain ends,  $A_{2H}$  and  $A_{2D}$ , respectively (22) (structures are shown in Fig. 1A; for synthesis and characterization details, see figs. S1 to S3 and figs. S17 to S34). Such labeling provides a convenient method for precise measurement of primary loops by SILDAs (19). The PEG molecular weight ensures that the polymer solutions used to form gels are well below the entanglement regime (5, 12). The labeled ( $A_{2D}$ ) and non-labeled ( $A_{2H}$ ) polymers (referred to herein as “ $A_2$  monomers”) were mixed in a 1:1 molar ratio, and this mixture was allowed to react with a tris-alkyne ( $B_3$ ) or a tetra-alkyne ( $B_4$ ) (structures are shown in Fig. 1A) in propylene carbonate solvent to provide end-linked gels via copper-catalyzed azide-alkyne cycloaddition (23, 24). When the reactive group stoichiometry—azide and alkyne in this case—was carefully controlled to be 1:1, spectroscopic analysis demonstrated that dangling functionalities (unreacted azides or alkynes) could be minimized (19) such that their impact on elasticity is negligible. Gels with varied fractions of topological defects were synthesized by varying the initial concentrations of  $A_2$  and  $B_3$  or  $B_4$  monomers (22).

For measurement of the shear elastic modulus as a function of gel preparation conditions, gel samples 1.59 mm thick were formed in situ in Teflon molds under an inert atmosphere (fig. S4). Gel disks (diameter 12 mm) were punched (Fig. 1A) and loaded onto an oscillatory shear rheometer equipped with parallel-plate geometry. Propylene carbonate was chosen as the solvent

<sup>1</sup>Department of Chemistry, Massachusetts Institute of Technology, Cambridge, MA 02139, USA. <sup>2</sup>Department of Chemical Engineering, Massachusetts Institute of Technology, Cambridge, MA 02139, USA.

\*These authors contributed equally to this work. †Corresponding author. Email: bdolsen@mit.edu (B.D.O.); jaj2109@mit.edu (J.A.J.)

# Bibliography

- [1] S. M. Albrecht, A. P. Higginbotham, M. Madsen, F. Kuemmeth, T. S. Jespersen, J. Nygård, P. Krogstrup, and C. M. Marcus. Exponential protection of zero modes in majorana islands. *Nature*, 531(7593):206–209, 03 2016.
- [2] Jason Alicea. Majorana fermions in a tunable semiconductor device. *Phys. Rev. B*, 81:125318, Mar 2010.
- [3] Jason Alicea, Yuval Oreg, Gil Refael, Felix von Oppen, and Matthew P. A. Fisher. Non-abelian statistics and topological quantum information processing in 1d wire networks. *Nat Phys*, 7(5):412–417, 2011.
- [4] B. P. Anderson and M. A. Kasevich. Loading a vapor-cell magneto-optic trap using light-induced atom desorption. *Phys. Rev. A*, 63:023404, Jan 2001.
- [5] M.H. Anderson, J.R. Ensher, M.R. Matthews, C.E. Wieman, and E.A. Cornell. Observation of Bose-Einstein condensation in a dilute atomic vapor. *Science*, 269:198–201, 1995.
- [6] M. R. Andrews, C. G. Townsend, H. J. Miesner, D. S. Durfee, D. M. Kurn, and W. Ketterle. Observation of interference between two Bose-Einstein condensates. *Science*, 275(5300):637–641, 1997.
- [7] Bindiya Arora, M. S. Safronova, and Charles W. Clark. Magic wavelengths for the  $np$ – $ns$  transitions in alkali-metal atoms. *Phys. Rev. A*, 76:052509, Nov 2007.
- [8] W. S. Bakr, A. Peng, M. E. Tai, R. Ma, J. Simon, J. I. Gillen, S. Fölling, L. Pollet, and M. Greiner. Probing the superfluid-to-Mott insulator transition at the single-atom level. *Science*, 329(5991):547–550, 2010.
- [9] Waseem S. Bakr. *Microscopic Studies of Quantum Phase Transitions in Optical Lattices*. PhD thesis, Harvard University, 2011.
- [10] Waseem S. Bakr, Jonathon I. Gillen, Amy Peng, Simon Fölling, and Markus Greiner. A quantum gas microscope for detecting single atoms in a Hubbard-regime optical lattice. *Nature*, 462(7269):74–77, 2009.

- [11] Jean-Sébastien Bernier, Corinna Kollath, Antoine Georges, Lorenzo De Leo, Fabrice Gerbier, Christophe Salomon, and Michael Köhl. Cooling fermionic atoms in optical lattices by shaping the confinement. *Phys. Rev. A*, 79:061601, Jun 2009.
- [12] R. Blankenbecler, D. J. Scalapino, and R. L. Sugar. Monte carlo calculations of coupled boson-fermion systems. i. *Phys. Rev. D*, 24:2278–2286, Oct 1981.
- [13] S. Blatt, A. Maziurenko, M. F. Parsons, C. S. Chiu, F. Huber, and M. Greiner. Low-noise optical lattices for ultracold  ${}^6\text{Li}$ . *Phys. Rev. A*, 92:021402, Aug 2015.
- [14] Immanuel Bloch, Jean Dalibard, and Wilhelm Zwerger. Many-body physics with ultracold gases. *Rev. Mod. Phys.*, 80(3):885–964, 2008.
- [15] Martin Boll, Timon A. Hilker, Guillaume Salomon, Ahmed Omran, Jacopo Nespoli, Lode Pollet, Immanuel Bloch, and Christian Gross. Spin- and density-resolved microscopy of antiferromagnetic correlations in fermi-hubbard chains. *Science*, 353(6305):1257–1260, 2016.
- [16] Eric Braaten and Lucas Platter. Exact relations for a strongly interacting fermi gas from the operator product expansion. *Phys. Rev. Lett.*, 100(20):205301, 2008.
- [17] Peter T. Brown, Debayan Mitra, Elmer Guardado-Sánchez, Peter Schauß, S. Stanimir Kondov, Ehsan Khatami, Thereza Paiva, Nandini Trivedi, David A. Huse, and Waseem S. Bakr. Observation of canted antiferromagnetism with ultracold fermions in an optical lattice. *preprint arXiv:1612.07746*, 2016.
- [18] Henrik Bruus and Karsten Flensberg. *Many-Body Quantum Theory in Condensed Matter Physics*. Oxford University Press, 2004.
- [19] J.P. Burke, Jr., C.H. Greene, and J.L. Bohn. Multichannel cold collisions: Simple dependences on energy and magnetic field. *Phys. Rev. Lett.*, 81:3355, 1998.
- [20] Lawrence W. Cheuk, Matthew A. Nichols, Katherine R. Lawrence, Melih Okan, Hao Zhang, Ehsan Khatami, Nandini Trivedi, Thereza Paiva, Marcos Rigol, and Martin W. Zwierlein. Observation of spatial charge and spin correlations in the 2d fermi-hubbard model. *Science*, 353(6305):1260, 09 2016.
- [21] Lawrence W. Cheuk, Matthew A. Nichols, Katherine R. Lawrence, Melih Okan, Hao Zhang, and Martin W. Zwierlein. Observation of 2d fermionic mott insulators of  ${}^{40}\text{K}$  with single-site resolution. *Phys. Rev. Lett.*, 116:235301, Jun 2016.
- [22] Lawrence W. Cheuk, Matthew A. Nichols, Melih Okan, Thomas Gersdorf, Vinay V. Ramasesh, Waseem S. Bakr, Thomas Lompe, and Martin W. Zwierlein. Quantum-gas microscope for fermionic atoms. *Phys. Rev. Lett.*, 114:193001, 2015.

- [23] Lawrence W. Cheuk, Ariel T. Sommer, Zoran Hadzibabic, Tarik Yefsah, Waseem S. Bakr, and Martin W. Zwierlein. Spin-injection spectroscopy of a spin-orbit coupled fermi gas. *Phys. Rev. Lett.*, 109(9):095302, 2012.
- [24] Cheng Chin, Rudolf Grimm, Paul Julienne, and Elite Tiesinga. Feshbach resonances in ultracold gases. *Rev. Mod. Phys.*, 82(2):1225, 2010.
- [25] J.K. Chin, D.E. Miller, Y. Liu, C. Stan, W. Setiawan, C. Sanner, K. Xu, and W. Ketterle. Evidence for superfluidity of ultracold fermions in an optical lattice. *Nature*, 443(7114):961–964, 2006.
- [26] C. Cohen-Tannoudji, J. Dupont-Roc, and G. Grynberg. *Atom-Photon Interactions*. Wiley, New York, 1992.
- [27] Jean Dalibard, Fabrice Gerbier, Gediminas Juzeliūnas, and Patrik Ōhberg. Colloquium. *Rev. Mod. Phys.*, 83:1523–1543, Nov 2011.
- [28] Andrea Damascelli, Zahid Hussain, and Zhi-Xun Shen. Angle-resolved photoemission studies of the cuprate superconductors. *Rev. Mod. Phys.*, 75(2):473, 2003.
- [29] K. B. Davis, M.-O. Mewes, M. R. Andrews, N. J. van Druten, D. S. Durfee, D. M. Kurn, and W. Ketterle. Bose-Einstein condensation in a gas of sodium atoms. *Phys. Rev. Lett.*, 75(22):3969–3973, 1995.
- [30] B. DeMarco and D.S. Jin. Onset of Fermi degeneracy in a trapped atomic gas. *Science*, 285:1703–1706, 1999.
- [31] Rémi Desbuquois, Tarik Yefsah, Lauriane Chomaz, Christof Weitenberg, Laura Corman, Sylvain Nascimbène, and Jean Dalibard. Determination of scale-invariant equations of state without fitting parameters: Application to the two-dimensional bose gas across the berezinskii-kosterlitz-thouless transition. *Phys. Rev. Lett.*, 113(2):020404, 2014.
- [32] Raimundo R. dos Santos. Introduction to quantum Monte Carlo simulations for fermionic systems. *Brazilian Journal of Physics*, 33:36 – 54, 03 2003.
- [33] G. J. A. Edge, R. Anderson, D. Jervis, D. C. McKay, R. Day, S. Trotzky, and J. H. Thywissen. Imaging and addressing of individual fermionic atoms in an optical lattice. *Phys. Rev. A*, 92:063406, 2015.
- [34] M. Endres, M. Cheneau, T. Fukuhara, C. Weitenberg, P. Schauß, C. Gross, L. Mazza, M. C. Bañuls, L. Pollet, I. Bloch, and S. Kuhr. Observation of correlated particle-hole pairs and string order in low-dimensional mott insulators. *Science*, 334(6053):200–203, 2011.
- [35] M. Endres, M. Cheneau, T. Fukuhara, C. Weitenberg, P. Schauß, C. Gross, L. Mazza, M. C. Bañuls, L. Pollet, I. Bloch, and S. Kuhr. Single-site- and single-atom-resolved measurement of correlation functions. *Appl. Phys. B*, 113(1):27–39, 2013.

- [36] T. Esslinger. Fermi-Hubbard physics with atoms in an optical lattice. *Annu. Rev. Condens. Matter Phys.*, 1:129–152, 2010.
- [37] Michael Feld, Bernd Frohlich, Enrico Vogt, Marco Koschorreck, and Michael Kohl. Observation of a pairing pseudogap in a two-dimensional fermi gas. *Nature*, 480(7375):75–78, 2011.
- [38] Bernd Fröhlich, Michael Feld, Enrico Vogt, Marco Koschorreck, Wilhelm Zwerger, and Michael Köhl. Radio-frequency spectroscopy of a strongly interacting two-dimensional fermi gas. *Phys. Rev. Lett.*, 106(10):105301, 2011.
- [39] Bryce Gadway. Atom-optics approach to studying transport phenomena. *Phys. Rev. A*, 92:043606, Oct 2015.
- [40] Victor Galitski and Ian B. Spielman. Spin-orbit coupling in quantum gases. *Nature*, 494(7435):49–54, 02 2013.
- [41] Thomas Christian Joachim Gersdorf. *A Quantum Gas Microscope for Fermionic Atoms*. Masters thesis, ETH Zürich, 2012.
- [42] A. Gozzini, F. Mango, J. H. Xu, G. Alzetta, F. Maccarrone, and R. A. Bernheim. Light-induced ejection of alkali atoms in polysiloxane coated cells. *Il Nuovo Cimento D*, 15(5):709–722, 1993.
- [43] S. R. Granade, M. E. Gehm, K. M. O’Hara, and J. E. Thomas. All-optical production of a degenerate Fermi gas. *Phys. Rev. Lett.*, 88:120405, 2002.
- [44] D. Greif, T. Uehlinger, G. Jotzu, L. Tarruell, and T. Esslinger. Short-range quantum magnetism of ultracold fermions in an optical lattice. *Science*, 340(6138):1307–1310, 2013.
- [45] Daniel Greif, Maxwell F. Parsons, Anton Mazurenko, Christie S. Chiu, Sebastian Blatt, Florian Huber, Geoffrey Ji, and Markus Greiner. Site-resolved imaging of a fermionic mott insulator. *Science*, 351(6276):953–957, 2016.
- [46] S. Gupta, Z. Hadzibabic, M.W. Zwierlein, C.A. Stan, K. Dieckmann, C.H. Schunck, E.G.M. van Kempen, B.J. Verhaar, and W. Ketterle. RF spectroscopy of ultracold fermions. *Science*, 300:1723–1726, 2003.
- [47] Z. Hadzibabic. *Studies of a Quantum Degenerate Fermionic Lithium Gas*. Ph.d. thesis, Massachusetts Institute of Technology, 2003.
- [48] Z. Hadzibabic, C. A. Stan, K. Dieckmann, S. Gupta, M.W. Zwierlein, A. Goyert, and W. Ketterle. Two species mixture of quantum degenerate Bose and Fermi gases. *Phys. Rev. Lett.*, 88:160401, 2002.
- [49] Zoran Hadzibabic, Peter Kruger, Marc Cheneau, Baptiste Battelier, and Jean Dalibard. Berezinskii-kosterlitz-thouless crossover in a trapped atomic gas. *Nature*, 441(7097):1118–1121, 2006.

- [50] F. D. M. Haldane. Model for a quantum hall effect without landau levels: Condensed-matter realization of the "parity anomaly". *Phys. Rev. Lett.*, 61(18):2015–2018, 1988.
- [51] E. Haller, J. Hudson, A. Kelly, D. A. Cotta, B. Peaudecerf, G. D. Bruce, and S. Kuhr. Single-atom imaging of fermions in a quantum-gas microscope. *Nat. Phys.*, 11:738–742, 2015.
- [52] R. A. Hart, P. M. Duarte, Tsung-Lin Yang, X. Liu, T. Paiva, E. Khatami, R. T. Scalettar, N. Trivedi, D. A. Huse, and R. G. Hulet. Observation of anti-ferromagnetic correlations in the Hubbard model with ultracold atoms. *Nature*, 519:211–214, 2015.
- [53] M. Z. Hasan and C. L. Kane. Colloquium: Topological insulators. *Rev. Mod. Phys.*, 82(4):3045–3067, 2010.
- [54] A. J. Heeger, S. Kivelson, J. R. Schrieffer, and W. P. Su. Solitons in conducting polymers. *Rev. Mod. Phys.*, 60(3):781–850, 1988.
- [55] Michael Hermele and Victor Gurarie. Topological liquids and valence cluster states in two-dimensional  $su(n)$  magnets. *Physical Review B*, 84(17):174441–, 11 2011.
- [56] Michael Hermele, Victor Gurarie, and Ana Maria Rey. Mott insulators of ultracold fermionic alkaline earth atoms: Underconstrained magnetism and chiral spin liquid. *Physical Review Letters*, 103(13):135301–, 09 2009.
- [57] J. Higbie and D. M. Stamper-Kurn. Periodically dressed bose-einstein condensate: A superfluid with an anisotropic and variable critical velocity. *Phys. Rev. Lett.*, 88:090401, Feb 2002.
- [58] Timon A. Hilker, Guillaume Salomon, Fabian Grusdt, Ahmed Omran, Martin Boll, Eugene Demler, Immanuel Bloch, and Christian Gross. Revealing hidden antiferromagnetic correlations in doped hubbard chains via string correlators. *preprint arXiv:1702.00642*, 2017.
- [59] Tin-Lun Ho and Qi Zhou. Squeezing out the entropy of fermions in optical lattices. *Proc. Natl. Acad. Sci.*, 106(17):6916–6920, 2009.
- [60] Carsten Honerkamp and Walter Hofstetter. Ultracold fermions and the  $SU(n)$  hubbard model. *Phys. Rev. Lett.*, 92:170403, Apr 2004.
- [61] Florian Gerhard Huber. *Site-Resolved Imaging with the Fermi Gas Microscope*. Ph.d. thesis, Harvard University, 2014.
- [62] Chen-Lung Hung, Xibo Zhang, Nathan Gemelke, and Cheng Chin. Observation of scale invariance and universality in two-dimensional bose gases. *Nature*, 470(7333):236–239, 2012.

- [63] M Inguscio, W Ketterle, and C Salomon, editors. *Ultracold Fermi Gases*. Proceedings of the International School of Physics "Enrico Fermi", Course CLXIV, Varenna, 20 - 30 June 2006. IOS Press, Amsterdam, 2008.
- [64] R. Islam, R. Ma, P. M. Preiss, M. E. Tai, A. Lukin, M. Rispoli, and M. Greiner. Measuring entanglement entropy in a quantum many-body system. *Nature*, 528(15750):77–83, 2015.
- [65] R. Jackiw and C. Rebbi. Solitons with fermion number 1/2. *Phys. Rev. D*, 13(12):3398–3409, 1976.
- [66] S. Jochim, M. Bartenstein, G. Hendl, J. Hecker-Denschlag, R. Grimm, A. Mosk, and M. Weidemüller. Magnetic field control of elastic scattering in a cold gas of fermionic lithium atoms. *Phys. Rev. Lett.*, 89:273202, 2002.
- [67] Robert Jördens, Niels Strohmaier, Kenneth Günter, Henning Moritz, and Tilman Esslinger. A Mott insulator of fermionic atoms in an optical lattice. *Nature*, 455(7210):204–207, 2008.
- [68] Gregor Jotzu, Michael Messer, Remi Desbuquois, Martin Lebrat, Thomas Uehlinger, Daniel Greif, and Tilman Esslinger. Experimental realization of the topological haldane model with ultracold fermions. *Nature*, 515(7526):237–240, 11 2014.
- [69] A. M. Kaufman, B. J. Lester, and C. A. Regal. Cooling a single atom in an optical tweezer to its quantum ground state. *Phys. Rev. X*, 2:041014, Nov 2012.
- [70] Adam M. Kaufman, M. Eric Tai, Alexander Lukin, Matthew Rispoli, Robert Schittko, Philipp M. Preiss, and Markus Greiner. Quantum thermalization through entanglement in an isolated many-body system. *Science*, 353(6301):794–800, 2016.
- [71] Andrew J. Kerman, Vladan Vuletić, Cheng Chin, and Steven Chu. Beyond optical molasses: 3D raman sideband cooling of atomic cesium to high phase-space density. *Phys. Rev. Lett.*, 84:439, 2000.
- [72] W. Ketterle, D.S. Durfee, and D.M. Stamper-Kurn. Making, probing and understanding Bose-Einstein condensates. In M. Inguscio, S. Stringari, and C.E. Wieman, editors, *Bose-Einstein condensation in atomic gases, Proceedings of the International School of Physics Enrico Fermi, Course CXL, Varenna, 7-17 July 1998*, pages 67–176. IOS Press, Amsterdam, 1999.
- [73] W. Ketterle and M.W. Zwierlein. Making, probing and understanding ultracold Fermi gases. In M. Inguscio, W. Ketterle, and C. Salomon, editors, *Ultracold Fermi Gases, Proceedings of the International School of Physics "Enrico Fermi", Course CLXIV, Varenna, 20 - 30 June 2006. Reprinted in Rivista del Nuovo Cimento*, 31(5), 247 (2008). IOS Press, Amsterdam., 2008.

- [74] Ehsan Khatami and Marcos Rigol. Thermodynamics of strongly interacting fermions in two-dimensional optical lattices. *Phys. Rev. A*, 84:053611, 2011.
- [75] C. Klempert, T. van Zoest, T. Henninger, O. Topic, E. Rasel, W. Ertmer, and J. Arlt. Ultraviolet light-induced atom desorption for large rubidium and potassium magneto-optical traps. *Phys. Rev. A*, 73:013410, Jan 2006.
- [76] Michael Knap, Adrian Kantian, Thierry Giamarchi, Immanuel Bloch, Mikhail D. Lukin, and Eugene Demler. Probing real-space and time-resolved correlation functions with many-body ramsey interferometry. *Phys. Rev. Lett.*, 111:147205, Oct 2013.
- [77] Michael Köhl, Henning Moritz, Thilo Stöferle, Kenneth Günter, and Tilman Esslinger. Fermionic atoms in a three dimensional optical lattice: Observing Fermi surfaces, dynamics, and interactions. *Phys. Rev. Lett.*, 94:080403, 2005.
- [78] J. S. Krauser, J. Heinze, S. Götze, M. Langbecker, N. Fläschner, L. Cook, T. M. Hanna, E. Tiesinga, K. Sengstock, and C. Becker. Investigation of feshbach resonances in ultracold  $^{40}\text{K}$  spin mixtures. *Phys. Rev. A*, 95:042701, Apr 2017.
- [79] Mark J. H. Ku. *Thermodynamics and solitonic excitations of a strongly-interacting Fermi gas*. PhD thesis, Massachusetts Institute of Technology, 2015.
- [80] Mark J. H. Ku, Ariel T. Sommer, Lawrence W. Cheuk, and Martin W. Zwierlein. Revealing the superfluid lambda transition in the universal thermodynamics of a unitary Fermi gas. *Science*, 335(6068):563–567, 2012.
- [81] Mark J.H. Ku, Wenjie Ji, Biswaroop Mukherjee, Elmer Guardado-Sánchez, Lawrence W. Cheuk, Tarik Yefsah, and Martin W. Zwierlein. Motion of a solitonic vortex in the bec-bcs crossover. *Phys. Rev. Lett.*, 113:065301, 2014.
- [82] Christian Langmack, Marcus Barth, Wilhelm Zwerger, and Eric Braaten. Clock shift in a strongly interacting two-dimensional fermi gas. *Physical Review Letters*, 108(6):060402–, 02 2012.
- [83] Patrick A. Lee, Naoto Nagaosa, and Xiao-Gang Wen. Doping a Mott insulator: Physics of high-temperature superconductivity. *Rev. Mod. Phys.*, 78(1):17, 2006.
- [84] Junru Li, Wujie Huang, Boris Shteynas, Sean Burchesky, Furkan Çağrı Top, Edward Su, Jeongwon Lee, Alan O. Jamison, and Wolfgang Ketterle. Spin-orbit coupling and spin textures in optical superlattices. *Phys. Rev. Lett.*, 117:185301, Oct 2016.
- [85] Y. J. Lin, K. Jimenez-Garcia, and I. B. Spielman. Spin-orbit-coupled bose-einstein condensates. *Nature*, 471(7336):83–86, 2011.

- [86] E. Y. Loh and J. E. Gubernatis. Stable numerical simulations of models of interacting electrons in condensed-matter physics. In W. Hanke and Y. V. Kopaev, editors, *Modern Problems in Condensed Matter Sciences*, volume 32, pages 177–235, Amsterdam, 1992. North-Holland.
- [87] Anton Masurenko, Christie S. Chiu, Geoffrey Ji, Maxwell F. Parsons, Márton Kanász-Nagy, Richard Schmidt, Fabian Grusdt, Eugene Demler, Daniel Greif, and Markus Greiner. Experimental realization of a long-range antiferromagnet in the hubbard model with ultracold atoms. *preprint arXiv:1612.08436*, 2016.
- [88] J. M. McGuirk, D. M. Harber, J. M. Obrecht, and E. A. Cornell. Alkali-metal adsorbate polarization on conducting and insulating surfaces probed with bose-einstein condensates. *Phys. Rev. A*, 69:062905, Jun 2004.
- [89] Martin Miranda, Ryotaro Inoue, Yuki Okuyama, Akimasa Nakamoto, and Mikio Kozuma. Site-resolved imaging of ytterbium atoms in a two-dimensional optical lattice. *Phys. Rev. A*, 91:063414, Jun 2015.
- [90] G. Modugno, C. Benkő, P. Hannaford, G. Roati, and M. Inguscio. Sub-doppler laser cooling of fermionic  $^{40}\text{K}$  atoms. *Phys. Rev. A*, 60:R3373–R3376, Nov 1999.
- [91] C. Monroe, D. M. Meekhof, B. E. King, S. R. Jefferts, W. M. Itano, D. J. Wineland, and P. Gould. Resolved-sideband Raman cooling of a bound atom to the 3D zero-point energy. *Phys. Rev. Lett.*, 75:4011–4014, Nov 1995.
- [92] V. Mourik, K. Zuo, S. M. Frolov, S. R. Plissard, E. P. A. M. Bakkers, and L. P. Kouwenhoven. Signatures of majorana fermions in hybrid superconductor-semiconductor nanowire devices. *Science*, 336(6084):1003–1007, 2012.
- [93] A. Muramatsu. Quantum Monte Carlo for lattice fermions. In M. P. Nightingale and C. J. Umrigar, editors, *Quantum Monte Carlo Methods in Physics and Chemistry*, pages 343–373, Dordrecht, 1999. NATO Science Series, Kluwer Academic Press.
- [94] Stevan Nadj-Perge, Ilya K. Drozdov, Jian Li, Hua Chen, Sangjun Jeon, Jungpil Seo, Allan H. MacDonald, B. Andrei Bernevig, and Ali Yazdani. Observation of majorana fermions in ferromagnetic atomic chains on a superconductor. *Science*, 346(6209):602–607, 2014.
- [95] Chetan Nayak, Steven H. Simon, Ady Stern, Michael Freedman, and Sankar Das Sarma. Non-abelian anyons and topological quantum computation. *Rev. Mod. Phys.*, 80(3):1083–1159, 2008.
- [96] J. M. Obrecht, R. J. Wild, and E. A. Cornell. Measuring electric fields from surface contaminants with neutral atoms. *Phys. Rev. A*, 75:062903, Jun 2007.
- [97] J. Oitmaa, C. Hamer, and W. Zheng. *Series Expansion Methods for Strongly Interacting Lattice Models*. Cambridge University Press, Cambridge, England, 2006.

- [98] Ahmed Omran, Martin Boll, Timon A. Hilker, Katharina Kleinlein, Guillaume Salomon, Immanuel Bloch, and Christian Gross. Microscopic observation of pauli blocking in degenerate fermionic lattice gases. *Phys. Rev. Lett.*, 115:263001, 2015.
- [99] R. Onofrio, C. Raman, J. M. Vogels, J.R. Abo-Shaeer, A. P. Chikkatur, and W. Ketterle. Observation of superfluid flow in a Bose-Einstein condensed gas. *Phys. Rev. Lett.*, 85:2228–2231, 2000.
- [100] Yuval Oreg, Gil Refael, and Felix von Oppen. Helical liquids and majorana bound states in quantum wires. *Phys. Rev. Lett.*, 105:177002, Oct 2010.
- [101] J. Orenstein and A. J. Millis. Advances in the physics of high-temperature superconductivity. *Science*, 288(5465):468–474, 2000.
- [102] Herwig Ott. Single atom detection in ultracold quantum gases: a review of current progress. *Rep. Prog. Phys.*, 79(5), 2016.
- [103] Thereza Paiva, R. T. Scalettar, Carey Huscroft, and A. K. McMahan. Signatures of spin and charge energy scales in the local moment and specific heat of the half-filled two-dimensional hubbard model. *Phys. Rev. B*, 63:125116, 2001.
- [104] Gunnar Pálsson and Gabriel Kotliar. Thermoelectric response near the density driven mott transition. *Phys. Rev. Lett.*, 80:4775–4778, May 1998.
- [105] Jee Woo Park, Cheng-Hsun Wu, Ibon Santiago, Tobias G. Tiecke, Sebastian Will, Peyman Ahmadi, and Martin W. Zwierlein. Quantum degenerate bose-fermi mixture of chemically different atomic species with widely tunable interactions. *Phys. Rev. A*, 85:051602, May 2012.
- [106] Maxwell F. Parsons, Florian Huber, Anton Mazurenko, Christie S. Chiu, Widagdo Setiawan, Katherine Wooley-Brown, Sebastian Blatt, and Markus Greiner. Site-resolved imaging of fermionic  ${}^6\text{Li}$  in an optical lattice. *Phys. Rev. Lett.*, 114:213002, 2015.
- [107] Maxwell F. Parsons, Anton Mazurenko, Christie S. Chiu, Geoffrey Ji, Daniel Greif, and Markus Greiner. Site-resolved observations of antiferromagnetic correlations in the hubbard model. *preprint arXiv:1605.02704*, 2016.
- [108] Y. S. Patil, S. Chakram, L. M. Aycock, and M. Vengalattore. Nondestructive imaging of an ultracold lattice gas. *Phys. Rev. A*, 90:033422, Sep 2014.
- [109] D. S. Petrov and G. V. Shlyapnikov. Interatomic collisions in a tightly confined bose gas. *Phys. Rev. A*, 64:012706, Jun 2001.
- [110] Hannes Pichler, Lars Bonnes, Andrew J. Daley, Andreas M. Läuchli, and Peter Zoller. Thermal versus entanglement entropy: a measurement protocol for fermionic atoms with a quantum gas microscope. *New Journal of Physics*, 15(063003), 2013.

- [111] L. P. Pitaevskii and A. Rosch. Breathing modes and hidden symmetry of trapped atoms in two dimensions. *Phys. Rev. A*, 55:R853–R856, Feb 1997.
- [112] Philipp M. Preiss, Ruichao Ma, M. Eric Tai, Alexander Lukin, Matthew Rispoli, Philip Zupancic, Yoav Lahini, Rajibul Islam, and Markus Greiner. Strongly correlated quantum walks in optical lattices. *Science*, 347(6227):1229, 03 2015.
- [113] Th. Pruschke, D. L. Cox, and M. Jarrell. Hubbard model at infinite dimensions: Thermodynamic and transport properties. *Phys. Rev. B*, 47:3553–3565, Feb 1993.
- [114] Xiao-Liang Qi and Shou-Cheng Zhang. Topological insulators and superconductors. *Rev. Mod. Phys.*, 83(4):1057–1110, 2011.
- [115] C. Raman, J.R. Abo-Shaeer, J. M. Vogels, K. Xu, and W. Ketterle. Vortex nucleation in a stirred Bose-Einstein condensate. *Phys. Rev. Lett.*, 87:210402, 2001.
- [116] Vinay Venkatesh Ramasesh. *Construction of a Quantum Gas Microscope for Fermionic Atoms*. Ph.d. thesis, Massachusetts Institute of Technology, 2013.
- [117] Mohit Randeria, Ji-Min Duan, and Lih-Yir Shieh. Bound states, Cooper pairing, and Bose condensation in two dimensions. *Phys. Rev. Lett.*, 62(9):981, 1989.
- [118] Ákos Rapp and Achim Rosch. Ground-state phase diagram of the repulsive  $su(3)$  hubbard model in the gutzwiller approximation. *Phys. Rev. A*, 83:053605, May 2011.
- [119] C. A. Regal, M. Greiner, and D. S. Jin. Observation of resonance condensation of fermionic atom pairs. *Phys. Rev. Lett.*, 92(4):040403, 2004.
- [120] Cindy A. Regal. *Experimental realization of BCS-BEC crossover physics with a Fermi gas of atoms*. Ph.d. thesis, University of Colorado, 2005.
- [121] Marcos Rigol, Tyler Bryant, and Rajiv R. P. Singh. Numerical linked-cluster approach to quantum lattice models. *Phys. Rev. Lett.*, 97:187202, Nov 2006.
- [122] M. J. Rozenberg, G. Kotliar, H. Kajueter, G. A. Thomas, D. H. Rapkine, J. M. Honig, and P. Metcalf. Optical conductivity in mott-hubbard systems. *Phys. Rev. Lett.*, 75:105–108, Jul 1995.
- [123] Brandon P. Ruzic, Chris H. Greene, and John L. Bohn. Quantum defect theory for high-partial-wave cold collisions. *Phys. Rev. A*, 87:032706, Mar 2013.
- [124] Jay D. Sau, Roman M. Lutchyn, Sumanta Tewari, and S. Das Sarma. Generic new platform for topological quantum computation using semiconductor heterostructures. *Phys. Rev. Lett.*, 104(4):040502, 2010.

- [125] U. Schneider, L. Hackermüller, S. Will, Th Best, I. Bloch, T. A. Costi, R. W. Helmes, D. Rasch, and A. Rosch. Metallic and insulating phases of repulsively interacting fermions in a 3D optical lattice. *Science*, 322(5907):1520–1525, 2008.
- [126] Ulrich Schneider. *Interacting Fermionic Atoms in Optical Lattices - A Quantum Simulator for Condensed Matter Physics*. Ph.d. thesis, Johannes Gutenberg-Universitat, 2010.
- [127] F. Schreck, L. Khaykovich, K. L. Corwin, G. Ferrari, T. Bourdel, J. Cubizolles, and C. Salomon. Quasipure Bose-Einstein condensate immersed in a Fermi sea. *Phys. Rev. Lett.*, 87:080403, 2001.
- [128] Jacob F. Sherson, Christof Weitenberg, Manuel Endres, Marc Cheneau, Immanuel Bloch, and Stefan Kuhr. Single-atom-resolved fluorescence imaging of an atomic Mott insulator. *Nature*, 467(7311):68–72, 2010.
- [129] Jonathan Simon, Waseem Bakr, Ruichao Ma, M. Eric Tai, Philipp M. Preiss, and Markus Greiner. Quantum simulation of antiferromagnetic spin chains in an optical lattice. *Nature*, 472(7343):307–312, 2011.
- [130] Ariel T. Sommer. *Strongly Interacting Fermi Gases: Non-Equilibrium Dynamics and Dimensional Crossover*. PhD thesis, Massachusetts Institute of Technology, 2013.
- [131] Ariel T. Sommer, Lawrence W. Cheuk, Mark J. H. Ku, Waseem S. Bakr, and Martin W. Zwierlein. Evolution of fermion pairing from three to two dimensions. *Phys. Rev. Lett.*, 108(4):045302, 2012.
- [132] D. M. Stamper-Kurn, H. J. Miesner, S. Inouye, M. R. Andrews, and W. Ketterle. Collisionless and hydrodynamic excitations of a Bose-Einstein condensate. *Phys. Rev. Lett.*, 81(3):500–503, 1998.
- [133] J. Struck, J. Simonet, and K. Sengstock. Spin-orbit coupling in periodically driven optical lattices. *Phys. Rev. A*, 90:031601, Sep 2014.
- [134] Baoming Tang, Ehsan Khatami, and Marcos Rigol. A short introduction to numerical linked-cluster expansions. *Computer Physics Communications*, 184(3):557 – 564, 2013.
- [135] J. D. Thompson, T. G. Tiecke, A. S. Zibrov, V. Vuletić, and M. D. Lukin. Coherence and Raman sideband cooling of a single atom in an optical tweezer. *Phys. Rev. Lett.*, 110:133001, 2013.
- [136] Matthias Troyer and Uwe-Jens Wiese. Computational complexity and fundamental limitations to fermionic quantum monte carlo simulations. *Phys. Rev. Lett.*, 94:170201, 2005.

- [137] Andrew G. Truscott, Kevin E. Strecker, William I. McAlexander, Guthrie B. Partridge, and Randall G. Hulet. Observation of Fermi pressure in a gas of trapped atoms. *Science*, 291:2570–2572, 2001.
- [138] K. Van Houcke, F. Werner, E. Kozik, N. Prokof/'ev, B. Svistunov, M. J. H. Ku, A. T. Sommer, L. W. Cheuk, A. Schirotzek, and M. W. Zwierlein. Feynman diagrams versus fermi-gas feynman emulator. *Nat Phys*, 8(5):366–370, 2012.
- [139] J.M. Vogels, K. Xu, C. Raman, J. R. Abo-Shaeer, and W. Ketterle. Experimental observation of the bogoliubov transformation for a Bose-Einstein condensed gas. *Phys. Rev. Lett.*, 88:060402, 2002.
- [140] Enrico Vogt, Michael Feld, Bernd Fröhlich, Daniel Pertot, Marco Koschorreck, and Michael Köhl. Scale invariance and viscosity of a two-dimensional fermi gas. *Phys. Rev. Lett.*, 108:070404, Feb 2012.
- [141] Vladan Vuletić, Cheng Chin, Andrew J. Kerman, and Steven Chu. Degenerate Raman sideband cooling of trapped cesium atoms at very high atomic densities. *Phys. Rev. Lett.*, 81:5768–5771, Dec 1998.
- [142] Pengjun Wang, Zeng-Qiang Yu, Zhengkun Fu, Jiao Miao, Lianghui Huang, Shijie Chai, Hui Zhai, and Jing Zhang. Spin-orbit coupled degenerate fermi gases. *Phys. Rev. Lett.*, 109(9):095301, 2012.
- [143] D. S. Weiss, J. Vala, A. V. Thapliyal, S. Myrgren, U. Vazirani, and K. B. Whaley. Another way to approach zero entropy for a finite system of atoms. *Phys. Rev. A*, 70:040302, 2004.
- [144] Christof Weitenberg. *Single-Atom Resolved Imaging and Manipulation in an Atomic Mott Insulator*. PhD thesis, Ludwig-Maximilians-Universität München, 2011.
- [145] Christof Weitenberg, Manuel Endres, Jacob F. Sherson, Marc Cheneau, Peter Schausz, Takeshi Fukuhara, Immanuel Bloch, and Stefan Kuhr. Single-spin addressing in an atomic mott insulator. *Nature*, 471(7338):319–324, 03 2011.
- [146] S. R. White, D. J. Scalapino, R. L. Sugar, E. Y. Loh, J. E. Gubernatis, and R. T. Scalettar. Numerical study of the two-dimensional hubbard model. *Phys. Rev. B*, 40:506–516, Jul 1989.
- [147] R. A. Williams, M. C. Beeler, L. J. LeBlanc, K. Jiménez-García, and I. B. Spielman. Raman-induced interactions in a single-component fermi gas near an s-wave feshbach resonance. *Phys. Rev. Lett.*, 111(9):095301, 2013.
- [148] Cheng-Hsun Wu. *Strongly Interacting Quantum Mixtures of Ultracold Atoms*. Ph.d. thesis, Massachusetts Institute of Technology, 2013.

- [149] Tarik Yefsah, Ariel T. Sommer, Mark J. H. Ku, Lawrence W. Cheuk, Wenjie Ji, Waseem S. Bakr, and Martin W. Zwierlein. Heavy solitons in a fermionic superfluid. *Nature*, 499(7459):426–430, 2013.
- [150] M. W. Zwierlein. *High-temperature superfluidity in an Ultracold Fermi Gas*. PhD thesis, Massachusetts Institute of Technology, 2006.
- [151] M. W. Zwierlein, J. R. Abo-Shaeer, A. Schirotzek, C. H. Schunck, and W. Ketterle. Vortices and superfluidity in a strongly interacting Fermi gas. *Nature*, 435:1047–1051, 2005.
- [152] M.W. Zwierlein, C.A. Stan, C.H. Schunck, S.M.F. Raupach, A.J. Kerman, and W. Ketterle. Condensation of pairs of fermionic atoms near a Feshbach resonance. *Phys. Rev. Lett.*, 92:120403, 2004.